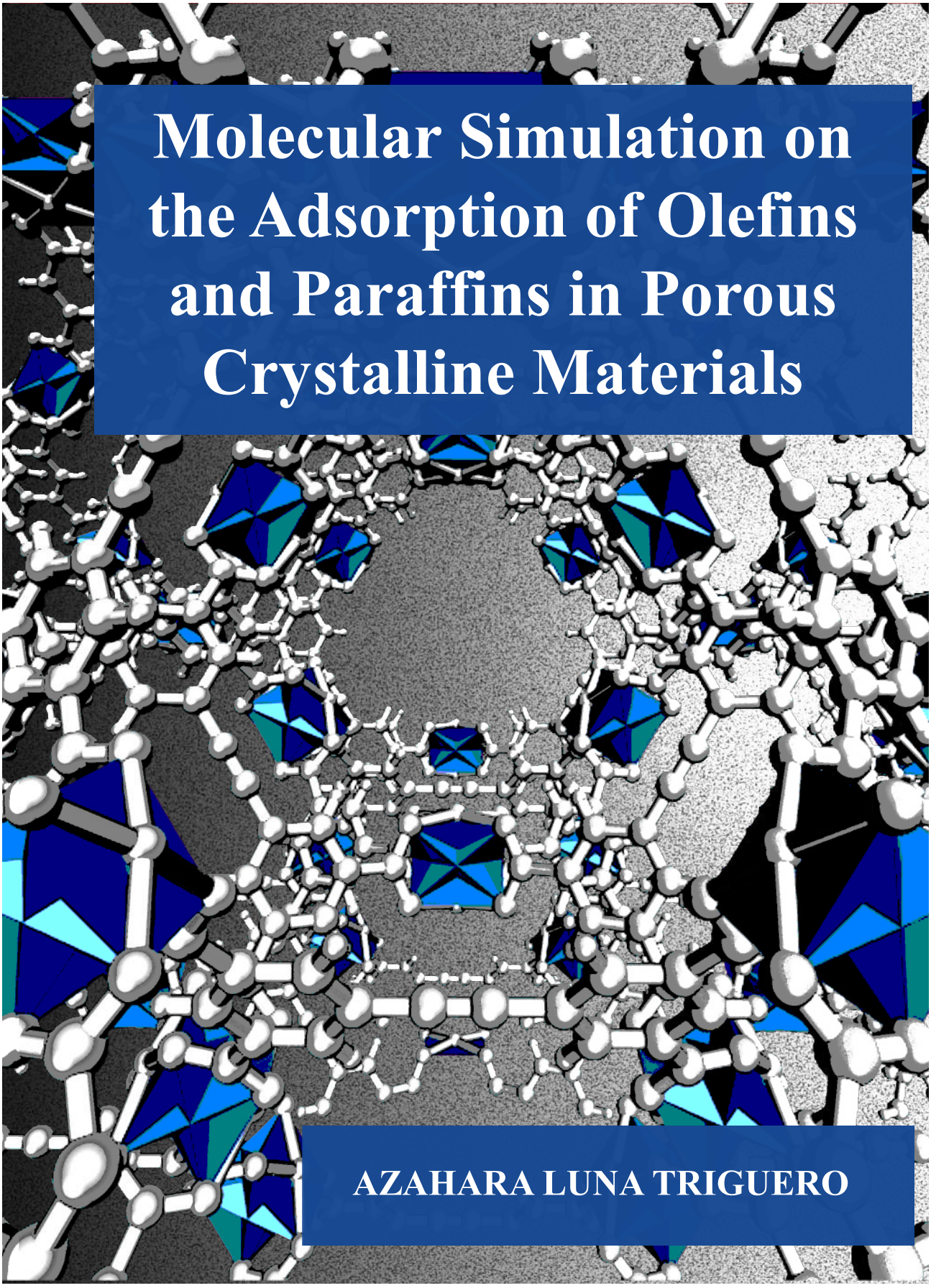

Molecular Simulation on the Adsorption of Olefins and Paraffins in Porous Crystalline Materials

AZAHARA LUNA TRIGUERO

Molecular Simulation on the Adsorption of Olefins and Paraffins in Porous Crystalline Materials

AZAHARA LUNA TRIGUERO

Licenciada en Física

Department of Physical, Chemical, and Natural Systems

UNIVERSITY PABLO DE OLAVIDE

SUPERVISORS

Sofía Calero

Prof. University Pablo de Olavide

Paula Gómez Álvarez

Dr. University of Huelva

Dissertation submitted to obtain the degree of Doctor with international mention.

SEVILLE, JUNE 2019

ISBN: 978-84-09-11339-2

0000-0001-9936-3802

Printed by: LLARdigital

Table of Contents

CHAPTER 1

Introduction

ADSORBATES:

Olefins and Paraffins

Olefins and paraffins are raw materials widely used in petrochemical industry. Their uses are related to the number of carbon atoms. Paraffins from methane to butane are mainly used as fuels for heating and cooking purposes. Methane and ethane are the main components of natural gas.[1,2] Propane is used in gas burners and as a fuel for road vehicles,[3,4] and butane is used for space heating, lighters and as a propellant in aerosol sprays such as deodorants.[5] From pentane to octane, they are used as solvents for nonpolar substances and as fuels in internal combustion engines. The branched isomers are preferred due to their higher octane number.[6] Paraffins from nonane to hexadecane are used in diesel and aviation fuels. Longer saturated hydrocarbons are used as components of fuel oil, lubricants, anticorrosive agents, and paraffin wax.[7]

Light olefins have many uses in chemical industry, specially α-olefins. The worldwide production of ethene and propene is constantly growing and most of their production goes to polyethylene and polypropylene manufacturing.[8] Also, 1-butene, 1-hexene and 1-octene are used as comonomers for high density polyethylene, linear low density polyethylene resins, and butylene oxide products.[9] Another significant use for α-olefins from 4 to 8 carbon atoms is the production of linear aldehyde via oxo synthesis to generate short-chain fatty acid and linear alcohols for plasticizer applications.[10] Olefins from 1-decene to 1-tetradecene are used into aqueous detergent applications. But the main application of 1-decene is in synthetic lubricants and 1-tetradecene is used as fuel, and replacing diesel and kerosene with significant advantages: it is more biodegradable alternative, less toxic, and irritate the skin less.[11] Longer alpha olefins are used to produce linear olefins with internal position of the double bond which are preferred for lubricant manufacturing.[7]

Olefins and paraffins are usually obtained primarily by the steam cracking or as a product of fluid catalytic cracking of gas oils in refineries.[10] The product of this technique is a mixture of linear and branched olefins and paraffins. These molecules need to be separated to obtain high quality products. The most commonly used technique in the industry for this separation is cryogenic distillation.[?] The separation process needs a refrigeration system to liquify the mixture of gases, and gas compressors.[12] The required operational conditions (low temperatures and high pressures) make this process energy-intensive. Cryogenic distillation is based on the differences in the boiling points of the components in the mixture. Olefins and paraffins with the same number of carbon atoms have similar boiling points. Therefore, the olefin/paraffin separation becomes challenging and effectiveness using this technique.

Adsorption-based separation as pressure swing adsorption (PSA) is one of the most promising alternatives. PSA use porous materials to perform the separation of mixtures kinetically and/or thermodynamically.[13,14] The adsorption-based separation technology involves low energy consumption, which can contribute to reduce the emissions of greenhouse gases and their impact in climate change. Also, this technique can reduce significantly the operational expenses.[15] While cryogenic distillation relies in differences in the boiling points of the constituents, adsorptive separations take advantage of their dissimilar physical properties such as kinetic diameter, polarity or polarizability. In this regard, the choice of a proper adsorbent in terms of capacity and selectivity is a key factor in the design of an effective adsorption process.

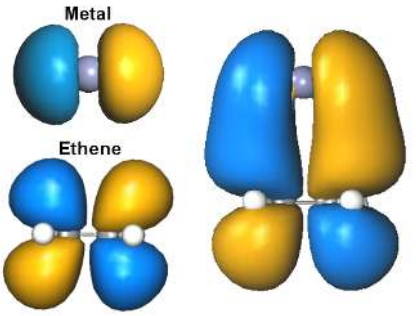

Figure 1. Orbital diagram of isolated metal atom and ethene molecule (left). Representation of π-complexation by orbital overlapping (right).

In this thesis we explore the adsorption separation processes taking advantage of the dissimilar properties of the components of a given mixture. We focus on the π-complexation, also known as π-bonding, between a complexing agent and the double or triple bond of alkenes and alkynes. The π-complex theory is based on the nature of the double bond.[16?] The bouble bond of the olefins is actually formed by the combination of σ-bond and π-bond. The π-bond is a electron probability cloud in a perpendicular plane of the σ-bond plane. The π-bonding is therefore a covalent electron bond because the overlap of electron orbitals of an electron donor

(olefin) and acceptor (Figure 1). The acceptor is usually a transition metal of the d-block.

MATERIALS

Metal Organic Frameworks

Metal-Organic Frameworks (MOFs) are hybrid nanoporous solids constructed by organic ligands connected through metal ions or metal clusters (Figure 2). The organic units are typically di-, tri-, or teradentate ligands.[17,18] The work of Hoskins and Robson[19] was one of the starting points in the study of MOFs. They introduced the design of the construction of three-dimentional structures using organic molecular building blocks and metal ions. After about one decade, MOF-5[20] and HKUST-1[20] were synthesized. The properties observed in these materials such as the robust porosity, the high stability, and the prospect in potential applications promoted the rapidly development of the field. The number of synthetised structures has been increasing and nowadays about 1 million of MOFs have been synthetised and deposited in the Cambridge Structural Database.[21] Their properties (high surface area and pore volume, low density, storage capacity, etc.) have attracted intense research for potential applications. Advantages of MOFs are their controllable porous structure and versatile chemical compositions, high porosity and easy tunability of the pore size and shape from microporous to mesoporous scale by changing the connectivity of the inorganic moiety and the nature and length of the organic linkers.[22–25] MOFs are proposed for many applications including catalysis,[26,27] gas storage,[28,29] and separation,[30] drug delivery,[31?] energy storage,[32] and conversion devices.[33]

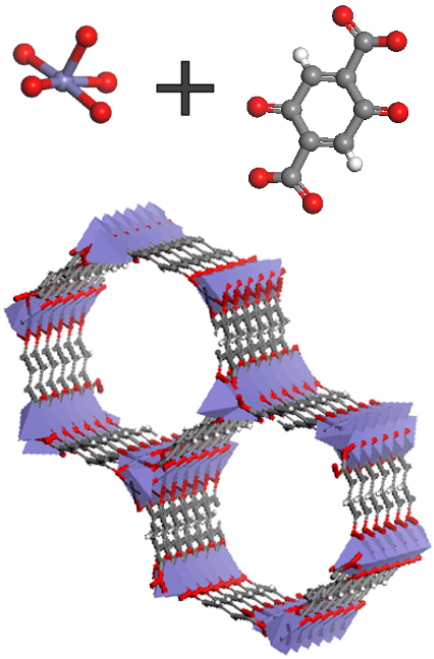

Figure 2. Schematic representation of building units and atomic connectivity of MOF-74.

Among the mentioned properties of MOFs, the structural flexibility or dynamic frameworks are unique characteristics to explore. Flexible MOFs are classified as the 3^{rd} generation,[25,34] being the 1^{st} generation those frameworks with guest molecules that usually collapse after the removal of the guest, and the 2^{nd} generation the robust and stable porous frameworks with permanent poros-

ity. 3^{rd} generation corresponds to flexible frameworks that show reversible structural changes in the presence of external stimuli. Some examples of external stimuli are temperature, pressure, guest molecules, and light. Schneemann et al.[35] distinguish six classes of dynamic frameworks in relation to the dimension on the network. Figure 3 summarizes the modes of framework flexibility induced by guest molecules: Breathing, swelling, linker rotation, and subnetwork displacement. Breathing is defined as reversible transitions from large pore (lp) to narrow pore (np) or *vice versa*, where the displacement of the atoms is accompained by a change in the cell volume. Swelling mode is characterized by gradual changes in the volume of the cell without changes in the space groups. Linker rotation consists on continuous transition where the spatial alignment of a linker rotates around an axis. Subnetwork displacement is a phenomenon showed by interpenetrated three dimentional frameworks. The system has individual non-connected frameworks and the subnets can drift, relocate, or shift in regard to each other.[36]

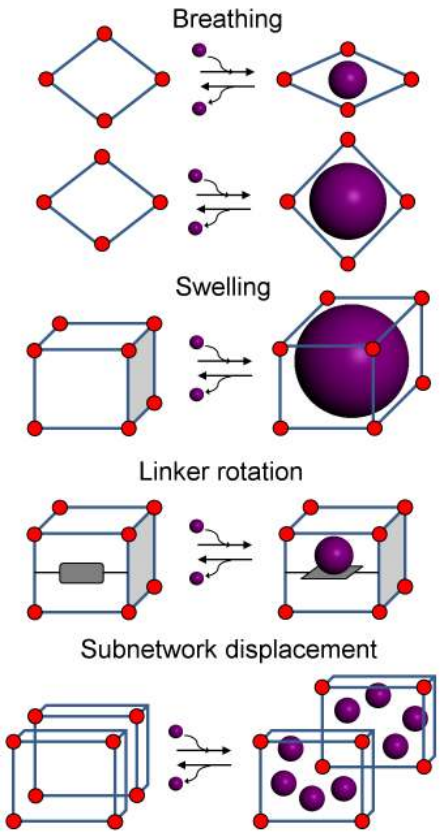

Figure 3. Representation of flexibility modes induced by adsorbed guests.

Zeolites

Zeolites are considered traditional porous solids. The first zeolitic structures were reported at the very begining of 1930s[37–39] and since then, zeolites have been widely studied. More than 245 topologies are identified and indexed in the International Zeolite Assosiation (IZA) Database including natural and synthetized structures.[40] Zeolites are inorganic nanoporous structures with Primary Building Units (PBUs) that are tetrahedral coordinates T atoms,

where T is usually silica or aluminium atoms. T is linked by oxygen atoms forming different configurations of the Secondary Building Units (SBUs). The link of SBUs leads to the formation of three-dimentional framework structures that form uniformly sized pores of molecular dimensions, tipically between 3-10 Å. Different types of zeolites result from differences in the way the T atoms may join in the space (Figure 4). Silica zeolites are based on SiO_4 units, aluminosilicate zeolites consist on SiO_4 and AlO_4 units. Aluminosilicates can be defined as partially substituted zeolite, Si^{4+} by Al^{3+}, where Al-O-Al linkage is forbidden by the Löwenstein rule.[41] The substitutions carry net negative charge in the framework, and extraframework cations are added in order to preserve the electroneutrality of the zeolite. The cations are mobile and exchangeable for other cationic species. Cations are Na^+, Ca^{2+}, Li^+, K^+, Rb^+, Cs^+, Ba^{2+}, Ag^{2+}, among others.[42,43] Since 1982 new families of materials based on zeolitic topologies are described. The most studied are aluminophosphates (AlPO) silicoaluminophospates (SAPO), metaloaluminophosphates (MeAPO), and metallosilicoaluminophosphates (MeAPSO).[44?–47] Zeolites have many industrial applications due to their molecular sieving effects, relatively high surface areas and capacities, and high chemical and thermal stability. They are widely used as molecular sieves, cation exchangers, or catalysts in petrochemical industry. They are also used in industry to remove atmospheric pollutants, separation and recovery of paraffins, and catalysis of hydrocarbon reaction.[48?–50] Other properties such as electrostatic field, hydrophilicity/hydrophobicity and acidity of the surface, depend on topology, composition and nature of cation species. Unlike MOFs, most zeolites have high degree of regularity and rigidity, showing small structural deformations. Nevertheless, some zeolites show phase transitions under external stimuli and fluctuations under hydration.[51,52]

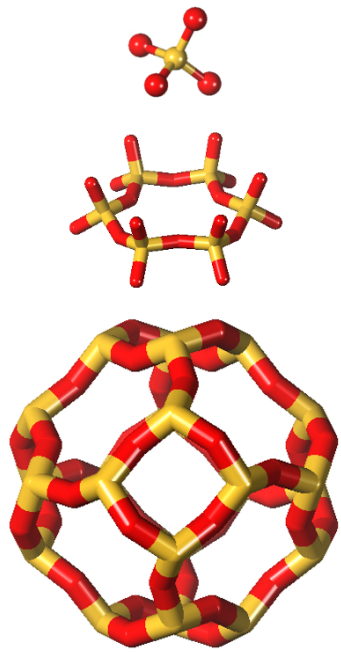

Figure 4. Schematic representation of primary (top) and secondary building units (middle), and atomic connectivity of zeolites (bottom).

METHODS AND MODELS

In this section we summarize the overall molecular simulation techniques applied in this thesis and the most relevant related concepts. Specific details and conditions are described in each chapter.

Statistical Mechanics

In the framework of this thesis, molecular simualations are used to study porous materials (hosts) and the molecules (guests) adsorbed in them. We use classical force fields to model the host, the guest, the guest-guest, and the host-guest interactions. Sometimes we use host-host interactions too. Computer simulations play an important role in the description of the mechanisms that take place inside the systems. They are a useful tool to understand and predict thermodynamic properties for the characterization of the structures.[53?] Therefore they can be used to screen materials for specific end-uses. Molecular simulation allows modelling systems by describing the atomic interations. In this way, we can relate the microscopic properties of the system with macroscopic properties that can be measured experimentally. Molecular simulations can handle systems with many particles, but not all the properties can be measured in a simulation. In other words, not all the quantities computed in simulations correspond to properties measured in experiments. The connection between the microscopic and macroscopic properties can be achieved by using statistical mechanics.[54,55] The first principle of statistical mechanics postulates that, given an isolated system in thermodynamic equilibrium, each microestate with the same total energy has equal probability to be found. The probability density is defined as $\wp(\Gamma) = \delta(H(\Gamma) - E)$ Γ is the space phase, $3N$ spatial and $3N$ linear momentum coordinates, being N the number of particles of the system. H is the Hamiltonian function of the total energy of the system, and $\delta(x)$ is de Dirac function. For a non-isolated system with volume V, temperature T, and number of particles N the determination of the average value of an observable A is related to the sum over the density of all microstates of the system and is proportional to the Boltzmann factor $e^{-\frac{H(\Gamma)}{k_B T}}$ with k_B the Boltzmann constant. The thermal average of the macroscopic property A can be computed as:

$$\langle A \rangle = \frac{\int e^{-\frac{H(\Gamma)}{k_B T}} A(\Gamma) d\Gamma}{\int e^{-\frac{H(\Gamma)}{k_B T}} d\Gamma} \qquad (1.1)$$

where the denominator term corresponds to the partition function: $Z = \int e^{-\frac{H(\Gamma)}{k_B T}} d\Gamma$, and $\wp(\Gamma) = \frac{e^{-\frac{H(\Gamma)}{k_B T}}}{Z}$ represents the probability density of finding the system in a certain microestate, Γ. However, the partition function rarely can be computed. The averages of a thermodynamic property is computed at certain statistical ensemble instead.[54]

Ensembles

A statisitical ensemble represents all the possible microstates compatible with a certain macrostate, these are the accessible microstates.

For systems that are in equilibrium, the thermodynamic state can be specified with a finite and small number of thermodynamic variables. Specifically, only three variables are necessary, one of each pair of extensive/intensive variables: $[N, \mu]$ number of particles or chemical potential, $[V, P]$ volume or pressure, and $[E, T]$ internal energy and temperature. Eight possible statistical ensembles can be described and the labels correspond to the variables that define the macrostate.[53?]

Based on the systems and properties studied in this thesis, the statistical ensembles used are canonical ensemble, isobaric-isothermal ensemble, and grand-canonical ensemble.[54] These ensembles are described in detail below.

Canonical ensemble NVT

The canonical ensemble is the statistical ensemble formed by all the accessible microstates of a mechanical system characterized by the invariability of the number of particles N, volume V, and temperature T. It is useful to describe closed systems in thermal equilibrium.[53?] The partition function is:

$$Z_{NVT} = \frac{1}{\Lambda^{3N} N!} \int e^{-\frac{U(\vec{r}^N)}{k_B T}} (\vec{r}^N) d\vec{r}^N \quad (1.2)$$

The de Broglie wavelength $\Lambda = \sqrt{\frac{h^2}{(2\pi m k_B T)}}$ is the quantum mechanical wavelength of a gas particle with momentum determined by the average thermal kinetic energy per degree of freedom $k_B T$. $\vec{r}^N$ is a 3N-dimensional vector which contains the information of the position of the N particles of the system and $U(\vec{r}^N)$ is the total potential energy of the system. The probability of finding the system in a configuration $\vec{r}^N$ is given by

$$\wp_{NVT} \propto e^{-\frac{U(\vec{r}^N)}{k_B T}} \quad (1.3)$$

The average of the macroscopic property A in NVT ensemble is

$$\langle A(\vec{r}^N) \rangle = \frac{\int e^{-\frac{U(\vec{r}^N)}{k_B T}} A(\vec{r}^N) d\vec{r}^N}{\int e^{-\frac{U(\vec{r}^N)}{k_B T}} d\vec{r}^N} \quad (1.4)$$

Isobaric-isothermal ensemble NPT

The isothemal-isobaric ensemble is the statistical ensemble formed by all the accessible microstates of a mechanical system characterized by the invariability of the number of particles N, the pressure P, and temperature T. It is useful to describe closed systems in thermal and isobaric equilibrium.[53?] In this ensemble the volume of the simulation cell is considered as a variable and therefore can change. For this reason, it is more convinient to redefine the positions in fractional coordinates $\vec{r}_i = L\vec{s}_i$ for $i = 1, 2, ..., N$ being $L = V^{1/3}$ the length of a cubic cell. The average of a

macroscopic property A in NPT ensemble is given by

$$\langle A(\vec{s}^N)\rangle = \frac{1}{Z_{NPT}} \int_0^\infty e^{-\frac{PV}{k_B T}} V^N \left(\int_0^1 e^{-\frac{U(\vec{s}^N)}{k_B T}} A(\vec{s}^N) d\vec{s}^N \right) dV \tag{1.5}$$

where the partition function is

$$Z_{NPT} = \frac{P}{k_B T \Lambda^{3N} N!} \int e^{-\frac{PV}{k_B T}} V^N \left(\int e^{-\frac{U(\vec{s}^N)}{k_B T}} d\vec{s}^N \right) dV \tag{1.6}$$

The probability density of finding the system in a configuration in the fractional coordinates at given volume is:

$$\wp\left(V, \vec{s}^N\right) \propto V^N e^{-\frac{PV}{k_B T}} e^{-\frac{U(\vec{s}^N)}{k_B T}} \tag{1.7}$$

A non-constrained case of NPT ensemble is the NPT Parrinello-Rahman ensemble. NPT-PR is a fully-flexible-cell NPT ensemble, in which all components of the simulation, cell vectors and angles, i.e. fractional coordinates and momentums, are allowed to fluctuate.[56]

Grand-canonical ensemble μVT

The grand-canonical ensemble is the statistical ensemble formed by all the accessible microstates of a mechanical system characterized by the invariability of the chemical potential μ, the volume V, and temperature T. It is useful to describe open systems with energy and matter exchange (the number of particles is a fluctuating variable). It is the most common ensemble to compute adsorption phenomena. In adsorption studies one would like to know the amount of material adsorbed as a function of pressure and temperature of the reservoir with which the adsorbent is in contact. In the simulation, this is performed by coupling the system under study to an infinite reservoir which has the same μ and T, and fixing the volume of the system.[53?] The partition function of this ensemble is given by

$$Z_{\mu VT} = \sum_{N=0}^{\infty} \frac{e^{-\frac{\mu N}{k_B T}} V^N}{\Lambda^{3N} N!} \int e^{-\frac{U(\vec{s}^N)}{k_B T}} d\vec{s}^N \tag{1.8}$$

the corresponding probability density of a particular configuration is

$$\wp_{\mu VT} \propto \frac{e^{-\frac{\mu N}{k_B T}} V^N}{\Lambda^{3N} N!} e^{-\frac{U()\vec{s}^N}{k_B T}} \tag{1.9}$$

Force Fields

A force field is a set of functional forms and corresponding parameters used to describe the potential energy of a system of atoms or molecules in molecular simulation. The most popular force fields are designed to be generic. A large number of generic force fields can be found in literature. In this thesis we use Universal Force Field (UFF),[57] Dreiding,[58] and TraPPE[59] generic force fields and also specific force fields developed for particular systems. The sets of parameters used and developed during this thesis are described in each chapter. It is evident from the above

information that the determination of a macroscopic property A requieres the calculation of the kinetic and/or potential energy of the system. The assessment of the potential energy is a key point in molecular simulations. The total potential energy of a system given by a classical force field can be split into by bonded (intramolecular) and non-bonded (intermolecular) interaction terms.

$$U^{total} = U^{bonded} + U^{non-bonded} \quad (1.10)$$

In this section we described the different functional forms employed in this work.

Intramolecular Interactions

The intramolecular interactions consider the interaction between two, three and four consecutive atoms (Figure 5). The contribution to the bonded interaction is given by:

$$U^{bonded} = U^{bond} + U^{bend} + U^{torsion} \quad (1.11)$$

Neighboring atoms bonds can be modeled by keeping them at a fixed bond-distance. Nevertheless, for fully flexible molecules U^{bond} is a function of the interatomic distances where the distance is defined as $\vec{r}_{ij} = \vec{r}_j - \vec{r}_i$. This interaction is usually defined by the harmonic potential given by:

$$U^{bond} = \frac{1}{2} k_{ij} \left(r_{ij} - r_{eq}\right)^2 \quad (1.12)$$

where k_{ij} is the equilibrium constant, r_{ij} is the distance and r_{eq} is the equilibrium distance between the atoms.

The angle between i, j, k atoms can be modeled as fixed bend-angle. For flexible molecules, the interaction between three consecutive atoms i, j, k is described by the U^{bend}. The harmonic form of this potential energy is given by:

$$U^{bend}(\theta_{ijk}) = \frac{1}{2} k_{ijk} \left(\theta_{ijk} - \theta_{eq}\right)^2 \quad (1.13)$$

being k_{ijk} the bend constant, θ_{ijk} and θ_{eq} the angle and the equilibrium angle formed by the i, j, k atoms.

The contribution of the torsion potential energy, $U^{torsion}$, is weaker than the bond and bend potential energies. Given a chain of atoms where i, j, k, l are four consecutive atoms. We can describe two planes containing the atoms i, j, k, and j, k, l, respectively. The torsion angle formed by the two planes is the torsion angle ϕ_{ijkl}. The dihedral angle potentials take into account the interaction arising from torsional forces between the atoms of a chain. This potential energy can be described by several functional forms. One of them is the cosine potential:

$$U^{torsion}(\phi_{ijkl}) = k_{ijkl} \left[1 + \cos(n\phi_{ijkl} - \delta)\right] \quad (1.14)$$

where k_{ijkl} gives the energy barrier of rotation, $n = 1, 2, 3$ in $n\phi$ is the number of maxima in the full rotation, and δ is a phase factor.

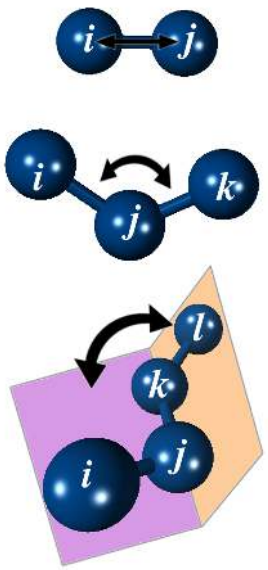

Figure 5. Schematic representation of intramolecular interactions.

Intermolecular Interactions

The intermolecular or non-bonded potentials are those accounting for the interaction between atoms separated by five or more consecutive atoms. The overall expression for the non-bonded potential energy of a system of particles follows:

$$U = \sum_i U_1(\vec{r}_i) + \sum_i \sum_{j>i} U_2(\vec{r}_i, \vec{r}_j) + \\ + \sum_i \sum_{j>i} \sum_{k>j>i} U_3(\vec{r}_i, \vec{r}_j \vec{r}_k) + \ldots \quad (1.15)$$

the first term U_1 represents the effect of a external field, U_2 is the potential between pairs of particles and U_3 is the potential between triplets. The two-body interaction is the domminant term, and higher terms are usually neglected. The three-body interaction can also be important in some cases, but the addition of this interaction rapidly increases the simulation time. Hence, in the absence of an external field, the potential energy is usually expressed as a sum of pairwise interactions. While van der Waals interactions are enough to describe non-polar fluids, more complete description of the potential energy for polar systems also involves the electrostatic interactions:

$$U^{non-bonded} = U^{vdW} + U^{elec} \quad (1.16)$$

The most used model to describe the van der Waals (vdW) interaction is the Lennard-Jones potential.[60] The interaction of two particles i and j approaching to each other can be modeled as a combination of attraction and repulsion forces.

$$U^{LJ}(r_{ij}) = 4\varepsilon_{ij}\left[\left(\frac{\sigma_{ij}}{r_{ij}}\right)^{12} - \left(\frac{\sigma_{ij}}{r_{ij}}\right)^{6}\right] \quad (1.17)$$

where r_{ij} is the distance between the atoms, ε_{ij} is the depth of the minimum energy, and σ_{ij} represents the finite distance at which the interatomic potential is zero. This is the distance between the interacting atoms at which the attraction and repulsion is balanced. To make the simulations tractable, the van der Waals potentials are truncated at a certain distance (*cut-off*) where the interactions are considered small enough. The energy correction due to the truncation is called tail-correction. The tail-correction and the *cut-off* shoud be considered as part of the force

field. These concepts are disscused in the next section.

The parameters for generic force fields are usually self-parameters and a mixing-rule is needed to compute the interaction between i and j where they are different atom types. There are some funtional forms to describe the cross interaction parameters. In this thesis, we mainly employ the Lorentz-Berthelot mixing rules[61] which estimate the cross terms parameters through geometrical and arithmetical means:

$$\varepsilon_{ij} = \sqrt{\varepsilon_{ii}\varepsilon_{jj}} \tag{1.18}$$

$$\sigma_{ij} = \frac{\sigma_{ii} + \sigma_{jj}}{2} \tag{1.19}$$

In some cases the estimation of the crossing parameters with the mixing-rules does not provide accurate results and specific pair interactions parameters need to be defined.

Electrostatic interactions are described by a classical Coulombic potential:

$$U^{elec}(r_{ij}) = \frac{1}{4\pi\varepsilon_0\varepsilon_r}\frac{q_i q_j}{r_{ij}} \tag{1.20}$$

where ε_0 is the permittivity in the vaccum, ε_r is the relative permittivity of the material, q_i and q_j are the charges of the particles i, j, and r_{ij} the distance between the interacting atoms.

As in the case of vdW attractive interactions, the long-range nature of electrostatic interactions create convergence problems. Special methods are required to calculate the total energy in finite boxes (stablishing a *cut-off*) combined with periodic boundary conditions. To compute the electrostatic interactions we use the Ewald summation method.[62]

Boundary Conditions

Modeling materials by molecular simulations has some practical limitations. One is related to the number of positions and momentum coordinates of particles in the system that can be efficiently stored in the computer memory. Simulations of hundreds of thousands of atoms have been reported but this number is still far from the thermodynamic limit. We use periodic boundary conditions to tackle this limitation and enhance the convergence of the finite-size system results to macroscopic quantities.[53,63,64] All the atoms of the initial simulation box are artificially replicated throughout space. This also solves the problem of undesirable surface effects. The only information stored is the related to the initial box (primary box). The positions and momenta of the periodic images can be calculated using translation operators for all the particles in the original box. The minimum-image convention is used to calculate the interaction between particles, where the distance between two particles is the shortest distance between their periodic images.[53] One uses the minimum-image convention, and a truncation and shifted potential stablishing a *cut-off* at some distance smaller than half of the box

length to be consistent with the minimum image convention. The advantage of using a truncated and shifted potential is that the intermolecular forces are always finite.

In crystallography, the usual way to define a unit cell is by the cell lengths a, b, c, the angles between the cells α, β, γ, and by the fractional coordinates s of the particles within the unit cell. These coordinates are defined in an orthonormal dimensionless space. The following transformation matrix gives the cartesian space from fractional space:

$$h = \begin{pmatrix} a & bcos(\gamma) & ccos(\beta) \\ 0 & bsin(\gamma) & c\zeta \\ 0 & 0 & c\sqrt{1-cos(\beta)-\zeta^2} \end{pmatrix} \tag{1.21}$$

with

$$\zeta = \frac{cos\left(\alpha - cos(\gamma)cos(\beta)\right)}{sin(\gamma)} \tag{1.22}$$

Conversely, the inverse of the transformation matrix, h^{-1} transforms cartesian space in fractional space coordinates. With h the box lenghts are normalized to 1. The force fields are defined in cartesian space so it is convenient to store positions in cartesian space and transform them into fractional space. Then, one applies periodic boundary conditions in fractional space, and goes back to cartesian space to compute distances within the simulation box.

Molecular Simulation Techniques

This section summarizes the fundamentals of the classical molecular simulation techniques, that have been employed in this thesis: Monte Carlo, Molecular Dynamics, and Energy Optimization.

Monte Carlo

Monte Carlo (MC) is a computer-based exploitation of the Law of Large Numbers to estimate a certain probability or expectation.[65] In other words MC is a numerical stochastic method which uses random numbers and probability theory to solve problems having a probabilistic interpretation. We use this method to get an approximation of the thermodynamic properties of a given system. To estimate the average properties of systems with many accessible microstates, we used the Markov Chain Monte Carlo method (MCMC) based in Metropolis algorithm.[66] This method generates configurations with a probability proportional to the Boltzmann weigth $\left(e^{-\frac{U(\vec{r}^N)}{k_B T}}\right)$, where hereafter $\frac{1}{k_B T} = \beta$. To guarantee that microstates are visited with the correct frequency, random trial moves are generated. They take the system from the current microscopic state (o) to the new state (n). The acceptation or rejection of the new state depends on the energy difference and the additional generation of a random number. $P_B(o)$ and $P_B(n)$ denote the probability of finding the system in the microscopic state (o) and (n), respectively, and $\alpha(o \rightarrow n)$ denotes the

conditional probability to perform a trial move from $o \rightarrow n$. The application of the detailed balance condition gives the following relation

$$P_B(o)\alpha(o \rightarrow n)P_{acc}(o \rightarrow n) = \\ = P_B(n)\alpha(n \rightarrow o)P_{acc}(n \rightarrow o) \quad (1.23)$$

where P_{acc} is the acceptance probability. Metropolis *et al.* assumed that

$$\alpha(o \rightarrow n) = \alpha(n \rightarrow o) \quad (1.24)$$

and fixed the acceptance probability using

$$P_{acc}(o \rightarrow n) = min\left(1, \frac{P_B(n)}{P_B(0)}\right) \quad (1.25)$$

CONFIGURATIONAL-BIAS MONTE CARLO (CBMC)

Conventional MC is time-consuming for long chain molecules. The fraction of successful insertions into the pore of the structure is too low. To increase the number of successfully inserted molecules we apply the CBMC technique.[59] In CBMC the potential energy is conveniently expressed as $U = U^{int} + U^{ext}$. U^{int} is the bonded potential, used to generate the orientations. U^{ext} is the external potential and is used to bias the selection of a site from the set of trial sites. In the CBMC technique the long chain molecules are grown segment by segment. For each segment a set of k trial orientations is generated according to the internal energy and the external energy of each trial position j of segment i is computed. The probability is

$$P_i(j) = \frac{e^{-\beta U_i^{ext}(j)}}{\sum_{i=1}^{k} e^{-\beta U_i^{ext}(j)}} = \frac{e^{-\beta U_i^{ext}(j)}}{w_i} \quad (1.26)$$

The selected trial orientation is added to the chain and the procedure is repeated until the entire molecule is grown. For this newly grown molecule we compute the so-called Rosenbluth factor[67]

$$W^{new} = \prod_i w_i \quad (1.27)$$

To compute the Rosembluth factor W^{old} of an already existing chain, $k-1$ trial orientations are generated for each segment. These orientations, together with the already existing bond, form the set of k trial orientations. Every new configuration is accepted or rejected using an acceptance/rejection rule. There are two ways to obey the detailed balance:

- The system is coupled with an infinite reservoir in which the fluid is considered to behave as an ideal gas. The Rosebluth factor W^{IG} is computed when particle exchange between the system and the reservoir occurs. Since the reservoir is an ideal gas, only intramolecular interactions are involved.

- Detailed balance is also obeyed when W^{IG} is replaced by $\langle W^{IG} \rangle$, the average Rosenbluth weight of a chain in the reservoir. This implies

that $\langle W^{IG} \rangle$ has to be computed only once for a given molecule and temperature.

MONTE CARLO MOVES

MC simulations are divided in cycles, for each cycle different MC moves are employed, depending on the statistical ensemble used to describe the system.[53]

- Translation move. Is the random displacement of a selected molecule. The maximum displacement is usually taken in such a way that a reasonable amount of moves are accepted (tipically about 30-50 %). The acceptance rule is

$$acc(o \rightarrow n) = \\ = min\left(1, e^{-\beta(U^{new} - U^{old})}\right) \quad (1.28)$$

where the difference of the potential energies is the external energy.

- Rotation move. A selected molecule is randomly rotated around its center of mass. The maximum rotation angle is selected to achieve an acceptance ratio of about 0.3-0.5. The acceptance criterion is also given by Eq (1.28).

- Insertion move. A molecule is grown at a random position. The acceptance rule for insertion of the molecule is

$$acc(N \rightarrow N+1) = \\ = min\left(1 \frac{W^{new} \beta V}{N+1} \frac{f}{\langle W^{IG} \rangle}\right) \quad (1.29)$$

- Deletion move. A molecule is selected at a random position and the old Rosenbluth factor is computed. The acceptance rule for deletion of the particle is

$$acc(N \rightarrow N-1) = \\ = min\left(1 \frac{N}{W^{old} \beta V} \frac{\langle W^{IG} \rangle}{f}\right) \quad (1.30)$$

- Regrow move. The selected molecule is totally or partially regrown at a random position. The acceptance criterion is given by

$$acc(o \rightarrow n) = min\left(1, \frac{W^{new}}{W^{old}}\right) \quad (1.31)$$

- Identity Change move. Used in mixtures; a molecule of one of the components of the mixture is randomly selected and an attempt is made to change its identity. The acceptance rule is given by

$$acc(A \rightarrow B) = \\ = min\left(1, \frac{W^{new} f_B \langle W_A^{IG} \rangle N_A}{W^{old} f_B \langle W_B^{IG} \rangle (N_B + 1)}\right) \quad (1.32)$$

given a component i, f_i is the fugacity and N_i the number of particles.

Molecular Dynamics

The idea behind Molecular Dynamics simulations (MD) is to generate a representative trajectory of the system over time.[68] The ergodic hypothesis states that ensemble averages can be obtained from time averages. This means that we can follow the time evolution of the system instead of sampling the phase space by generating microstates with a certain probability. According to this, the time average value of a property can be obtained by

$$\langle A \rangle = \lim_{t\to\infty} \frac{1}{t} \int A(\vec{r}^N, t) dt \qquad (1.33)$$

In classical MD, the equations of motion of the particles are dominated by the Newton's laws. Successive configurations of the system are generated by integrating the equations of motion in a determined time using finite diferences methods. Integration of the equations of motion then yields a trajectory that describes the positions, velocities and accelerations of the particles and their variations over the time. At each time step, the forces on the atoms are calculated and combined with their current positions and velocities to create new positions and velocities. The atoms are moved to their new positions, the forces updated and a new cycle begins. These dynamically generated states are averaged in time to determine the system properties. The Verlet algorithm is the most used method for integrating the equations of motion. This implementation is according to:

$$\vec{r}(t+\Delta t) = \vec{r}(t) + \vec{v}(t)\Delta t + \frac{\vec{f}(t)}{2m}\Delta t^2 \qquad (1.34)$$

$$\vec{v}(t+\Delta t) = \vec{v}(t) + \frac{\vec{f}(t) + \vec{f}(t+\Delta t)}{2m}\Delta t \qquad (1.35)$$

where Δt is the time step of the MD simulation, $\vec{r}(t)$ and $\vec{v}(t)$ are the position and velocity vectors, respectively, $\vec{f}(t)$ is the force acting at time t, and m is the mass of the particles.

At long times, an energy drift ΔE could appear because of the numerical integration of the equations of motion. To test the energy drift of the numerical integration algorithm for a given time step Δt after M integration steps, we applied:

$$\Delta E(\Delta t) = \frac{1}{M} \sum_{i=1}^{M} \left| \frac{E(0) - E(i\Delta t)}{E(0)} \right| < 10^{-3} \qquad (1.36)$$

After equilibration, we perform the actual measurements by determining the average values of properties from the trajectories of the particles.

Energy Optimization

To know the most stable configuration of a given system, it is necessary to compute the minimum state of energy. The calculations presented in this section are performed at $T = 0K$, therefore no thermal effects are included.[69] This energy state corresponds to a minimum in the potential energy hypersurface where:

$$\frac{\partial U(\vec{r}^N)}{\partial r_i} = 0 \text{ for } i = 1,2,...,N \qquad (1.37)$$

being $U(\vec{r}^N)$ the total potential energy of the system for N particles. Since the energy can reach local minima, the calculation of the second derivative is needed to achieve the global minimum energy of the system. A wide range of minimization algorithms exists. Next, the minimization methods used in this thesis are described.

The Steepest Descent (SD) method is one of the most simplest algorithm to minimize a non linear function.[70,71] The general idea behind most minimization methods is to compute a step along a given direction

$$\vec{x}_{n+1} = \vec{x}_n + \alpha_n d_n \qquad (1.38)$$

where α_n is a self-adjustable parameter that gives the step length. In the steeped descendent method $d_n = -\vec{\nabla} f(\vec{x}_n)$.

Despite its simplicity, the SD method has played an important role in the development of the theory of optimization. Unfortunately, this method is quite slow. More powerful methods such as the Conjugate Gradient method or quasi-Newton methods are frequently used intead.

The Conjugate Gradient (CG) method involves the evaluation of the energy and its first derivatives.[72] It is a particular case of the Conjugate Directons (CD) method where the search directions are a set of orthogonal directions. Given a eigenvector e_n, with eigentvalue λ_e, where $\vec{r}_n = -\lambda_e e_n$, and given the Eq. (1.38), a restriction to find α_n is that e_{n+1} should be orthogonal to d_n. In CG method the search directions are constructed by conjugation of the residuals, setting $\vec{x}_n = \vec{u}_n$ being $\vec{u}_n$ the vectors that conform the d_n. In CG algotrthm d_n is then given by

$$d_n = -\vec{\nabla} f(\vec{x}_n) - \beta_n d_{n-1} \qquad (1.39)$$

$$\beta_n = \frac{\left(\vec{\nabla} f(\vec{x}_n) - \vec{\nabla} f(\vec{x}_{n-1})\right)^{\perp} \vec{\nabla} f(\vec{x}_n)}{\left(\vec{\nabla} f(\vec{x}_{n-1}) - \vec{\nabla} f(\vec{x}_{n-2})\right)^{\perp} \vec{\nabla} f(\vec{x}_n - 1)} \qquad (1.40)$$

CG method is the most efficient method at intermediate distances from that of minimum energy, but the method converges slowly when the system is close to the minimum energy. This convergence problem can be solved with Newton-Raphson method,[73] which uses the second derivative of the energy to accelerate the convergence to the minimum energy. Newton-Raphson method approximates the objective function by a quadratic surface at each step and moves to the minimum of that surface:

$$f(\vec{x} + \Delta\vec{x}) \simeq$$
$$\simeq f(\vec{x}) + \vec{\nabla} f(\vec{x})^{\perp} \cdot \Delta\vec{x} + \frac{1}{2} \Delta\vec{x}^{\perp} \cdot H \cdot \Delta\vec{x} \qquad (1.41)$$

$$\vec{\nabla} f(\vec{x} + \Delta\vec{x}) \simeq \vec{\nabla} f(\vec{x}) + h \cdot \Delta\vec{x} \qquad (1.42)$$

$$\Delta\vec{x} = -H^{-1} \cdot \vec{\nabla} f(\vec{x}) \qquad (1.43)$$

being the hessian $H = \frac{\partial^2 U}{\partial x_i x_j}$.
While SD and CG methods are cheap in terms of computational memory consumption, Newton-Raphson has a high computational memory cost, and the calculation of the Hessian is the most expensive part. This method can diverge if any of the eigenvectors or eigenvalues of the Hessian becomes negative. For this reason, it is usual to add a regulation matrix S then, $\Delta\vec{x} = -(H + \lambda S)^{-1} \cdot \vec{\nabla} f(\vec{x})$. Newton-Raphson method is designed to converge at a global minimum avoiding the local minimum energies of the system.

The Rational Function Optimization (RFO) consists of an approximation of the quadratic variation of the energy in the neiborhood of a given point.[74,75] When the RFO method is applied to locate transition states, the step length is frequently too large. To avoid it, a denominator depending on the step size is introduced:

$$f(\vec{x} + \Delta\vec{x}) \simeq \\ \simeq f(\vec{x}) + \frac{\vec{\nabla} f(\vec{x})^{\perp} \cdot \Delta\vec{x} + \frac{1}{2}\Delta\vec{x}^{\perp} \cdot H \cdot \Delta\vec{x}}{1 + \Delta\vec{x}^{\perp} \cdot S \cdot \Delta\vec{x}} \qquad (1.44)$$

The Baker's method, also known as the mode-following technique is the method used in the framework of this thesis.[76] This method is commonly employed for energy minimizations using the energy, first derivatives, second derivatives, and eigenvalues and eigenvectors of the Hessian matrix as the Hessian at the starting point. This method is able to provide the desired number of negative eigenvalues by construction, giving the correct solution, where other methods can give the wrong solution.

The most common approach to study material frameworks using molecular simulations is to consider them rigid, by fixing the atoms at the experimental crystallographic positions. This approximation can lead to erroneous predictions if the real structure shows flexibility. The energy optimization have been used not only to account for the framework flexibility but also to find the most stable configuration of the system in presence of guest molecules.

Computed Properties

Adsorption Isotherms

Adsorption isotherms and isobars are computed using Monte Carlo simulations in the grand canonical ensemble (GCMC). The system is coupled with a reservoir at the same temperature and chemical potential and the exchange of particles is allowed. The number of molecules, N, flucuates during the simulation, the average overall the adsorbed molecules is the value of the property, according to the MC method described before. The pressure p is fixed in the simulation and determines the fugacity f by the relation:

$$f = \Phi p \tag{1.45}$$

where Φ is the fugacity coefficient obtained from the equation of state of the vapor in the reservoir. Then the chemical potential is calculated using the fugacity

$$\mu(T,p) = \mu_0 + RT\ln f \tag{1.46}$$

where μ_0 is the reference chemical potential.

Henry Coefficients

Henry coefficients are related with the Rosenbluth factor and the Helmholtz free energy of the adsorbed molecules

$$K_H = \frac{1}{k_B T}\frac{\langle W^{IG}\rangle}{\langle W^{id}\rangle} \tag{1.47}$$

$$\Delta F = \frac{1}{k_B T}\ln\frac{\langle W^{IG}\rangle}{\langle W^{id}\rangle} \tag{1.48}$$

where W^{id} is the ideal Rosembluth factor. Widom particle insertion method is used to compute the free energy and therefore the Henry coefficients. This method computes the energy required for the insertion of a particle by the insertion of a probe molecule at random positions. Widom particle insertion method is used at low loadings because the probability to successfully insert a probe particle in a full system without overlapping is very low.

Energies and Entropy of Adsorption

1. Internal Energy (ΔU). The internal energy of a system involved in an adsorption process is given by

$$\Delta U = \langle U_{hg}\rangle - \langle U_h\rangle - \langle U_g\rangle \tag{1.49}$$

where $\langle U_{hg}\rangle$ denotes the average host-guest potential energy, $\langle U_h\rangle$ is the average host energy, and $\langle U_g\rangle$ the energy of the isolated chain molecule in the ideal gas.

2. Enthalpy of adsorption (ΔH). The enthalpy of adsorption or isosteric heat of adsorption can be obtained from the simulation of the adsorption isotherms or from Monte Carlo simulations in the NVT ensemble using the Widom particle insertion method.

$$\Delta H = -Q_{st} = \Delta U - RT \tag{1.50}$$

where R is the ideal constant gas and T the temperature.

3. Helmholtz free energy (ΔF). The Helmholtz free energy gives an idea of the work exchanged in a process. This energy can be computed using MC simulations and is given by the Eq.(1.48)

4. Gibbs free energy (ΔG). The Gibbs free energy is the minimun energy

at constant temperature and pressure of a sytem which is in chemical equilibrium. This can be related to the Helmholtz free energy by

$$\Delta G = \Delta F - RT \tag{1.51}$$

5. Entropy of Adsorption (ΔS). The entropy of adsorption is the entropy change caused by the adsorption of guest molecules. It can be computed from the adsorption energies:

$$\Delta S = \frac{\Delta U - \Delta F}{T} = \frac{\Delta H - \Delta G}{T} \tag{1.52}$$

Adsorption Selectivity

The adsorption selectivity is a key property to assess the suitability of a certain porous material for the adsorption-based separation of fluid mixtures. In this thesis we used two definitions of adsorption selectivity.

Ideal adsorption selectivity is the selectivity in the low coverage regime for the separation of two components A and B. It is estimated as the ratio of the Henry coefficients (or heats of adsorption) and allows qualitative estimation of the separation capability of the structure in this regime.

$$S_{ads_{id}} = \frac{K_{H_A}}{K_{H_B}} \tag{1.53}$$

The adsorption selectivity can be also computed as a relation of the molar fractions and the adsorbed loading of the components of the mixture:

$$S_{ads} = \frac{x_A / y_A}{x_B / y_B} \tag{1.54}$$

where x_i is the molar fraction in the adsorbed phase (loading) for the i component and y_i the molar fraction in the bulk phase. For equimolar mixtures, where $y_A = y_B$, the adsorption selectivity is simply $S_{ads} = \frac{x_A}{x_B}$.

Average Occupation Profiles

The average occupation profiles (AvOPs) are essentially histograms that account for the positions of the adsorbed molecules within the structure during the simulations. The average position probability of every particle is computed every cycle of the simulation and they can be stored in memory every n cycle. To obtain the average position probabilities to construct the AvOP, one computes the times that a certain position (with a certain tolerance) in the structure is visited by any of the guest particles. The usual representation of AvOPs is the projection in a plane of the 3-dimentional histogram, and the probability to find a molecule in a given position is measured by a coloured scale as shown in Figure 6.

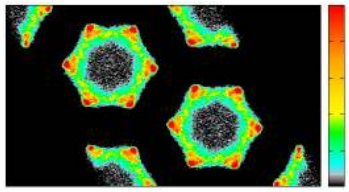

Figure 6. Average ocuppation profile of carbon dioxide in Co-MOF-74 at 100 kPa.

Radial Distribution Function

The Radial Distribution Function (RDF), denoted as $g(r)$, is a relevant structural property of the system. Given a reference particle, RDF can be defined as the normalized probability to find particles at a certain distance between distances r and $r+dr$.

The RDF of two particles A and B is computed via:

$$g_{AB}(r) = \frac{1}{\langle \rho_b \rangle} \frac{1}{N_A} \sum_{i=1}^{N_A} \sum_{j=1}^{N_B} \frac{\delta(r_{ij} - r)}{4\pi r^2} \quad (1.55)$$

where $\langle \rho_b \rangle$ is the B type averaged particle density and N_i is the number of i-type particles.

Diffusion Coefficient (D_s)

Diffusion coefficient or self-diffusion coefficient is a dynamical property that that accounts for the net movement of atoms or molecules from a reference state. The mean squared displacement (MSD) is based on the trajectories of the particles along the simulation time and can be used to compute the diffusion coefficents. Three dynamical regimes can be observed when plotting MSD *versus* time. At very short simulation times, the system is in the ballistic regime where the MSD is proportional to t^2. After this, the regime is controlled by the collisions between particles until they finally reach the diffusive regime, in which the MSD scales linearly with time. The self-diffusion coefficient in a 3-dimensional system can be extracted from the slope of the MSD in the diffusive regime by using the Einstein equation:

$$D_s = \lim_{t \leftarrow \infty} \frac{\langle \sum_i^n ||r(t) - r(0)||^2 \rangle}{6t} \quad (1.56)$$

Outline of the Thesis

This thesis addresses challenging separations of fluids via adsorption and diffusion processes in porous materials, from fundamental and industrial viewpoints. We used molecular simulation techniques, Monte Carlo (MC) and Molecular Dynamics (MD), to perform adsorption and diffusion processes in MOFs and zeolites. We are interested in the study of the separation capability of the selected materials of linear alkanes and alkenes with the same chain length as well as structural and chain isomers. We also explore the separation of acetylene from mixtures with ethane, ethene, and carbon dioxide. The separation of the C2 hydrocarbons and carbon dioxide from a mixture is difficut by convetional routes because of their similar size and properties.

This thesis studies the adsorption mechanisms in porous materials of pure components to understand the adsorption process. The configuration of the molecules inside the structures has been analyzed. It is governed by intermolecular interactions, and specific host-guest interactions if needed. We evaluate the suitability of the materials to perform specific separa-

tions. We study the separations, understand their behaviors, and predict the sieving capacity of other materials with similar properties.

Adsorption and separation of isomeric hydrocarbons in pure silica zeolites. Chapters 2 and 3

Chapter 2 is focused on the effect of the zeolite topology and pore size on the energies, the enthalpy of adsorption and the Henry coefficients. We evaluate these magnitudes and their behavior of saturated and unsaturated hydrocarbons with different chain lengths: linear alkenes, with the double bond placed in different positions, and 1,4-dienes. Four zeolites in pure-silica form were selected: Three with cage-like topology (CHA, ERI, and ITQ- 29) and one zeolite test with one-dimensional channels (OFF). The adsorption performance was assessed in terms of energies and enthalpies of adsorption as well as on the Henry coefficients and ideal adsorption selectivity.

Chapter 3 reports a screening of pure silica zeolites for separating hexane isomers. We calculated the adsorption isotherms of single components at 433 K. We considered an equimolar mixture to permorm the multi-components adsorption isotherms. The self-diffusion coefficents of the mixture were calculated at saturation pressures. We conduct the MD simulations using as starting point the equilibrium configuration from MC simulations at the same conditions. In the basis of the results, a stepped adsorption selective process was proposed for this specific separation.

Exploiting MOFs with open metal sites for alkane/alkene separation. Chapters 4, 5, and 6

Chapters 4 and 5 focus on the adsorption and separation of ethane/ethene and propane/propene in Cu-BTC and M-MOF-74 (M= Co, Fe, Ni, and Mn). Generic force fields usually fail in predicting the adsorption isotherms because of the specific interaction of the open metal site and the double bound of alkenes. Hence, specific cross host-guest interaction parameters were developed by fitting to available experimental data of single-component isotherms. We assessed the adsorption selectivity of the competitive adsorption of the binary alkane/alkene mixtures using this parametrization. In chapter 5, we extend the study to Cu-BTC for binary paraffin/olefin mixtures from 2 to 5 carbon atoms (ethane/ethene, propane/propene, butane/1-butene, isobutane/isobutene and pentane/1-pentene). The force field parametrization developed in this chapter was found transferable.

Chapter 6 is aimed at studying the adsorption-based separation of C4 olefin and 1,3-butadiene. We used ZJNU-30, a recently synthesized MOF for this pur-

pose. We consider MOFs with open metal sites Cu-BTC, Co- and Fe-MOF-74, and the pure silica zeolite RRO. To predict the separation capacity of the MOFs with open metal sites, the force field parameters already developed in chapters 4 and 5 were used.

Insight into mechanims of adsorption for light gases separation applications. Chapters 7, 8, and 9

In chapter 7 we used a stepped procedure to create the framework of aluminosilicates with LTA, and FAU topology with different compositions. Structural minimizations of the zeolite cell containing the adsorbates and the charge-balancing cations were conducted and compared with experimental data of single-component adsorption. This allowed the development of a specific force field accounting for olefin-cation interactions, which in turn allows the prediction of the competitive olefin adsorption. We conducted the olefin/paraffin separation in aluminosilicates with different compositions We evaluate the influence exerted by the amount and nature of the extra-framework cations in the separations.

Chapter 8 shows that the guest-induced phase transition of ZJU-198 allows the separation of light gases. Acetylene, carbon dioxide and ethene can induce the breathing in the MOF. These molecules are adsorbed over nitrogen and methane that cannot induce the phase transition.

In chapter 9 we investigate the separation of light gases, carbon dioxide, acetylene, and methane in some MOFs. CO_2/C_2H_2 separation deserves special attention due to the similar sizes, shapes, and physical properties of these molecules. We explore the separation capability of MOFs with and without open metal sites, the adsorption mechanisms of pure and multicomponent adsorption, the adsorption energies, and the most stable configurations adopted by the molecules inside the pores.

Bibliography

[1] Cornell, C. B. *Gas* **2008**, *2*.

[2] Düren, T.; Sarkisov, L.; Yaghi, O. M.; Snurr, R. Q. *Langmuir* **2004**, *20*, 2683–2689.

[3] Fleming, R. D.; Allsup, J. R.; Hurn, R. W. *Conference: LP-gas engine fuel symposium, Detroit, MI, USA, 21 Oct 1970*; ; Bureau of Mines, Bartlesville, Okla. (USA). Bartlesville Petroleum Research Center, 1970; p Medium: X; Size: Pages: 21.

[4] Marchionna, M.; Patrini, R.; Sanfilippo, D.; Migliavacca, G. *Fuel Processing Technology* **2008**, *89*, 1255–1261.

[5] Frischkorn, G. L.; Kuchar, P. J.; Olson, R. K. *Conference: American Institute of Chemical Engineers summer national meeting, Minneapolis, MN, USA, 16 Aug 1987; Other Information: Technical Paper 4D*; American Institute of Chemical Engineers,New York, NY; None, 1987; p Medium: X; Size: Pages: 14.

[6] Myers, A. L. In *Chemical Thermodynamics for Industry*; Letcher, T. M., Ed.; Royal Society of Chemistry: Cambridge, 2004.

[7] Wagner, H.; Luther, R.; Mang, T. *Applied Catalysis A: General* **2001**, *221*, 429–442.

[8] Aitani, A. M. **2006**,

[9] Alsadoun, A. W. *Applied Catalysis a-General* **1993**, *105*, 1–40.

[10] Aljarallah, A. M.; Anabtawi, J. A.; Siddiqui, M. A. B.; Aitani, A. M.; Alsadoun, A. W. *Catalysis Today* **1992**, *14*, R9–&.

[11] Benda, R.; Bullen, J. V.; Plomer, A. J. Biodegradable

polyalphaolefin fluids and formulations containing the fluids. 2000.

[12] Fainshtein, V. I. *Chemical and Petroleum Engineering* **2007**, *43*, 96–101.

[13] Sircar, S. *Industrial & Engineering Chemistry Research* **2006**, *45*, 5435–5448.

[14] Yang, R. T. Gas separation by adsorption processesImperial College Press. 1997.

[15] Allen, D. T.; Torres, V. M.; Thomas, J.; Sullivan, D. W.; Harrison, M.; Hendler, A.; Herndon, S. C.; Kolb, C. E.; Fraser, M. P.; Hill, A. D.; Lamb, B. K.; Miskimins, J.; Sawyer, R. F.; Seinfeld, J. H. *Proceedings of the National Academy of Sciences* **2013**, *110*, 17768–17773.

[16] King, C. J. Separation processes based on reversible chemical complexation. 1987.

[17] Ma, L.; Abney, C.; Lin, W. *Chemical Society Reviews* **2009**, *38*, 1248–1256.

[18] Férey, G. *Chemical Society Reviews* **2008**, *37*, 191–214.

[19] Abrahams, B. F.; Hoskins, B. F.; Robson, R. *Journal of the American Chemical Society* **1991**, *113*, 3606–3607.

[20] Li, H.; Eddaoudi, M.; O'Keeffe, M.; Yaghi, O. M. *Nature* **1999**, *402*, 276.

[21] Cambridge database. `https://www.ccdc.cam.ac.uk/`.

[22] Eddaoudi, M.; Kim, J.; Rosi, N.; Vodak, D.; Wachter, J.; O'Keeffe, M.; Yaghi, O. M. *Science* **2002**, *295*, 469–472.

[23] Jhung, S. H.; Khan, N. A.; Hasan, Z. *Crystengcomm* **2012**, *14*, 7099–7109.

[24] Yaghi, O. M.; O'Keeffe, M.; Ockwig, N. W.; Chae, H. K.; Eddaoudi, M.; Kim, J. *Nature* **2003**, *423*, 705–714.

[25] Kitagawa, S.; Kitaura, R.; Noro, S. *Angewandte Chemie-International Edition* **2004**, *43*, 2334–2375.

[26] Lee, J.; Farha, O. K.; Roberts, J.; Scheidt, K. A.; Nguyen, S. T.; Hupp, J. T. *Chemical Society Reviews* **2009**, *38*, 1450–1459.

[27] Hwang, Y.; Hong, D.-Y.; Chang, J.-S.; Jhung, S.; Seo, Y.-K.; Kim, J.; Vimont, A.; Daturi, M.; Serre, C.; Férey, G. *Angewandte Chemie International Edition* **2008**, *47*, 4144–4148.

[28] Liu, J.; Thallapally, P. K.; McGrail, B. P.; Brown, D. R.; Liu, J. *Chemical Society Reviews* **2012**, *41*, 2308–2322.

[29] Wu, H.; Gong, Q.; Olson, D. H.; Li, J. *Chemical Reviews* **2012**, *112*, 836–868.

[30] Li, J.-R.; Sculley, J.; Zhou, H.-C. *Chemical Reviews* **2012**, *112*, 869–932.

[31] Horcajada, P.; Gref, R.; Baati, T.; Allan, P. K.; Maurin, G.; Couvreur, P.; Férey, G.; Morris, R. E.; Serre, C. *Chemical Reviews* **2012**, *112*, 1232–1268.

[32] Liu, C.; Li, F.; Ma, L.-P.; Cheng, H.-M. *Advanced Materials* **2010**, *22*, E28–E62.

[33] Cao, X.; Tan, C.; Sindoro, M.; Zhang, H. *Chemical Society Reviews* **2017**, *46*, 2660–2677.

[34] Kondo, M.; Yoshitomi, T.; Matsuzaka, H.; Kitagawa, S.; Seki, K. *Angewandte Chemie International Edition in English* **1997**, *36*, 1725–1727.

[35] Schneemann, A.; Bon, V.; Schwedler, I.; Senkovska, I.; Kaskel, S.; Fischer, R. A. *Chemical Society Reviews* **2014**, *43*, 6062–6096.

[36] Uemura, K.; Matsuda, R.; Kitagawa, S. *Journal of Solid State Chemistry* **2005**, *178*, 2420–2429.

[37] Pauling, L. *Proceedings of the National Academy of Sciences of the United States of America* **1930**, *16*, 453–459.

[38] Bragg, W. L. *Nature* **1930**, *125*, 510–511.

[39] Taylor, W. H.; Bragg William, L. *Proceedings of the Royal Society of London. Series A, Containing Papers of a Mathematical and Physical Character* **1934**, *145*, 80–103.

[40] IZA Database. `http://www.iza-structure.org/databases/`.

[41] Loewenstein, W. *American Mineralogist* **1954**, *39*, 92–96.

[42] Egerton, T. A.; Stone, F. S. *Journal of the Chemical Society, Faraday Transactions 1: Physical Chemistry in Condensed Phases* **1973**, *69*, 22–38.

[43] Kladnig, W.; Noller, H. *Journal of Catalysis* **1973**, *29*, 385–394.

[44] Lok, B. M.; Cannan, T. R.; Messina, C. A. *Zeolites* **1983**, *3*, 282–291.

[45] Chen, J.; Thomas, J. M. *Journal of the Chemical Society, Chemical Communications* **1994**, 603–604.

[46] Lok, B. M.; Messina, C. A.; Patton, R. L.; Gajek, R. T.; Cannan, T. R.; Flanigen, E. M. Crystalline silicoaluminophosphates. 1984.

[47] Flanigen, E. M.; Patton, R. L.; Wilson, S. T. In *Studies in Surface Science and Catalysis*; Grobet, P. J., Mortier, W. J., Vansant, E. F., Schulz-Ekloff, G., Eds.; Elsevier, 1988; Vol. 37; pp 13–27.

[48] Davis, M. E. *Nature* **2002**, *417*, 813–821.

[49] Reut, S.; Prakash, A. *Fuel Processing Technology* **2006**, *87*, 217–222.

[50] Corma, A. *Journal of Catalysis* **2003**, *216*, 298–312.

[51] Verheyen, E.; Joos, L.; Martineau, C.; Dawson, C. J.; Weidenthaler, C.; Schmidt, W.; Yuan, R.; Breynaert, E.; Van Speybroeck, V.; Waroquier, M.; Taulelle, F.; Treacy, M. M. J.; Martens, J. A.; Kirschhock, C. E. A. *Materials Horizons* **2014**, *1*, 582–587.

[52] Catlow, C. R. A.; Van Speybroeck, V.; van Santen, R. *Modelling and Simulation in the Science of Micro- and Meso-Porous Materials*; Elsevier Science, 2017.

[53] Frenkel, D.; Smit, B. *Computational sciences series*; 2002; Vol. 1; pp 1–638.

[54] Tuckerman, M. *Statistical mechanics: theory and molecular simulation*; Oxford university press, 2010.

[55] Chandler, D. In *Introduction to modern statistical mechanics.*; Press, O. U., Ed.; 1987; Chapter 288.

[56] Parrinello, M.; Rahman, A. *Phys. Rev. Lett.* **1980**, *45*, 1196–1199.

[57] Rappe, A. K.; Casewit, C. J.; Colwell, K. S.; Goddard, W. A.; Skiff, W. M. *Journal of the American Chemical Society* **1992**, *114*, 10024–10035.

[58] Mayo, S. L.; Olafson, B. D.; Goddard, W. A. *Journal of Physical Chemistry* **1990**, *94*, 8897–8909.

[59] Smit, B.; Siepmann, J. I. *The Journal of Physical Chemistry* **1994**, *98*, 8442–8452.

[60] Jones, J. E.; Chapman, S. *Proceedings of the Royal Society of London. Series A, Containing Papers of a Mathematical and Physical Character* **1924**, *106*, 709–718.

[61] Lorentz, H. A. *Annalen der Physik* **1881**, *248*, 127–136.

[62] Wilmer, C.; Kim, K. C.; Snurr, R. Q. *The Journal of Physical Chemistry Letters* **2012**, *3*, 2506–2511.

[63] Dubbeldam, D.; Torres-Knoop, A.; Walton, K. S. *Molecular Simulation* **2013**, *39*, 1253–1292.

[64] Born, M.; von Kármán, T. *Z. Phys* **1912**, *13*, 297–309.

[65] Robert, C. P. *Monte carlo methods*; Wiley Online Library, 2004.

[66] Metropolis, N.; Rosenbluth, A. W.; Rosenbluth, M. N.; Teller, A. H.; Teller, E. *The Journal of Chemical Physics* **1953**, *21*, 1087–1092.

[67] Rosenbluth, M. N.; Rosenbluth, A. W. *The Journal of Chemical Physics* **1955**, *23*, 356–359.

[68] Rapaport, D. C. In *The Art of Molecular Dynamics Simulation*, 2nd ed.; Press, C. U., Ed.; 2004; Chapter 564.

[69] Horike, S.; Shimomura, S.; Kitagawa, S. *Nature Chemistry* **2009**, *1*, 695–704.

[70] Press, W. H.; Teukolsky, S. A.; Vetterling, W. T.; Flannery, B. P.; Metcalf, M. *The art of scientific computing,(Cambridge, 1996)* **1992**,

[71] Shewchuk, J. R. An introduction to the conjugate gradient method without the agonizing pain. 1994.

[72] Meza, J. C. *Wiley Interdisciplinary Reviews: Computational Statistics* **2010**, *2*, 719–722.

[73] Nocedal, J.; Wright, S. *Numerical optimization*; Springer Science & Business Media, 2006.

[74] Byrd, R. H.; Gilbert, J. C.; Nocedal, J. *Mathematical programming* **2000**, *89*, 149–185.

[75] Besalú, E.; Bofill, J. M. *Theoretical Chemistry Accounts* **1998**, *100*, 265–274.

[76] Baker, J. *Journal of Computational Chemistry* **1986**, *7*, 385–395.

CHAPTER 2

Understanding and Exploiting Window Effects for Adsorption and Separations of Hydrocarbons

Azahara Luna-Triguero, José Manuel Vicent-Luna, David Dubbeldam, Paula Gómez-Álvarez, and Sofía Calero

The suitability of zeolites for a certain application strongly depends on their structural features. Among the types of shape selectivity, there is the still quite unexplored "cage or window effect" consisting of an unusual nonmonotonic increase of the Henry coeffcient with chain length in cagelike zeolites when the guest hydrocarbon becomes too long to fit comfortably inside the wider part of the cages.

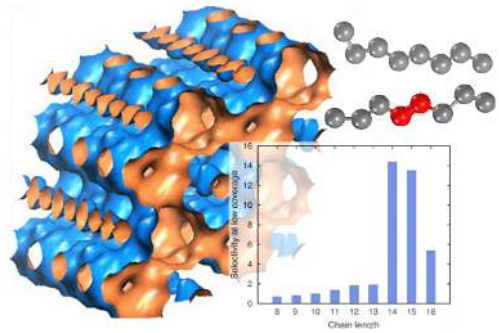

This phenomenon has been addressed for alkanes in various zeolites, but a study dealing with alkenes is lacking. Because of both scientific interest and the impact on the petrochemical industry, we aimed at assessing window effects for a variety of alkenes regarding the position and number of the double bond. We used advanced molecular simulation techniques and considered the rigid all-silica channel-like OFF and cagelike ERI, CHA, and ITQ-29 zeolites. Our study reveals results similar to those of alkanes when the double bond is located at the chain extremes. Conversely, less molecular flexibility induced by intermediate positions of the double bond or the presence of more than one bond lead to a weakness of the window effect, except for the ITQ-29 because of its considerably larger cage. These findings result in signficant values of this type of selectivity for separations of saturated and unsaturated hydrocarbons with chain lengths commensurate with the zeolite cages.

INTRODUCTION

Zeolites are nanoporous crystalline structures based essentially on tetrahedral coordinated T atoms, where T is usually silica or aluminum, linked together by oxygen atoms to shape a three-dimensional system of cavities of molecular dimensions. Different types of zeolites result from differences in the way the T atoms may join in the space. These materials are widely used as molecular sieves, cation exchangers, or catalysts in petrochemical applications. It is well-known that the performance of zeolites for a given task strongly depends on the structural features. While their active sites are related with catalytic activity of zeolites, the diameter, interconnectivity, and dimensionality of the pore system give rise to the molecular sieving action. This ability to discriminate among reactants, products, or reaction intermediates according to shape and size of pores is called shape selectivity, and it is of great importance and widely exploited in catalysis. Three main types of shape selectivity have been described, namely reactant shape selectivity (RSS),[1] product shape selectivity (PSS),[1] and restricted transition-state selectivity (TSS).[2] They are related with the effect of zeolite topology on the barriers to adsorption, desorption, and reaction, respectively. Other types are the subject of debate, such as the so-called "cage" or "window effect".[3–7] The origin of the window effect is a relatively unfavorable adsorption for the chain lengths close to the cage size combined with a low orientational freedom as the chains are stretched across a cage tethered at opposite windows. For instance, the cavity of erionite has dimensions similar to the length of n-octane, which is responsible for the "window effect". A deep molecular-level characterization of this phenomenon within the nanopores is essential to understand many processes of relevance, from a scientific point of view to industrial applications. In this regard, molecular simulation is a powerful tool that allows detailed exploration of the molecular arrangements of the confined fluid. Conventional molecular simulations are generally limited to relatively fast diffusing molecules or small rigid molecules, and only Dubbeldam et al.[8–11] addressed this subject for alkanes in various zeolites by using advanced molecular simulation techniques.[12–14] Overall, longer n-alkanes have more attractive adsorbent-adsorbate interactions and thus a lower adsorption enthalpy. Likewise, they have fewer conformations in the adsorbed phase as compared to the gas phase and thus lower adsorption entropy. The decrease in enthalpy offsets the decrease in entropy, so that the Gibbs free energy of adsorption decreases (and the Henry coefficient increases) with the lengthening of the n-alkane. However, their simulations indicated that the compensation theory applies for channel-type zeolites as OFF-type, which exhibit the described usual monotonic increase of the Henry coeffi-

cient with the chain length. However, for cage-type zeolites with small windows, the described behavior occurs only for effective chain lengths much smaller than the cage size. From a certain alkane chain length of comparable size to the zeolite cage, their results revealed a distinct decrease in the Henry adsorption constants. The linear relationship breaks down. Instead of attractive adsorbate-adsorbent interactions, these windows exert repulsive adsorbate-adsorbent interactions that increase the adsorption enthalpy of any n-alkane partially adsorbed inside such a window. Accordingly, the usual compensation between adsorption enthalpy and adsorption entropy ceases as soon as n-alkanes become too long to fit comfortably inside the wider part of these pores (cages). For these n-alkanes, the loss of entropy with increasing length dominates their adsorption properties. Dubbeldam et al.[8–11] corroborated the existence of the window effect for ERI-type zeolite as well as for CHA and LTA sieves. The CHA-type cages are slightly shorter than the elongated ERI-type cages, and both cage types are significantly smaller than the spherical LTA-type cages. Therefore, the heats of adsorption in this zeolite were found also to be nonmonotonic but only for large alkanes, particularly those longer than 21 carbon atoms. Despite the efforts on parffins,[8–11,15] to our knowledge a study of this phenomenon dealing with olefins is lacking. However, this is crucial because separation of mixtures of alkane and alkene molecules is of great interest in the petrochemical industry. Besides, adsorption-based separations[16] of hydrocarbons are low-cost alternatives to other separation technologies, such as cryogenic distillation. Thus, in this work we evaluate the window effects for a variety of alkenes in regard to the position and number of double bonds. Specifically, we conducted configurational-bias Monte Carlo (CBMC) simulations to compute heats of adsorption and Henry coefficients and analyzed these magnitudes as a function of the carbon chain length. With the aim of comparing with alkanes, we also used the rigid all-silica OFF-, ERI-, CHA-, and LTA-type zeolites. From the Henry coeffcients, we calculate the selectivity at dilute regime to assess the effectiveness of olefin-paraffin as well as olefin-olefin separations.

METHODOLOGY

The zeolite lattices (illustrated in Figure 1) were modeled as rigid crystals with the framework atoms placed at the crystallographic positions. Detailed structural description of these zeolites can be found elsewhere. We used the united-atom model reported by Liu et al.[17] for describing the alkenes. The CH_3 (sp3), CH_2 (sp3 and sp2) and CH (sp2) groups are thus considered as single interaction centers with their own effective potentials. The bonded interactions include bond-stretching, bond-bending, and torsion potentials. The beads in the chain are connected by harmonic

bonding potentials. The bond bending between three neighboring beads is modeled by a harmonic cosine bending potential, and changes in the torsional angle are controlled by TraPPE cosine series potential. The beads in a chain separated by more than three bonds interact with each other through a Lennard-Jones potential. Nonbonded interactions consisted of dispersive Lennard-Jones interactions between guest molecules and also with the oxygen framework atoms. The interactions with the silica atoms are implicitly taken into account in this effective potential. The potential is cut and shifted with the cutoff distance set to 12 Å with periodic boundary conditions[18] exerted in the three dimensions. In all-silica structures, the electric field does not vary much across the channels and cages, and Coulomb contributions to the energy of the alkenes can be neglected. These force fields were proved suitable to accurately reproduce the adsorption properties of short alkenes in all-silica zeolites. Torsion interactions when the double bond is not located in the first position of the chain was described with a potential recently developed in our group in the basis of quantum calculations.[19] In order to establish a comparison, simulations of alkanes were also carried by using parameters reported in Dubbeldam et al.[14] All the used intra and intermolecular force field parameters are summarized in Table A1.1 in the Appendix 1.

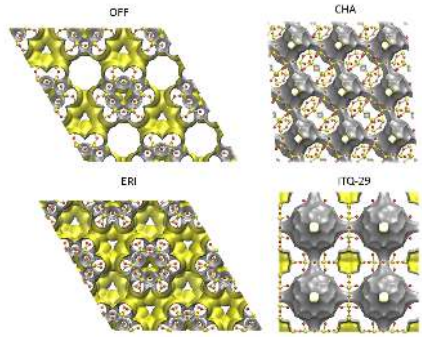

Figure 1. Atomic structure and solvent surface of the targeted zeolites.

Using the above-described models and force fields, CBMC simulations were conducted to efficiently characterize the low-coverage adsorption of saturated and unsaturated hydrocarbons in the targeted porous structures. In the CBMC scheme, molecules are grown atom by atom biasing the growth process towards energetically favorable configurations and avoiding overlap with the zeolite. A comprehensively description can be found in previously reported works.[12–14] Simulations were performed using the RASPA code.[20,21] We used the NVT ensemble with the Widom particle-insertion method[22] to account for the heats of adsorption Q_{st} and Henry coefficients K_H. Both magnitudes were calculated for a wide range of chain lengths and at 600 K, since this is the temperature of interest in catalytic processes. All simulations consist on 50000 equilibration cycles and 2000000 production cycles. Likewise, Molecular Dynamics (MD) s imulations in the NVT ensem-

ble were conducted to characterize molecular conformations within the pores along the time. We fixed the temperature using Nose-Hoover thermostat.[23,24] We used a time step of 0.5 fs and executed the production runs for 10 million of steps (5 ns).

RESULTS AND DISCUSSION

Since the adsorptive phenomenon under study is closely related to the topology and pore dimensions of the zeolite frameworks, a number of host properties were computed using Zeo++.[25] This is a software package used for analysis of crystalline porous materials from a geometric viewpoint on the basis of the Voronoi decomposition. On the one hand, two quantities of particular interest characterizing the pores are the Pore Limiting Diameter (PLD) and the Largest Cavity Diameter (LCD). The PLD, also known as the maximum free sphere diameter,[26] is defined as the largest diameter that a sphere can have within the framework, so that it can move through the structure without overlapping one or more frameworks atoms. The LCD, also called maximum included sphere diameter,[26] is defined as the largest spherical particle that can be inserted at some point within the pores without overlapping with any framework atoms. On the other hand, two important geometrical parameters characterizing the accessible space are surface area and pore volume. The Accessible Surface Area (S_A), originally defined by Lee and Richards,[27] represents the surface traced by the center of a spherical probe as it is rolled along the atomic surface. The Accessible Volume (V_A), it can be analogously defined as the volume reachable by the center of the probe. Unlike pore sizes, these magnitudes are thus a function of the size of the guest molecules. Table 1 collects both the characteristic pore sizes and the accessible space using helium (kinetic radius of 1.3 Å) as a probe molecule for the targeted zeolites. The channel-like topology of OFF means slight differences between the PLD and the LCD, while LCD is about twice the value of the PLD in the cage-like zeolites, and even more in the case of ITQ-29. The LCD of the latter is further larger than that of the remaining zeolites, which is 7 Å approximately. In addition, Figure 2 displays the Pore Size Distributions to give information on the void space that corresponds to certain pore sizes. Virtually the whole accessible space in CHA, ERI and ITQ-29 corresponds to the cages.

Figure 3 shows the heats of adsorption and Henry coefficients as a function of chain length for alkanes and their respective 2- and 4- alkenes for the four

Table 1. Characteristic diameters and accessible space (probe radius = 1.3 Å) of the zeolites obtained using Zeo++ code.[25]

Zeolite	Pore size		$S_A\,[m^2/g]$	$V_A\,[cm^3/g]$
	PLD [Å]	LCD [Å]		
OFF	6.27	7.04	1056	0.0792
CHA	3.43	7.00	1331	0.0999
ERI	3.24	6.91	1033	0.0780
ITQ-29	3.66	10.58	1079	0.1216

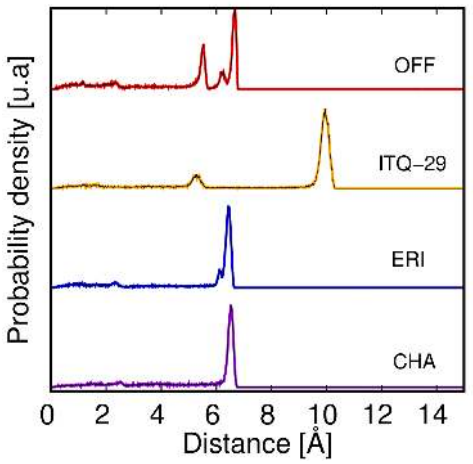

Figure 2. Pore size distributions of zeolites CHA (purple), ERI (blue), ITQ-29 (yellow) and OFF (red).

considered all-silica zeolites at 600 K. Results are qualitatively in agreement since they are closely related magnitudes. Data for alkanes agree with these previously reported.[8–11] As occurs for alkanes, the heat of adsorption and Henry coefficients of alkenes in OFF increase linearly with carbon chain length, because the enthalpy gained by molecule-wall interaction outweighs the loss in entropy. Only tiny differences in their respective values can be observed regardless of the position of the double bond. For the remaining zeolites, the window effect found for alkanes is also observed for the studied alkenes: ERI- and CHA-structures show a non-monotonic, periodic behavior, which occurs also for ITQ-29 but only for chains longer than 21 carbon atoms. The local maxima in Henry coefficients indicate that the shape of chains with 5 or 6 carbon atoms is commensurate with that of a CHA-type cage, whereas in ERI-type cage it occurs for chains lengths of 8 or 9 atoms. These extrema are maintained for all the plotted hydrocarbons. The following sharp decrease denotes that the molecules are forced to curl up, so as to fit into a single cage. When they are even longer, this conformation becomes too unfavorable, and they stretch across two cages instead, as reflect the local minima in both magnitudes. For alkanes, the first molecule to stretch across two cages is dodecane in CHA and tetradecane in ERI-type zeolite. These minima are slightly shifted towards larger chain lengths for the 2-alkenes in relation to the respective alkanes. When the double bond is located at a more intermediate position, in particular the fourth carbon, the window effect is found considerably less noticeable. Increasing the chain length improves adsorption again. Unlik e the small, elongated CHA- and ERI-type cages, molecules have more orientational freedom in the large, spherical LTA-type cages. The largest molecules that fit inside a single cage are these with 22-24 carbon atoms, and represent the local minimum in the adsorption properties. In this case, results are virtually invariant with the presence and position of the double bond in the hydrocarbons. To illustrate the above information, Figure 4 displays snapshots from NVT calculations in all the zeolites for the specific case of 2-alkene with 20 carbon atoms.

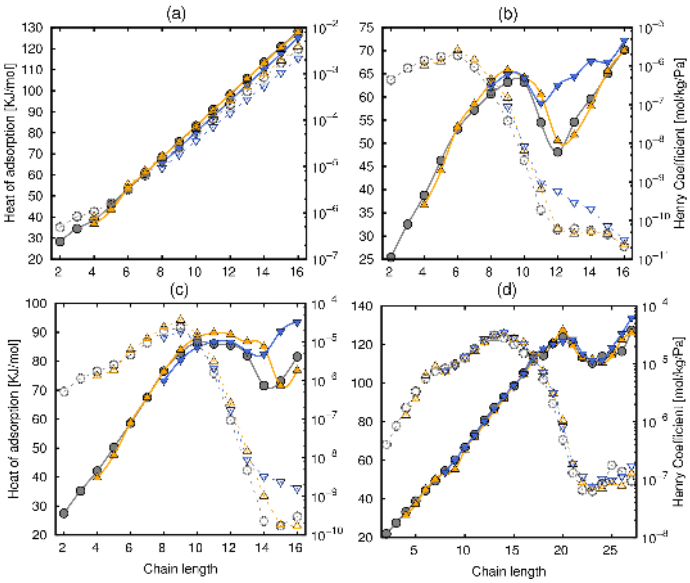

Figure 3. Henry coefficients (empty symbols) and heats of adsorption (full symbols) as a function of the chain length of alkanes (grey symbols) and their respective alkenes with the double bond located in position 2 (yellow symbols) and position 4 (blue symbols) in a) OFF, b) CHA, c) ERI, and d) ITQ-29 zeolites at 600 K.

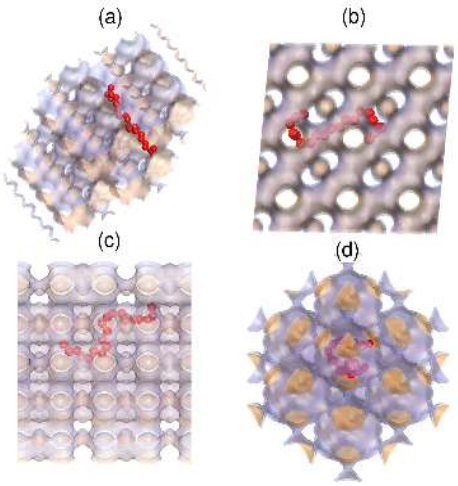

Figure 4. Snapshot of the molecular conformation of an unsaturated hydrocarbon of 20 carbon atoms and double bond in position 2 within the pores of a) OFF, b) CHA, c) ERI, and d) ITQ-29 zeolites at 600 K.

The figure allows one to neatly observe the stretching across two cages in CHA and ERI whereas the adsorbate is still rolled up in the cage of ITQ-29.

In order to evaluate the influence of both the position and number of double bonds, we computed heats of adsorption in CHA and ERI zeolites for alkenes with two double bonds located in positions 1 and 4 (Figure 5). The respective minima reveal that the window effect of these unsaturated hydrocarbons becomes relatively less pronounced in CHA zeolite and virtually negligible in ERI. This can be explained in terms of the enthalpic and entropic variations. Tables A1.2-A1.7 in the Appendix 1 provide the energies, en-

thalpies, and entropies of adsorption at zero coverage for all the systems. The increase (decrease in absolute value) of these magnitudes as consequence of the window effect diminishes for unsaturated hydrocarbons. As can be observed in Figure A1.1 in the Appendix 1, this phenomenon is however still present in ITQ-29 zeolite even for alkenes with a double bond every four carbon atoms. This can be attributed to the large size of the zeolite cages.

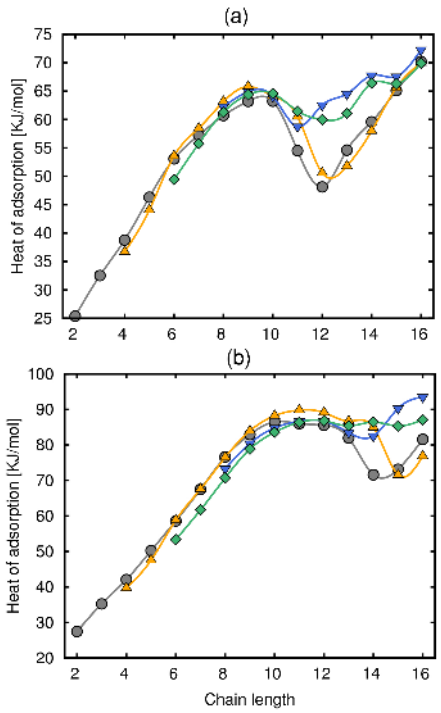

Figure 5. Heats of adsorption as a function of the chain length for alkanes (grey symbols) and their respective alkenes with the double bond located in position 2 (yellow symbols), position 4 (blue symbols), and both positions 1 and 4 (green symbols) in a) CHA and b) ERI zeolites at 600 K.

We find both the position and the number of double bonds of the guest hydrocarbons to notably affect this quite unexplored cage phenomenon. To gain insights into the microscopic source, the molecular flexibility and conformation of the adsorbates is quantitatively evaluated. In Figure 6, we plot the average distance between the extreme carbon atoms of the hydrocarbon chain as a function of the chain length for saturated and unsaturated hydrocarbons in all the zeolites. The obtained curve is indeed in close relation with the adsorption behavior reported in the above figures. As exposed, the position of the minima in heat of adsorption (or in Henry coefficients) indicates a crossover point. Below this cross-over point the molecules fit into a single cage, above this point the chains start to find it energetically more favorable to stretch across two cages. This fact is clearly apparent from the plots in the cage-like structures, where abrupt increases of the average distance denoting the molecular stretching is observed at the previously commented chain lengths in each zeolite. In the channel-like OFF zeolite, we found the expected linear trend.

Figure 7 shows the distribution of the value along the time of the distance between the extreme carbon atoms of 2-alkenes for i) a short chain (in blue), ii) a chain commensurating with the framework cage (in yellow), and iii) a longer chain (violet) in the studied zeolites. The information obtained for alkanes and 4-alkenes is provided in Figures A1.2 and A1.3 in the Appendix 1, respectively.

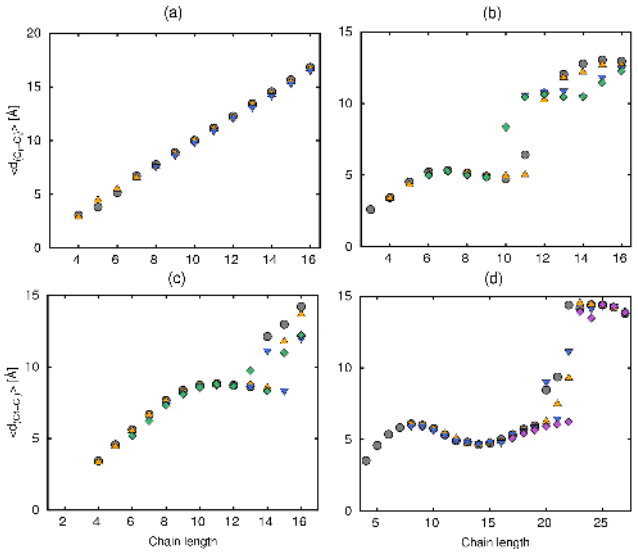

Figure 6. Average distance between the extreme carbon atoms of the hydrocarbons as a function of the chain length for alkanes (grey symbols) and their respective alkenes with the double bond located in position 2 (yellow symbols), position 4 (blue symbols), and both positions 1 and 4 (green symbols) in a) OFF, b) CHA, and c) ERI zeolites, and also every four carbon atoms (pink symbols) in d) ITQ-29 zeolite.

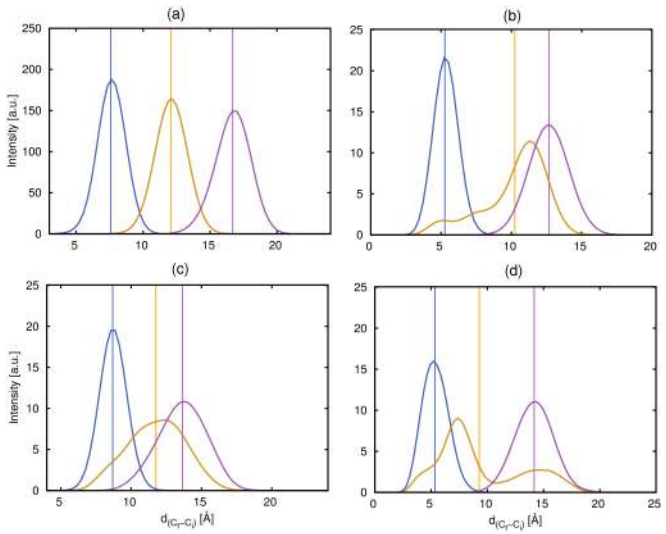

Figure 7. Distribution of the value along the time of the distance between the extreme carbon atoms of 2-alkenes with a short chain (blue), a chain commensurating with the zeolite cage (yellow), and a longer chain (violet) in a) OFF, b) CHA, c) ERI, and d) ITQ-29 zeolites.

The fluctuating data with most probable values shifted from the average when the carbon chains commensurate with the shape of the cages evidence the described unstable conformation. In addition, Figure A1.4 in the Appendix 1 shows this distance as a function of the simulation time for the specific case of a 2-alkene with 20 carbon atoms in all the zeolites, providing quantitative data to the situations visualized in Figure 4. The lowest value, circa 5 Å, corresponds to the ITQ-29 zeolite, denoting the rolling up of the hydrocarbon.

The different behaviour of the saturated and unsaturated hydrocarbons when their chain lengths commensurate with the zeolite cages can be exploited for their separation. The efficiency of this type of selectivity (window effect) is next evaluated in terms of the Henry coefficients. This magnitude is a useful way to gauge if a material can be adsorption-selective. Particularly, the selectivity at low coverage for the separation of two molecules is estimated as the ratio of their Henry coefficients, and allows one to qualitatively observe the separation ability of the structure in this regime. In Figure 8 (top), we plot the ratios of Henry constants for 4-alkene/alkane as a function of the chain length in CHA and ERI zeolites. Results for OFF and ITQ-29 zeolites are also displayed in Figure A1.5 in the Appendix 1. The selectivity is indeed remarkably larger for the chain lengths corresponding to window effects in each zeolite. Thus, CHA and ERI zeolites can be promising candidates for the separation of these hydrocarbons for chains of about 11-13 and 14-16 carbon atoms, respectively. As ERI exhibits the largest selectivity values, Figure 8 (bottom) show the results for various hydrocarbon pairs in this specific zeolite. Those for CHA zeolite are given in Figure A1.6 in the Appendix 1. Specifically, we evaluated the separation of an alkane from the respective 2-alkene, 4-alkene and $n-1$,4-diene, as well as of 4-alkenes from 2-alkenes. As can be seen, the selectivity for the separation of these adsorbate pairs increases notably for carbon chains of 14-16 atoms due to window effects, except for 2-alkene/alkane. Whereas ERI zeolite is the most selective for this binary mixture for chains shorter than 14 carbon atoms, this separation is notably the less feasible for the range of chain length corresponding to cage effects in this zeolite. This is due to only slight variations in the behaviour of the 2-alkene in relation to the alkane. As previously exposed, the relatively weakness of the window effect is rather more significant for the 4-alkenes and n-1,4-dienes, which results in the displayed high values of selectivity. Results for 4-alkene/2-alkene reveal the effectiveness of window effects for also separating unsaturated hydrocarbon isomers in regards to the position of the double bond.

The effect exerted on the heat of adsorption by the type of framework and by temperature is shown in Figure 9. Figure 9a compiles the results of this property for alkanes and 1-alkenes in all the

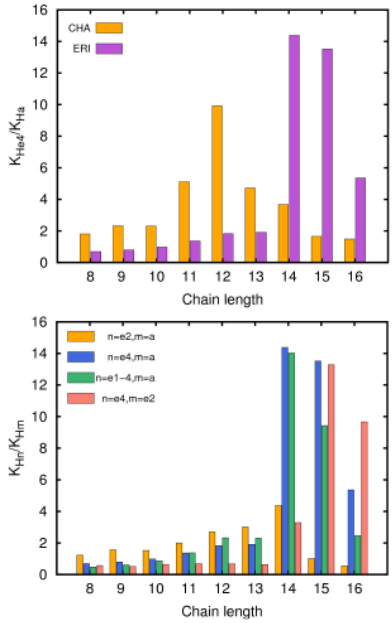

Figure 8. Selectivity at low coverage from Henry coefficients plotted against the chain length for 4-alkene/alkane separation in CHA and ERI zeolites (top) and for various adsorbate pairs in ERI zeolite (bottom) at 600 K. Nomenclature used for the hydrocarbons: alkane (a), alkenes with double bond in position 2 (e2), position 4 (e4), and positions 2 and 4 (e1-4).

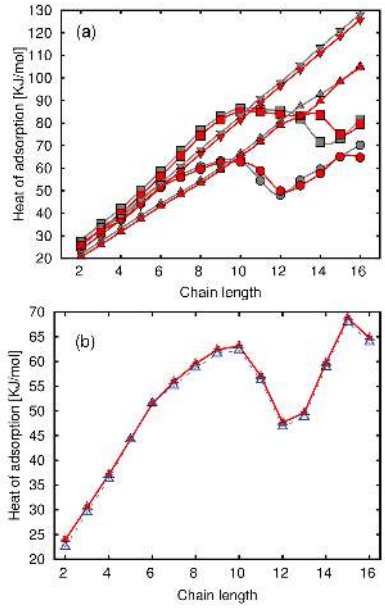

Figure 9. Heats of adsorption as a function as chain length a) alkane (grey) and 1-alkene (red) OFF (down triangles), CHA (circles), ERI (squares) and ITQ-29 (top triangles) zeolites and b)1-alkenes at 300 K (blue symbols) and 600 K (red symbols) in CHA zeolite.

structures. For short chains, the heats of adsorption are quite similar in all structures except for ITQ-29, which exhibits lower values. This is consistent with the pore sizes reported in Table 1. For the hydrocarbons with the longest chains, the highest values of heats of adsorption were found for OFF, followed by ITQ-29, ERI, and CHA. In the 1D channel OFF, the hydrocarbons have strong interactions, and they curl up in ERI and CHA cavities, exhibiting the lowest interactions. Size and window effects lead to the different described situations at low-coverage regime for short and long chains.

Finally, we have checked that temperature does not affect the window effect for the alkenes, as evidenced by Dubbeldam et al. [10] for alkanes. Figure 9b shows the isosteric heats of adsorption for 1-alkenes in CHA at 300 and 600 K.As expected, heat of adsorption is almost independent of temperature; therefore, the maximum for 10 carbon atoms and the minimum for 12 car-

bon atoms remain unaltered.

Conclusions

We performed molecular simulations of adsorption of hydrocarbons in zeolites to account for the influence exerted by the number and position of double bonds. When evaluating the heats of adsorption as a function of the chain lengths, we found alkenes to exhibit similar behavior to those previously reported or alkanes. In particular, they show a monotonic increasing trend for the channel-like OFF zeolite and window effects in the cagelike CHA, ERI, and ITQ-29 zeolites. The less conformational freedom induced by intermediate positions and mainly the presence of various double bonds in the alkenes lead to a weakness and even a vanishing of the window effect in CHA and ERI zeolites. Just slight deviations in enthalpy and entropy from the linearly increasing (in absolute value) tendency are appreciated for these alkenes with chain lengths commensurate with the cage sizes. Conversely, this is not the case in ITQ-29, where this phenomenon is preserved for the studied unsaturated hydrocarbons because of its notably larger cages. The different degrees of window effect for the targeted hydrocarbons were shown to be, in terms of the selectivity at low loading calculated from the Henry coefficients, efficient for olefin-paraffin and olefin-olefin separation applications. Although the largest computed values of selectivity correspond to ERI zeolite, the choice of the optimal cagelike zeolite exploiting this type of selectivity depends on the chain length. Because separations of light alkenes/alkanes are the most challenging and recognized to be a key technology in the petrochemical industry, structures with small cages would appear competitive in this respect.

Bibliography

[1] Weisz, P. B. *Pure and Applied Chemistry* **1980**, *52*, 2091–2103.
[2] Csicsery, S. M. *Pure and Applied Chemistry* **1986**, *58*, 841–856.
[3] Gorring, R. L. *Journal of Catalysis* **1973**, *31*, 13–26.
[4] Miale, J. N.; Chen, N. Y.; Weisz, P. *Journal of Catalysis* **1966**, *6*, 278–287.
[5] Chen, N. Y.; Lucki, S. J.; Mower, E. B. *Journal of Catalysis* **1969**, *13*, 329–332.
[6] Chen, N. Y.; Garwood, W. E. *Molecular Sieves*; American Chemical Society: Michigan, 1973; Vol. 121; Chapter 52, pp 575–582.
[7] Young, L. B. Alkylation in presence of phosphorus-modified crystalline luminosilicate catalyst. 1976.
[8] Dubbeldam, D.; Calero, S.; Maesen, T. L. M.; Smit, B. *Angewandte Chemie-International Edition* **2003**, *42*, 3624–3626.
[9] Dubbeldam, D.; Calero, S.; Maesen, T. L. M.; Smit, B. *Physical Review Letters* **2003**, *90*, 245901.
[10] Dubbeldam, D.; Smit, B. *Journal of Physical Chemistry B* **2003**, *107*, 12138–12152.
[11] Maesen, T. L. M.; Beerdsen, E.; Calero, S.; Dubbeldam, D.; Smit, B. *Journal of Catalysis* **2006**, *237*, 278–290.
[12] Calero, S.; Dubbeldam, D.; Krishna, R.; Smit, B.; Vlugt, T. J. H.; Denayer, J. F. M.; Martens, J. A.; Maesen, T. L. M. *Journal of the American Chemical Society* **2004**, *126*, 11377–11386.
[13] Dubbeldam, D.; Calero, S.; Vlugt, T. J. H.; Krishna, R.; Maesen, T. L. M.; Beerdsen, E.; Smit, B. *Physical Review Letters* **2004**, *93*, 88302.
[14] Dubbeldam, D.; Calero, S.; Vlugt, T. J. H.; Krishna, R.; Maesen, T. L. M.; Smit, B. *Journal of Physical Chemistry B* **2004**, *108*, 12301–12313.
[15] Daems, I.; Baron, G. V.; Punnathanam, S.; Snurr, R. Q.; Denayer, J. F. M. *Journal of Physical Chemistry C* **2007**, *111*, 2191–2197.
[16] Suib, S. L. *Science* **2003**, *302*, 1335–1336.
[17] Liu, B.; Smit, B.; Rey, F.; Valencia, S.; Calero, S. *Journal of Physical Chemistry C* **2008**, *112*, 2492–2498.

[18] Frenkel, D.; Smit, B. *Computational sciences series*; 2002; Vol. 1; pp 1–638.
[19] Ortiz-Roldan, J. M.; Vicent-Luna, J. M.; Ruiz-Salvador, A. R.; Calero, S.; Hamad, S.
[20] Dubbeldam, D.; Torres-Knoop, A.; Walton, K. S. *Molecular Simulation* **2013**, *39*, 1253–1292.
[21] Dubbeldam, D.; Calero, S.; Ellis, D. E.; Snurr, R. Q. *Molecular Simulation* **2015**, *42*, 81–101.
[22] Widom, B. *The Journal of Chemical Physics* **1963**, *39*, 2808–2812.
[23] Nose, S. *Molecular Physics* **2002**, *100*, 191–198.
[24] Hoover, W. G. *Physical Review A* **1985**, *31*, 1695.
[25] Willems, T. F.; Rycroft, C.; Kazi, M.; Meza, J. C.; Haranczyk, M. *Microporous and Mesoporous Materials* **2012**, *149*, 134–141.
[26] Foster, M. D.; Rivin, I.; Treacy, M. M. J.; Friedrichs, O. D. *Microporous and Mesoporous Materials* **2006**, *90*, 32–38.
[27] Lee, B.; Richards, F. M. *Journal of molecular biology* **1971**, *55*, 379–400.

CHAPTER 3

Adsorptive Process Design for the Separation of Hexane Isomers Using Zeolites

Azahara Luna-Triguero, Paula Gómez-Álvarez, and Sofía Calero

The product of catalytic isomerization is a mixture of linear and branched hydrocarbons that are in thermodynamic equilibrium, and their separation becomes necessary in the petrochemical industry. Zeolite 5A is usually industrially used to sieve alkane isomers, but its pore size allows only the separation of linear alkanes from the monobranched and dibranched alkanes by a kinetic mechanism. A more efficient approach to improve the average research octane number would be to adsorptively separate the di-methyl alkanes as products and recycle both the linear and mono-methyl alkanes to the isomerization reactor. Since the microscopic processes of adsorbates in zeolites are generally difficult or impossible to determine by experiments, especially in the case of mixtures, molecular simulation represents an attractive alternative. In this computational study, we propose a conceptual separation process for hexane isomers consisting of several adsorptive steps. Different zeolite topologies were examined for their ability to conduct this separation based on adsorption equilibrium and kinetics.

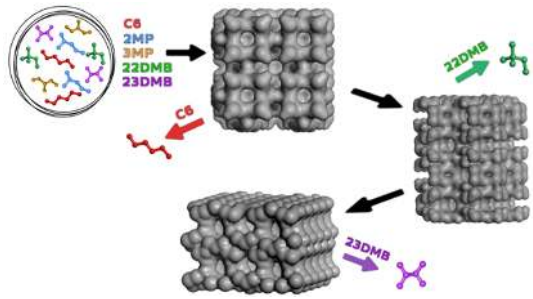

Introduction

In catalytic isomerization processes, straight-chain hydrocarbons are converted to their mono- or di-branched structures. However, the product of catalytic isomerization is a mixture of linear and branched hydrocarbons that are in thermodynamic

equilibrium. The separation of the linear, mono-branched, and di-branched isomers of alkanes is significant in the petrochemical industry.[1] Currently, about two million barrels of hexanes (and pentanes) are processed daily.[1] The value of a particular isomer as a component in the gasoline pool is related to its research octane number (RON). This is highest for the dibranched hexanes 2,3-dimethyl- butane (23DMB) and 2,2-dimethylbutane (22DMB), which have values of 105 and 94, respectively. The RONs for the mono- branched hexane isomers 2-methylpentane (2MP) and 3-methyl- pentane (3MP) are substantially lower, 74 and 75, respectively, and the value for linear n-hexane (nC6) is only 30. The separation of the alkane isomers can be achieved by distillation, selective adsorption, or a combination of both unit operations. Efficient separation by adsorption is challenging since the involved molecules are chemically inert and have similar polarizabilities,[2] their shape being the main property for their differentiation. Among porous materials, zeolites have interesting sieving properties applicable in hexane isomer separation by exploiting the subtle differences in molecular configurations. They have well-defined channels that are accessible to different adsorbates, and are readily available, thermally and chemically stable, and cheap. These properties have enabled zeolites to be widely implemented in industrial applications. The separation of alkane isomers usually employs zeolite 5A.[3?] Its pore aperture is sufficiently large to adsorb linear alkanes, but mono- and dibranched alkanes are excluded from the micropores. It therefore enables the removal of linear alkanes from an isomerate mixture, which is returned to the isomerization reactor, generating a mixture of the other four isomers with a final RON of about 83.[1,4,5] However, it is the di-methyl alkanes that are the most desired because they have the highest octane numbers. Hence it appears necessary a separation process that selectively isolates the most valuable products in order to achieve a further improvement of the average RON. Moreover, this would reduce the use of toxic aromatic compounds currently added to boost the octane number of gasoline.[6] The other disadvantage of sorption separation using zeolite 5A is that its diffusivity is very low.

Numerous attempts have been made to identify potential adsorbents for efficient separation of hexane isomers. Separation of monobranched and dibranched alkanes using silicalite, among other zeolites, has been proposed.[7–12] Other authors have also worked on the possibility of using to this end Metal-Organic Frameworks (MOFs)[12–19] and Zeolite Imidazolate Frameworks (ZIFs).[12,20–25] ZIF-8 was widely studied[21–25] and found to likely be an interesting substitute for zeolite 5A because of its higher adsorption capacity and the ability to separate (part of) the monobranched alkanes from the isomer mixture, increasing the octane number of the product. Dubbeldam et al.[12] however con-

cluded that ZIF-77 was the best structure for hydrocarbon isomer separation among various types of studied nanoporous materials. Herm et al.[19] recently proposed a $Fe_2(BDP)_3$ MOF with triangular channels for efficient hexane isomer separation. Despite these efforts, to our knowledge, an ideal adsorbent or adsorptive process design for the separation of mono- and dibranched alkanes is not industrially employed as of today. Moreover, due to the difficulty in experimentation of the hydrocarbon mixtures, it is highly desirable to predict the adsorption and transport properties of adsorbates from fundamental knowledge of the system. The molecular simulation techniques[26] Monte Carlo (MC) and Molecular Dynamics (MD) are sufficiently advanced in terms of both speed and accuracy to explore the adsorption and diffusion behaviors, respectively, of the fluids inside the pores. Most computational work are however based on pure compounds from Ideal Adsorbed Solution Theory (IAST) calculations.[27]

The aim of this research is to develop a selective process for the separation of hexane isomers by several adsorption steps. We seek potential candidates among all known zeolite topologies. The first step in our screening procedure is to pre-select, for further examination, those zeolite lattices that have pore sizes in the range of the molecular size of the hexane isomers. This condition is based on allowing accommodation of the molecules and diffusion-controlled separation. A large accessible space was also a prior condition. After this pre-screening, we performed a complete molecular simulation study on the selected structures. We conducted MC and MD simulations to compute adsorption isotherms of equimolar mixtures in a wide range of pressures, and diffusion calculations, respectively, at a typical reactor temperature of 433 K.

METHODOLOGY

We used zeolite topologies optimized from those extracted from the International Zeolite Association (IZA) database.[28] Detailed information can be found elsewhere.[29] The structures were treated as rigid frameworks[30] since, overall, the framework flexibility in zeolites is low. As a sieve for zeolite screening, we address pore characterization using the Zeo++ software package.[31] In particular, we pay attention to the Pore Limiting Diameter (PLD), also known as the maximum free sphere diameter. It is defined as the largest diameter that a sphere can have in order to be able to travel through the structure without overlapping one or more framework atoms. Although real molecules are not hard spheres, it is clear that molecules with kinetic diameters above the PLD of a porous structure will likely not be able to diffuse freely through the material. Hence, it provides information about accessibility of molecules into the pore network and its ensuing effect on molecular diffusion and separation. Also

we used Zeo++ [31] to determine the largest cavity diameter LCD (the largest spherical particle that can be inserted at some point within the pores without overlapping with any framework atoms) and the accessible space of the materials, which are indicators of the adsorption capacity. The accessible space is a function of the guest molecules, and was calculated for a probe radius of 1.7 Å. This size corresponds to the kinetic radius of CO_2 , which is a probe molecule commonly used in the experimental characterization of porous materials. [32] Regarding the framework atoms, we considered the radii of 1.52 Å (O) and 2.10 Å (Si) according to the recommendation of the Cambridge Crystallographic Database Centre (CCDC).

The single and multi-component adsorption isotherms were obtained at 433 K using the configurational-bias Monte Carlo algorithm in the grand-canonical ensemble (μVT). In this ensemble, the volume V, temperature T, and chemical potential μ are kept constant. The number of molecules is then allowed to fluctuate until equilibrium at the required chemical potential is attained. The chemical potential is imposed with fugacity, which is the effective thermodynamic pressure. We converted the fugacity to the corresponding pressure using the Peng-Robinson equation of state. [33] All mixtures in this work maintained equimolar amounts in the reservoir and the affinity of the components for the adsorbent conducts to different numbers of molecules within the adsorbent. We examined the competitive adsorption of the five isomers, and also performed binary and ternary mixtures when convenient. The systems were modeled in full atomistic detail using validated classical force fields. The alkane-zeolite and alkane-alkane interactions are described by the Lennard-Jones (L-J) potential. The interactions of zeolite with the alkanes are dominated by the framework oxygen atoms. The intramolecular interactions include bond-stretching, bond-bending, and torsion potentials. The beads in hydrocarbon chains separated by more than three bonds interact through the L-J potential. The force-field parameters are reported by Dubbeldam et al. [34,35] The number of unit cells in the simulation box was chosen such that the minimum length in each of the coordinate directions was larger than twice the cutoff distance, which was set to 12 Å. Periodic boundary conditions are exerted in the three dimensions. [28] Simulations are performed in cycles; in each cycle, N attempts (N is equal to the number of absorbed molecules if it is > 20, and equal to 20 otherwise) are made to perform one of the following molecular moves: translation, rotation, partial regrowth, insertion/deletion, and change in the molecule identity in the case of mixtures. We conducted 50000 cycles for equilibrating the system and 500000 cycles to sample the data.

The diffusion calculations of the adsorbed molecules were calculated using MD simulations. The force fields employed

in the GCMC simulations were also used in the MD simulations for consistency. The initial configuration for MD simulation was taken from the last configuration of the previous GCMC simulation. The MD simulation was performed in the NVT ensemble. The temperature was set to 433 K and fixed using the Nose-Hoover thermostat.[36,37] The time step was set to 0.5 fs, and runs of 10^8 time steps (50 ns) were used for obtaining statistics of the properties. We checked from the obtained Mean Square Displacements (MSDs) as a function of time that simulations of 50 ns are large enough. The self-diffusion coefficients are obtained by calculating in the diffusive regime the slope of the MSDs for the centre of mass of the molecules. The coefficients are calculated for saturation loadings (10^6 Pa) for each system, and averaged over the three directions. All simulations were performed using RASPA software.[38,39] To validate the efficiency of the above-described models and methods, we conducted several simulations to compare the calculated results with the available experimental data.[40–44] Calculated and experimental data are in agreement. Moreover, a recently published work also reflects the agreement of our data for linear hydrocarbons in MFI and MEL zeolites.[45] The results are collected in Figure A1.1 of the Appendix 2, together with a table summarizing the used force field parameters taken from ref. 34 and 3537.

Results and Discussion

The efficiency of an adsorbent is assessed in terms of (a) the selectivity and (b) the adsorption capacity. On the one hand, to accommodate the hexane isomers and ensure good kinetic separation, we select zeolite lattices with PLDs close to the kinetic diameters of the adsorbates, which range from 4.3 Å for nC6 to 6.2 Å for 23DMB. On the other hand, we delimit the preselected zeolites by ruling out those with a comparatively lower Accessible Surface Area (S_A), particularly those with S_A below 500 m^2/g . For the calculation of this property, we used a probe radius of 1.7 Å. The resulting set of zeolites under study is listed in Table 1 together with both the PLD and S_A values. The LCDs, closely related to the accessible space, are also given. To conduct this pore analysis, we used the Zeo++ code.[31] The second level of screening involved interatomic potential-based calculations to assess the adsorption performance of the selected zeolites. There are two main processes that are exploited to perform gas separation using porous materials. One mechanism is controlled by the preferential equilibrated uptake of the adsorbent for one species relative to another. The other mechanism is accomplished due to great differences in diffusion coefficients of the mixture components through the pores. Here we conduct both adsorption and diffusion calculations using GCMC and MD simulations, respectively.

Table 1. Pre-selected zeolites for the separation of hexane isomers on the basis of pore sizes and accessible surface areas. These properties were calculated using the geometric-based code Zeo++.

Zeolite	PLD [Å]	LCD [Å]	S_A $[m^2/g]$
AFS	5.58	8.94	824
AFY	5.47	7.63	1128
BEA	5.57	6.14	917
BOZ	4.69	8.57	1187
BPH	5.58	8.95	882
CON	4.94	7.07	820
EZT	5.54	6.06	561
IFR	5.88	6.73	644
IWR	5.16	7.2	829
MFI	4.69	6.47	504
MWW	4.30	9.07	717
OBW	4.84	8.91	980
OSI	5.74	6	329
OSO	5.67	5.88	1278
SFE	5.52	5.9	445
SFF	5.06	7.35	562
SFS	5.4	7.09	680
SSF	5.57	6.94	567
SSY	5.3	6.65	467
STF	5.21	7.56	630
TUN	5.02	8.04	562
VET	5.59	5.76	312

For a better understanding of the mixture adsorption followed by an accurate separation process design, we investigate the competitive adsorption of the five isomers. This represents a step forward since previous work in this field is mainly based on pure-component data. As commented above, we consider an equimolar composition for the mixture in the GCMC simulations, and the equilibrated configurations from the latter in diffusion calculations. Based on the results, we developed a separation scheme in various steps using several adsorbents. For the removal of nC6 from the isomer mixture, we found various candidates. Although this separation can be easily feasible by using zeolite 5A, [3?] it is not fully practical due to the low diffusivity. SFS topology appears optimal to separate 22DMB by excluding this more bulky molecule. We found BEA, SFE or mainly SSY zeolites suitable for the separation by equilibrated uptake of the other dibranched isomer, 23DMB. This is apparent from either the five-component mixture or the 23DMB/2MP/3MP ternary mixture. Since the separation of dibranched hydrocarbons is the most desirable, the separation of the remaining monobranched isomers, 2MP and 3MP, is unmeaningful. Besides, they have almost the same octane numbers. Even so, we observe and propose two zeolite topologies for this separation. In the following lines, we comprehensively address each adsorptive individual process.

Among the zeolites of Table 1, only those collected in Table 2 allow diffusion of all or some hexane isomer compounds. This is hence the set of possible adsorbents. The provided self-diffusion coefficients D correspond to co-diffusion phenomena in the mixture. Hence, not only host-guest interactions but also interactions between the molecules (and of different types) are considered. We considered the equilibrated configurations of the five-component mixture at high pressures from GCMC simulations as starting configurations for the diffusion calculations. As can be seen in Table 2, the removal of nC6

Table 2. Diffusion coefficients D at 433 K of the hexane isomers in the five-component mixture in equilibrium at saturation in the preselected zeolites (Table 1). They were calculated from MD simulations with initial configurations taken from results of CGMC simulations under such conditions. Only those zeolites allowing diffusion of all or some compounds are listed. The missing values correspond to a lack of diffusion or diffusion coefficients lower than $10^{-14}\,[m^2/s]$

	$D\,[m^2/s]\,10^{-10}$				
Zeolite	***n*C6**	**2MP**	**3MP**	**22DMB**	**23DMB**
BEA	14	12	7.3	6.8	9.2
CON	1.9	0.04	0.03	-	0.03
FAU	12	9.4	9.9	8.0	12
IRR	18	18	16	9.7	12
MFI	2.1	0.16	-	-	-
MWW	6.7	-	-	-	-
OBW	2.9	-	-	-	-
OSI	12	19	4.9	17	5.1
OSO	14	18	17	23	11
RWY	15	8.7	8.8	6.1	5.7
SFE	0.9	1.7	4.1	2.0	3.9
SFS	3.9	0.2	0.3	-	0.2
SSF	3.5	2.2	2.9	3.2	2.5
SSY	-	0.4	1.1	0.02	0.6
VET	0.15	3.5	2.0	4.8	1.9

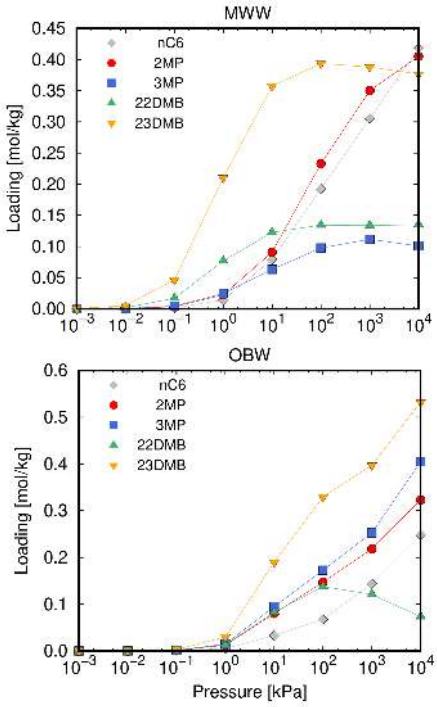

Figure 1. Computed five-component adsorption isotherms in MWW and OBW zeolites at 433 K.

by exploiting the adsorption kinetics is possible using MWW and OBW zeolites. The PLDs of 4.3 Å (MWW) and 4.8 Å (OBW) are consistent with our findings. The PLDs of these structures are lower than the kinetic diameter of the branched isomers but large enough to allow diffusion of *n*C6, with a kinetic diameter of 4.3 Å. Figure 1 shows the computed competitive adsorption of the isomer mixture in these zeolites. However, based on molecular diffusion, artificial pore blocking during MC simulations for the branched hexane isomers in these zeolites would be necessary to avoid the occupation of pores large enough for molecular accommodation but inaccessible. Also CON zeolite, with a PLD of almost 5 Å could be a suitable candidate for this kind of separation. It excludes 22DMB, and the diffusion of the remaining branched isomers is two orders lower than that of the linear hexane. In agreement with previous work,[12] MFI appears selective to nC6 versus the hexane branched isomers from the mixture, as is clearly apparent from Figure 2. The adsorption of *n*C6 in the mixture occurs mainly beyond atmospheric pressure,

which would be the optimal operating condition. In this sense, MWW or OBW topologies represent better options. In regard to the storage assessment, OBW is preferred mong all these zeolites since it has the highest ASA (Table 1). As commented above, the removal of nC6 from the isomer mixture, primarily caused by the exclusion of the branched isomers from the zeolite, is usually addressed using 5A.

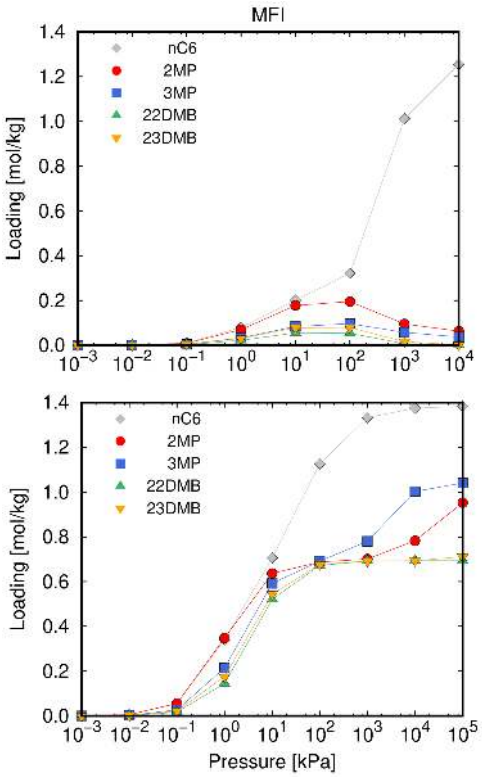

Figure 2. Computed five-component adsorption isotherm (top) and single- component adsorption isotherms of the five hexane isomers (bottom) in MFI zeolite at 433 K.

However, the diffusivity of nC6 in this zeolite is low, which is surpassed in these proposed structures, with D values in between 10^{-9} and $10^{-10}[m^2/s]$. While the exclusion of the linear hexane is relatively easily feasible, the separation among the branched isomers appears complicated. It is however highly desirable since the dibranched isomers have a considerably larger octane number. Overall, 2,2-dibranched and 2,3-di-branched isomers have very different adsorption behaviors in the mixture. 23DMB is usually most adsorbed and the opposite for 22DMB. For the separation of the latter molecule, we found SFS zeolite as a potential candidate. In Figure 3, we plot the multi-component adsorption isotherm in this zeolite. SFS adsorbs all hexane isomers except 22DMB. This molecule possesses an exceptionally bulky environment around one of its carbon atoms. Indeed, it is the only isomer in the study that is di-branched on the same carbon atom. Therefore, it cannot enter narrow channels or pores unlike the remaining mixture components. The dibranched 2,3-dimethylbutane isomer is the most desirable, owing to its highest RON value. Based on the diffusion coefficients listed in Table 2, the rest of the zeolite topologies are large enough to accommodate all hexane isomers, and any specific structure cannot be clearly concluded for the kinetically driven isolation of this isomer. However, we identify various zeolite topologies for the separation based on equilibrium adsorption.

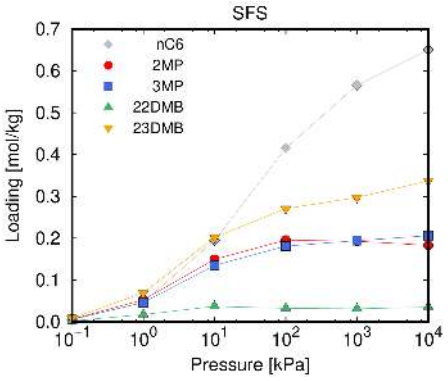

Figure 3. Computed five-component adsorption isotherm in SFS zeolite at 433 K.

Specifically, the adsorption of 23DMB in BEA, SFE and mainly SSY is notably favoured in relation to the remaining components. Figure 4 shows the five-component adsorption isotherms in these zeolites. Also, the results of equimolar ternary 23DMB/ 3MP/2MP are provided, as a consecutive step to the previously exposed individual processes to remove *n*C6 and 22DMB.For both multi-component mixtures, the onset pressures of adsorption range from 10^2 to 10^3 Pa, approximately, regardless of the structure and the adsorbate. However, the adsorption curves exhibit different degrees of steepness until reaching saturation, in relation to the adsorption strength. The results evidence a considerably larger pore filling of 23DMB from about atmospheric pressure, giving a good perspective for the separation of this component from the monobranched isomers.

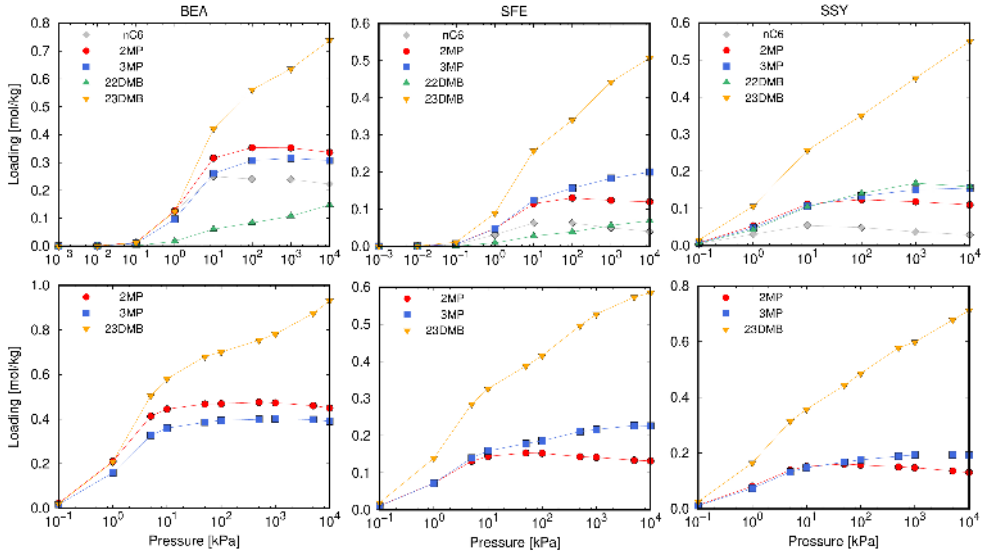

Figure 4. Computed adsorption isotherms of the five-component (top) and 23DMB/2MP/3MP ternary (bottom) mixtures in BEA, SFE, and SSY zeolites at 433 K.

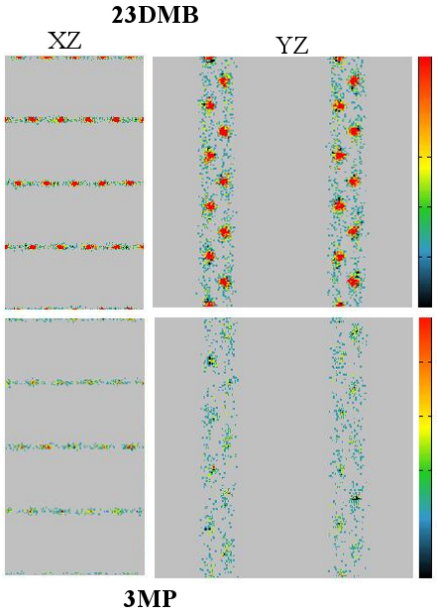

Figure 5. Average occupation profiles in XZ and YZ views of 23DMB (top) and 3MP (bottom) from GCMC simulations of equimolar 23DMP/3MP/2MP mixture in the one-dimensional SSY zeolite at 433 K and 10^7 Pa. The relation between color and occupation probability density (from blue to red) is shown in the bar color ramp.

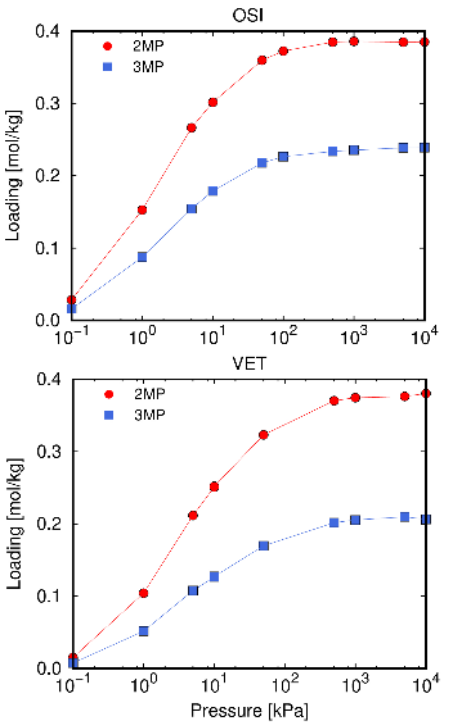

Figure 6. Computed adsorption isotherms of equimolar 2MP/3MP binary mixture in OSI and VET zeolites at 433 K.

To illustrate this, Figure 5 provides information about the occupation density of 23DMB in relation to 3MP inside the one-dimensional SSY zeolite at the highest pressure. The occupation density profiles, represented for projections on XZ and YZ planes, are related to the color gradation.

Once dibranched isomers are removed from the mixture, the separation of monobranched isomers is unmeaningful since they have similar octane numbers. Even so, we pay attention to this task. Overall, a poor separation was found between these components. However, we observe considerable differences in adsorption of both these isomers from the five-component mixture in OSI and VET zeolites. This is corroborated by the binary mixture equilibrium results, which are depicted in Figure 6.

CONCLUSIONS

In this work different zeolite topologies were tested for the separation of hexane isomers. Molecular simulation techniques

in conjunction with geometric-based software for pore characterization proved potentially useful for modelling this separation process. The efficiency of the adsorbent depends on both the selectivity and the adsorption capacity, based on which we set up a screening strategy. With the aid of the pore characterization, we selected a number of zeolites with limiting pore sizes in the range of guest molecular sizes and having a large accessible space. For this set of zeolites, we conducted MC and MD simulations to compute the adsorption isotherms and diffusion behavior, respectively, of mixtures of hydrocarbon isomers. This represents a step forward since most previous studies address the single component properties instead of those of the mixture. Based on the results, we propose a separation scheme that is composed of consecutive steps to yield individual isomers by exploiting either equilibrium adsorption or adsorption kinetics. First, OBW zeolite could potentially operate as a molecular sieve for separating *n*C6, surpassing the limited diffusion in zeolite 5A. Subsequently, SFS can be used to separate 22DMB, which is too bulky to enter its pore system. In a final step, the results suggest that the separation of 23DMB should be achieved from equilibrium processes. BEA, SFE, and mainly SSY demonstrate a significant selective behavior in favor of this isomer from about atmospheric pressure.

Bibliography

[1] Myers, A. L. In *Chemical Thermodynamics for Industry*; Letcher, T. M., Ed.; Royal Society of Chemistry: Cambridge, 2004.

[2] Desty, D. H.; Swanton, W. T. *The Journal of Physical Chemistry* **1961**, *65*, 766–774.

[3] Ruthven, D. M.; Farooq, S.; Knaebel, K. S. *Pressure swing adsorption*; VCH: [New York]; [Weinheim]; [Cambridge], 1994.

[4] Clavier, R. *Wiley Critical Content: Petroleum Technology*; John Wiley and Sons Ltd: Hoboken, United States, 2007; p 2000.

[5] Jasra, R. V.; Bhat, S. G. T. *Separation Science and Technology* **1988**, *23*, 945–989.

[6] Nadim, F.; Zack, P.; Hoag, G. E.; Liu, S. **2001**, *29*, 1–5.

[7] Krishna, R.; Smit, B.; Calero, S. *Chemical Society Reviews* **2002**, *31*, 185–194.

[8] Bárcia, P. S.; Silva, J. A. C.; Rodrigues, A. E. *Aiche Journal* **2007**, *53*, 1970–1981.

[9] Lu, L.; Wang, Q.; Liu, Y. *The Journal of Physical Chemistry B* **2005**, *109*, 8845–8851.

[10] Vlugt, T. J. H.; Krishna, R.; Smit, B. *The Journal of Physical Chemistry B* **1999**, *103*, 1102–1118.

[11] Ferreira, A. F. P.; Mittelmeijer-Hazeleger, M. C.; Bliek, A. *Adsorption* **2007**, *13*, 105–114.

[12] Dubbeldam, D.; Krishna, R.; Calero, S.; YazaydÄśn, A. Ö. *Angewandte Chemie International Edition* **2012**, *51*, 11867–11871.

[13] Bárcia, P. S.; Zapata, F.; Silva, J. A. C.; Rodrigues, A. E.; Chen, B. *The Journal of Physical Chemistry B* **2007**, *111*, 6101–6103.

[14] Dubbeldam, D.; Galvin, C. J.; Walton, K. S.; Ellis, D. E.; Snurr, R. Q. *Journal of the American Chemical Society* **2008**, *130*, 10884–10885.

[15] Chen, B.; Liang, C.; Yang, J.; Contreras, D. S.; Clancy, Y. L.; Lobkovsky, E. B.; Yaghi, O. M.; Dai, S. *Angewandte Chemie International Edition* **2006**, *45*, 1390–1393.

[16] Jiang, J. W.; Sandler, S. I. *Langmuir* **2006**, *22*, 5702–5707.

[17] Zhang, L.; Wang, Q.; Wu, T.; Liu, Y. *ChemistryâĂŞA European Journal* **2007**, *13*, 6387–6396.

[18] Bárcia, P. S.; Guimarães, D.; Mendes, P. A. P.; Silva, J. A. C.; Guillerm, V.; Chevreau, H.; Serre, C.; Rodrigues, A. E. *Microporous and Mesoporous Materials* **2011**, *139*, 67–73.

[19] Herm, Z. R.; Wiers, B. M.; Mason, J. A.; van Baten, J. M.; Hudson, M. R.; Zajdel, P.; Brown, C. M.; Masciocchi, N.; Krishna, R.; Long, J. R. *Science* **2013**, *340*, 960–964.

[20] Gücüyener, C.; van den Bergh, J.; Gascon, J.; Kapteijn, F. *Journal of the American Chemical Society* **2010**, *132*, 17704–17706.

[21] Ferreira, A. F. P.; Mittelmeijer-Hazeleger, M. C.; Granato, M. A.; Martins, V. F. D.; Rodrigues, A. E.; Rothenberg, G. *Physical Chemistry Chemical Physics* **2013**, *15*,

8795–8804.

[22] Mendes, P. A. P.; Rodrigues, A. E.; Horcajada, P.; Serre, C.; Silva, J. A. C. *Microporous and Mesoporous Materials* **2014**, *194*, 146–156.

[23] Peralta, D.; Chaplais, G.; Simon-Masseron, A.; Barthelet, K.; Pirngruber, G. D. *Industrial & Engineering Chemistry Research* **2012**, *51*, 4692–4702.

[24] Zhang, K.; Lively, R. P.; Zhang, C.; Chance, R. R.; Koros, W. J.; Sholl, D. S.; Nair, S. *The Journal of Physical Chemistry Letters* **2013**, *4*, 3618–3622.

[25] Chang, N.; Gu, Z.-Y.; Yan, X.-P. *Journal of the American Chemical Society* **2010**, *132*, 13645–13647.

[26] Frenkel, D.; Smit, B. *Computational sciences series*; 2002; Vol. 1; pp 1–638.

[27] Myers, A. L.; Prausnitz, J. M. *Aiche Journal* **1965**, *11*, 121–127.

[28] IZA Database. `http://www.iza-structure.org/databases/`.

[29] Gómez-Álvarez, P.; Hamad, S.; Haranczyk, M.; Ruiz-Salvador, A. R.; Calero, S. *Dalton Transactions* **2016**, *45*, 216–225.

[30] Bezus, A. G.; Kiselev, A. V.; Lopatkin, A. A.; Du, P. Q. *Journal of the Chemical Society, Faraday Transactions 2: Molecular and Chemical Physics* **1978**, *74*, 367–379.

[31] Willems, T. F.; Rycroft, C.; Kazi, M.; Meza, J. C.; Haranczyk, M. *Microporous and Mesoporous Materials* **2012**, *149*, 134–141.

[32] Thommes, M. *Chemie Ingenieur Technik* **2010**, *82*, 1059–1073.

[33] Robinson, D. B.; Peng, D.-Y.; Chung, S. Y. K. *Fluid Phase Equilibria* **1985**, *24*, 25–41.

[34] Dubbeldam, D.; Calero, S.; Vlugt, T. J. H.; Krishna, R.; Maesen, T. L. M.; Beerdsen, E.; Smit, B. *Physical Review Letters* **2004**, *93*, 88302.

[35] Dubbeldam, D.; Calero, S.; Vlugt, T. J. H.; Krishna, R.; Maesen, T. L. M.; Smit, B. *Journal of Physical Chemistry B* **2004**, *108*, 12301–12313.

[36] Nose, S. *Molecular Physics* **2002**, *100*, 191–198.

[37] Hoover, W. G. *Physical Review A* **1985**, *31*, 1695.

[38] Dubbeldam, D.; Calero, S.; Ellis, D. E.; Snurr, R. Q. *Molecular Simulation* **2015**, *42*, 81–101.

[39] Dubbeldam, D.; Torres-Knoop, A.; Walton, K. S. *Molecular Simulation* **2013**, *39*, 1253–1292.

[40] Du, H. W.; Kalyanaraman, M.; Camblor, M. A.; Olson, D. H. *Microporous and Mesoporous Materials* **2000**, *40*, 305–312.

[41] Zhu, W.; Kapteijn, F.; van der Linden, B.; Moulijn, J. A. *Physical Chemistry Chemical Physics* **2001**, *3*, 1755–1761.

[42] Jolimaitre, E.; Tayakout-Fayolle, M.; Jallut, C.; Ragil, K. *Industrial & Engineering Chemistry Research* **2001**, *40*, 914–926.

[43] Cavalcante, C. L. J.; Ruthven, D. M. *Industrial & Engineering Chemistry Research* **1995**, *34*, 177–184.

[44] Jolimaitre, E.; Ragil, K.; Tayakout-Fayolle, M.; Jallut, C. *Aiche Journal* **2002**, *48*, 1927–1937.

[45] Slawek, A.; Vicent-Luna, J. M.; Marszalek, B.; Balestra, S. R. G.; Makowski, W.; Calero, S. *Journal of Physical Chemistry C* **2016**, *120*, 25338–25350.

CHAPTER 4

Effective Model for Olefin/Paraffin Separation using (Co, Fe, Mn, Ni)-MOF-74

Azahara Luna-Triguero, Jose Manuel Vicent-Luna, Tim M. Becker, Thijs J. H. Vlugt, David Dubbeldam, Paula Gómez-Álvarez, and Sofia Calero

An increase in demand for energy efficient processes for the separation of saturated and unsaturated light hydrocarbons mixtures drives the need of noncryogenic processes. The adsorptive separation using Metal-Organic Frameworks with coordinatively unsaturated metal sites may provide a cost-effective alternative due to the strong binding of the metal cation with the unsaturated hydrocarbons. Since experiments on adsorption equilibrium of gas mixtures are challenging, we propose classical force field based simulations to analyse the ability of MOF-74 with different metal substitutions for the separation of C2 and C3 olefin/paraffin binary mixtures. We parameterized the force field by fitting to available experimental single-component adsorption isotherms of ethane, ethene, propane, and propene in M-MOF-74 (M=Co, Fe, Mn, and Ni). The force field was validated for a variety of temperatures ranged from 273 K to 353 K. We then conducted Monte Carlo simulations in the Grand-Canonical ensemble to elucidate the adsorption mechanisms of the saturated/unsaturated hydrocarbon mixtures, at 318 K and 353 K. We computed the adsorption isotherms, and from these the adsorption selectivity, and addressed the variations of MOF properties with different metal cations. Fe-based MOF-74 appears the best option for both ethane/ethane and propane/propene separation applications. This finding partly agrees with previous work based on the Ideal Adsorbed Solution Theory.

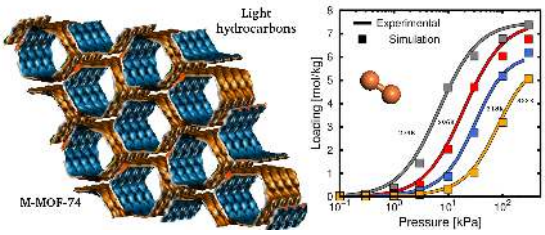

INTRODUCTION

Hydrocarbons with carbon numbers in the 1-3 range, namely methane, ethylene, ethane, propylene, and propane are very important energy resources and raw chemicals. The separation of light hydrocarbon mixtures is hence of great importance in the petrochemical and energy sectors, but it is challenging to perform this separation at the industrial scale.[1] Currently, the most commonly employed method is cryogenic distillation, which is based on the difference in the boiling points of the constituents.[2] This technology is however very energy-intensive due to the requirement of low temperatures and high pressures.[1] Thus, replacing large-scale cryogenic distillation with higher-temperature separation processes could potentially save energy consumption and reduce operating expenses. Among several new energy-efficient alternatives, adsorptive separation is one of the most promising.[3] While cryogenic distillation relies on small differences in the boiling points of olefin and paraffin components, adsorptive separations take advantage of other dissimilar physical properties, namely the kinetic diameter, polarity or polarizability of guest molecule. In this regard, the selection of a proper adsorbent with adequate selectivity and capacity is an important step in designing the adsorption process. The adsorptive separation of methane from C2 and C3 hydrocarbons is relatively easier since CH4 is the smallest and least polarizable molecule, and hence it has weaker interactions within the pores.[4–6] However, separation of C2 and C3 olefin/paraffin mixtures is very difficult because these individual pair molecules have comparable sizes.

Metal-Organic Frameworks (MOFs) are porous materials that are receiving considerable attention for adsorptive gas separation applications.[7] They are crystalline organic-inorganic hybrid compounds formed by coordination of metal ions or clusters with organic linkers (bivalent or trivalent aromatic carboxylic acids or azoles) to form robust porous periodic frameworks. MOFs are well-known for their extremely high porosity, large surface areas, controllable pore structures, and versatile chemical compositions.[8] MOFs with coordinatively unsaturated metal clusters, which may be created by evacuation of frameworks that have metal-bound solvent molecules, have emerged as promising candidates to separate mixtures of saturated/unsaturated hydrocarbons at high temperatures,[9,10] dispensing with the need for cryogenic cooling. The unsaturated coordination sites at the metal center within the bulk of the material (also referred to as open metal sites, OMS) allow for the preferential adsorption of one hydrocarbon

over the other based on the difference in their electronic properties. Specifically, the OMS in the framework bind stronger olefins over paraffins. Several reports [11–15] have recently demonstrated the potential use of M_2(dobdc) compounds (M=Zn, Mn, Fe, Co, Ni; dobdc^{4-}= 2,5-dioxido-1,4-benzenedicarboxylate) for the separation of light hydrocarbons, as well as for other gas separations. [16–18] The members of M_2(dobdc) series are likewise referred to as M-MOF-74 and CPO-27-M. Zn-MOF-74 was first reported in 2005, [19] and isostructural systems with other metal centres have been subsequently presented. [20–23] The M-MOF-74 structures share the same network topology (bnn), infinite-rod secondary building unit (SBU) coordination scheme, 1-periodic hexagonal pore channel, and dobcd4- linkers. Their crystal structures reveal nearly identical pore dimensions of approximately 12 Å. Available literature on olefin/paraffin separation in M-MOF-74 series is however based on results of the single-component adsorption performance. [11–13] Because of the difficulty of measuring adsorption equilibrium data of gas mixtures, the selectivity of the binary mixtures has been only theoretically estimated to date by using the Ideal Adsorbed Solution Theory (IAST) of Myers and Prausnitz from pure-component adsorption isotherms. [24] The molecular simulation technique represents a useful tool, but standard force fields often fail in describing adsorption at OMS, [25,26] probably attributed to interactions with the double bond of alkenes. Additionally, molecular simulations on adsorption equilibrium of mixtures entail high computational cost. With this in mind, the aim of our work is twofold: First, to parameterize the force field for these systems, and then, use molecular simulations to predict the separation process of the binary mixtures. More specifically, we parameterized the cross guest-host Lennard-Jones interaction for ethane, ethene, propane, and propene in M-MOF-74 series (M= Co, Fe, Mn, and Ni) by fitting to experimental data in the literature on pure-component adsorption equilibrium. The force field parameters were validated by comparing with experiments at different temperatures. This allowed us the computation of the adsorption isotherms of the saturated/unsaturated binary mixtures. For these adsorption calculations, we conduct Grand-Canonical Monte Carlo (GCMC) simulations at 318 K and 353 K, in order to observe the effect of the temperature, up to pressures of 100 bar. To evaluate whether a material is adsorption-selective for a particular task, the calculation of selectivity is extremely valuable. We evaluate changes in the adsorption properties of the MOF with variation of only the framework metal cation, and the efficiency of each material in terms of the adsorption selectivity.

The paper is organized as follows. Details of the simulations are described in Methods. The first part of Results section is devoted to force field parametrization

and validation. Then, we report and analyze the adsorption performance of the saturated/unsaturated C2 and C3 binary mixtures in the various MOFs. In the Conclusions our main results are briefly summarized.

METHODOLOGY

Non-bonded interactions consist of guest-guest and guest-host Lennard-Jones (L-J) interactions. The effects of polarity, polarizability (caused by the OM), $\pi - \pi$ interactions, and possible charge transfer are all taken into account in effective L-J interactions for the guest-host interactions. L-J interatomic potential is truncated and shifted with the cutoff distance set to 12 Å. The number of unit cells in the simulation box was chosen such that the minimum length in each of the coordinate directions was larger than twice the cutoff distance. Periodic boundary conditions[27] were exerted in three dimensions. The series of M-MOF-74 (Co, Fe, Mn, and Ni) were treated as rigid during simulations. The L-J parameters for framework atoms were taken from DREIDING[28] except those for metallic atoms, which correspond to UFF,[29] as these are commonly used force fields adopted by the community. For describing the alkanes and alkenes, we used the models reported by Dubbeldam et al.[30,31] and Liu et al.,[32] respectively. On these models, the hydrocarbon molecules are modeled using a single L-J united-atom description with each site electronically neutral, and each CHn group is considered as a single interaction center with effective potential parameters. For describing cross guest-host interactions, we developed a force field parametrization predicting experimental data on pure-component equilibrium adsorption of the hydrocarbons. The starting set of parameters for the fitting was obtained by applying Lorentz-Berthelot mixing rules.

We perform simulations in the grand-canonical (μVT) ensemble, where temperature T, volume V, and chemical potential μ are fixed. The chemical potential is related to the imposed values of fugacity, from which pressures can be determined using the Peng-Robinson equation of state.[33] Three types of trial moves were randomly attempted, namely molecular translation, rotation, and swap between the reservoirs which includes creation and deletion with equal probability, and also identity change trial moves in the case of the binary mixtures. Each point of the isotherms was obtained after equilibration runs of 10000 cycles followed by production runs of 100000 cycles, which were checked large enough. Each cycle consists of N steps, where N is the amount of molecules, with a minimum of 20 steps. Simulations were conducted using RASPA code.[34,35] We assess the selectivity of C2 and C3 olefin/paraffin mixtures in each MOF with different metal substitution. This quantity represents the preferential adsorption of a molecule over another. It is controlled by the ratio of the loading

obtained for the adsorbate molecules as well as of their respective concentrations in the bulk phase. For more detail the reader is referred to ref. 36.

Results and Discussion

Pure-component adsorption isotherms: Force field parametrization and validation.

As it is exposed in the simulation details, the L-J parameters for framework atoms were taken from DREIDING[28] except those for metallic atoms, which correspond to UFF.[29] For describing the alkanes and alkenes, we used the models reported by Dubbeldam et al.[30,31] and Liu et al.,[32] respectively. For these descriptions of the framework atoms and hydrocarbon guest molecules, Table 1 shows the proposed cross guest-host interaction parametrization. We obtained this force field by fitting to experimental data on pure-component equilibrium adsorption isotherms for ethane, ethene, propane, propene, as shown in the following figures. Specifically, the force field parameters were fitted to data at 318 K taken from Geier et al.[11] for all the metal sites except for Fe, which was taken from Bloch et al.[13] Then, the force field was validated for Mn, Ni, Fe by comparing with data at 353 K taken from Geier et al.,[11] Mishra et al.,[14] and Bloch et al.,[13] respectively. In the case of Co, we compared with data from He et al.[12] at 273 K and 296 K, and from Geier et al.[11] and Mishra et al.[14] at 353 K. The set of starting fitting parameters were obtained by applying Lorentz-Berthelot (L-B) mixing rules and are listed in Table A3.1 in the Appendix 3. We mainly increased σ parameters, and slightly modified ε parameters characterizing cross interactions between adsorbate pseudo atoms and linker of the frameworks to obtain the shape of experimental isotherm. Then, we fit the metal-adsorbate parameters to reproduce accurately the isotherm for the different M-MOF-74 structures. With this procedure, we obtain the same set of parameters for the adsorbate-organic linker interactions for all structures. The proposed force field only differs for the specific adsorbate-metal parameters and the fitting procedure causes the differences observed in them. It should be noted that M-MOF-74 structures are different, not only because they have different chemical composition, also the structure properties (i.e unit cell dimensions, surface area, pore volume, etc.) change slightly with the substitution of the metal.[11,37]

With this in mind, the differences in the adsorption isotherm for the different M-MOF-74 could not be only related with the adsorbate-metal interactions. Also the interaction between the hydrocarbons with the environment near the metal should be considered and it is different for each structure. Moreover, hydrocarbons are modelled using a united atom description of the molecules which is de-

veloped for simplicity and transferability. Therefore the potential parameters for an isolated pseudo-atom and metal interaction cannot be related with the physical properties of the atoms.

Figure 1 shows experimental pure-component isotherms in a pressure range of 0-1000 kPa for the set of hydrocarbons along with computational results from using both standard L-B mixing rules (Table A3.1) and the proposed cross L-J parametrization (Table 1) at 318 K for the specific case of Co-MOF-74. As can be seen, simulations using L-B mixing rules produce larger onset pressures of adsorption, especially in the case of unsaturated hydrocarbons, and uptakes that are lower than experiments. This disagreement, found also in the literature,[38,39] clearly reveals the need of an appropriate force field for these systems. The force field parameters developed here allow the satisfactory experimental reproduction of the single-component isotherms of both alkanes and alkenes in Co-MOF-74. This can be extended for the rest of metal cations as shown in Figures A3.1-A3.3 in the Appendix 3.

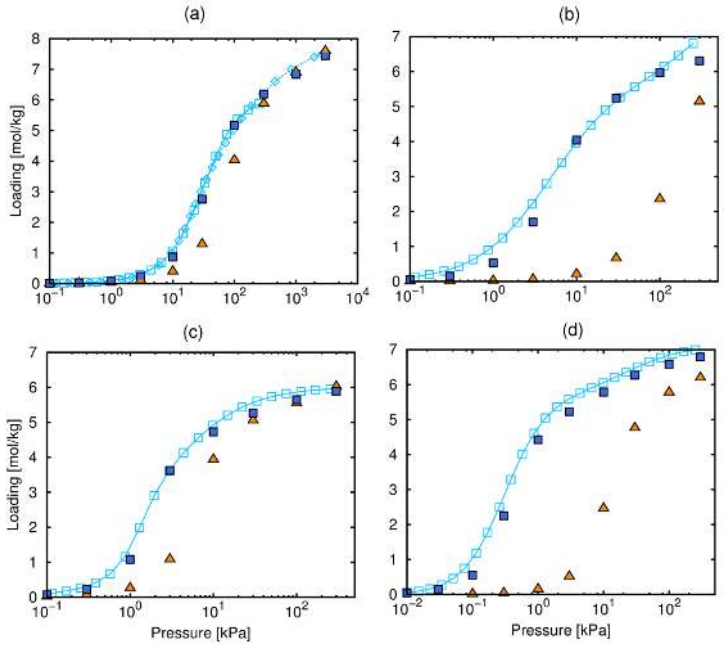

Figure 1. Pure-component adsorption isotherms of ethane (a), ethene (b), propane (c), and propene (d) in Co-MOF-74 at 318 K: Experiments[11] (open squares), computational data using standard Lorentz-Berthelot mixing rules (triangles), and using the proposed guest-host force field parametrization (closed squares).

The suitability of the set of L-J parameters obtained by fitting to adsorption measurements of Figure 1 at 318 K has been explored at other temperatures for which experimental data are available. Figures 2 and 3 show the computed and experimental pure-component adsorption isotherms for the various adsorbates in Co-MOF-74 and for ethane in the four members of the M-MOF-74 series (M=Co, Fe, Mn, and Ni), respectively, at temperatures ranging from 273 K to 353 K.

As temperature increases, the onset pressures increase and the hydrocarbon uptakes decrease. We found our data to match with measurements with relatively high accuracy for all considered adsorbates (Figure 2) and adsorbents (Figure 3). This agreement with experiments for the variety of temperatures points to the reliability and validation of the force field parametrization.

Similar plots involving the remaining adsorbents and adsorbates are collected in Figures A3.4-A3.9 in the Appendix 3, and also lead to such conclusion. Taking into account that we based on force fields describing C_n alkanes and alkenes, namely Dubbeldam et al.[30,31] and Liu et al.[32] respectively, this analysis could be extended to larger hydrocarbons, as it was previously shown for zeolites.[30–32] However, we cannot guarantee this due to the absence of experimental data.

Table 1. Lennard-Jones parameters characterizing cross interactions between hydrocarbon (saturated and unsaturated) and framework atoms developed in this work. ε_{ij}/k_B in K (top) and σ_{ij} in Å (bottom).

	Guest Atoms			
MOF Atoms	CH_3-sp_3	CH_2-sp_3	CH_2-sp_2	$CH-sp_2$
O	72.142 3.532	51.948 3.566	66.945 3.967	88.441 3.285
C	71.895 3.761	51.770 3.791	66.716 4.223	88.138 3.498
H	28.745 3.435	20.698 3.471	26.673 3.854	35.238 3.194
Co	27.597 3.317	79.49 3.325	25.609 3.684	115.997 3.149
Fe	34.555 3.304	114.842 3.277	98.664 3.767	148.965 3.642
Mn	26.695 3.359	20.108 3.365	24.679 3.731	130.414 3.667
Ni	28.567 3.299	20.57 3.307	26.509 3.664	35.02 3.039

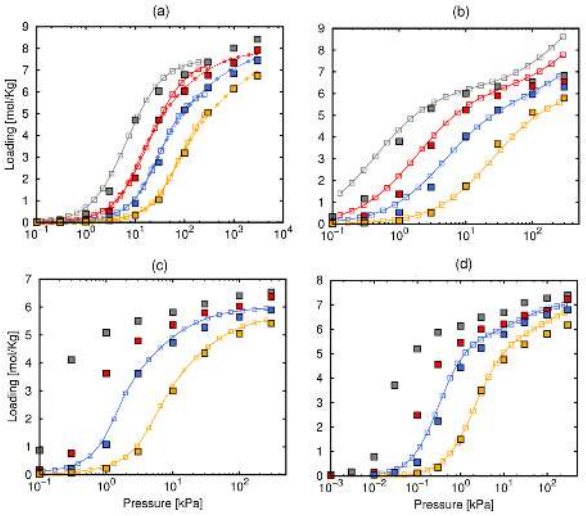

Figure 2. Pure-component adsorption isotherms of ethane (a), ethene (b), propane (c) and propene (d) in Co-MOF-74 at 273 K (grey), 296 K (red), 318 K (blue), 353 K (yellow): Experiments (open symbols),[11,12,14] computational using the proposed guest-host force field parametrization (closed symbols)

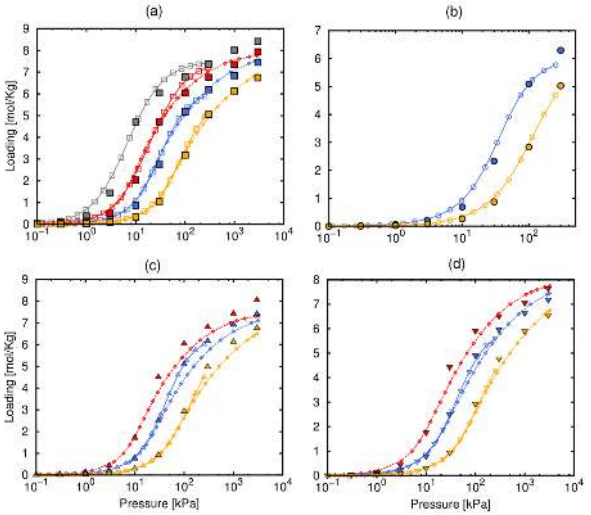

Figure 3. Pure-component adsorption isotherms of ethane in Co-MOF-74 (a), Fe-MOF-74 (b), Mn-MOF-74 (c), and Ni-MOF-74 (d) at 273 K (grey), 296 K (red), 318 K (blue), 353 K (yellow): Experiments (open symbols),[11–14] computational using the proposed guest-host force field parametrization (closed symbols).

To compare the behavior of adsorbates and adsorbents, Figure 4 shows the pure-component adsorption isotherms for all guest molecules in each MOF at 318 K. Regardless of the metal, the onset pressures of adsorption follow the trend ethane > ethene > propane > propene. This is due to the increasing molecular size of the gas molecule, but also to the interaction of the exposed metal cations with the olefin π-bond. While polarizability is an important factor in unsaturated hydrocarbon adsorption, the electron donating and accepting properties of the metal center must also be considered. Specifically, the framework metals that are more capable of accepting π-electron density and/or donating electron density into the empty π-orbital of the olefin are expected to show a stronger interaction. The ability to model the experimental adsorption isotherms is an indication that proper adjustment of vdW terms seems to mimic the π-bonding in a approximate way. This is due to the proposed model could describe properly the entropic effects that govern the adsorption process as they depends mostly on the available space to a molecule and this is less sensitive to the potential energy surface.

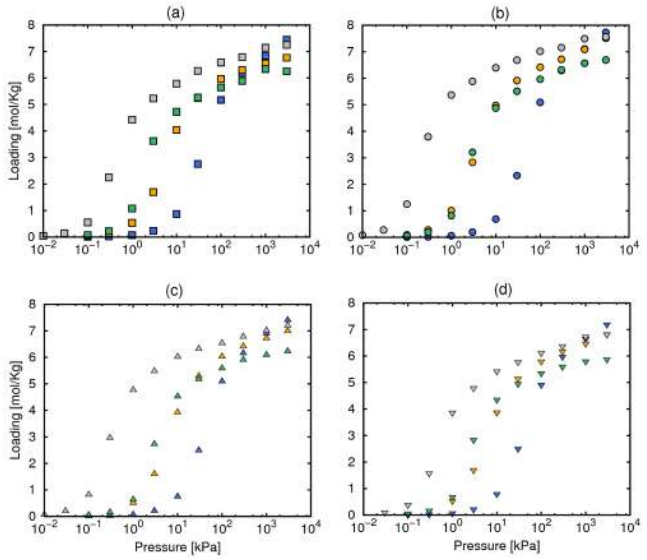

Figure 4. Computed pure-component adsorption isotherms of ethane (blue), ethene (yellow), propane (green) propene (grey) in Co-MOF-74 (a), Fe-MOF-74 (b), Mn-MOF-74 (c), and Ni-MOF-74 (d) at 318 K

It is worth noting however the approximate character of the parametrization approach of this work, in the sense that QM calculations would be necessary for a precise description of the metal-hydrocarbon interactions [35-40] which describes accurately the potential energy surface. But this is out of the scope of this work. Also, the uptake of the hydrocarbons in the low-coverage and intermediate regimes follows such (opposite) trend: ethane < ethene < propane <propene. At the highest values of pressure, packing effects play a role and the largest uptake corresponds to ethane. However, for C3 hydrocarbons, the amount of unsaturated hydrocarbon adsorbed is larger than the amount of saturated hydrocarbon over the entire pressure range in all the MOFs. The adsorption loadings vary between 6 and 8 mol/kg depending on the adsorbate and, in a less extent, on the adsorbent. We reported energetic factors in Figure 5, where we depict the average guest-host potential energy per mol of adsorbed guest molecules as a function of fugacity for each system. The variation of the identity of the metal leads to considerable variations in the binding energies, which are closely related to the isotherms in Figure 4. This suggests that the strong interactions of adsorbates with the open metal sites govern the adsorption processes.

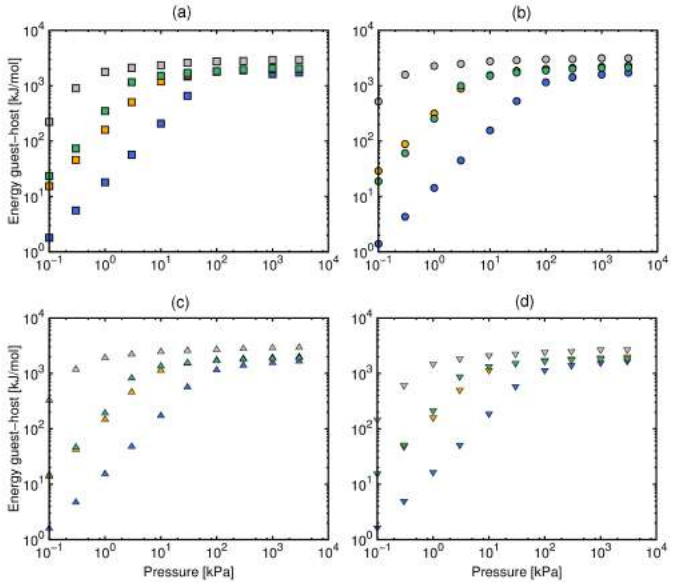

Figure 5. Average guest-host potential energy per mol of adsorbed guest molecules of pure ethane (blue), ethene (yellow), propane (green) and propene (grey) in in Co-MOF-74 (a), Fe-MOF-74 (b), Mn-MOF-74 (c), and Ni-MOF-74 (d) at 318 K.

The trends of both curves are however qualitatively distinctive at the highest pressures (and so uptakes) due to the significant guest-guest interactions. In the light of these results, a high adsorption selectivity for the unsaturated over saturated hydrocarbons is expected in the binary mixture adsorption.

Olefin/paraffin binary mixtures: adsorption isotherms and selectivity.

Since adsorption isotherms of gas mixtures cannot be conveniently and rapidly measured, its behavior has been predicted to date using adsorption models such as IAST[40] from experimental pure-component isotherms. Here we use the validated force field parameters of Table 1 to estimate the competitive adsorption of the saturated and unsaturated hydrocarbons. Figures 6 and 7 show the adsorption isotherms of the equimolar olefin/paraffin mixtures for C2 and C3, respectively, at 318 K and pressures up to 100 bar for the M-MOF-74 members, together with IAST calculations from data reported in Geier et al.[11] The much higher adsorption affinity to alkenes over alkanes is evident from both methods, IAST using the theoretical fittings for pure-component isotherms reported by Geier et al.[11] and simulated isotherms for binary mixtures, which exhibit good agreement, especially at low pressures and for C2 hydrocarbons. As can be seen, this preferential alkene adsorption by the strong complexation between metal ions and the π orbital is more noticeable for C3 hydrocarbons. The adsorption of propane from the mixture is less than 1 mol/kg regardless of the MOF. Generally speaking, for the purpose of comparing different materials and a rational choice of adsorbent for mixture separation, both high adsorption capacities and selectivities are desirable. In regards the former property, MOF-74 members further overcomes other candidate materials with limited uptake capacities, such as most zeolites. As it is apparent from these figures, although rather slightly larger for Fe-MOF-74, the capacity of the considered M-MOF-74 members is similar. The 12 Å-wide channels of these materials lead to large pore volumes and consequently high adsorption capacities. Besides, Fe-MOF-74 seems to be likewise the most selective, as well as Mn-MOF-74 in the case of C3 hydrocarbons. We next comprehensively evaluate the adsorption selectivity. From the adsorption isotherms of the equimolar mixtures in Figures 6 and 7, we calculated the selectivity of alkenes over alkanes in each MOF-74 throughout the fugacity range in order to evaluate the efficacy of these materials for the proposed separations as well as the optimal pressure conditions. The obtained adsorption selectivities as a function of fugacity are shown in Figure 8.

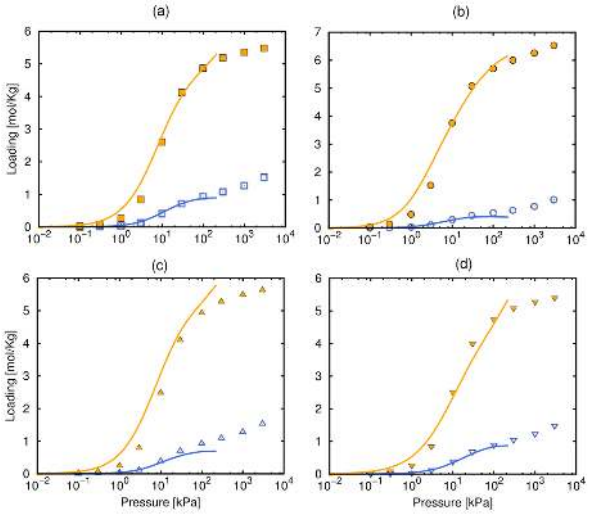

Figure 6. Computed adsorption isotherms of the equimolar binary ethane/ethene mixture in Co-MOF-74 (a), Fe-MOF-74 (b), Mn-MOF-74 (c), and Ni-MOF-74 (d) at 318 K from our MC simulations (points) and using IAST (lines) from theoretical fittings of pure-component isotherms reported in Geier et al.[11]

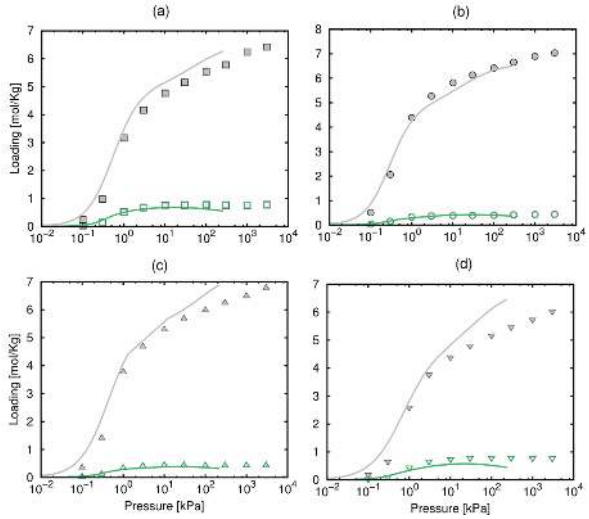

Figure 7. Computed adsorption isotherms of the equimolar binary propane/propene mixture in Co-MOF-74 (a), Fe-MOF-74 (b), Mn-MOF-74 (c), and Ni-MOF-74 (d) at 318 K from our MC simulations (points) and using IAST (lines) from theoretical fittings of pure-component isotherms reported in Geier et al.[11]

As can be seen, Fe-MOF-74 has the highest selectivity for separating both ethane/ethylene and propane/propylene pairs, in consistency with literature,[11,12] but Mn-MOF-74 shows also high selectivity (> 10) for the latter pair. Particularly, the performance of Mn-MOF-74 is comparable to that of Fe-MOF-74 at the highest pressures. The Co and Ni analogues exhibit the lowest and similar selectivities for both separations, which is likely due to the weaker interactions between these metal cations and the unsaturated hydrocarbons. While the equilibrium selectivity of Fe-MOF-74 is maximum at low pressures and follows a clearly decreasing trend with fugacity for C2 hydrocarbons, it slightly varies with fugacity and reaches its highest values at atmospheric pressure for C3 hydrocarbons, which represents the lowest-operational costs. Since the exact composition of the olefin-paraffin mixture may vary significantly depending on the application, we conduct additional calculations throughout the concentration range. In Figure 9, we plot the adsorption loading of alkane/alkene mixtures for C2 and C3 hydrocarbons in Co-MOF-74 at 318 K and atmospheric pressure as a function of the respective alkane mole fractions in the bulk phase. The uptake of the unsaturated hydrocarbons is larger than for saturated except for high concentrations of the alkane in the bulk phase (above 90% approximately). Results for the remaining MOFs are qualitatively the same and provided in the Appendix 3. Figure 10 shows our results of selectivity of alkenes over their alkane analogues as a function of the mixture composition in each MOF-74, together with IAST selectivity calculations for the same thermodynamic conditions (318 K, 1 bar) taken from Geier et al.[11] The selectivity values obtained by IAST are of the same order than ours but not coincident, and qualitative inconsistencies are also evident.

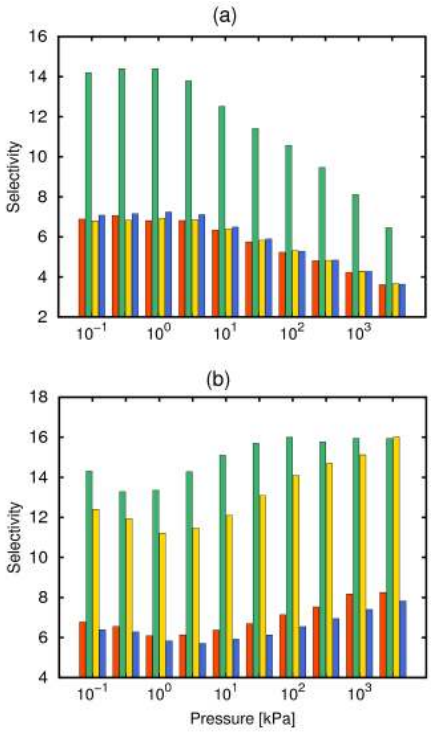

Figure 8. Adsorption selectivity of the equimolar ethane/ethene (a) and propane/propene (b) binary mixtures as a function of fugacity in Co-MOF-74 (red), Fe-MOF-74 (green), Mn-MOF-74 (yellow), and Ni-MOF-74 (blue) at 318K.

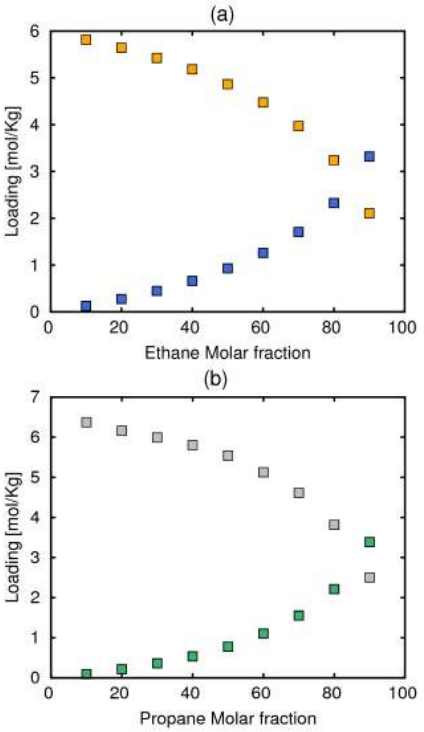

Figure 9. Adsorption loading of ethane (blue)/ethene (yellow), and propane (green)/propene (grey) in Co-MOF-74 at 318 K and 1 bar as a function of the alkane concentrations in the bulk phase for the respective binary mixtures.

Our values reveal that ethane/ethane selectivity slightly increases with increasing alkane concentration whereas it is unchanged or even decreases in the case of C3 hydrocarbons. The opposite trend is observed when using the IAST theory from pure-component adsorption data. Similarly to that occurring along the pressure range for equimolar mixtures, we identify Fe-MOF-74 as the best option for both saturated/unsaturated separations at any mixture contents, especially for ethane/ethylene. The selectivity of Mn-MOF-74 is also significant for C3 hydrocarbons. Geier et al.[11] found that Fe-MOF-74 and Mn-MOF-74 exhibit the highest selectivities for the separation of ethylene-ethane and propylene-propane mixtures, respectively. Nevertheless, it is worth noting that these considerable differences in the selectivity, and thus in the choice of the optimal candidates, between both methods actually arise from slight variations in the hydrocarbon loadings, as it is apparent from Figures 6 and 7 for the equimolar mixture.

Since the selectivity entails the ratio of the uptakes of the mixture compounds, it is very sensitive to such values, especially for low values (below 1) as it is the case of alkanes. According to the reported results at 318 K, we can state that the energy costs associated with large-scale industrial separation of light hydrocarbons by cryogenic distillation could be hence potentially lowered using these solid adsorbents (mainly Fe-MOF-74 and also Mn-MOF-74 for propane/propene) which operate at high temperatures. From a qualitative viewpoint, our simulations at 353 K reveal almost the same behavior on the adsorption selectivity for these binary mixtures in the MOF-74 members as that reported for 318 K throughout either the pressure or the composition range. This is evident from Figures A3.13 and A3.14 in the Appendix 3. The selectivity values are however considerably reduced at such operating temperature.

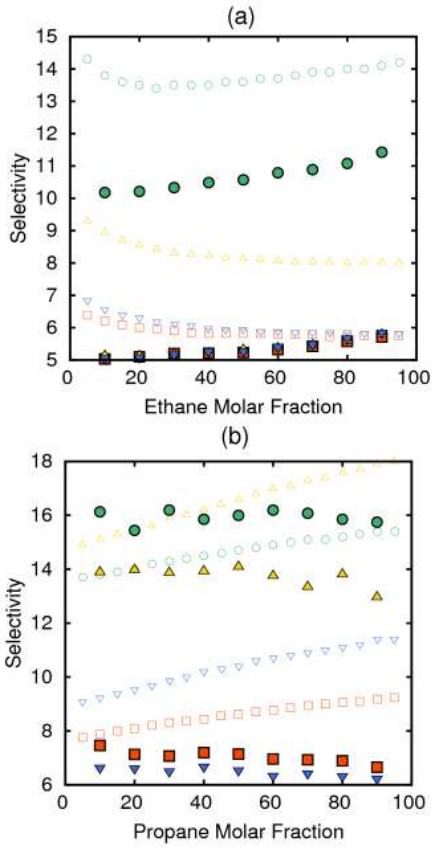

Figure 10. Adsorption selectivity of ethane/ethene (a) and propane/propene (b) binary mixtures as a function of the alkane concentrations in the bulk phase in Co-MOF-74 (red), Fe-MOF-74 (green), Mn-MOF-74 (yellow), and Ni-MOF-74 (blue) at 318 K and 1 bar together with results reported by Geier et al.[11] using IAST theory (open symbols with the same colour code).

As a downside, as reveal results of heats of adsorption for alkenes in Figure A3.15 in the Appendix 3, the force field is not developed for precise energetic interactions that one molecule feels. It is developed for adsorption at finite loading and temperature. The model is therefore not straightforwardly transferable to other systems, and limited to the MOF-74 topology. MOF-74 is however a very challenging system by itself and the force field does allow to predict selectivities of mixtures, which is very hard to address experimentally. Besides, our results show that we do not need an accurate description of the QM-level interaction with the metal, but that, at finite temperature and loading, it can be effectively included in the adjusted Lennard-Jones interactions.

CONCLUSIONS

We studied the feasibility of M-MOF-74 (M=Co, Fe, Ni, Mn) series for olefin/paraffin separation by GCMC molecular simulations. Our computational results on pure-component adsorption match the experimental gas adsorption data for ethane, ethene, propane and propene, suggesting that the proposed force field parameters adequately capture the metal-guest interactions. These cross interactions are likely transferable to larger hydrocarbons. Using these sets of LJ parameters, simulations on the C2 and C3 saturated/unsaturated binary mixtures have been reported for the first time. The open metal sites in coordinatively unsaturated MOFs play a fundamental role to differentiate their interactions with the light hydrocarbons. The adsorption capacities are almost the same for all considered adsorbents, but the adsorption selectivity varies considerably. We found unsat-

urated hydrocarbons to be selectively retained by each considered material, but Fe-MOF-74 appears by far the best candidate for ethane/ethene separation applications. The adsorption selectivity of the Fe-based material is also the highest in the case of C3 hydrocarbon mixtures, but the performance of Mn-MOF-74 is likewise outstanding. These findings are qualitatively kept throughout the pressure and the composition ranges. In regards to the temperature dependence, we found selectivity values to notably decrease with increasing temperature, but the described behavior is likewise unchanged. While the most selective behavior of Fe-MOF-74 for separations of equimolar alkane/alkene mixtures involving C2 hydrocarbons is observed at low pressures, the optimal performance for C3 hydrocarbons occurs at the lowest-cost operational conditions (atmospheric pressure). Interestingly, our results on selectivity at 1 bar and 318 K as a function of the mixture composition partially match previously reported IAST calculations at the same thermodynamic conditions. This is due to the sensitivity of this magnitude to slight changes in the component uptakes. Indeed, we showed for the adsorption isotherms of the equimolar mixtures the agreement through both methods.

Bibliography

[1] J.A. Moulijn A. van Diepen. Comyns, Alan E., M. M. *Applied Organometallic Chemistry*; John Wiley & Sons, Ltd.: Chichester, United Kingdom, 2013; p 566.

[2] Eldridge, R. B. *Industrial & Engineering Chemistry Research* **1993**, *32*, 2208–2212.

[3] Gascon, J.; Blom, W.; van Miltenburg, A.; Ferreira, A.; Berger, R.; Kapteijn, F. *Microporous and Mesoporous Materials* **2008**, *115*, 585–593.

[4] Triebe, R. W.; Tezel, F. H.; Khulbe, K. C. *Gas Separation & Purification* **1996**, *10*, 81–84.

[5] Brown, A. J.; Brunelli, N. A.; Eum, K.; Rashidi, F.; Johnson, J. R.; Koros, W. J.; Jones, C. W.; Nair, S. *Science* **2014**, *345*, 72–75.

[6] Tan, Z.; Gubbins, K. E. *Journal of Physical Chemistry* **1992**, *96*, 845–854.

[7] Millward, A. R.; Yaghi, O. M. *Journal of the American Chemical Society* **2005**, *127*, 17998–17999.

[8] Silva, P.; Vilela, S. M. F.; Tome, J. P. C.; Paz, F. A. A. *Chemical Society Reviews* **2015**, *44*, 6774–6803.

[9] Ferreira, A. F. P.; Santos, J. C.; Plaza, M. G.; Lamia, N.; Loureiro, J. M.; Rodrigues, A. E. *Chemical Engineering Journal* **2011**, *167*, 1–12.

[10] Li, K.; Olson, D. H.; Seidel, J.; Emge, T. J.; Gong, H.; Zeng, H.; Li, J. *Journal of the American Chemical Society* **2009**, *131*, 10368–10369.

[11] Geier, S. J.; Mason, J. A.; Bloch, E. D.; Queen, W. L.; Hudson, M. R.; Brown, C. M.; Long, J. R. *Chemical Science* **2013**, *4*, 2054–2061.

[12] He, Y.; Krishna, R.; Chen, B. *Energy & Environmental Science* **2012**, *5*, 9107–9120.

[13] Bloch, E. D.; Queen, W. L.; Krishna, R.; Zadrozny, J. M.; Brown, C. M.; Long, J. R. *Science* **2012**, *335*, 1606–1610.

[14] Mishra, P.; Edubilli, S.; Mandal, B.; Gumma, S. *Journal of Physical Chemistry C* **2014**, *118*, 6847–6855.

[15] Verma, P.; Xu, X. F.; Truhlar, D. G. *Journal of Physical Chemistry C* **2013**, *117*, 12648–12660.

[16] Caskey, S. R.; Wong-Foy, A. G.; Matzger, A. J. *Journal of the American Chemical Society* **2008**, *130*, 10870–10871.

[17] Botas, J. A.; Calleja, G.; Sanchez-Sanchez, M.; Gisela Orcajo, M. *International Journal of Hydrogen Energy* **2011**, *36*, 10834–10844.

[18] Rosnes, M. H.; Opitz, M.; Frontzek, M.; Lohstroh, W.; Embs, J. P.; Georgiev, P. A.; Dietzel, P. D. C. *Journal of Materials Chemistry A* **2015**, *3*, 4827–4839.

[19] Rosi, N. L.; Kim, J.; Eddaoudi, M.; Chen, B.; O'Keeffe, M.; Yaghi, O. M. *Journal of the American Chemical Society* **2005**, *127*, 1504–1518.

[20] Dietzel, P. D. C.; Morita, Y.; Blom, R.; Fjellvåg, H. *Angewandte Chemie* **2005**, *117*, 6512–6516.

[21] Zhou, W.; Wu, H.; Yildirim, T. *Journal of the American Chemical Society* **2008**, *130*, 15268–15269.

[22] Bhattacharjee, S.; Choi, J.-S.; Yang, S.-T.; Choi, S. B.; Kim, J.; Ahn, W.-S. *Journal of Nanoscience and Nanotechnology* **2010**, *10*, 135–141.

[23] Dietzel, P. D. C.; Panella, B.; Hirscher, M.; Blom, R.; Fjellvag, H. *Chemical Communications* **2006**, 959–961.

[24] Myers, A. L.; Prausnitz, J. M. *Aiche Journal* **1965**, *11*, 121–127.

[25] Chmelik, C.; Kaerger, J.; Wiebcke, M.; Caro, J.; van

Baten, J. M.; Krishna, R. *Microporous and Mesoporous Materials* **2009**, *117*, 22–32.
[26] Mileo, P. G. M.; Cavalcante Jr., C. L.; Moellmer, J.; Lange, M.; Hofmann, J.; Lucena, S. M. P. *Colloids and Surfaces a-Physicochemical and Engineering Aspects* **2014**, *462*, 194–201.
[27] Frenkel, D.; Smit, B. *Computational sciences series*; 2002; Vol. 1; pp 1–638.
[28] Mayo, S. L.; Olafson, B. D.; Goddard, W. A. *Journal of Physical Chemistry* **1990**, *94*, 8897–8909.
[29] Rappe, A. K.; Casewit, C. J.; Colwell, K. S.; Goddard, W. A.; Skiff, W. M. *Journal of the American Chemical Society* **1992**, *114*, 10024–10035.
[30] Dubbeldam, D.; Calero, S.; Vlugt, T. J. H.; Krishna, R.; Maesen, T. L. M.; Beerdsen, E.; Smit, B. *Physical Review Letters* **2004**, *93*, 88302.
[31] Dubbeldam, D.; Calero, S.; Vlugt, T. J. H.; Krishna, R.; Maesen, T. L. M.; Smit, B. *Journal of Physical Chemistry B* **2004**, *108*, 12301–12313.
[32] Liu, B.; Smit, B.; Rey, F.; Valencia, S.; Calero, S. *Journal of Physical Chemistry C* **2008**, *112*, 2492–2498.
[33] Peng, D.-Y.; Robinson, D. B. *Industrial & Engineering Chemistry Fundamentals* **1976**, *15*, 59–64.
[34] Dubbeldam, D.; Calero, S.; Ellis, D. E.; Snurr, R. Q. *Molecular Simulation* **2015**, *42*, 81–101.
[35] Dubbeldam, D.; Torres-Knoop, A.; Walton, K. S. *Molecular Simulation* **2013**, *39*, 1253–1292.
[36] Myers, A. L. In *Chemical Thermodynamics for Industry*; Letcher, T. M., Ed.; Royal Society of Chemistry: Cambridge, 2004.
[37] Yu, D.; Yazaydin, A. O.; Lane, J. R.; Dietzel, P. D. C.; Snurr, R. Q. *Chemical Science* **2013**, *4*, 3544–3556.
[38] Bae, Y.-S.; Lee, C. Y.; Kim, K. C.; Farha, O. K.; Nickias, P.; Hupp, J. T.; Nguyen, S. T.; Snurr, R. Q. *Angewandte Chemie International Edition* **2012**, *51*, 1857–1860.
[39] Bao, Z.; Alnemrat, S.; Yu, L.; Vasiliev, I.; Ren, Q.; Lu, X.; Deng, S. *Langmuir* **2011**, *27*, 13554–13562.
[40] Balestra, S. R. G.; Bueno-Perez, R.; Calero, S. GAIAST. 2016.

CHAPTER 5

Olefin/Paraffin Separation in Open Metal Site Cu-BTC Metal-Organic Framework

Azahara Luna-Triguero, José Manuel Vicent-Luna, Paula Gómez-Álvarez, and Sofía Calero

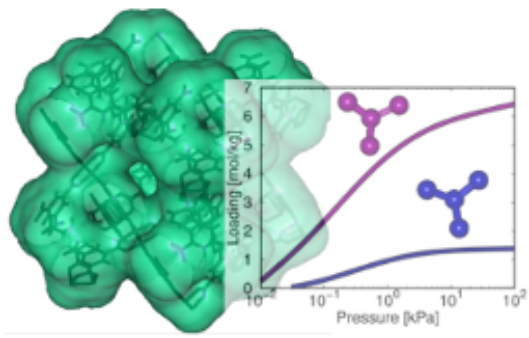

Adsorption in Metal-Organic Frameworks with coordinatively unsaturated sites (CU's) offers a cost-effective alternative to cryogenic processes for olefin/paraffin separation. Since experiments on adsorption equilibrium of gas mixtures are challenging, molecular simulation methods can be exploited to characterise the adsorption at CU's. This work computationally addresses the adsorptive olefin/paraffin separation using Cu-BTC. To this end, we developed a parametrization of specific interactions between hydrocarbon molecules and the CU's, which is of great interest for the modelling community. We obtain the host-guest interacting parameters for linear hydrocarbons by fitting to experimental single-component adsorption isotherms of ethane, ethene, propane, and propene, and examine their transferability to larger hydrocarbons. In addition, we propose force field parameters for branched isobutane and isobutene. We then predict the adsorption selectivity of the binary alkane/alkene mixtures for chains from two to five carbon atoms. Cu-BTC was found potential candidate for the separation, especially for isobutane/isobutene (iC4) mixtures. Besides, our results allowed the rationalization of the difference in the uptakes experimentally observed between both iC4 hydrocarbons.

INTRODUCTION

The separation of olefin/paraffin mixtures is a commercially important process that has a wide range of applications in the chemical industry. For instance, unsaturated hydrocarbons are chemicals usually used as feedstock for polymers manufacture, and saturated hydrocarbons find applications as fuels. Current methods of separation such as cryogenic distillation have high-energy costs due to the requirement of low temperature and high pressure.[1] Adsorptive separation technique involves low energy consumption and could hence reduce significantly operating expenses. Metal-organic frameworks (MOFs), which are nanoporous materials constructed by organic ligands and metal ions, have attracted intense research interest because of their controllable porous structures, versatile chemical compositions, huge surface areas, and potential applications as adsorbents. MOFs containing coordinatively unsaturated metal sites (CU's) -or open metal sites (OMS)- have particularly emerged as candidates for olefin/paraffin separation. Previous work[2–4] reported that the CU's within the bulk of the material act as preferential adsorption sites offering selective olefin binding. Among this type of MOFs, HKUST-1,[5] often denoted as Cu-BTC, has received remarkable attention in gas adsorption and separation. The pore network of this MOF has a simple cubic symmetry ($a = b = c = 26.343$ Å; $\alpha = \beta = \gamma = 90°$). Two octahedral coordinated copper atoms connected to eight oxygen atoms of tetra-carboxylate units to form an open framework with fcc (face-centered cubic) symmetry. The pore structure consists of large central cavities (L2 and L3) of 9 Å in diameter surrounded by small cavities (S1) of 5.0 Å in diameter. These cavities are connected through triangular-shaped 3.5 Å diameter apertures. Figure 1 depicts the structure of Cu-BTC.

In this work we evaluate the coordinately unsaturated Cu-BTC MOF for olefin/paraffin separation by using molecular simulation (MS) techniques. Since experimental isotherms of these gas mixtures cannot be conveniently and rapidly measured, MS is an excellent tool to predict the adsorption behaviour.

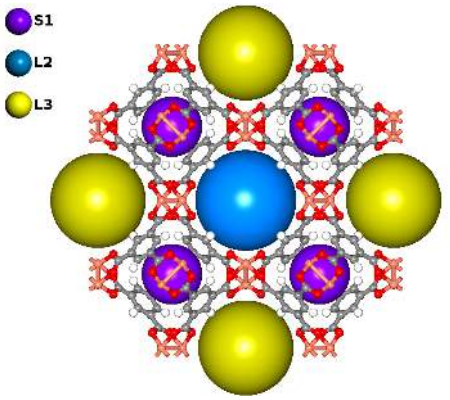

Figure 1. Framework structure of Cu-BTC. Carbon atoms are depicted in grey, hydrogen atoms in white, oxygen atoms in red and copper atoms in orange. The colours denote the different cages in the structure, which are labelled at the top left corner of the figure

Besides, MS techniques are cheap and provide unique microscopic insight and great control on the thermodynamic conditions. There are various computational studies of hydrocarbons in Cu-BTC.[6–9] However, previous work is mainly focused on saturated hydrocarbons, for which the reported force fields describing the interactions in the system provide reasonable agreement with experiments for short chains (1, 2, and 3 carbon atoms).[9] The consistency with experimental data in the case of unsaturated hydrocarbons is however rather poor. Hence we parametrized the cross host-guest Lennard-Jones interactions for ethene and propene by fitting to experimental pure-component isotherms in the literature. To compute adsorption we conduct Grand-Canonical Monte Carlo simulations. The force field was extended for 1-butene and 1-pentene. To improve the agreement with experiments, we proceed similarly for the alkanes. We developed force field parameters for the short alkanes, in such a way that they are transferable for longer hydrocarbons. Branched chains from propane require at the development of specific parameters. We also addressed this issue for the particular cases of isobutane and isobutene (iC4). For the force field development and validation, we examine temperatures at which experimental data on pure hydrocarbons are available. We then use this force field to predict adsorption for saturated/unsaturated binary mixtures of chains from two to five carbon atoms (C2 to C5) at 298 K.

METHODOLOGY

Adsorption isotherms were calculated using Monte Carlo simulations in the grand canonical ensemble μVT, where the chemical potential μ, volume V, and temperature T are kept fixed. The chemical potential is related to the imposed values of fugacity, from which pressures can be determined using the Peng-Robinson equation of state.[10] Simulations were performed using the RASPA code.[11,12] The non-bonded energy potential consists of guest-guest and host-guest Lennard-Jones (L-J) interactions. The potential is truncated and shifted with cutoff distance set to 12 Å and the periodic boundary conditions exerted in the three dimensions.[13] The simulation box corresponds to one unit cell of Cu-BTC, which fulfills that the minimum length in each of the coordinate directions is larger than twice the cutoff distance. Cu-BTC was modeled as a rigid crystal with the framework atoms placed at the crystallographic positions. The L-J parameters for the framework atoms are taken from DREIDING[14] except those for copper atoms, for which we use UFF.[15] For the hydrocarbons we consider united atom models.[16–18] The CH_3, CH_2, and CH groups are described as single interaction centers with their own effective potentials. The hydrocarbons are modeled as nonpolar molecules and the possible effects of polarizability caused by the CU's and

charge transfer are taken into account in the L-J parameters. The bonded interactions include bond-stretching, bond-bending, and torsion potentials. The beads in hydrocarbon chains separated more than tree bonds interact through L-J potential. The Monte Carlo moves involve molecular translation, rotation, regrowth at random position, insertion and deletion, as well as identity changes in the case of mixtures. Each point of the isotherms is obtained after equilibration runs of 10^4 cycles (one cycle involves N moves, being N the number of adsorbed molecules or 20 when the loading is lower) followed by production runs of 10^5 cycles.

Results and Discussion

Force field development and validation: pure-component adsorption isotherms.

We refine the host-guest L-J parameters by fitting to experimental data. We used the standard Lorentz-Berthelot (L-B) mixing rules to obtain the starting fitting parameters. These mixing rules are based on an arithmetic and a geometric average for the calculation of the cross σ_{ij} and ε_{ij} parameter, respectively, from those of i and j atoms (or pseudo-atoms). We mainly increased σ_{ij} parameters, and slightly modified ε_{ij} parameters characterizing cross interactions between each adsorbate pseudo atoms (i: $CH_3\_sp_3$, $CH_2\_sp_3$, CH_sp_3, $CH_2\_sp_2$, CH_sp_2, and C_sp_2) and framework atoms (j: Cu, C, O, and H) simultaneously. With this procedure we obtain a set of parameters for the linear and branched hydrocarbons reproducing accurately the experimental adsorption isotherms. Table 1 collects the entire set of proposed parameters based on single-component adsorption isotherms for C2 and C3 saturated and unsaturated hydrocarbon pairs, and iC4 pair.

Table 1. Host-guest Lennard-Jones interacting parameters proposed in this work for adsorption of saturated and unsaturated hydrocarbons in Cu-BTC. ε_{ij}/k_B in K (top) and σ_{ij} in Å (bottom).

	Guest Pseudoatoms					
	$CH_3\_sp_3$	**$CH_2\_sp_3$**	**CH_sp_3**	**$CH_2\_sp_2$**	**CH_sp_2**	**C_sp_2**
Cu	16.49	11.88	7.2	15.3	12.71	8.52
	3.51	3.61	3.97	3.91	3.94	4.11
O	72.14	51.95	31.48	66.95	55.59	37.25
	3.46	3.56	3.93	3.86	3.89	4.06
C	71.89	51.77	31.38	66.72	55.4	37.13
	3.69	3.79	4.15	4.12	4.15	4.32
H	28.74	20.7	12.54	26.67	22.15	14.84
	3.37	3.47	3.83	3.76	3.79	3.95

Saturated hydrocarbons. For alkanes, parameter refinement involves $CH_3\_sp_3$ and $CH_2\_sp_3$ groups. The pure-component isotherms for ethane and propane up to 100 kPa at 296 K and 303 K respectively are shown in Figure 2. We compare the experimental data taken from experiments[19,20] and computational results using both the standard L-B mixing rules and the proposed parameters in Table 1.

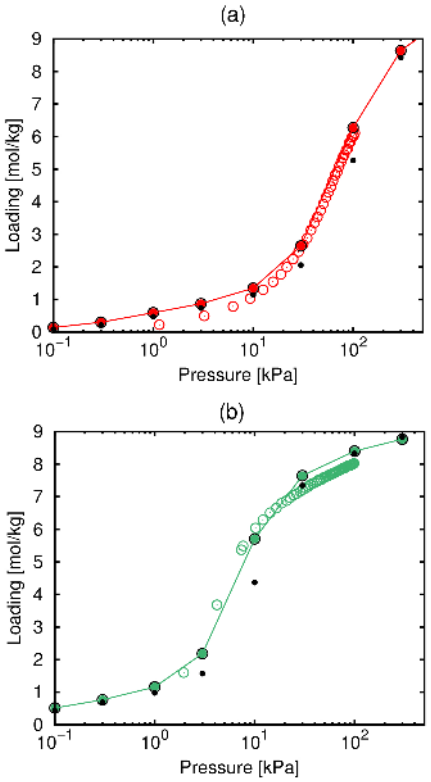

Figure 2. Pure-component adsorption isotherms of ethane (a) at 296 K and propane (b) at 303 K in Cu-BTC. Experiments (open symbols) taken from literature,19-20 computational results using L-B mixing rules (black circles) and using the developed force field parameters (red and green closed circles).

Simulations using L-B mixing rules provide reasonable agreement with experiments, but non-negligible differences are observed, especially for propane We improved the results to ensure the transferability of the force field for longer hydrocarbons. The adjusted atomic groups are also involved in the later refinement for alkenes. To validate the obtained parameters and evaluate their transferability to longer hydrocarbons, we predict the adsorption isotherms of butane and pentane. Figure 3 shows the experimental pure-component adsorption isotherms of ethane at 296 K,[19] propane at 303 K,[20] butane at 298 K,[9] and pentane at 296 K,[21] all ones with the respective computational results using the proposed cross parameters. We found good agreement except for butane at saturation pressures.

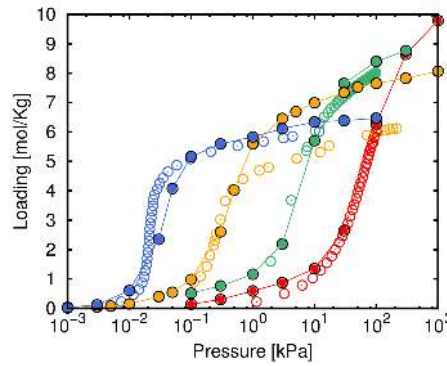

Figure 3. Pure-component adsorption isotherms of ethane (red) at 296 K, propane (green) at 303 K, butane (yellow) at 298 K, and pentane (blue) at 293 K in Cu-BTC. Experiments taken from literature (open symbols),[9,19–21] and computational results using the developed force field parameters (closed symbols).

However, the experimental saturation loading for butane is lower than that for pentane, which is inconsistent with previous work in other MOFs.[22] The sample used for pentane adsorption in Zukal et al.[21] has comparable surface area and pore volume than those reported in Millward and Yaghi[23] and Rowsell and Yaghi.[24] This information leads to conclude that the disagreement with our data could arise from the presence of impurities in the experimental sample used for butane adsorption.

Unsaturated hydrocarbons. Besides cross interactions of the framework atoms with $CH_3\_sp_3$ and $CH_2\_sp_3$, the $CH_2\_sp_2$ and CH_sp_2 groups are also required in the case of alkenes. Similarly to alkanes, we obtain these specific cross parameters by fitting to experimental pure-component adsorption isotherms for ethene[19] and propene.[20] The experimental data and the calculated values using both L-B standard mixing rules and the proposed parameters (four first columns in Table 1) are depicted in Figure 4 for ethene at 296 K and for propene 303 K. Simulations using L-B mixing rules disagree with experiments, with loadings that are significantly lower than experiment for all pressure range. This reveals the need of an accurate force field for the adsorption of the unsaturated hydrocarbons in Cu-BTC. The parametrization proposed in this work achieves high consistency, especially for propane. We used the obtained parameters to compute the pure-component adsorption isotherms of larger unsaturated hydrocarbons with the same pseudo-atoms groups, specifically 1-butene and 1-pentene. Force field transferability to these larger hydrocarbons cannot be checked due to the absence of experimental data. Instead, we assess the force field reliability by comparing the behavior obtained for the various carbon chain

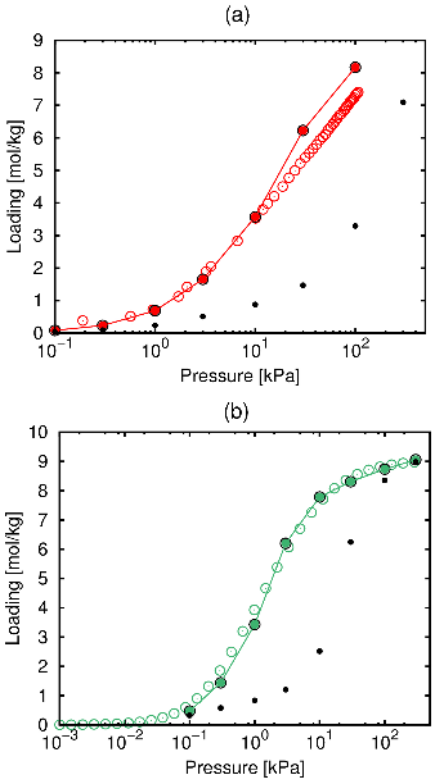

Figure 4. Pure-component adsorption isotherms of ethene (a) at 296 K and propene (b) at 303 K in Cu-BTC. Experiments taken from literature (open symbols),[19,20] computational results using L-B mixing rules (black circles) and using the developed force field parameters (red and green closed circles).

lengths. Figure 5 collects the calculated adsorption isotherms of C2-C5 linear alkenes at near room temperatures. As for saturated hydrocarbons, we can see correlative trends with chain length. Specifically, the onset pressures of adsorption and the adsorption capacities decrease with increasing chain length. We can hence conclude that the adsorption of unsaturated hydrocarbons can be suitably reproduced by using the set of developed parameters.

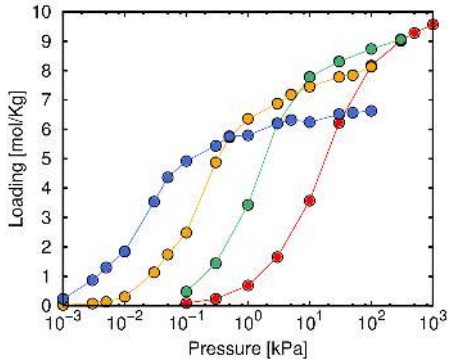

Figure 5. Pure-component adsorption isotherms of ethene (red) at 296 K, propene (green) at 303 K, 1-butene (yellow) at 298 K, and 1-pentene (blue) at 298 K in Cu-BTC from computational results using the developed force field parameters.

Branched hydrocarbons. The description of non-linear or branched hydrocarbons additionally requires a refined set of parameters for interactions of framework atoms with CH_sp_3 and C_sp_2 groups. To this end, we fit to available experimental data on pure-component adsorption isotherms for isobutane and isobutene.[25] They reported that the saturation uptake for single-component adsorption in Cu-BTC of isobutene is slightly larger than that of isobutane, opposite for linear hydrocarbons, for which the loading of the alkane and the alkene are almost the same. This phenomenon can be explained in terms of cage accessibility: While isobutane is not adsorbed within the small S1 cages, the double bond of isobutene allows it to fit inside. To address this issue we performed an additional simulation in order to compute the adsorption capacity (at 1000 kPa and 298 K) of Cu-BTC for isobutene and isobutane (iC4 pairs) using artificial blockage to S1 cages for the latter. We also compute this property for C2-C5 linear saturated and unsaturated hydrocarbon pairs. Results are collected in Table 2. Accordingly to experiments, the adsorption capacity of Cu-BTC for linear alkane and alkene is found similar. Likewise, the loading difference experimentally observed for isobutane-isobutene pair is computationally predicted. The adsorption loading of iC4 pairs along the pressure range is shown in Figure 6. As for linear hydrocarbons, the figure shows experimental results from literature on the pure-component adsorption isotherms for isobutane and isobutene together with computational results using both L-B mixing rules and our developed parameters. The provided force field clearly improves the agreement with experiments in relation to L-B mixing rules, which largely fails in reproducing the adsorption of isobutene. In Figure 6a we include adsorption of

Table 2. Adsorption loading [mol/kg] in Cu-BTC of saturated and unsaturated hydrocarbon chains at 298K and at saturation conditions (1000 kPa).

	C2	C3	C4	C5	iC4
alkane	9.79	9.19	8.06	6.64	7.24
alkene	9.56	9.37	8.24	6.72	8.43

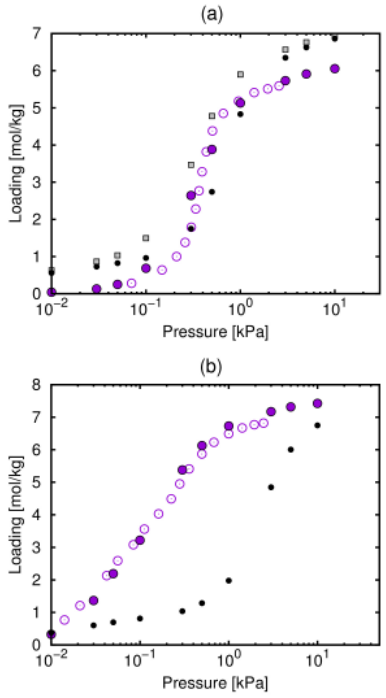

Figure 6. Pure-component adsorption isotherms of isobutane (a) and isobutene (b) at 303 K in Cu-BTC. Experiments taken from literature (open symbols),[25] calculated values using L-B mixing rules (black circles) and using the developed force field (closed violet circles). Squares in plot (a) represent the isobutane adsorption without artificial blockage to S1 cages.

isobutane with and without using artificial blockage to S1 cages. We found excellent agreement with experiments when using the pore blocks, not only at saturation conditions, but also for the entire range of studied pressures. We hence rationalized the uptake difference between isobutane and isobutene.

Prediction of adsorption of olefin/paraffin mixtures in Cu-BTC

Using the developed and validated force field parameters of Table 1 we study the competitive adsorption of the saturated/unsaturated pairs in equimolar mixtures at 298 K. Figure 7 shows the results for olefin/paraffin binary mixtures of C2-C5 linear hydrocarbons. The adsorption in Cu-BTC of alkenes is significantly favored in relation to the alkane analogues. The open metal centers have selective interactions with olefin by the π-complexation. The same behaviour is observed in Figure 8a for the isobutane/isobutene binary mixture. Isobutene exhibits lower onset pressures and higher loadings than isobutane. Figure 8b shows a snapshot of the equimolar mixture at high pressure. One the one hand, both branched hydrocarbons can be adsorbed in the large cavities, but the double bond of isobutene interacts strongly with the open metal site which is only accessible in L3 cavities (see Figure 1). On the other hand, the slightly lower size of isobutene compared with isobutane allows it to fill the small cages (S1) while isobutane is excluded from them. These two effects make this structure highly selective for isobutene over isobutane.

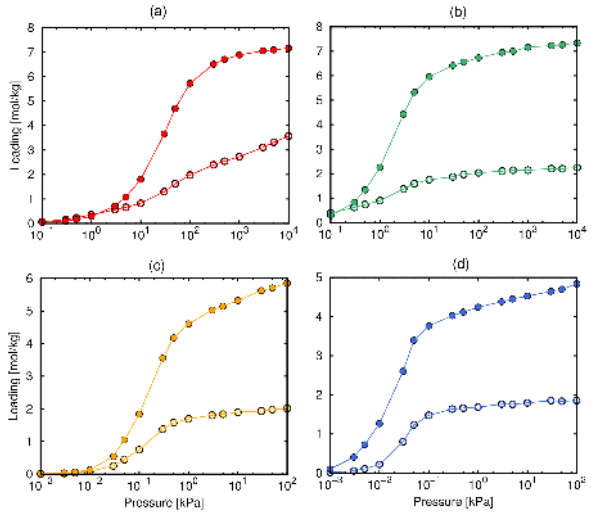

Figure 7. Calculated adsorption isotherms of equimolar mixtures of (a) ethane/ethane, (b) propane/propene, (c) butane/1-butene, and (d) pentane/1-pentene at 298 K in Cu-BTC. Saturated hydrocarbons are depicted as open symbols and unsaturated as closed symbols.

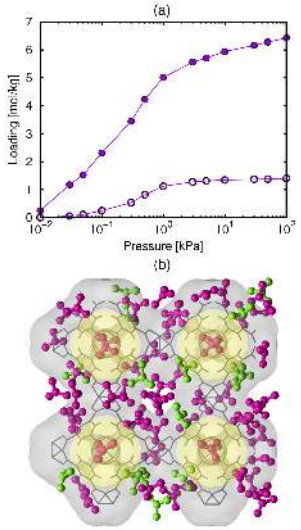

Figure 8. a) Calculated adsorption isotherm of the equimolar binary mixture of isobutane (open symbols) and isobutene (closed symbols) at 298 K in Cu-BTC. b) Snapshot of the adsorption of equimolar mixture of isobutane (green) and isobutene (purple) at 100 kPa and 298 K in Cu-BTC. S1 cages are highlighted in yellow.

Figure 9 shows the adsorption selectivity of the alkene over the alkane of the targeted mixtures in Cu-BTC. This property is defined as $S = \frac{(x_A/y_A)}{(x_B/y_B)}$, were x_i is the molar fraction in the adsorbed phase for the i component and y_i the molar fraction in the bulk phase. Figure 9a shows selectivity as a function of pressure. Two different trends are clearly distinguishable. On the one hand, the adsorption selectivity for the binary mixtures of saturated/unsaturated hydrocarbons from C2 to linear C4 increases with the pressure. On the other hand, in the case of C5 and iC4 pairs the calculated adsorption selectivity shows the highest value at the low pressure regime. This is attributed to the low onset pressures of the C5 and iC4 unsaturated hydrocarbons due to high

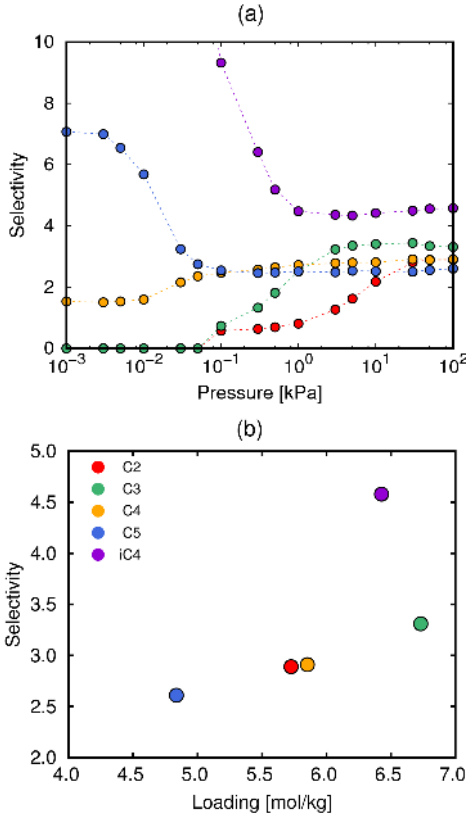

Figure 9. Adsorption selectivity of the alkene over the alkane for the equimolar binary mixtures as a function of pressure (a) and as a function of loading of unsaturated hydrocarbons at 100 kPa (b) for ethane/ethane (red), propane/propene (green), butane/1-butene (yellow) pentane/1-pentene (blue), and isobutane/isobutene (violet) at 298 K in Cu-BTC.

affinity (size effects). Overall, the pressure at which the selectivity reaches saturation values increases with decreasing the hydrocarbon chain length, and it is below atmospheric pressure in all cases. These values for selectivity are in the range of 2-4 for all the linear hydrocarbons and slightly above 4 for the C4 branched alkane/alkene mixture. The selectivity in favor of the alkene over the alkane is the highest for the iC4 pair not only at the lowest-cost operational conditions (atmospheric pressure) but also throughout the pressure range. Based on these results, Cu-BTC seems a potential candidate for separation of C2-C5 olefin/paraffin mixtures and especially for the isobutane/isobutene mixture. Apart from high adsorption selectivities, high adsorption capacities are generally desirable. In order to assess both the separation and the storage ability, figure 9b shows the selectivity values as a function of the uptakes of the unsaturated hydrocarbons at 100 kPa. Due to the ability of branched molecules for molecular packing in this structure, the loading of isobutene results quite large, only slightly overcome by that of propene. Taking both adsorption metrics into account, we conclude the performance of Cu-BTC for olefin/paraffin separation to be the best for the iC4 mixture, followed by the C3 mixture. Finally it is worth noting that although the C5 mixture exhibits the lowest values of both properties at saturation conditions, Cu-BTC is highly selective for pentene over pentane at low pressures.

CONCLUSIONS

We studied the ability of Cu-BTC for olefin/paraffin separation using Monte Carlo simulations in the Grand-Canonical

ensemble. Based on available experimental adsorption isotherms, we developed a force field parametrization describing host-guest interactions for ethane, ethene, propane, and propene. The cross interactions were proved transferable to larger linear hydrocarbons, namely C4 and C5 chains. Additionally, we provided a set of L-J parameters that suitably reproduce experiments for the branched isobutane/isobutene pair. We demonstrated by using artificial pore blockage that the experimental difference in loading between isobutane and isobutene is consequence of non-accessibility of isobutane in the small S1 cages. Using the developed force field, we predicted the adsorption behaviour of equimolar binary mixtures of saturated/unsaturated hydrocarbon pairs from C2 to C5 chains. As in previous work on adsorption of olefin/paraffin mixtures in MOFs with open-metal sites, we found alkenes to be selectively retained.[26] This is based on differences in their electronic properties. The adsorption selectivity (for the alkene over the alkane) of Cu-BTC considerably varies depending on the guest hydrocarbon pair. While lowest-cost operational conditions (atmospheric pressure) are the optimal for C2-C4 linear hydrocarbon pairs, the selectivity for isobutane/isobutene and pentane/pentene is the highest in the low pressure regime. We found Cu-BTC to be more selective for isobutane/isobutene throughout the pressure range. The ability for molecular packing of branched molecules leads likewise to high saturation loadings of isobutene, which is of interest for storage. Among the mixtures of saturated/unsaturated linear hydrocarbons, the best separation performance of Cu-BTC is found for propane/propene mixtures.

Bibliography

[1] J.A. Moulijn A. van Diepen. Comyns, Alan E., M. M. *Applied Organometallic Chemistry*; John Wiley & Sons, Ltd.: Chichester, United Kingdom, 2013; p 566.

[2] Ferreira, A. F. P.; Santos, J. C.; Plaza, M. G.; Lamia, N.; Loureiro, J. M.; Rodrigues, A. E. *Chemical Engineering Journal* **2011**, *167*, 1–12.

[3] Li, K.; Olson, D. H.; Seidel, J.; Emge, T. J.; Gong, H.; Zeng, H.; Li, J. *Journal of the American Chemical Society* **2009**, *131*, 10368–10369.

[4] Heinen, J.; Burtch, N. C.; Walton, K. S.; FonsecaâĂĒGuerra, C.; Dubbeldam, D. *Chemistry âĂŞ A European Journal* **2016**, n/a–n/a.

[5] Chui, S. S. Y.; Lo, S. M. F.; Charmant, J. P. H.; Orpen, A. G.; Williams, I. D. *Science* **1999**, *283*, 1148–1150.

[6] Chmelik, C.; Kaerger, J.; Wiebcke, M.; Caro, J.; van Baten, J. M.; Krishna, R. *Microporous and Mesoporous Materials* **2009**, *117*, 22–32.

[7] Wehring, M.; Gascon, J.; Dubbeldam, D.; Kapteijn, F.; Snurr, R. Q.; Stallmach, F. *Journal of Physical Chemistry C* **2010**, *114*, 10527–10534.

[8] Rubes, M.; Wiersum, A. D.; Llewellyn, P. L.; Grajciar, L.; Bludsky, O.; Nachtigall, P. *Journal of Physical Chemistry C* **2013**, *117*, 11159–11167.

[9] Mileo, P. G. M.; Cavalcante Jr., C. L.; Moellmer, J.; Lange, M.; Hofmann, J.; Lucena, S. M. P. *Colloids and Surfaces a-Physicochemical and Engineering Aspects* **2014**, *462*, 194–201.

[10] Peng, D.-Y.; Robinson, D. B. *Industrial & Engineering Chemistry Fundamentals* **1976**, *15*, 59–64.

[11] Dubbeldam, D.; Calero, S.; Ellis, D. E.; Snurr, R. Q. *Molecular Simulation* **2015**, *42*, 81–101.

[12] Dubbeldam, D.; Torres-Knoop, A.; Walton, K. S. *Molecular Simulation* **2013**, *39*, 1253–1292.

[13] Frenkel, D.; Smit, B. *Computational sciences series*; 2002; Vol. 1; pp 1–638.

[14] Mayo, S. L.; Olafson, B. D.; Goddard, W. A. *Journal of Physical Chemistry* **1990**, *94*, 8897–8909.

[15] Rappe, A. K.; Casewit, C. J.; Colwell, K. S.; Goddard, W. A.; Skiff, W. M. *Journal of the American Chemical Society* **1992**, *114*, 10024–10035.

[16] Dubbeldam, D.; Calero, S.; Vlugt, T. J. H.; Krishna, R.; Maesen, T. L. M.; Beerdsen, E.; Smit, B. *Physical Review Letters* **2004**, *93*, 88302.
[17] Dubbeldam, D.; Calero, S.; Vlugt, T. J. H.; Krishna, R.; Maesen, T. L. M.; Smit, B. *Journal of Physical Chemistry B* **2004**, *108*, 12301–12313.
[18] Liu, B.; Smit, B.; Rey, F.; Valencia, S.; Calero, S. *Journal of Physical Chemistry C* **2008**, *112*, 2492–2498.
[19] He, Y.; Krishna, R.; Chen, B. *Energy & Environmental Science* **2012**, *5*, 9107–9120.
[20] Yoon, J. W.; Jang, I. T.; Lee, K. Y.; Hwang, Y. K.; Chang, J. S. *Bulletin of the Korean Chemical Society* **2010**, *31*, 220–223.
[21] Zukal, A.; Opanasenko, M.; Rubes, M.; Nachtigall, P.; Jagiello, J. *Catalysis Today* **2015**, *243*, 69–75.
[22] Jiang, J. W.; Sandler, S. I. *Langmuir* **2006**, *22*, 5702–5707.
[23] Millward, A. R.; Yaghi, O. M. *Journal of the American Chemical Society* **2005**, *127*, 17998–17999.
[24] Rowsell, J. L. C.; Yaghi, O. M. *Journal of the American Chemical Society* **2006**, *128*, 1304–1315.
[25] Hartmann, M.; Kunz, S.; Himsl, D.; Tangermann, O.; Ernst, S.; Wagener, A. *Langmuir* **2008**, *24*, 8634–8642.
[26] Luna-Triguero, A.; Vicent-Luna, J.; Becker, T.; Vlugt, T.; Dubbeldam, D.; Gómez-Álvarez, P.; Calero, S. *ChemistrySelect* **2017**, *2*.

CHAPTER 6

Improving Olefin Purification using Metal Organic Frameworks with Open Metal Sites

Azahara Luna-Triguero, José Manuel Vicent-Luna, Ali Poursaeidesfahani, Thijs J.H. Vlugt, Rocío Sánchez-de-Armas, Paula Gómez-Álvarez, and Sofía Calero

A The separation and purification of light hydrocarbons is challenging in industry. Recently, ZJNU-30 metal-organic framework has been found potential for adsorption-based separation of olefins and diolefins with four carbon atoms [H. M. Liu et al. Chem. - Eur. J. 2016, 22, 14988-14997]. Our study corroborates this finding but reveals Fe-MOF-74 as a more efficient candidate for the separation due the open metal sites. We performed adsorption-base separation, transient breakthrough curves, and density functional theory calculations. This combination of techniques provides an extensive understanding of the studied system. Using this MOF we propose a separation scheme to obtain high purity product.

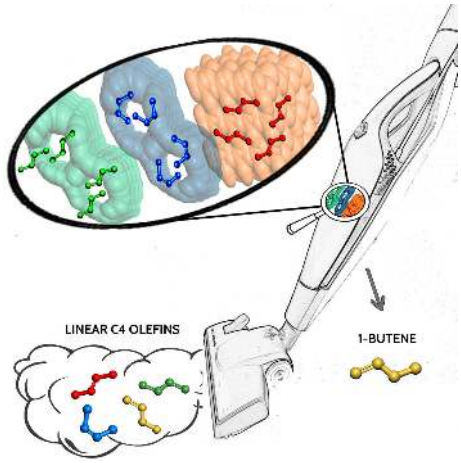

INTRODUCTION

The C4 olefin separation is an industrially important task. 1-Butene is used as comonomer for high density polyethylene and linear low density polyethylene resins and butylene oxide products.[1] It is also a source for heavier olefins by the metathesis reaction. 1-Butene is typically produced by stream- cracking and refinery

processes,[2] but these techniques generate the four isomers of butene (1-butene, 2-cis-butene, 2-trans- butene, and isobutene) as well as 1,3-butadiene. The latter is an industrial chemical used in the production of rubbers. The separation of 1-butene from the other C4 alkenes by distillation is difficult and less energy-efficient[3] because of their similar boiling points and physical properties. The boiling points of 1- butene and isobutene are particularly close to each other, and this is the reason for which chemical separation processes such as acid catalysis are needed.[4] An alternative purification method is pressure swing adsorption, using porous adsorbents to separate gas mixtures either thermodynamically or kinetically.[5,6] Zeolites are being widely studied for the separation of 1-butene from liquid or gas-phase C4 feed streams.[3,7,8] Zeolite RUB-41 (RRO) has been reported for separation of 1-butene from 2- butenes in the liquid phase because 2-butenes are more efficiently packed inside the pores than 1-butene.[3] There are also experimental and theoretical studies using metal-organic frameworks (MOFs) and zeolitic imidazolate frameworks for this process.[9–12] Despite the efforts, obtaining high-purity 1-butene is still challenging nowadays. Recently, MOF ZJNU-30 has been synthetized and reported for butene separation.[13] Also, MOFs with open metal sites (OMS) have been proved successful for the separation of saturated and unsaturated hydrocarbons because of high interactions between OMS and unsaturated hydrocarbons by the π bond.[14,15] MOF-74 has been proposed for ethane/ethene and propane/propene separation both experimentally[16–18] and theoretically,[19,20] and Fe-MOF-74 was targeted for butene isomer separation using density functional theory (DFT) calculations.[11] A recent review on C4 hydrocarbon separations using microporous materials[21] concludes that most studies on these separations are focused on single-component gas adsorption experiments (up to 100 kPa). However, operating pressures in industrial processes are usually higher to minimize costs. With this in mind, we aimed here at gaining insights into the performance of ZJNU-30 and Fe-MOF-74 for butene- efficient competitive adsorption and separation. To this end, we used molecular simulation techniques as well as DFT. These methods are detailed in the next section. The results are comprehensively discussed below and lead to a promising adsorptive-based proposal for extracting high-purity 1-butene at ambient temperatures and pressures up to 1000 kPa.

METHODOLOGY

Adsorption isotherms are calculated using Monte Carlo simulations in the Grand canonical ensemble (GCMC), where chemical potential, volume, and temperature are fixed. The chemical potential is related to the imposed fugacity, from which the pressure is determined using Peng-

Robinson equation of the state.[22] We perform 2×10^5 production runs after 10^4 cycles of initialization for pure component isotherms and 5×10^5 production runs for multicomponent isotherms to ensure an equilibrium fluctuation around a mean value of loading of adsorbates. The heat of adsorption (Q_{st}) is calculated using the Widom particle insertion method[23,24] in the NVT ensemble, using 5×10^5 and 5×10^4 cycles for equilibration and production runs. All these simulations were conducted at ambient temperature using RASPA code.[25–27] The structures are modeled as rigid crystals with the framework atoms placed in the crystallographic positions. For the unsaturated hydrocarbons, we used united atom models.[28] The CH_3 , CH_2 , and CH groups are described as single-interaction centers with their own effective potentials. Adsorbates are modeled as nonpolar molecules, and the possible effects of polarizability caused by the OMS and charge transfer are taken into account in Lennard-Jones (L-J) parameters. We used standard Lorentz-Berthelot (L-B) mixing rules for guest-guest interactions and specific parameters developed in previous works[19,29] for host-guest interactions. The latter were obtained by fitting to experimental data with starting parameters calculated from L-B mixing rules and parameters given in DREIDING[30] and UFF[31] for the framework atoms and the metal sites, respectively. Indeed, studied MOFs without OMS were defined simply using these both generic force fields. As can be seen in Figure S1 of the Supporting Information, the specific set of parameters accurately reproduces the experimental adsorption isotherms of the available olefins in Cu-BTC and M-MOF-74 (M = Co, Fe, Mn, and Ni). Used force-field parameters for MOF-74 are listed in Table A4.1. For the adsorption of these compounds in zeolites, we used the force field reported by Liu et al.[32] We provide in Figure A4.2 in the Appendix 4 a comparison between experimental and simulated isotherms of C4 olefins and diolefins in zeolites. We also performed energy minimizations for Fe-MOF-74 filling with about 18 molecules per unit cell to obtain the preferred site of adsorption. To this aim, we used Baker's[33] method in the NVT ensemble. We performed molecular dynamics (MD) simulations in the NVT ensemble to study the mobility of a single molecule of the adsorbate in the structure. To this aim, we located the molecule in (a) the small cage, (b) the large cage, and (c) the medium- sized cage in ZJNU-30. We used 10^8 MD steps for the production run and time step intervals of 1 fs after 10^5 equilibration cycles.

The adsorption of butene isomers on Fe-MOF-74 has been studied within DFT using the Vienna ab initio simulation package (VASP) code,[34–36] employing the generalized gradient approximation with the Perdew-Burke-Ernzerhof exchange-correlation functional[37] and projector-augmented wave potentials.[38,39] An effective Hubbard correction of 2 eV has been used to describe the localized Fe 3d or-

bitals using Dudarev's approach.[40] This value has recently shown to give structures in very good agreement with experiments for hydrocarbons adsorbed on Fe-MOF-74.[41] Valence electrons are described using a plane-wave basis set with a cutoff of 500 eV, and the gamma point is used for integrations in the reciprocal space.[42] We used a cell containing 162 atoms (including 18 metal centers), and we fully relaxed the structure. The calculated parameters for the bare Fe- MOF-74 unit cell are a = 26.73Å, c = 6.92Å, α = 90.0, β = 90.0, γ = 120.0, which is in good agreement with previous calculations.[43] The ionic relaxation has been performed until the Hellmann-Feynman forces were lower than 0.025 eV/Å. van der Waals interactions were taken into account through the DFT-D2 method of Grimme.[44] To study the adsorption of butene isomers on Fe-MOF-74, one molecule has been placed in the model, starting from 10 different sensible initial geometries for each molecule. We have checked that both for the bare MOF and after adsorption, intrachain ferromagnetic ordering and interchain antiferromagnetic ordering are always preferred.

The efficiency of an adsorbent for a certain separation is determined by the selectivity as well as by the adsorption capacity. In this sense, we also conducted transient breakthrough simulations to assess the combined effect of both properties. In our simulations, we used the methodology described in the literature[45,46] and assumed the following: (1) the system is isothermal; (2) there is no axial dispersion; (3) radial variations in the concentration are negligible compared to axial variations in the bed; (4) mass transfer between the gas phase and the adsorbed phase can be described by the effective linear driving force model; and (5) the gas phase behaves as an ideal gas. The equilibrium loadings for components present in the mixture are computed using the ideal adsorption solution theory (IAST). The material balance for each component in the gas phase is described by (6.1)

$$\frac{1}{RT}\frac{\partial p_i}{\partial t} = -\frac{1}{RT}\frac{\partial u p_i}{\partial z} - \left(\frac{1-\epsilon}{\epsilon}\right)\rho_p k_{L,i}(q_{i,eq} - \bar{q}_{i,ads}) \tag{6.1}$$

The system of equations is discretized in time and space using finite difference approximations and solved step-wise in time. The numerical method of lines with the implicit trapezoidal rule is used to perform integration in time.

The parameters used for breakthrough simulations are as follows: length of packed bed, L = 0.3 m; voidage of packed bed, ϵ = 0.4; superficial gas velocity in the inlet, u = 0.04 m/s; the framework density of the studied MOFs is 1126.7, 1180.5, and 879.1 kg/m^3 for Fe-MOF-74, Co-MOF-74, and Cu-BTC, respectively.

Results and Discussion

ZJNU-30 is a Zr-based MOF with a C3-symmetrical trigonal tricarboxylate linker.

The structure has a cubic symmetry with cell parameters of 28.35 Å. This MOF was reported with octahedral and cuboctahedral cages of about 14 and 22 Å in diameter, respectively. These two cages are interconnected throughout the four-membered windows to form one-dimen- sional channels.[13] Apart from the reported cages, our calculations on pore size distribution (PSD) revealed a third cavity of about 7 Å in diameter. Figure 1a depicts the atomic connectivity and the framework cages, and the calculated PSDs are shown in Figure 1b. As it is apparent from the average occupation density profiles shown in Figure 1c, the small cavities that we identified are inaccessible to *n*-butenes but could be useful in other applications. This finding is evidenced for the specific case of 1,3-butadiene given in the left side of Figure 1c, which shows the average occupation profile obtained by MD simulations for single molecules that are artificially located in the small cages. These molecules cannot cross to the other cages. However, a homogeneous occupation distribution is observed when the molecule is initially placed in the large- or medium-sized cages (Figure 1c right). Hence, the small cages require being blocked during Monte Carlo runs for these adsorbates. As shown in Figure 2, the simulated single- component isotherms of 1-butene, 1,3-butadiene, 2-*cis*-butene, and 2-*trans*-butene in the properly blocked ZJNU-30 structure are in good agreement with experimental data

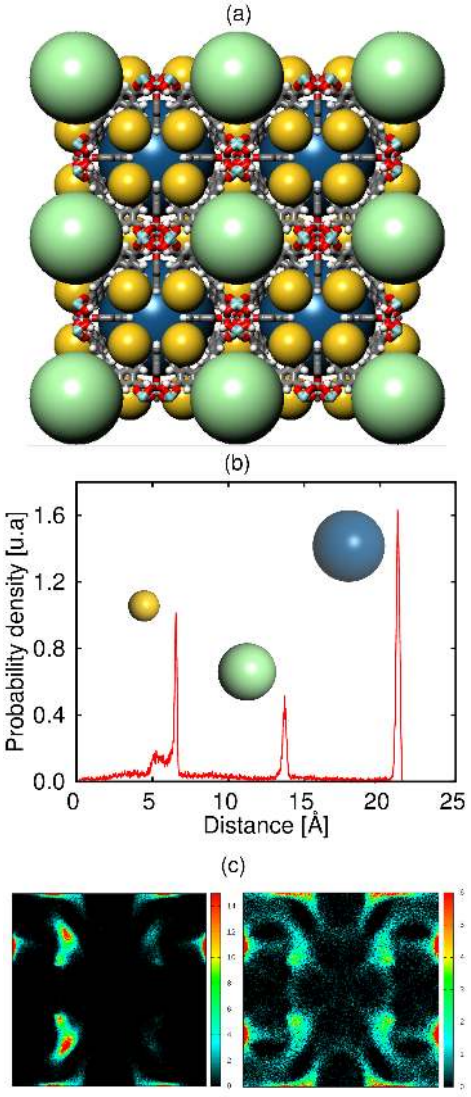

Figure 1. (a) Schematic representation of the atomic connectivity of ZJNU-30. Carbon atoms in gray, oxygen atoms in red, hydrogen atoms in white, and zirconium atoms in turquoise. The spheres represent the pore cages. (b) PSD of ZJNU-30. (c) Average occupation profiles for ZJNU-30 from MD simulations using one molecule of 1,3-butadiene (left: initial position in small cages, right: initial position in large or medium cages).

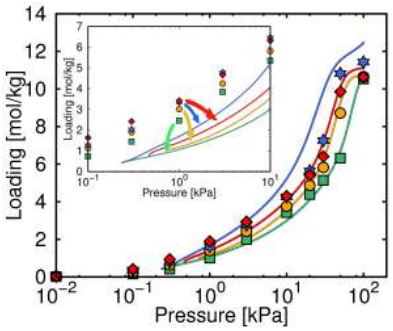

Figure 2. Calculated (symbols) and experimental isotherms (lines),[13] of 2-*cis*-butene (blue), 2-*trans*-butene (red), 1-butene (yellow), and 1,3-butadiene (green) in ZJNU-30 at 298 K. Inset figure shows the calculated values (symbols) if appropriate pore blocks are disregarded.

reported by Liu et al.[13] A systematical overestimation of experimental results would occur if artificial blocks were disregarded (inset Figure 2).

Figure 3 shows the adsorption behavior of 1,3-butadiene, 2- *cis*-butene, 2-*trans*-butene, and 1-butene in Fe-MOF-74 at ambient temperatures. The single-component adsorption isotherms (Figure 3a) reveal that Fe-MOF-74 exhibits the highest affinity to the diolefin: the onset adsorption fugacity of 1,3-butadiene is about 1 order of magnitude lower than that of the olefins. Among them, the geometrical isomer leads to an evident adsorption discrimination, with preferential adsorption decreasing in the trend 2-cis-butene > 2-trans-butene > 1- butene. This adsorption hierarchy is the same as that found in ZJNU-30. The highest affinity of Fe-MOF-74 to the diolefin is likewise noticeable by the results for the heat of adsorption Q_{st} , which are provided as a function of loading from isotherms in Figure 3b. However, the Q_{st} values corresponding to the olefins are quite close. In all the cases, the heat of adsorption decreases with the increasing amount of adsorbed molecules. The error in Q_{st} is accumulative with the loading, as shown in the error bars. Results at low coverage agree well with these obtained using the Widom test-particle method: -58.2, -51.6, -48.9, and -48.3 kJ/mol for 1,3-butadiene, 2-*cis*-butene, 2-*trans*-butene, and 1- butene, respectively.

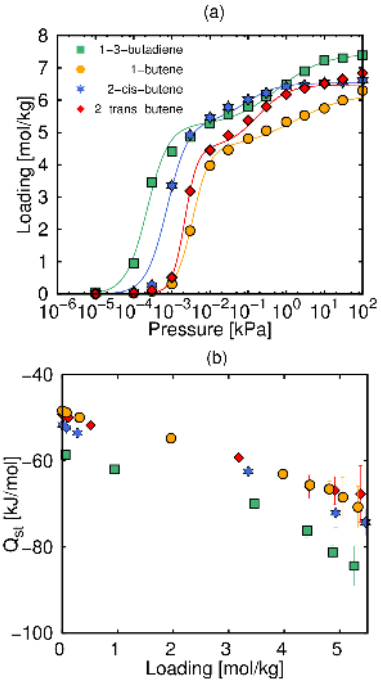

Figure 3. a) Pure adsorption isotherms (symbols) and isotherm fits (lines) and (b) heat of adsorption as a function of loading of 1,3- butadiene, 1-butene, 2-*cis*-butene, and 2-*trans*-butene in Fe-MOF-74 at 298 K.

Kim and Jung[11] provided theoretical calculations, indicating that 1-butene could approach the metal binding sites more closely than the other butene isomers, enabling stronger bonding and π-back-bonding interactions with MOF-74. Potential π complexation is significantly hindered sterically for 2-butenes, and hence, their adsorption in the MOF is mainly governed by van der Waals interactions. They observed that steric repulsion follows the trend trans > cis > isobutene > 1-butene and concluded MOF-74 to be suitable for separating 1-butene from the other isomers. Liao et al.[47] conducted experimental breakthrough curves for an equimolar mixture of butane, 1-butene, isobutene, and 1,3-butadiene in Co-MOF-74 and observed a trend in such an order (of citing). They provided experimental evidence that MOF-74 exhibits higher affinity to isobutene than to 1-butene. Our DFT calculations show that 1,3-butadiene has higher interactions than 1-butene in concordance with the experimental observations. Additionally, we observed that 1-butene is more stable than 2-butenes. The obtained binding energies are listed in Table A4.2 in the Appendix 4 and compared with calculations from the literature.[11] We also found discrepancies in the average distances between the Fe atom and C_sp_2 but the same trend (Table A4.3). Despite the fact that DFT shows higher affinity of 1-butene with the metal center, we observe slight differences in the heat of adsorption between the isomers. The pure adsorption isotherms (Figure 3a) show different trends too, and 2-*cis*-butene has preferential adsorption. This could be attributed to size effects because the kinetic diameter of 2-*cis*-butene (4.96 Å) is considerably larger than that of 1,3-butadiene (4.31 Å), 2-*trans*-butene (4.31 Å), and of 1-butene (4.46 Å).[19,48] However, adsorption of 2-trans-butene is surprisingly favored in relation to 1-butene. This could be explained in terms of a second preferential adsorption site for 2- *trans*-butene, which is evident from the average occupation profiles and energy minimizations at saturation conditions depicted in Figure 4a,b. The new site of adsorption is due to a combination of the size effect, the weaker interaction energy, and the distance to the metal center. This adsorption site is likewise observed for 1,3-butadiene because of its similar size, but it vanishes for 1-butene and 2-*cis*-butene. Similarly, it was found in Cu-MOF-74 for carbon dioxide, with less affinity for the molecule than the other M-MOF-74.[49] Figure 4c shows the equilibrium distances between C_sp_2 and the Fe atom of the MOF, which are listed in Table A4.2 in the Appendix 4.

In addition to the study carried out for Fe-MOF-74, we calculated pure-component adsorption isotherms of 1,3-butadiene, 2-*cis*-butene, 2-*trans*-butene, and 1-butene in Co- MOF-74 and Cu-BTC.

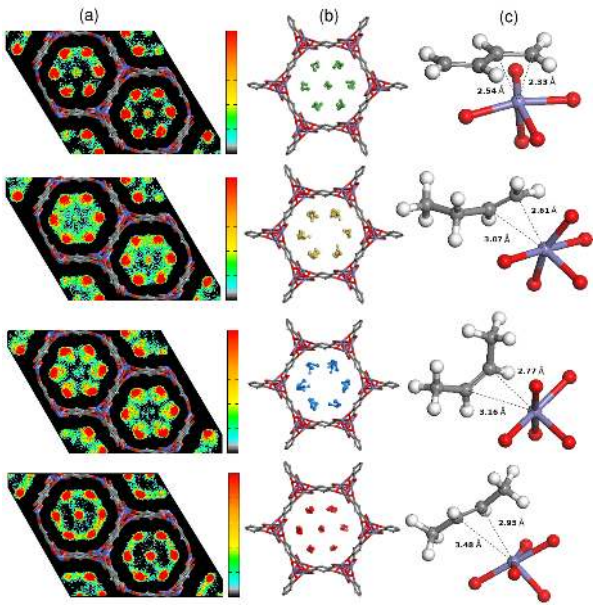

Figure 4. (a) Average occupation profiles (b) and equilibrium positions from classical minimizations at saturation conditions and (c) equilibrium distances between C_sp$_2$ and the metal center of the structure from DFT calculations. From top to bottom: 1,3-butadiene, 1-butene, 2-*cis*-butene, and 2-*trans*-butene in Fe-MOF-74.

For the latter, we also calculated the adsorption isotherm of butane and isobutene to compare with a recently reported paper that provides the experimental breakthrough for an equimolar mixture of 1,3-butadiene, 1- butene, butane, and isobutene.[47] The adsorption isotherms of the single components in Fe-MOF-74, Co-MOF-74, and Cu- BTC were fitted using the Langmuir-Freundlich dual-site model (Figures A4.3 and A4.4). The fitting parameters are listed in Tables A4.3-A4.5 in the Appendix 4. We performed breakthrough calculations of the mentioned mixture for Cu-BTC and the four-component equimolar mixture of 1,3-butadiene, 2-*cis*-butene, 2-*trans*-butene, and 1-butene in Cu-BTC, Co-MOF-74, and Fe-MOF-74 at total pressure of 100 kPa. We obtained for Cu-BTC the following adsorption hierarchy: butane > 1-butene > isobutene > 1,3-butadiene (Figure A4.5). This finding is in agreement with the experimental breakthrough reported for the same mixture.[49] The sequence of the calculated breakthrough (Figures 5, A4.5, and A4.6) on the three structures is 1-butene > 2-*trans*-butene > 2-*cis*-butene > 1,3-butadiene, which matches with the above reported competitive adsorption of the mixture. The adsorption selectivity $S_{AB} = \frac{(x_A/y_A)}{(x_B/y_B)}$ gauges if a material exhibits selec-

tive adsorption for the component A over B. This value is calculated in a straightforward manner from the molar fractions in the adsorbed phase (x_A , x_B) and the molar fractions in the bulk phase (y_A , y_B). Figure 6 depicts adsorption selectivities of ZJNU-30 and Fe-MOF-74 calculated from the equimolar four-component mixture of 1-butene, butadiene, 2- *cis*-butene, and 2-*trans*-butene at 298 K. The adsorption loadings from the multicomponent mixture in Fe-MOF-74 were obtained by conducting GCMC simulations using a specifically developed force field.[19] For ZJNU-30, we used IAST,[50,51] and pure-component experimental isotherms pro- vided by Liu et al.[13] We found adsorption selectivity to be independent of pressure in ZJNU-30 and to reach the highest values at low pressure (from 0.1 to 10 Pa) in Fe-MOF-74.

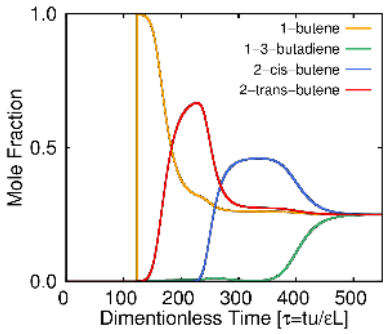

Figure 5. a) Transient breakthrough simulations for the separation of an equimolar multicomponent mixture of 1,3-butadiene, 1-butene, 2-*cis*-butene, and 2-*trans*-butene in Fe-MOF-74 at 298 K.

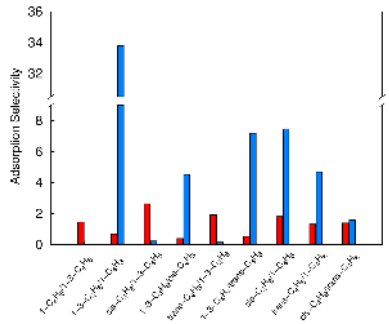

Figure 6. a) Adsorption selectivity for 2-cis-butene/1,3-butadiene, 1,3- butadiene/2-cis-butene, 2-trans-butene/1,3-butadiene, 1,3-butadiene/ 2-trans-butene, 2-cis-butene/1-butene, 2-trans-butene/1-butene, and 2-cis-butene/2-trans-butene calculated from the a adsorption isotherms of equimolar quaternary mixtures in ZJNU-30 and Fe-MOF-74 at 298 K and 10 kPa.

This is ascribed to the differences in the onset pressures of adsorption of the compounds in this MOF. In Figure 6, we plot the adsorption selectivity at 10 kPa. We choose this value because it is a practical operational condition and, at this pressure, the loadings are already large enough to obtain reliable adsorption selectivity. ZJNU-30 and Fe-MOF-74 favor the adsorption for different butene isomers. The adsorption selectivity in Fe-MOF-74 is always in favor of the diolefin, whereas ZJNU-30 preferentially adsorbs the cis- and trans- isomers. In both structures, the cis-/trans-selectivity is similar, and the less adsorbed component is 1-butane for Fe-MOF-74 and the diolefin for ZJNU-30.

Another interesting finding is that Fe-MOF-74 exhibits larger selectivity values than ZJNU-30. The selectivity of 1,3- bu-

tadiene over 1-butene is 50 times larger in Fe-MOF-74 than in ZJNU-30 because of the higher interaction of the double bond and the metallic center of the structure with OMS. Overall, we found Fe-MOF-74 unquestionably more selective than ZJNU-30 for butene separation. Hence, we can use this MOF to obtain high-purity 1-butene from C4 feed streams at ambient temperatures and operational pressures from 100 to 1000 kPa (Figure 7). First, Fe-MOF-74 can be used to separate diolefin 1,3-butadiene from the other components of the equimolar quaternary mixture (left plot). This MOF is also suitable for the separation of 2-cis-butene from the remaining ternary mixture of 2-cis-butene (24%), 2-trans-butene (30%), and 1-butene (46%) (center plot). Finally, the separation of 1- butene from 2-trans-butene can be satisfactorily addressed using RRO zeolite. The competitive adsorption of the 1-butene (72%)/2-trans-butene (28%) binary mixture in this zeolite results in the exclusion of 1-butene yielding a 94% of the purity product for the operating conditions (right plot).

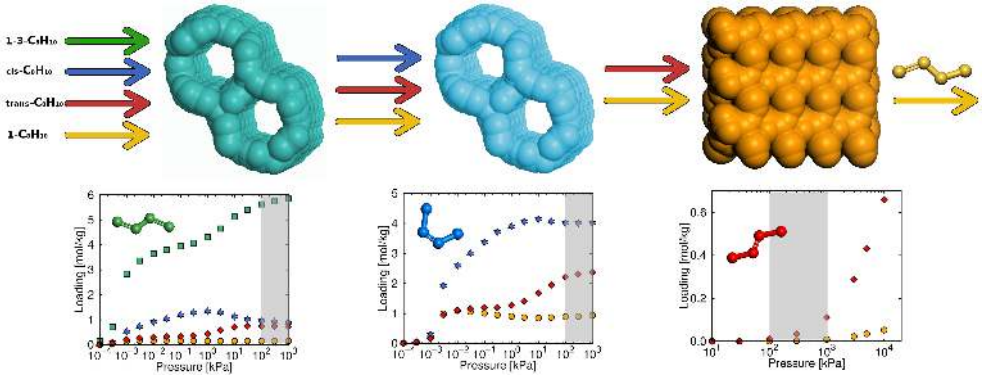

Figure 7. Proposed adsorptive-based separation process of 1-butene from the C4 alkene mixture. Multicomponent adsorption isotherms in Fe-MOF-74 (a,b) and RRO zeolite (c) at 298 K. 2-*cis*-Butene (blue), 2-*trans*-butene (red), 1-butene (yellow), and 1,3-butadie (green).

CONCLUSIONS

In summary, MOFs with OMs are able to sepatate diolefins from 1-butene, 2-trans-butene, and 2-cis-butene because of the higher affinity with the metal center of the structure. In particular, GCMC simulations and DFT calculations evidence this higher interaction for the diolefin with the Fe atom of MOF-74. The separation between 2-cis-butene from the remaining butene isomers is due to the steric effects. We found a new site of adsorption shown by 2-trans-butene, which explains its higher saturation in the pure adsorp-

tion isotherm than for 1-butene. On the basis of these findings, we propose an adsorptive base separation process which explores the ability of MOF-74 to separate the diolefin and 2-cis-butene from the studied mixture. We propose the separation of remaining compounds (1-butene and 2-trans-butene) using zeolite RRO. The hierarchy shown by adsorptive separation is supported by breakthrough curves.

Bibliography

[1] Alsadoun, A. W. *Applied Catalysis a-General* **1993**, *105*, 1–40.

[2] Aljarallah, A. M.; Anabtawi, J. A.; Siddiqui, M. A. B.; Aitani, A. M.; Alsadoun, A. W. *Catalysis Today* **1992**, *14*, R9–&.

[3] Herm, Z. R.; Bloch, E. D.; Long, J. R. *Chemistry of Materials* **2014**, *26*, 323–338.

[4] Tijsebaert, B.; Varszegi, C.; Gies, H.; Xiao, F. S.; Bao, X. H.; Tatsumi, T.; Muller, U.; De Vos, D. *Chemical Communications* **2008**, 2480–2482.

[5] Sircar, S. *Industrial & Engineering Chemistry Research* **2006**, *45*, 5435–5448.

[6] Yang, R. T. Gas separation by adsorption processesImperial College Press. 1997.

[7] Jousse, F.; Leherte, L.; Vercauteren, D. P. *Journal of Physical Chemistry B* **1997**, *101*, 4717–4732.

[8] Zhu, W.; Kapteijn, F.; Moulijn, J. A.; Den Exter, M. C.; Jansen, J. C. *Langmuir* **2000**, *16*, 3322–3329.

[9] Alaerts, L.; Maes, M.; van der Veen, M. A.; Jacobs, P. A.; De Vos, D. E. *Physical Chemistry Chemical Physics* **2009**, *11*, 2903–2911.

[10] van den Bergh, J.; Gücüyener, C.; Pidko, E. A.; Hensen, E. J. M.; Gascon, J.; Kapteijn, F. *ChemistryâĂŞA European Journal* **2011**, *17*, 8832–8840.

[11] Kim, H.; Jung, Y. *Journal of Physical Chemistry Letters* **2014**, *5*, 440–446.

[12] Kishida, K.; Okumura, Y.; Watanabe, Y.; Mukoyoshi, M.; Bracco, S.; Comotti, A.; Sozzani, P.; Horike, S.; Kitagawa, S. *Angewandte Chemie-International Edition* **2016**, *55*, 13784–13788.

[13] Liu, H. M.; He, Y. B.; Jiao, J. J.; Bai, D. J.; Chen, L.; Krishna, R.; Chen, B. L. *Chemistry-a European Journal* **2016**, *22*, 14988–14997.

[14] Bae, Y.-S.; Lee, C. Y.; Kim, K. C.; Farha, O. K.; Nickias, P.; Hupp, J. T.; Nguyen, S. T.; Snurr, R. Q. *Angewandte Chemie International Edition* **2012**, *51*, 1857–1860.

[15] Bao, Z.; Alnemrat, S.; Yu, L.; Vasiliev, I.; Ren, Q.; Lu, X.; Deng, S. *Langmuir* **2011**, *27*, 13554–13562.

[16] Geier, S. J.; Mason, J. A.; Bloch, E. D.; Queen, W. L.; Hudson, M. R.; Brown, C. M.; Long, J. R. *Chemical Science* **2013**, *4*, 2054–2061.

[17] Bloch, E. D.; Queen, W. L.; Krishna, R.; Zadrozny, J. M.; Brown, C. M.; Long, J. R. *Science* **2012**, *335*, 1606–1610.

[18] He, Y.; Krishna, R.; Chen, B. *Energy & Environmental Science* **2012**, *5*, 9107–9120.

[19] Luna-Triguero, A.; Vicent-Luna, J.; Becker, T.; Vlugt, T.; Dubbeldam, D.; Gómez-Álvarez, P.; Calero, S. *ChemistrySelect* **2017**, *2*.

[20] Verma, P.; Xu, X. F.; Truhlar, D. G. *Journal of Physical Chemistry C* **2013**, *117*, 12648–12660.

[21] Gehre, M.; Guo, Z.; Rothenberg, G.; Tanase, S. *ChemSusChem* **2017**, *10*, 3947–3963.

[22] Peng, D.-Y.; Robinson, D. B. *Industrial & Engineering Chemistry Fundamentals* **1976**, *15*, 59–64.

[23] Widom, B. *The Journal of Chemical Physics* **1963**, *39*, 2808–2812.

[24] Poursaeidesfahani, A.; Torres-Knoop, A.; Rigutto, M.; Nair, N.; Dubbeldam, D.; Vlugt, T. J. H. *The Journal of Physical Chemistry C* **2016**, *120*, 1727–1738.

[25] Dubbeldam, D.; Torres-Knoop, A.; Walton, K. S. *Molecular Simulation* **2013**, *39*, 1253–1292.

[26] Dubbeldam, D.; Calero, S.; Ellis, D. E.; Snurr, R. Q. *Molecular Simulation* **2015**, *42*, 81–101.

[27] Dubbeldam, D.; Frost, H.; Walton, K. S.; Snurr, R. Q. *Fluid Phase Equilibria* **2007**, *261*, 152–161.

[28] Wick, C. D.; Martin, M. G.; Siepmann, J. I. *The Journal of Physical Chemistry B* **2000**, *104*, 8008–8016.

[29] Luna-Triguero, A.; Vicent-Luna, J.; Gómez-Álvarez, P.; Calero, S. *Journal of Physical Chemistry C* **2017**, *121*.

[30] Mayo, S. L.; Olafson, B. D.; Goddard, W. A. *Journal of Physical Chemistry* **1990**, *94*, 8897–8909.

[31] Rappe, A. K.; Casewit, C. J.; Colwell, K. S.; Goddard, W. A.; Skiff, W. M. *Journal of the American Chemical Society* **1992**, *114*, 10024–10035.

[32] Liu, B.; Smit, B.; Rey, F.; Valencia, S.; Calero, S. *Journal of Physical Chemistry C* **2008**, *112*, 2492–2498.

[33] Baker, J. *Journal of Computational Chemistry* **1986**, *7*, 385–395.

[34] Kresse, G.; Hafner, J. *Physical Review B* **1993**, *47*, 558.

[35] Kresse, G.; Hafner, J. *Physical Review B* **1994**, *49*, 14251.

[36] Kresse, G.; Furthmüller, J. *Computational materials science* **1996**, *6*, 15–50.

[37] Perdew, J. P.; Burke, K.; Ernzerhof, M. *Physical Review Letters* **1996**, *77*, 3865.

[38] Blöchl, P. E. *Physical Review B* **1994**, *50*, 17953.

[39] Kresse, G.; Joubert, D. *Physical Review B* **1999**, *59*, 1758.

[40] Dudarev, S. L.; Botton, G. A.; Savrasov, S. Y.;

Humphreys, C. J.; Sutton, A. P. *Physical Review B* **1998**, *57*, 1505.

[41] Verma, P.; Maurice, R.; Truhlar, D. G. *The Journal of Physical Chemistry C* **2016**, *120*, 9933–9948.

[42] Monkhorst, H. J.; Pack, J. D. *Physical Review B* **1976**, *13*, 5188.

[43] Lee, J. S.; Vlaisavljevich, B.; Britt, D. K.; Brown, C. M.; Haranczyk, M.; Neaton, J. B.; Smit, B.; Long, J. R.; Queen, W. L. *Advanced Materials* **2015**, *27*, 5785–5796.

[44] Grimme, S. *Journal of Computational Chemistry* **2006**, *27*, 1787–1799.

[45] Krishna, R. *Microporous and Mesoporous Materials* **2014**, *185*, 30–50.

[46] Krishna, R.; Long, J. R. *The Journal of Physical Chemistry C* **2011**, *115*, 12941–12950.

[47] Liao, P.-Q.; Huang, N.-Y.; Zhang, W.-X.; Zhang, J.-P.; Chen, X.-M. *Science* **2017**, *356*, 1193–1196.

[48] Gucuyener, C.; van den Bergh, J.; Joaristi, A. M.; Magusin, P. C. M. M.; Hensen, E. J. M.; Gascon, J.; Kapteijn, F. *Journal of Materials Chemistry* **2011**, *21*, 18386–18397.

[49] Queen, W. L.; Hudson, M. R.; Bloch, E. D.; Mason, J. A.; Gonzalez, M. I.; Lee, J. S.; Gygi, D.; Howe, J. D.; Lee, K.; Darwish, T. A. *Chemical Science* **2014**, *5*, 4569–4581.

[50] Myers, A. L.; Prausnitz, J. M. *Aiche Journal* **1965**, *11*, 121–127.

[51] Balestra, S. R. G.; Bueno-Perez, R.; Calero, S. GAIAST. 2016.

CHAPTER 7

Olefin/Paraffin Separation Using Aluminosilicates

Azahara Luna-Triguero; Andrezj Sławek; Rocío Sánchez-de-Armas; Juan José Gutiérrez-Sevillano; Conchi O. Ania; José B. Parra; José Manuel Vicent-Luna; and Sofía Calero

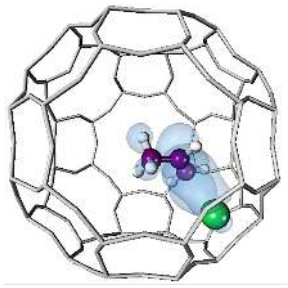

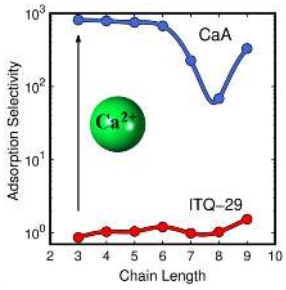

The purification of the α-olefins though challenging, is mandatory step for their use in the chemical industry. Since adsorptive separation using zeolites is one of the most promising alternatives for olefin/paraffin separation in terms of energy efficiency, we use a combination of experiments and molecular simulations to study the effect that the topology and chemical composition of the zeolite exert on the purification of olefins. To this aim we developed an effective potential for the cations with the double bond of the olefins. The potential parameters were validated with our experimental adsorption isotherms and isobars of propylene and 1-hexene. We performed an extensive study of propane/propylene separation in more than 200 all silica zeolites and several aluminosilicates. We also performed DFT and classical optimization of the structures which is key factor for the adsorption mechanisms. DFT calculations also allowed the analysis of binding energies and binding geometries of propane and propylene in NaY and LTA5A. We discussed the effect exerted by the cations on the separation performance of the zeolites. Our study shows that aluminosilicates with calcium cations are the best candidates to separate olefins from paraffins, due to the stronger interaction of the double bond of olefins with these divalent cations.

INTRODUCTION

Linear α-olefins are widely used in industry. Propylene is an important light olefin used in refinery operations. It is a petrochemical raw material used in rubber and plastic industries, and as intermediate compound for the production of polypropylene. The propylene demand is growing due to the increment of polypropylene production.[1] However, the production of propylene is limited.[2] Larger α-olefins with chain length from four to eight carbon atoms (C4-C8) are used for production of aldehydes *via* oxo synthesis to produce short fatty acids.[2] 1-butene, 1-hexene and 1-octene are used as comonomers in the manufacture of high-density polyethylene (HDPE) and linear low-density polyethylene (LLDPE).[3] Light olefins are obtained primarily by stream cracking or as a product of fluid catalytic cracking of gas oils in refineries. In order to obtain the polymer-grade olefin, the separation of olefin from paraffin is required. This separation is a challenging procedure that is conventionally achieved by distillation, which is energy-intensive and has a high operational cost due to the close boiling point of the compounds.[4] Among several new energy-efficient alternatives, adsorptive separation is one of the most promising techniques.[5] While cryogenic distillation relies on small differences in the boiling points of olefin and paraffin components, adsorptive separations take advantage of dissimilar physical properties such as kinetic diameters, polarity, and polarizability of the adsorbates. In this regard, the selection of adsorbents with optimal selectivity and adsorption capacity is an important step when designing the whole adsorption process. Zeolites have been extensively studied for olefin/paraffin separation. Pure silica zeolites rarely achieve great separations except for kinetic separation in some zeolites, for instance ITQ-12.[6–8] Sodium and calcium forms of zeolite X were studied via gas chromatographic methods to determine the potential separation of ethylene from ethane and methane,[9] and a large variety of 13X zeolites[10–12] including Li^+, K^+, Rb^+, and Cs^+ cation exchanged forms have been proposed for olefin/paraffin separation.[13,14] There are many experimental studies on the adsorption of olefin and paraffin in zeolites LTA4A and LTA5A. These zeolites have also been proposed as adsorbent for some targeted separations.[15–17]

There are a large number of zeolites covering a wide range of topologies and chemical composition. This makes difficult the search of an efficient adsorbent for a given process. In this sense, molecular simulation is an efficient tool to predict physical and chemical properties of materials. The accuracy of classical simulations depends on the models and force fields used to describe the systems. Experimental data are in most cases crucially important for validation of the force fields used in simulation. The use of molecular simulations for adsoption isotherms of paraf-

fins in pure silica zeolites is being reported in many works.[8,18–20] Most of these works use the force field developed for Dubbeldam et al.,[21] that is accurate and can reproduce experimental data for pure silica zeolites. However, olefins have not been extensively studied using molecular simulation for being more complex. In these molecules, electrostatic interactions play an important role, particularly in aluminosilicates. In this work we propose a set of Lennard-Jones parameters to model the interaction of cations (Na^+ and Ca^{2+}) with the double bond of olefins. This is essential contribution by itself since (1) molecular simulation studies in aluminosilicate zeolites for olefin/paraffin separation are scarce and (2) available parameters are reported for a given structures and not transferable to other topologies.[17,22,23] In this regard, we developed a transferable set of parameters to reproduce the experimental adsorption of olefins in aluminosilicates with different chemical compositions.

We performed an extensive study of propane/propylene separation in pure silica zeolites and aluminosilicates including LTA5A, CaA, NaY, NaX, and CaX structures. We analyzed the influence of concentration and type of cations in the separation capability of the structures. We also conducted structure minimizations using both, density functional theory (DFT) and classical optimization methods obtaining accurate models for the zeolite frameworks. We evaluated the importance of the structural optimization and the location of the cations in crystallographic positions for a correct description of the adsorption processes.

METHODOLOGY

Experimental Details

Experimental gas adsorption isotherms were performed in a volumetric analyser (3Flex, Micromeritics) provided with a turbomolecular vacuum pump and three pressure transducers (0.13, 1.33 and 133 kPa, uncertainty within 0.15% of each reading). The volumetric analyser was coupled to a thermostatic circulating bath provided with an internal sensor that allows a fine temperature control between 253-373 K with a stability of ± 0.1 K. Isotherms were recorded in the pressure range between 10-2 and 120 kPa using ca. 250 mg of sample. Before the analysis, the samples were outgassed under dynamic vacuum using a turbomolecular pump (5K/min up to 363 K for 1 hour, and then up to 623 K for 7 hours). All gases were supplied by Air Products at an ultrahigh purity (i.e., 99.995%).

For adsorption measurements of *n*-hexane and 1-hexene we used commercial zeolites 5A (CaNa-LTA, Arkema, Poland) and NaY (Si/Al ratio of 2.61, Institute of Industrial Chemistry, Poland). Structures were confirmed by analysis of X-ray diffraction patterns (XRD) recorded by a Rigaku MiniFlex powder diffractometer with Cu $K\alpha$ radiation at 10 mA and 10 kV, 2θ step scans of 0.02°, and a counting time

of 1 s per step. Adsorption measurements of *n*-hexane and 1-hexene were performed with the use of quasi-equilibrated temperature programmed desorption and adsorption (QE-TPDA).[24,25] QE-TPDA uses a home-made setup similar to the one exploited in temperature programmed desorption (TPD). During the measurement the adsorbate admixed to helium is flowing through the sample, while its concentration is monitored with the TCD detector. Desorption and adsorption is induced by changing of the temperature of the sample.

The studied materials were pressed into pellets, crushed and sieved to obtain fraction of 400-500 μm. Prior to each QE-TPDA measurements the sample of 10-12 mg was activated in pure helium (Air Products, purity 5.0) with flow set to 6.75 cm^3/min by heating up to 500 °C(10 °C/min ramp). Afterwards, the sample was cooled to room temperature and the flow was switched to helium containing small admixture (0.6-0.7 mol%) of n-hexane (analytical pure, Acros Organics) or 1-hexene (99% Acros Organics) resulting in isothermal room temperature (RT) adsorption. When RT adsorption was finished, the actual QE-TPDA experiment was performed by cyclic heating and cooling the sample in a He/hydrocarbon flow with different rates of changing the temperature, from 2 to 10 °C/min. The sample was kept in RT for at least 2 hours between the following desorption-adsorption cycles.

The dependence of temperature on specific sorption rate (ssr) -the value proportional to the amount of desorbing/adsorption hydrocarbon- is referred as QE-TPDA profile. In order to obtain adsorption isobars, the profiles measured with the rate of changing temperature of 4 °C/min (1-hexene) or 5 °C/min (*n*-hexane) were integrated and recalculated with adequate calibration constants. A detailed description of the QE-TPDA apparatus and data reduction formalism can be found in earlier works.[24–26]

Simulation Details

Adsorption isotherms and isobars were calculated using grand-canonical Monte Carlo simulations (GCMC). Chemical potential and pressure are related to fugacity through the Peng-Robinson equation of state[27] and the fugacity coefficient. Simulations were performed using RASPA code.[28,29] Equimolar mixtures of propane/propylene in all pure silica zeolites were predicted using GAIAST,[30] a genetic algorithm based on ideal adsorption solution theory (IAST). In the case of competitive adsorption in aluminosilicates, we used GCMC simulations to compute the adsorption of equimolar mixtures.

During the GCMC simulations we considered the zeolites as rigid frameworks with silicon, oxygen, and aluminium atoms placed at the crystallographic positions. Extra-framework sodium and calcium cations were allowed to move during the simulation. The point charges used for the framework atoms and extra-

framework cations are collected in Table S1. Note that we used different point charges for oxygen atoms bridging one Si and one Al atom (O_{Al}), and oxygen atoms bridging two Si atoms (O_{Si}).[18] However, the set of point charges are the same for all the zeolites independently of the number Si/Al ratio (Table S1). The pure silica structures for the screening are taken from the International Zeolite Association (IZA) database.[31] The structure of LTA5A were reported by J.J. Pluth and J.V. Smith.[32] The structure of NaY and NaX were created as follows, starting with the pure silica structure. 1) Using random substitution, silicon atoms were replaced by aluminium atoms obeying Löwenstein's rule. A set of 50 structures with the same composition but different configurations was generated; 2) From the 50 structures we choose that with the most favorable (less energetic) configuration; 3) the extra-framework cations were placed in the most probable crystallographic positions reported in literature.[33–37] Schematic representation of FAU-type, and LTA-type zeolites and the description of the cations sites can be found in Figure A5.11 in the Appendix 5. We created the CaX and the CaA structures by placing the calcium cations in the structure of NaX and LTA5A, respectively. Classical structural minimizations of the aluminosilicates with the cations placed in the crystallographic positions were performed using Baker's method[38] and the well-known core-shell potential of Sanders et al.[39,40] We carried out simulations in NPT ensemble, that allows the variation of box lengths (i.e. the volume of the cell) but keeping fixed the angles ($\alpha = \beta = \gamma = 90°$) to maintain the triclinic crystal system.

Adsorbates are described using united atom models, where each CH_n group is considered as a single interaction center. Propane and longer linear paraffins are modeled as non-polar molecules and their interaction parameters were taken from Dubbeldam et al.[18,21,41] For propylene we compare the accuracy of a non-polar model reported by Liu et. al.[42] and a point charge model with partial charges located in CH_n_sp_2 groups and one extra point charge between the two carbon atoms linked by the double bond. The latter model was developed and validated by Gutierrez-Sevillano et. al.[8] and can be extended to longer α-olefins in a simple way. Figure A5.2 shows the good agreement between our experimental and simulation data with these taken from the literature.[43–45] The Lennard-Jones (LJ) interaction parameters for sp_3 carbon atoms, extra-framework cations, and the zeolite atoms are taken from reference 18. The interaction parameters for sp_2 carbon atoms of non-polar and point charge propylene with silica and oxygen zeolite atoms are also taken from the literature.[8,42] The new set of parameters for sp_2 carbon atoms and extra-framework cations were developed to reproduce the experimental isotherms. To this aim, we fit the potential parameters of the cross interactions between

propylene and sodium cations in NaY zeolite at room temperature. Once validated, we used this new set of parameters to fit the interaction of propylene with calcium cations in LTA5A. We validated the model by comparing with experimental adsorption isotherms measured in this work and comparing with independent experiments found in literature.[13,46–48] We checked the transferability of the set of parameters by computing adsorption isotherms in other zeolites and for α-olefins with longer chains. The LJ parameters developed in this work are collected in Table A5.1 in the Appendix 5. We computed the binding geometries using the classical force field by a simulated annealing process based on molecular dynamics (MD) simulations in the NVT ensemble. During this process, we started with zeolites loaded at 273 K and 1 bar. Then, the temperature was reduced in intervals of 10 degrees until 3 K and then until 1 K. With this procedure we minimized the effect of temperature on the vibration of the molecules making more accurate the comparison with the DFT calculations. We run each MD simulation for 10^6 steps and using a time step of 0.5 fs. More details about the MD methodology can be found in ref.[7]

In addition to classical simulations, we performed density functional theory (DFT) calculations to optimize the structure of LTA5A and NaY zeolites. The geometry of these zeolites were fully optimized using the Vienna ab initio simulation package (VASP) code,[49–51] employing the generalized gradient approximation (GGA) with the Perdew-Burke-Ernzerhof exchange-correlation functional[52] and projector-augmented wave (PAW) potentials.[53,54] Valence electrons are described using a plane-wave basis set with a cutoff of 500 eV and the gamma point is used for integrations in the reciprocal space.[55] The ionic relaxation has been performed until the Hellmann-Feynman forces were lower than 0.02 eV/Å. We compared the resulting structures from the classical and DFT optimization methods. In addition to the geometry optimization, we also computed the binding energy and binding geometry of a single molecule of propane and propylene in the two mentioned zeolites. Van der Waals interactions were taken into account through the DFT-D2 method of Grimme[56] to gain insights into the particular interaction between the alkene molecules and the monovalent and divalent cations of the zeolites. The position of the molecule was optimized keeping the zeolite atoms and the cations in the previously optimized positions. As these results can be influenced decisively by the starting geometry, we used several starting geometries for each molecule to ensure stability. We used the strategy of performing preliminary short *ab-initio* MD simulations at low temperature to identify the most stable configuration prior to start the optimizations.

Results and Discussion

Propane and propylene adsorption in pure silica zeolites

To identify the optimal topology for propane/propylene separation, we used the models and force field from the literature[8,21] to calculate the adsorption isotherms of propane and propylene in most zeolites of the IZA database in the pure silica form (more than 200 topologies). Adsorption selectivity was used as a measure of the separation factor of the mixture. Adsorption selectivity is defined as $S = (x_A/y_A)/(x_B/y_B)$ were x_i is the molar fraction in the adsorbed phase for the component i and y_i is the molar fraction in the bulk phase. Figure 1 shows the adsorption selectivity as a function of pore volume at 100 kPa and 298 K, for the studied zeolites. For clarity purposes, we classified the zeolite structures in those exhibiting preferential adsorption for propane (Figure 1a) or for propylene (Figure 1b). The selectivity obtained for most zeolites at these conditions is quite low (below 2) and only for a few of them is higher than 3. AVF, EZT, ESV, and MTW exhibit the highest adsorption selectivity for propane over propene, whereas ASV, SOF, and YUG show higher selectivity for propylene than for propane. Among them, the only zeolite that exists in their pure silica form is MTW, and the uptake is about 1 mol/kg in the studied conditions. Therefore, olefin/paraffin separation based on pure silica zeolites seems inefficient and unrealistic. To improve this separation it is necessary to take advance of other mechanisms which makes the difference between olefins and paraffins.

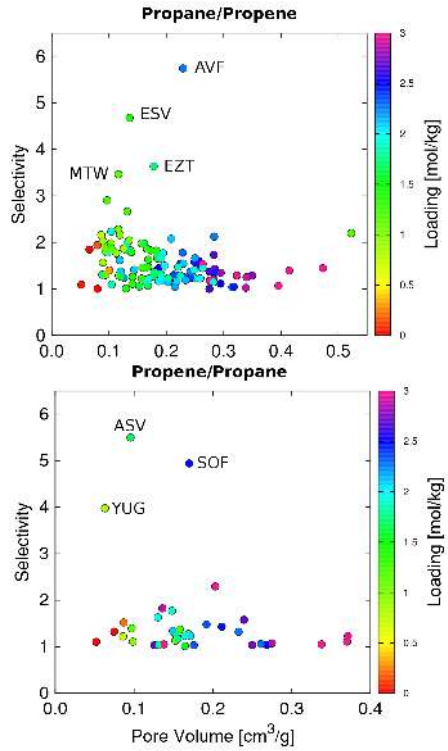

Figure 1. Adsorption selectivity as a function of pore volume for (top) propane over propylene and (bottom) propylene over propane at 298 K and 100 kPa for the studied zeolites. Color scale (right y-axis) represents the total amount adsorbed in the gas phase.

Effect of cations in the adsorption

It is well known that π-complexation (also known as π-bonding) enhances olefin/paraffin separation.[57–60] π-complexation is a subgroup of chemical complexation where a covalent bond is

formed between the electron donor (olefin) and the acceptor (complexing agent).[61] This phenomenon occurs in Metal-Organic Frameworks with open metal sites and it is also reported in zeolites with complexing agent which is usually a member of the d-block transition metals in the periodic table. The π-complexation formed stronger bonds than van der Waals forces, so it is possible to achieve higher adsorption selectivity and higher adsorption capacities.[62–65] Similarly, π-complexation can also occur in aluminosilicates due to the interaction of olefins with the extraframeworks cations.[57,59,60] The effect of the π-complexation results in differences in the adsorption properties of olefins and paraffins. To gain insights into these differences we measured the adsorption properties of olefins and paraffins in aluminosilicates containing sodium (NaY) and sodium and calcium cations (LTA5A).

First of all, we measured the QE-TPDA profiles of *n*-hexane and 1-hexene in NaY (Na-FAU, Si/Al=2.61) and LTA5A (CaNa-LTA, Si/Al=1) zeolites (Figure 2). QE-TPDA profiles should show similar behaviour for two adsorbate-adsorbent pairs when the adsorbed molecules have similar affinity to the structure. As seen, dissimilar profiles are obtained for olefin and paraffin, which is an indication of the mentioned π-complexation between the olefin and the cations. The profiles consist of desorption maxima and adsorption minima, which corresponds to the instantaneous amount of the component desorbing/adsorption in the material at given conditions. Desorption maxima are slightly shifted to higher temperatures when compared to adsorption minima, which is apparatus artifact. For adsorption of *n*-hexane and 1-hexene in NaY we observe sharp peaks, which for 1-hexene are shifted by ca. 35 K to higher temperatures. The higher desorption/adsorption temperatures of 1-hexene most likely result from stronger interactions of the olefin molecules with sodium cations. The low temperature range of the profiles (300-350 K) corresponds to dense adsorption states related to guest-guest interactions. While the QE-TPDA profiles of *n*-hexane and 1-hexene in NaY are quite similar, they significantly differ for LTA5A. For *n*-hexane in LTA5A we observe two clear desorption/adsorption peaks in the range of 350-550 K. As for NaY, the profiles of 1-hexene in LTA5A are shifted to the higher temperature, but they also differ in shape as we observe a wide signal extending from 400 to 650 K. The low-temperature peak at 315 K is separated from the rest of the profile, which may suggest noticeable difference between guest-guest and guest-host interactions of 1-hexene in LTA5A zeolite than in NaY. Summarizing the QE-TPDA results, 1-hexene is adsorbed at markedly higher temperature than *n*-hexene in both NaY and LTA5A zeolites. Moreover, the differences in the profiles are more relevant for LTA5A zeolite indicating that the calcium cations influence more than the sodium cations in the ad-

sorption process.

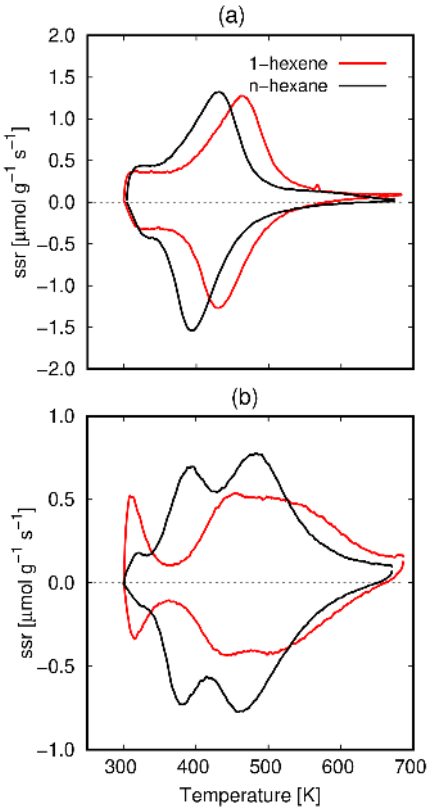

Figure 2. QE-TPDA profiles of *n*-hexane and 1-hexene in (a) NaY and (b) LTA5A. The partial pressure of *n*-hexane in NaY and LTA5A was *ca* 790 Pa and 680 Pa, respectively. For 1-hexene in NaY and LTA5A it was *ca* 560 Pa and 570 Pa, respectively.

Fitting Interaction between cations and CH_n_sp^2 groups

To gain insights into the differences in the adsorption of olefins and paraffins in aluminosilicates, we combined experimental and molecular simulation techniques. Molecular simulations offer useful information of the adsorption process from a microscopic point of view. As described in the methodology, we used previously validated force fields to study the adsorption of paraffins in aluminosilicates. However, there are not a transferable potential for the interaction of olefins with the extraframework sodium and calcium cations. In addition to the isobaric adsorption of 1-hexene, we measured the adsorption isotherms of propylene in the same adsorbents. We used these experimental values as reference to develop a set of effective potential parameters to study the adsorption process.

The particular interaction between extra-framework cations and olefins through the double bond makes challenging to reproduce the adsorption experiments using molecular simulations. We developed a set of Lennard-Jones parameters for the interaction between CH_n_sp^2 groups and Na^+ extra-framework cations by fitting to the experimental adsorption isotherm of propylene in CBV100 (NaY with Si/Al=2.55) at 298 K (Figure 3a). Once these values were fixed, we fit the Lennard-Jones parameters for the interaction between CH_n_sp^2 groups and Ca2+ using the experimental adsorption isotherm of propylene in LTA5A zeolite (Figure 3b). To check if the model can be applied to longer molecules, we compared the computed and the measured adsorption isobars of 1-hexene in NaY (Na-FAU, Si/Al=2.61) and LTA5A (CaNa-LTA, Si/Al=1) zeolites at 560 Pa and 570 Pa, re-

spectively. As shown in Figure 3c,d, we found a good agreement between experiments and simulations. Comparison with other experimental values reported for propylene and 1-butene in NaY, NaX, and LTA5A at several temperatures [13,46,48] can be found in Figure A5.3 and A5.4. The good agreement verifies that our set of Lennard-Jones parameters reproduce experimental adsorption isotherms and isobars of olefins (propylene and long chain hydrocarbons) and it is transferable to zeolites of different topology and to many operational values of temperature. Note that with the same force field we reproduced the experimental adsorption isobars and isotherms from this work and from the literature, which were measured with different samples, equipment and methodology. This gives consistency to the parameters developed in this work.

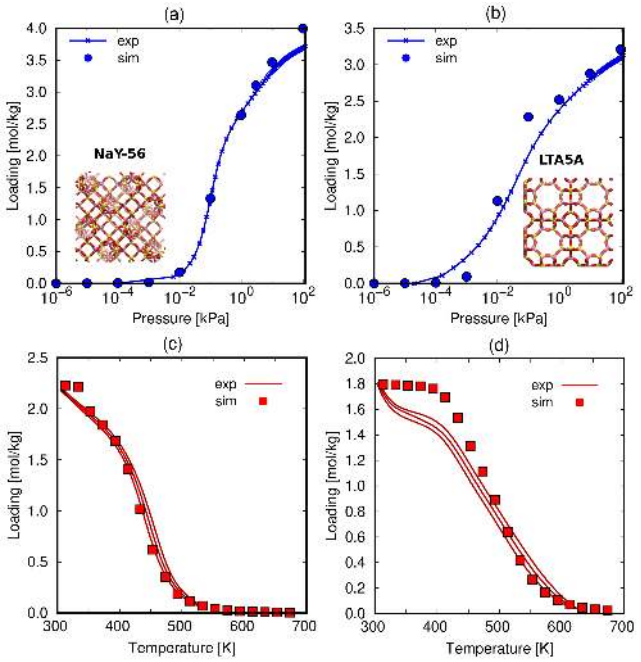

Figure 3. Adsorption isotherms of propylene in (a) NaY-56 and (b) LTA5A at 298 K. Adsorption isobars of 1-hexene in (c) NaY-56 at 560 Pa and (d) LTA5A at 550 Pa. Experimental results are represented with lines and calculated results with symbols. For isobars three curves are plotted, the curve shifted to the highest and lowest temperatures stand for desorption and adsorption, respectively. Averaging the adsorption and desorption curves we obtain the adsorption isobar reflected as the intermediate curve.

Energies and Binding geometries

Differences in the adsorption of olefins and paraffins in aluminosilicates are also reflected in the binding energies and in the structural organization of the adsorbates in the cavities of the zeolites. Binding or adsorption energies were obtained with DFT calculations of a single molecule of propane and propylene in NaY and LTA5A. The binding energies of propane and propene in NaY are -0.469 eV and -0.590 eV, respectively. The adsorption energy of propane in LTA5A is -0.694 eV, which is an average of the interaction with Ca^{2+} and Na^{+} cations. However, the structure containing propylene shows two favorable configurations: one when the molecule is near to the sodium cations and other near to calcium cations. In this case we found strong interactions between the molecule and the calcium cations which were missing during propane adsorption. When the molecule of propylene is near the Na^{+} cation, the adsorption energy is very similar to the propane adsorption energy (-0.667 eV) but when propylene is adsorbed near the Ca^{2+} cation the adsorption energy is -0.885 eV. This indicates that at low coverage propylene adsorbs preferentially binding to the calcium cations. In the two zeolites, propylene shows higher adsorption energy than propane. The differences in the adsorption energy between propylene and propane are 0.121 eV for NaY and 0.191 eV for LTA5A. The larger difference in energy showed by LTA5A compared to NaY is due to the presence of calcium cations, which is consistent with the huge differences observed in the QE-TPDA profiles (Figure 2).

The binding geometry of the adsorbates in the zeolite pores is also key factor to describe correctly the adsorption properties. From the same DFT calculations we also obtained the binding geometries for propane and propylene. The most stable configuration of the molecule of propane in LTA5A is between one calcium and one sodium cation, independently of the starting position of the molecule. In the optimized LTA5A the distances between one of the terminal carbon atoms of propane and the Na^{+} cation is 2.97 Å and the distance between the other terminal carbon atom of the molecule and the Ca^{2+} cation is 2.91 Å. The terminal carbon atom of propane is pointing to the cations forming an angle of about 170°. We found similar orientation of propane in NaY, with the same angle but the distance between the terminal carbon atom and the Na^{+} cation is 2.68 Å. In the case of propylene, we found a different behaviour of the structural organization of the adsorbate with respect to the cations. We quantify the binding geometry of propylene by defining the parameters d_1, d_2, and α according to the schematic representation of Figure 4a. d1 is the distance between the terminal carbon atom (CH_2_sp^2) with the cation, d_2 the distance of the central carbon atom with the cation, and α is the angle between the double bond and d_1. The propylene-

Na^+ distances are similar for both structures; d_2 is slightly larger in NaY than in LTA5A, which also implies larger α. The double bond is located approximately "parallel " to the cation ($\alpha \sim 90°$) in NaY while in LTA5A α is about 80°. To check the accuracy of the classical force field to reproduce the binding geometry, we computed the radial distribution functions RDFs between the atoms which define d_1 and d_2. Figure 5 compares the parameters obtained with DFT calculations with the RDFs from a classical MD simulation after a simulated annealing procedure. We obtained similar orientations of the molecule in the two structures with the mentioned techniques. The first peak of the RDF matches with the given distances by the DFT calculations. The largest displacement (0.3 Å) is found for d_1 for calcium cation in LTA5A.

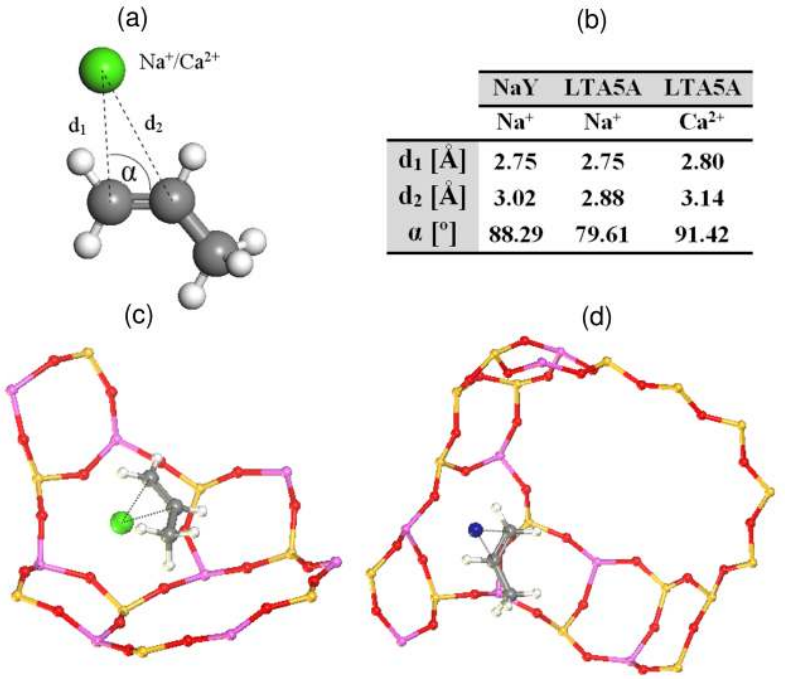

	NaY	LTA5A	LTA5A
	Na^+	Na^+	Ca^{2+}
d_1 [Å]	2.75	2.75	2.80
d_2 [Å]	3.02	2.88	3.14
α [°]	88.29	79.61	91.42

Figure 4. (a) Schematic representation of the parameters used to describe the binding geometry; (b) parametrs for the binding geometry of propylene with sodium and calcium cations obtained with DFT calculations and schematic representation of the most favorable configuration of propylene in (c) LTA5A and (d) NaY.

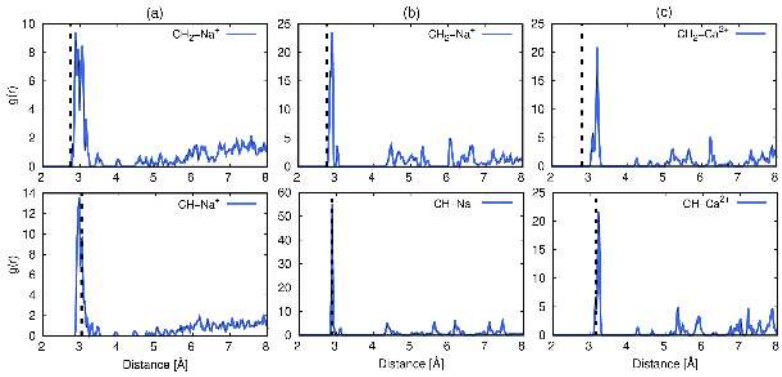

Figure 5. (a) Comparison of the binding geometry parameters d1 (top) and d2 (bottom) obtained with DFT (dashed vertical lines) and classical simulation (blue solid lines) of propylene with cations in (a) NaY and (b),(c) LTA5A. The parameters are used according to the schematic representation of Figure 4a.

We found that propane and propylene molecules orientate differently with respect to the cations (complexing agent), which is in agreement with the reported binding geometry for olefins in MOFs with open metal sites. In these systems, the double bond is located parallel to the metal ($\alpha \approx 90°$) for olefins but the angle is larger for paraffins.[60,64,66] These results reinforce the efficency of our set of Lennard-Jones parameters for olefins in aluminosilicates.

We analyzed the microscopic organization of the olefins as increasing the amount adsorbed. In NaY, propylene molecules are located closed to the sodium cations. However, in LTA5A the location of propylene near calcium or sodium cations depends on the quantity adsorbed. Figure 6 shows the most probable distance between the central carbon atom and the cation (average of d_2 over all the adsorbed molecules) as a function of loading in LTA5A at 298K. At low loading the adsorbed molecule is placed near the Ca^{2+} (circles) cations at a distance of 3.2 Å. This value remains constant with loading. On the other hand, the most probable distance between the central carbon atom and the Na^+ cations (triangles) at low loading is about 5.5 Å which is also the distance between the nearest Na^+ and Ca^{2+} cations. The distance remains constant up to 32 molecules per unit cell. At higher values of loading this distance decreases up to 2.9 Å. According to the first peak of the RDFs of Figure 6 (bottom), propylene molecules locate close to calcium cations independently of the loading. However, there is no significant presence of propylene near sodium cations at low or intermediate coverage (low intensity first peaks, below the unity, of the RDF).

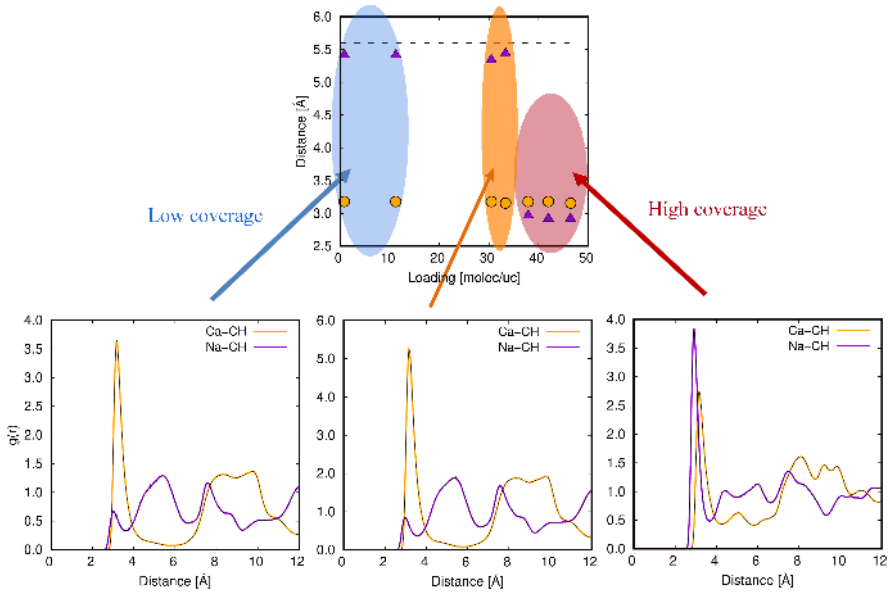

Figure 6. (Top) The most probable distance between CH pseudo-atom and Na^+ (purple triangles) and Ca^{2+} cations (orange circles) as a function of loading in LTA5A. Dashed line indicates the shorter distance between Na^+ and Ca^{2+} cations. (Bottom) RDF of CH pseudo-atom with cations at low coverage (left), medium coverage (center) and close to saturation (right).

When the loading of propylene exceeds the value of 32 molecules per unit cell, the first peak of RDF corresponding to CH-Na^+ shows a drastic increase. Note that the number of calcium cations per unit cell in LTA5A is 32. This means that once all the calcium cations are surrounded by propylene molecules, they begin to adsorb near to the sodium cations.

Effect of the structural optimization

Following the procedure explained in the methodology, we optimized the structures of the NaY and LTA5A zeolites using DFT and classical simulations to study the effect of the geometry. Then we computed adsorption isotherms and isobars of propane and propylene. Figure 7 shows a schematic representation of the 4-, 6-, 8-, and 12-member ring (MR) present in these aluminosilicates and the distances are summarized in Table 1. One can observe that there are tiny differences between the non-optimized and optimized building units of the zeolites. To corroborate it, we compared the experimental and the calculated XRD diffractograms (see Figure A5.5 in the Appendix 5). Our results show that there are non-significant displacement of the peaks in the pattern of the non-optimized and the optimized structures.

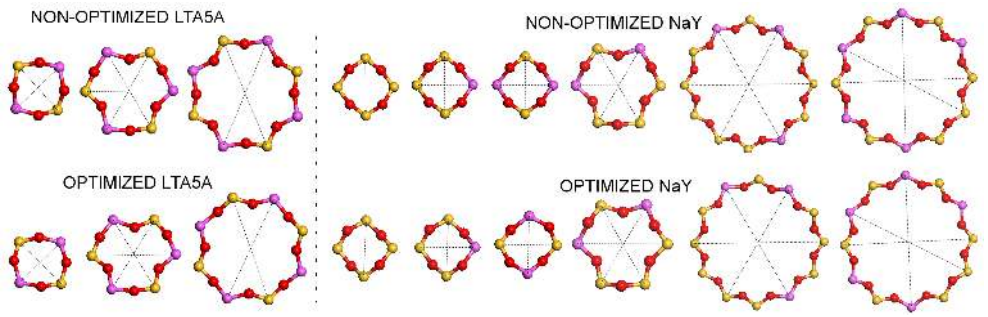

Figure 7. Schematic representation of 4-, 6-, 8-, and 12-member ring of non-optimized and classically optimized LTA5A and NaY structures. Dashed lines indicate the selected distances for the data listed in Table 1.

Table 1. Comparison of the unit cell and the distances between the atoms of the member ring for non-optimized and classically optimized structures.

		Distance [Å] Non-optimized structure	**Distance [Å] Optimized structure**
LTA5A			
Unit cell	$a = b = c$	24.7484	24.7529
4MR	Si-Si	4.56	4.56
	Al-Al	4.4	4.41
6MR	Al-Si	6.46	6.45
	Al-Si	6.46	6.45
	Al-Si	6.46	6.45
8MR	Si-Si	8.34	8.39
	Al-Al	8.42	8.5
NaY			
Unit cell	$a = b = c$	24.555	24.6668
4MR	Si-Si(Al=0)	4.45	4.37
	Si-Si(Al=1)	4.45	4.43
	Si-Al(Al=1)	4.39	4.37
	Si-Si(Al=2)	4.45	4.46
	Al-Al(Al=2)	4.39	4.36
6MR	Si-Si	6.29	6.27
	Al-Si	6.29	6.25
	Si-Al	6.29	6.28
12MR	Si-Si(Al=3)	11.62	11.77
	Al-Al(Al=3)	11.62	11.54
	Si-Al(Al=3)	11.62	11.55
	Si-Si(Al=5)	11.62	11.53
	Al-Al(Al=5)	11.62	11.68
	Si-Al(Al=5)	11.62	11.58

Then we conclude that the discrepancies in distances between adjacent planes are negligible between the different models for LTA5A and NaY. Nevertheless we found large variations in the adsorption of propylene and 1-hexene. Figure 8 illustrates the adsorption isotherms of propane, and propylene in LTA5A and NaY zeolites in the i) non-optimized structures, ii) optimized structures using DFT calculations and iii) optimized structures with classical simulations. The adsorption of propane in NaY and LTA5A is similar in all the structures in agreement with the experimental values. The main differences in the loading are found in the region of the inflection point of the isotherm, due to the small variation of the intracrystalline distances of the zeolites. On the other hand, the adsorption isotherms of propylene calculated in the non-optimized NaY and LTA5A zeolites do not match experimental data, while computed isotherms in the optimized structures are in better agreement with experiments. We analyzed the adsorption of *n*-hexane and 1-hexene in the optimized and non-optimized frameworks (Figure A5.6) and obtain similar conclusions. This means that the optimization of the structure is not needed for the adsorption of the paraffins, but increase significantly the accuracy of the predictions for the adsorption of the olefins in aluminosilicates. Small deviations of a given atom of the structure can produce changes in the electrostatic field inside the cavities affecting to the olefin adsorption; however this is irrelevant for the adsorption of paraffins.

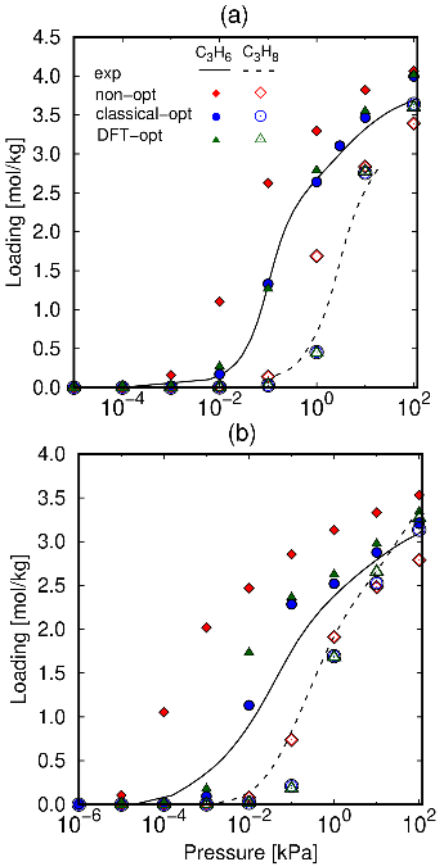

Figure 8. Comparison between adsorption isotherms (298 K) of propane (open symbols) and propylene (closed symbols) in (a) NaY and (b) LTA5A using non-optimized structures (red diamonds), DFT optimized structures (green triangles) and classically optimized structures (blue circles). Experimental data are represented by solid lines (this work) and dashed lines (literature).[67,68]

Effect of cations in the separation

We have shown that the calcium cations of LTA5A interact stronger with the olefins than the sodium cations. Now we add to

this study aluminosilicates that contain only calcium cations, such as CaA and CaX with LTA and FAU topologies, respectively. The influence of the nature of the cation in adsorption can be observed in the average occupation profiles (AvOPs). Figure 9 shows the AvOPs of propylene in zeolites with FAU topology (FAU-Si, NaY, NaX, and CaX) at 100 kPa and 298 K. At these conditions, the four structures have the same loading, but the preferential adsorption sites differ. The pure silica zeolite shows preferential adsorption in the center of the cages, and almost a homogenous distribution in the rest of the cavity. In the NaY and NaX structures, the Na^+ cations become new adsorption sites. These preferential sites allow for more heterogeneous distribution of the molecules during adsorption. The centers of the cages are practically non-occupied in presence of Ca^{2+} cations while the distribution of the adsorbed molecules of propylene is close to the cations. NaY and CaX have similar number of cations in the simulation box; 56 and 48, respectively. Thus the main difference in their occupation profiles is due to the type of cation (Na^+ or Ca^{2+}) and the location of the cations in the structure. The average occupation profiles obtained for the different compositions in LTA topology are provided in Figure A5.7 in the Appendix 5.

To quantify the effect exerted by the calcium cation in the separation of the paraffin/olefin mixture, we performed equimolar adsorption isotherms of propane/propylene mixture in zeolites with FAU topology (FAU-Si, HS-FAU, NaY, NaX, and CaX) and with LTA topology (ITQ-29, LTA5A, and CaA). Figure 10 shows that zeolites CaX and CaA are excellent candidates to separate propane from propylene. As seen, the calcium forms of these zeolites adsorb more than 3 mol/kg of propylene while propane is almost excluded from the mixture. The other structures with cations are also good candidates for separation as can be observed in Figure A5.8 (Appendix 5). As we have demonstrated before, this exceptional separation is a consequence of the strong interaction of the olefins with the cations.

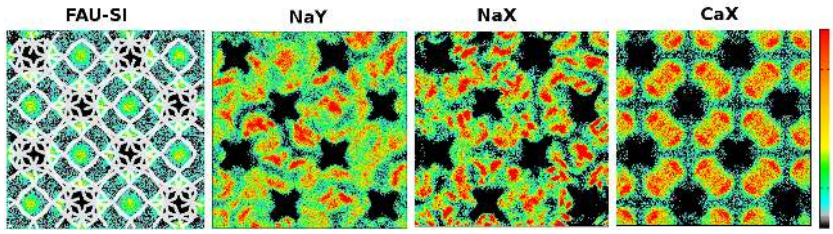

Figure 9. Average occupation profiles of propene in FAU topology at 100 kPa and 298 K.

The π-complexation between propylene and the extraframework cations makes the difference for the separation of propylene/propane in zeolites. To analyze the effect of the length of the alkyl chain in the olefin/paraffin separation, we extended our study to longer hydrocarbons. Figure 11 shows the olefin/paraffin adsorption selectivity as a function of the chain length in FAU and LTA type zeolites. This was obtained from the equimolar adsorption isotherms of olefin/paraffin pairs from C3 to C9 carbon atoms at 100 kPa and 298 K. As for propylene/propane, ITQ-29 (pure silica with LTA topology), FAU-Si (pure silica) and HS-FAU (high silica with a Si/Al ratio ≈ 100) cannot separate the olefin/paraffin mixtures. In NaY (circles) the adsorption selectivity in favor of the olefin is about 10 for all chain lengths, and the highest separation is obtained for C6 (1-hexene/*n*-hexane) with a selectivity value of 25. The pair olefin/paraffin with the highest values of adsorption selectivity depends on the density of the cations. The best separation performance in most FAU-type zeolites is found for the C6 mixture. In NaX zeolite, separation is better for C5 (selectivity ≈ 90). The behavior of NaX (diamonds) and LTA5A (squares) is alike in some ways, with very similar selectivity for all the pairs. As mentioned before the selectivity for propane/propylene separation in CaX (triangles) and NaY is similar too, but the increase in selectivity is not linear with the increase on chain length.

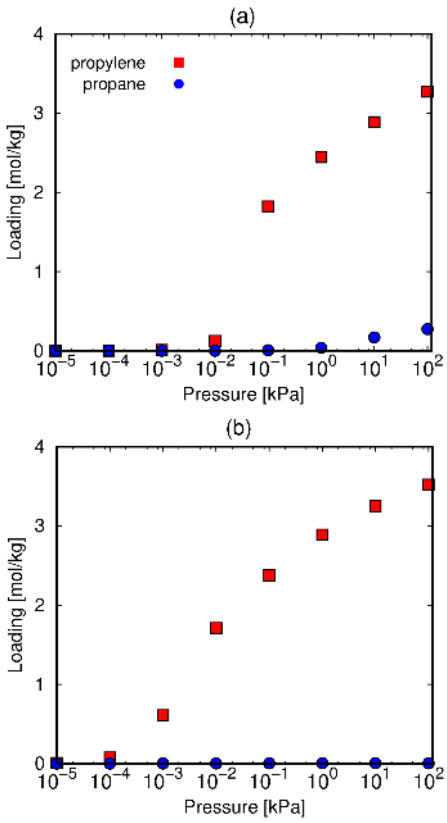

Figure 10. Equimolar adsorption isotherms of propane/propylene in (a) CaX and (b) CaA zeolites at 298 K.

We found a maximum for the C6 mixture and also good separation performance for the mixtures C7, C8 and C9. CaA is the zeolite with the best olefin/paraffin separation performance for all pairs. The separation values are particularly high for the C3, C4, C5, and C6 mixtures. On the other hand, FAU and LTA-type zeolites have similar adsorption capacity, represented by the color scale in Figure 11. LTA5A and CaA show olefins storage of about

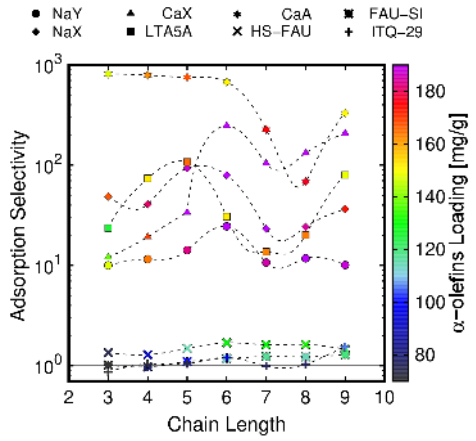

Figure 11. Adsorption selectivity of binary mixture (from C3 to C9) as a function of chain length in FAU and LTA zeolites at 100 kPa and 298 K. Color scale indicates the density of olefin adsorbed.

150-170 mg/g while the other aluminosilicates with FAU topology show higher capacity (about 185 mg/g). In general, an increase of the length of the hydrocarbon mixture up to 9 carbon atoms does not reduce the separation performance of aluminosilicates. This makes of these materials excellent candidates for the targeted separation.

CONCLUSIONS

We studied the olefin/paraffin separation for hydrocarbons with three to nine carbon atoms,using a combination of experimental and molecular simulation techniques. Separation of equimolar binary mixtures was predicted from the screening of the adsorption isotherms of pure components in more than 200 pure silica structures. This allowed the analysis of the effect of the zeolite topology in the propane/propylene separation in pure silica zeolites. Adsorption selectivity confirmed that pure silica zeolites cannot be used to separate these mixtures. Only in a few structures the values of adsorption selectivity were above 3 at room conditions, but in general, the adsorption capacity of these structures is extremely low. To achieve olefin/paraffin separation using zeolites, the use of aluminosilicates with extra-framework cations that interact strongly with the olefins are needed. Experimental adsorption measurements of propylene in commercial NaY and LTA5A zeolites at different temperatures allowed us to develop a set of Lennard-Jones parameters for the specific interactions between the extra-framework cations and the CH_n_sp_2 pseudo-atom groups of olefin models. These parameters provided good agreement between the experimental and computational adsorption isotherms of propylene for a wide range of temperatures and for a variety of zeolites with non-framework cations. Comparison with adsorption isobars of 1-hexene in NaY and LTA5A measured in this work confirmed the transferability of the force field parameters to longer hydrocarbons. We also found that for reproducing the adsorption of olefins in aluminosilicates the location of the cations and the optimization of the structures are key factors.

In aluminosilicates, π-bonding is

formed between the double bond of the molecule of propylene and one accessible Na^+ or Ca^{2+} cation. DFT calculations showed that the binding energies in NaY and LTA5A for propylene are much higher than the obtained for propane. The preferential adsorption sites are close to the cations and in particular, close to the Ca^{2+} cations in LTA5A. The binding geometries also reflect differences between propane and propylene. The double bond of propylene is oriented in parallel to the cation forming an angle of about 90°. For propane the terminal carbon atom is pointing to the cation and α is about 170°. We found agreement between the binding geometries obtained with DFT and classical calculations. In conclusion, zeolites with cations are excellent candidates for olefin/paraffin separation due to the strong interaction of the olefin with the cation though the π-bonding. The binding energies indicate that this interaction is stronger with divalent cations, such as calcium. Therefore, exchanging Na^+ cations for Ca^{2+} cation in zeolites might enhance the olefin/paraffin separation with complete exclusion of the paraffin from the mixture.

Bibliography

[1] Park, Y.-K.; Lee, C. W.; Kang, N. Y.; Choi, W. C.; Choi, S.; Oh, S. H.; Park, D. S. *Catalysis surveys from Asia* **2010**, *14*, 75–84.

[2] Wagner, H.; Luther, R.; Mang, T. *Applied Catalysis A: General* **2001**, *221*, 429–442.

[3] Alsadoun, A. W. *Applied Catalysis a-General* **1993**, *105*, 1–40.

[4] Eldridge, R. B. *Industrial & Engineering Chemistry Research* **1993**, *32*, 2208–2212.

[5] Gascon, J.; Blom, W.; van Miltenburg, A.; Ferreira, A.; Berger, R.; Kapteijn, F. *Microporous and Mesoporous Materials* **2008**, *115*, 585–593.

[6] Olson, D. H.; Yang, X.; Camblor, M. A. *The Journal of Physical Chemistry B* **2004**, *108*, 11044–11048.

[7] Min, J.; Luna-Triguero, A.; Byun, Y.; Balestra, S.; Vicent-Luna, J.; Calero, S.; Hong, S.; Camblor, M. *Langmuir* **2018**, *34*.

[8] Gutiérrez-Sevillano, J. J.; Dubbeldam, D.; Rey, F.; Valencia, S.; Palomino, M.; Martín-Calvo, A.; Calero, S. *The Journal of Physical Chemistry C* **2010**, *114*, 14907–14914.

[9] Hosseinpour, S.; Fatemi, S.; Mortazavi, Y.; Gholamhoseini, M.; Ravanchi, M. T. *Separation Science and Technology* **2010**, *46*, 349–355.

[10] Campo, M. C.; Ribeiro, A. M.; Ferreira, A.; Santos, J. C.; Lutz, C.; Loureiro, J. M.; Rodrigues, A. E. *Separation and Purification Technology* **2013**, *103*, 60–70.

[11] Lamia, N.; Wolff, L.; Leflaive, P.; LeinekugelâĂŘLeâĂŘCocq, D.; Sá Gomes, P.; Grande, C. A.; Rodrigues, A. E. *Separation Science and Technology* **2008**, *43*, 1124–1156.

[12] Calleja, G.; Jimenez, A.; Pau, J.; Dominguez, L.; Perez, P. *Gas Separation & Purification* **1994**, *8*, 247–256.

[13] Grande, C. A.; Gigola, C.; Rodrigues, A. E. *Industrial & Engineering Chemistry Research* **2002**, *41*, 85–92.

[14] Dzhigit, O. M.; Kiselev, A. V.; Mikos, K. N.; Muttik, G. G.; Rahmanova, T. A. *Transactions of the Faraday Society* **1971**, *67*, 458–467.

[15] Harper, R. J.; Stifel, G. R.; Anderson, R. B. *Canadian Journal of Chemistry* **1969**, *47*, 4661–4670.

[16] Grande, C. A.; Gigola, C.; Rodrigues, A. E. *Adsorption* **2003**, *9*, 321–329.

[17] Granato, M. A.; Vlugt, T. J. H.; Rodrigues, A. E. *Industrial & Engineering Chemistry Research* **2007**, *46*, 321–328.

[18] Calero, S.; Dubbeldam, D.; Krishna, R.; Smit, B.; Vlugt, T. J. H.; Denayer, J. F. M.; Martens, J. A.; Maesen, T. L. M. *Journal of the American Chemical Society* **2004**, *126*, 11377–11386.

[19] Maesen, T. L. M.; Beerdsen, E.; Calero, S.; Dubbeldam, D.; Smit, B. *Journal of Catalysis* **2006**, *237*, 278–290.

[20] Luna-Triguero, A.; Gómez-Álvarez, P.; Calero, S. *Physical Chemistry Chemical Physics* **2017**, *19*.

[21] Dubbeldam, D.; Calero, S.; Vlugt, T. J. H.; Krishna, R.; Maesen, T. L. M.; Smit, B. *Journal of Physical Chemistry B* **2004**, *108*, 12301–12313.

[22] Granato, M. A.; Vlugt, T. J. H.; Rodrigues, A. E. *Industrial & Engineering Chemistry Research* **2007**, *46*, 7239–7245.

[23] Zhang, Y.; Furukawa, S.-i.; Nitta, T. *Journal of chemical engineering of Japan* **2003**, *36*, 1085–1094.

[24] Makowski, W. *Thermochimica Acta* **2007**, *454*, 26–32.

[25] Makowski, W.; Ogorzałek, Ł. *Thermochimica Acta* **2007**, *465*, 30–39.

[26] Sławek, A.; Vicent-Luna, J. M.; Marszałek, B.; Makowski, W.; Calero, S. *The Journal of Physical Chemistry*

C **2017**, *121*, 25292–25302.
[27] Peng, D.-Y.; Robinson, D. B. *Industrial & Engineering Chemistry Fundamentals* **1976**, *15*, 59–64.
[28] Dubbeldam, D.; Torres-Knoop, A.; Walton, K. S. *Molecular Simulation* **2013**, *39*, 1253–1292.
[29] Dubbeldam, D.; Calero, S.; Ellis, D. E.; Snurr, R. Q. *Molecular Simulation* **2015**, *42*, 81–101.
[30] Balestra, S. R. G.; Bueno-Perez, R.; Calero, S. GAIAST. 2016.
[31] IZA Database. `http://www.iza-structure.org/databases/`.
[32] Pluth, J. J.; Smith, J. V. *Journal of the American Chemical Society* **1980**, *102*, 4704–4708.
[33] Adams, J. M.; Haselden, D. A. *Journal of Solid State Chemistry* **1984**, *51*, 83–90.
[34] Barrachin, B.; de Lara, E. C. *Journal of the Chemical Society, Faraday Transactions 2: Molecular and Chemical Physics* **1986**, *82*, 1953–1966.
[35] Olson, D. H. *Zeolites* **1995**, *15*, 439–443.
[36] Jang, S. B.; Song, S. H.; Kim, Y. *Journal of the Korean Chemical Society* **1995**, *39*, 7–13.
[37] Engelhardt, G. *Microporous materials* **1997**, *12*, 369–373.
[38] Baker, J. *Journal of Computational Chemistry* **1986**, *7*, 385–395.
[39] Jackson, R. A.; Catlow, C. R. A. *Molecular Simulation* **1988**, *1*, 207–224.
[40] Sanders, M. J.; Leslie, M.; Catlow, C. R. A. *Journal of the Chemical Society, Chemical Communications* **1984**, 1271–1273.
[41] García-Sánchez, A.; García-Pérez, E.; Dubbeldam, D.; Krishna, R.; Calero, S. *Adsorption Science & Technology* **2007**, *25*, 417–427.
[42] Liu, B.; Smit, B.; Rey, F.; Valencia, S.; Calero, S. *Journal of Physical Chemistry C* **2008**, *112*, 2492–2498.
[43] Zhu, W.; Kapteijn, F.; Moulijn, J. A.; Den Exter, M. C.; Jansen, J. C. *Langmuir* **2000**, *16*, 3322–3329.
[44] Olson, D. H.; Camblor, M. A.; Villaescusa, L. A.; Kuehl, G. H. *Microporous and Mesoporous Materials* **2004**, *67*, 27–33.
[45] Palomino, M.; Cantín, A.; Corma, A.; Leiva, S.; Rey, F.; Valencia, S. *Chemical Communications* **2007**, 1233–1235.
[46] Narin, G.; Martins, V. F. D.; Campo, M.; Ribeiro, A. M.; Ferreira, A.; Santos, J. C.; Schumann, K.; Rodrigues, A. E. *Separation and Purification Technology* **2014**, *133*, 452–475.
[47] van Miltenburg, A.; Gascon, J.; Zhu, W.; Kapteijn, F.; Moulijn, J. A. *Adsorption* **2008**, *14*, 309–321.
[48] Palmas, S.; Polcaro, A. M.; Carta, R.; Tola, G. *Journal of Chemical and Engineering Data* **1991**, *36*, 1–4.
[49] Kresse, G.; Hafner, J. *Physical Review B* **1993**, *47*, 558.
[50] Kresse, G.; Hafner, J. *Physical Review B* **1994**, *49*, 14251.
[51] Kresse, G.; Furthmüller, J. *Computational materials science* **1996**, *6*, 15–50.
[52] Perdew, J. P.; Burke, K.; Ernzerhof, M. *Physical Review Letters* **1996**, *77*, 3865.
[53] Blöchl, P. E. *Physical Review B* **1994**, *50*, 17953.
[54] Kresse, G.; Joubert, D. *Physical Review B* **1999**, *59*, 1758.
[55] Monkhorst, H. J.; Pack, J. D. *Physical Review B* **1976**, *13*, 5188.
[56] Grimme, S. *Journal of Computational Chemistry* **2006**, *27*, 1787–1799.
[57] Habgood, H. W. *Canadian Journal of Chemistry* **1964**, *42*, 2340–2350.
[58] Yang, R. T.; Kikkinides, E. S. *Aiche Journal* **1995**, *41*, 509–517.
[59] Khelifa, A.; Derriche, Z.; Bengueddach, A. *Applied Catalysis A: General* **1999**, *178*, 61–68.
[60] Aguado, S.; Bergeret, G.; Daniel, C.; Farrusseng, D. *Journal of the American Chemical Society* **2012**, *134*, 14635–14637.
[61] King, C. J. Separation processes based on reversible chemical complexation. 1987.
[62] Luna-Triguero, A.; Vicent-Luna, J.; Becker, T.; Vlugt, T.; Dubbeldam, D.; Gómez-Álvarez, P.; Calero, S. *ChemistrySelect* **2017**, *2*.
[63] Luna-Triguero, A.; Vicent-Luna, J.; Gómez-Álvarez, P.; Calero, S. *Journal of Physical Chemistry C* **2017**, *121*.
[64] Becker, T.; Luna-Triguero, A.; Vicent-Luna, J.; Lin, L.-C.; Dubbeldam, D.; Calero, S.; Vlugt, T. *Physical Chemistry Chemical Physics* **2018**, *20*.
[65] Luna-Triguero, A.; Vicent-Luna, J.; Poursaeidesfahani, A.; Vlugt, T.; Sánchez-De-Armas, R.; Gómez-Álvarez, P.; Calero, S. *ACS Applied Materials and Interfaces* **2018**, *10*.
[66] Bloch, E. D.; Queen, W. L.; Krishna, R.; Zadrozny, J. M.; Brown, C. M.; Long, J. R. *Science* **2012**, *335*, 1606–1610.
[67] Hampson, J. A.; Jasra, R. V.; Rees, L. V. C. *Studies in Surface Science and Catalysis*; Elsevier, 1991; Vol. 62; pp 509–517.
[68] Divekar, S.; Nanoti, A.; Dasgupta, S.; Chauhan, R.; Gupta, P.; Garg, M. O.; Singh, S. P.; Mishra, I. M. *Journal of Chemical & Engineering Data* **2016**, *61*, 2629–2637.

CHAPTER 8

Phase Transition Induced by Gas Adsorption in Metal-Organic Frameworks

Azahara Luna Triguero, José Manuel Vicent Luna, and Sofía Calero

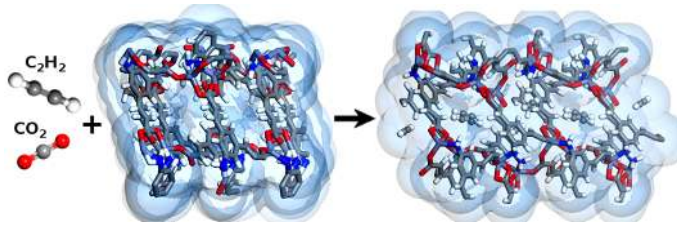

We present a molecular simulation study with the aim of investigating the structural phase transition of ZJU-198 metal-organic framework. This material has been recently synthetized with the appropriate control of window size, which performs well for the separation of mixtures of gases containing nitrogen and methane. We find that the adsorption of small gases in this structure is unusual, and provide an explanation of the molecular mechanisms involved. Using molecular simulation, we analyze the structural distortions exerted by the adsorption of carbon dioxide, nitrogen, methane, acetylene, and ethene. We found that the separation of mixtures composed of these gases in ZJU-198 is due to the organic linker of the structure. The rotation of this linker causes the expansion of the cavities and enhances gas separation by allowing the adsorption of molecules that a priori are too big to be adsorbed.

INTRODUCTION

Metal-organic frameworks (MOFs) are microporous crystalline materials formed by organic ligands and metal clusters. More than 200000 MOFs are currently listed in the Cambridge Structural Database (CSD).[1] Although they are considered flexible materials, less than 100 structures exhibit the so-called “breathing effect ”. This effect consists of a reversible phase transition that goes from the structure with nar-

row pore (NP) to the structure with large pore (LP) and *vice versa*.[2–9] The so-called breathing MOFs have at least two stable states as a function of adsorbed guest. This particular guest-induced flexibility mechanism could be useful for gas separation applications.[10–14] MOF ZJU-198 is a highly stable material formed by the organic linker 5-amino-H_2L((2E,2E')-3,3'-(5-amino-1,3-phenylene) diacrylic acid) that coordinates with four Zn^{2+} (empirical formula: $C_{12}H_7NO_4Zn$). It has been reported that this structure separates CO_2 from N_2, C_2H_2 from CH_4, and moderately C_2H_2 from C_2H_4.[15] This separation capability has been attributed to the channels of about 3.6×4.1 Å and 2.1 × 5.0 Å that exclude the molecule of nitrogen, and have low affinity for the molecule of methane. On the other hand, differences in the isosteric heat of adsorption of C_2H_2 and C_2H_4 allow this particular separation.[15,16] Figure A6.1 in the Appendix 6 shows the schematic connectivity of ZJU-198. To understand the adsorption mechanisms taking place at molecular level in this MOF, we performed energy minimization, Monte Carlo simulations in the grand canonical ensemble (GCMC), and molecular dynamics (MD) simulations using the RASPA software.[17,18] Our simulations show that, surprisingly, ZJU-198 exhibits a phase transition upon adsorption of guest molecules. This transition is due to a breathing effect that allows preferential adsorption of the molecules that favor the pore-opening configuration.

METHODOLOGY

We performed adsorption isotherms using Monte Carlo simulations in the grand canonical ensemble (GCMC). Each point of the isotherm is obtained after equilibration of 10^4 cycles followed by production of 10^5 cycles. Simulations were performed using RASPA software.[17,18] The Lennard-Jones parameters for the framework atoms are taken from DREIDING[19] and UFF (metal atoms).[20] For the adsorbents, we use models taken from the literature. The TraPPE united-atom model with effective interaction centers was used for methane[21] and for ethene.[22] For carbon dioxide and acetylene we used full atom models.[23,24] The charges of ZJU-198 were obtained using the EQeq[25] method based on Ewald sums. The obtained set of charges can be found in Table A6.3 in the Appendix 6. Atoms are labeled as shown in Figure A6.10. We calculated the surface area (S_A) of ZJU-198 by rolling a helium molecule over the surface of the framework. Hence, we have access to the amount of overlap with other framework atoms. The fraction of the overlap is multiplied by the area of the sphere, and the summation over all framework atoms gives the geometric surface area. The pore volume (V_p) is the void fraction times the unit cell volume, being the void fraction of the empty space of the structure divided by the total volume. According to experimental procedures, we also measured this fraction using helium at room temperature, which it

is easily computed from the Widom test particle insertion method.[26]

During adsorption, the frameworks are considered as rigid crystals. The configurations are selected from the optimization of the original crystal structure[15] preserving the symmetry. To obtain the ZJU-198-LP form, we performed geometry optimization of the structure via energy minimization simulations in the $N\sigma T$ ensemble. We used the smart algorithm allowing independent variations of the cell parameters and the angles.[27] The energy minimization is performed in saturation conditions according to experimental data (3.2 mol/kg of ethene).[16] We used the Dreiding[19] generic force field to model the flexibility of the structure. We also used this method to obtain the most favorable configuration of carbon dioxide and acetylene in ZJU-198-LP loaded with 3.5 mol/kg.

Molecular Dynamics (MD) simulations in the NVT ensemble were performed to calculate the diffusion of carbon dioxide in ZJU-198-LP and ZJU-198-NP at room temperature. Temperature is fixed with the Nose-Hoover thermostat.[28] We used 10^9 MD cycles for the production run and time step intervals of 2 fs after 10^5 equilibration cycles.

Adsorption selectivity is defined as $S = \frac{(x_A/y_A)}{(x_B/y_B)}$, where x_i is the molar fraction in the adsorbed phase for i component and y_i the molar fraction in bulk phase. The adsorption selectivity was calculated from the equimolar binary mixtures ($y_A = y_B$).

Results and Discussion

Figure 1 shows that the adsorption of ethene, calculated using the crystallographic structure of ZJU-198 (NP) at 298 K, is almost negligible. This was a surprising finding since the experimental value reported for this MOF is 3.2 mol/kg at 100 kPa. In order to meet this value, we performed MC simulations in an expanded structure. This structure, that we label as ZJU-198-LP, was obtained from geometric optimization, using a method of energy minimization with the framework previously loaded with adsorbates. Energy minimizations based on energy, first and second derivatives, and eigenvalues and eigenvectors of the Hessian matrix are fast, and guarantee accurate results for framework flexibility.[29] The breathing of the structure is evidenced by the transition from NP to LP ZJU-198 (Figure 1b), where the displacement of the atoms also implies variations of volume. The calculated isotherm agrees with the experimental results when the LP phase is considered at large pressures and the NP phase at low pressures.

We calculated adsorption isotherms for other adsorbates with the aim of analyzing this phenomenon in depth. The adsorption isotherms obtained for carbon dioxide, acetylene, nitrogen, and methane in ZJU-198-LP and in the synthetized ZJU-198-NP can be found in Figure A6.2 in the Appendix 6.

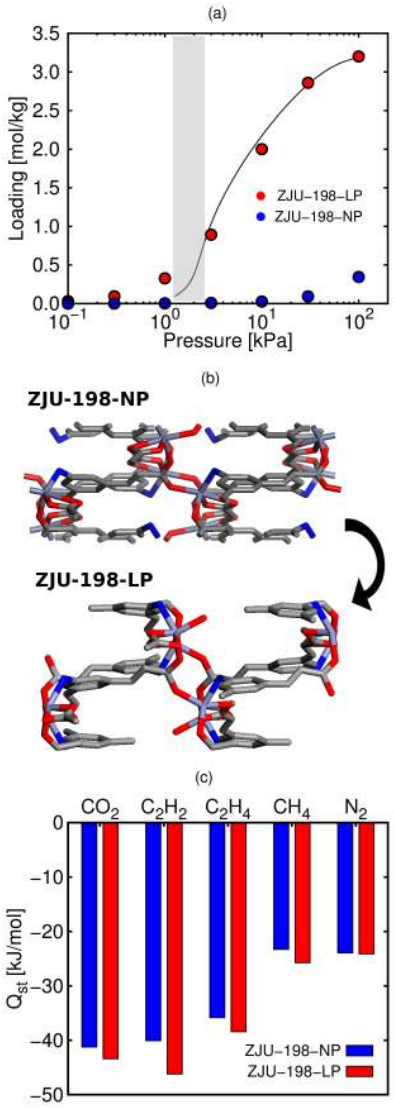

Figure 1. (a) Adsorption isotherm calculated for ethene in ZJU-198-NP (blue symbols) and ZJU-198-LP (red symbols) at 298 K. Experimental data are in- cluded for comparison (lines).[15,16] The highlight zone indicates the estimated pressure of the phase transition. (b) Schematic representation of ZJU-198. (c) Isosteric heats of adsorption in ZJU-198-NP and ZJU-198-LP.

The adsorption isotherms calculated for carbon dioxide, acetylene, and ethene in ZJU-198-LP are in excellent agreement with experiments. However, experimental adsorption of nitrogen and methane can only be reproduced with molecular simulations using the ZJU-198-NP structure. Figure 1c compares the isosteric heats of adsorption of the adsorbates in ZJU-198-NP and -LP. For all adsorbates, adsorption is more favorable in the LP structure. This is also shown by the adsorption energies and the entropies collected in Table A6.1. However, methane and nitrogen cannot trigger the phase transition, probably due to diffusion limitations. Accordingly, the differences observed in adsorption isotherms provide a first indication of a phase transition induced by the adsorbate. The breathing induced in the structure consists in two simultaneous changes: 1) reorientation of the linkers and 2) pore opening affecting the cavities. Similar linker rotation has been previously reported for other MOFs.[30–32]

Our simulations show that the rotation of the linker is due to variations in the torsion angles of the ligand (Figure A6.3 in the Appendix 6). The benzene group rotates, and this leads to a reorientation with the Zn atom through the amine group, and also with the bidentate carboxylate groups. The pore opening is shown in Figure 2a, which compares the pore size distributions (PSD) of the ZJU-198-NP and the ZJU-198-LP structures. The PSD shows a displacement of the

main peak of about 0.5 Å for the LP structure. This effect is also evidenced in the surface area, available pore volume, and framework density of the structures (Table 1). The experimental surface area calculated with nitrogen at 77 K, and also with carbon dioxide at 196 K, is in good agreement with the calculated surface area of ZJU-198-NP. As we show in this work, neither nitrogen nor carbon dioxide can open the structure under these conditions. Additional details about framework connectivity for ZJU-198-NP and ZJU-198-LP, including pore views, can be found in Figure A6.4. As can be seen, characteristic distances and angles of the cell change in the two distinct phases (NP to LP). Figure A6.5 shows the most favorable configurations of carbon dioxide and acetylene in ZJU-198-LP, where the adsorbates are placed near the carboxylate groups. Figure 2b depicts the calculated powder X-ray diffraction pattern for ZJU-198-NP and -LP.

Experimental PXRDs also show differences between the synthetized and the hydrated structure under several conditions.[15] The increase of about 8 % of the unit cell volume is considered as small swelling (from 2901 to 3158 $Å^3$) compared to the values found in the literature for other structures. For example, the unit cell volume of MIL-88 increases about 85 % (from 1135 to 2110 $Å^3$).[10,33,34] The large variations observed in the surface area and in the available pore volume (two times larger for LP structure) are responsible of the structural breathing, and therefore of the separation performance of the structure. Contrary to the

Table 2. Calculated surface area (S_A), available pore volume (V_P) and framework density (ρ_F) for ZJU-198-NP and -LP.

	S_A [m^2/g]	V_P [$Å^3$ uc]	ρ_F [cm^3/g]	ρ_F [g/cm^3]
ZJU-198-NP	460.8	575.1	0.15	1.36
ZJU-198-LP	956.4	1049.4	0.27	1.25

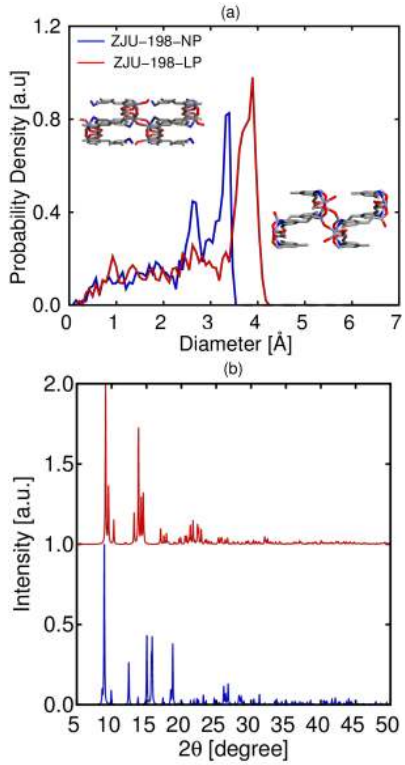

Figure 2. (a) Pore Size Distributions and (b) Powder X-ray diffraction patterns calculated for ZJU-198-NP (blue) and ZJU-198-LP (red).

structural flexibility reported for other MOFs,[35] the phase transition induced by carbon dioxide, acetylene, and ethene in ZJU-198 is independent of temperature for the range of pressures under study (Figure 3). These results reinforce the idea that flexibility is induced by the interactions of the quadrupole moment of carbon dioxide and acetylene, or by the polarizability of ethene with the framework. The adsorption isotherms calculated for methane and nitrogen in ZJU-198-NP at 273 K are also in agreement with experiments (Figure A6.6). The interactions exerted by the molecules of methane and nitrogen with the framework are weak and therefore, unable to induce the structural phase transition.

Another factor that should be taken into account is the size of the molecule. The kinetic sizes of acetylene, ethene, and carbon dioxide are smaller than these of methane and nitrogen (Table A6.2 of the Supporting Information). The expansion and contraction of interpenetrated frameworks exerted by the molecule of carbon dioxide were also reported by Schröder et al.[35] To study the diffusion of carbon dioxide at low coverage in the LP and NP structures we performed Molecular Dynamics simulations. The mean square displacements (MSD) show that the breathing of the MOF allows diffusion of carbon dioxide through the narrow channels in the LP structure, whereas in the NP structure diffusion is extremely low.

Besides, the partial contribution to

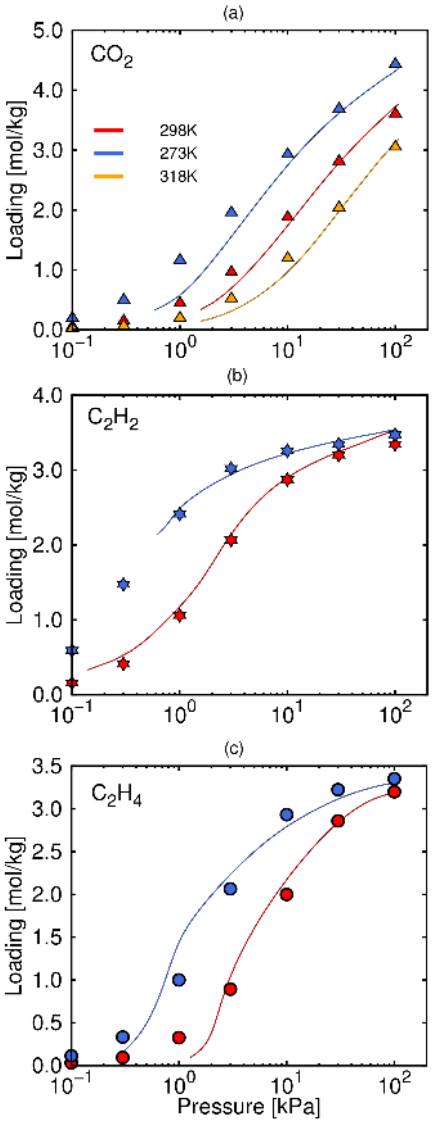

Figure 3. Calculated adsorption isotherms of (a) carbon dioxide, (b) acety- lene, and (c) ethene in ZJU-198-LP. Experimental values are taken from the literature [15, 16] (lines).

molecular transport is due the diffusion in x and z axes according to the pore connectivity (see Figure A6.7). The Aver-

age Occupation Profiles also show the increase of adsorption in the narrow channels due to the induced phase transition (Figure A6.8). Based on these findings, and in order to confirm the separation capabilities reported for ZJU-198 for the CO_2/N_2 mixture, we performed binary adsorption isotherms in ZJU-198-LP at 273 K. In addition, we calculated the adsorption isotherms for CO_2/CH_4, C_2H_2/CO_2, C_2H_2/C_2H_4, C_2H_2/CH_4, and C_2H_4/CH_4 equimolar mixtures in this structure. The reason of using the large pore structure is that at least one of the components of each mixture induces structural changes. The equimolar adsorption isotherms of CO_2/N_2, CO_2/CH_4, and C_2H_4/CH_4 at 273 K are shown in Figure 4 and prove that ZJU-198 performs well for separations, despite the increase of the pore volume. Gas separation based on adsorption should not be estimated with ideal adsorption solution theory (IAST)[36] in structures which exhibit phase transitions. This theory uses single component isotherms to predict the behavior of the mixture, and it could lead to erroneous predictions in structures with framework flexibility. The calculated adsorption selectivity values obtained for C_2H_2/C_2H_4 are in agreement with the values provided by L. Zhang et al[16] from IAST calculations (see Figure A6.9).

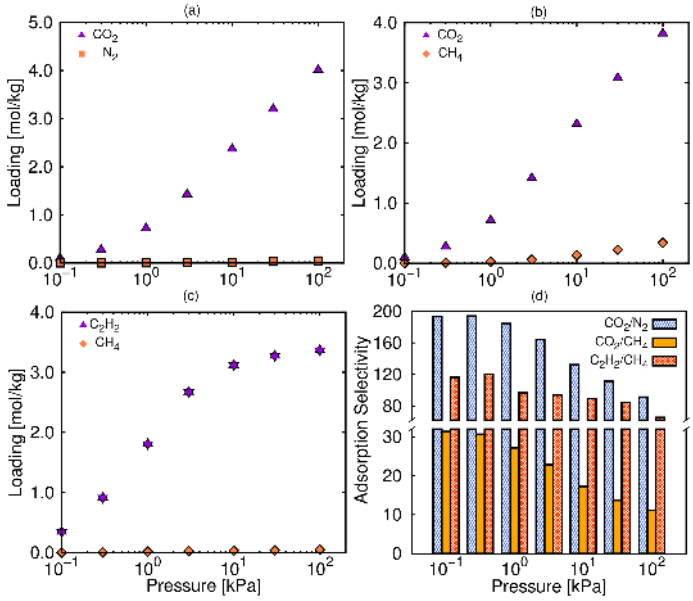

Figure 4. Adsorption isotherms of equimolar mixtures of (a)CO_2/N_2, (b) CO_2/CH_4 and (c) C_2H_2/CH_4 in ZJU-198-LP at 273 K. (d) Adsorption selectivity from the adsorption isotherms of the binary mixtures.

However, IAST calculations fail to reproduce the adsorption selectivity for C_2H_2/CH_4 at the low-pressure regime. The high adsorption selectivity values that we find for CO_2/N_2 and C_2H_2/CH_4 make ZJU-198 a potential candidate for these separations. We also found good separation performance for the CO_2/CH_4 and C_2H_4/CH_4 equimolar mixtures at the studied pressure range (Figure 4 and Figure A6.9 in the Appendix 6).

Conclusions

This findings complement the studies on experimental adsorption and provides a detailed picture of the adsorption mechanisms, as well as valuable information about this particular framework flexibility. They also evidence the need of acquiring deep knowledge for the system in order make accurate predictions. The methodology used in this work could be extended to other breathing MOFs, hence improving the capacity to foretell practical applications as gas mixture separations.

Bibliography

[1] Allen, F. H.; Bellard, S.; Brice, M. D.; Cartwright, B. A.; Doubleday, A.; Higgs, H.; Hummelink, T.; Hummelink-Peters, B. G.; Kennard, O.; Motherwell, W. D. S. *Acta Crystallographica Section B: Structural Crystallography and Crystal Chemistry* **1979**, *35*, 2331–2339.

[2] Kitagawa, S.; Kondo, M. *Bulletin of the Chemical Society of Japan* **1998**, *71*, 1739–1753.

[3] Horike, S.; Shimomura, S.; Kitagawa, S. *Nature Chemistry* **2009**, *1*, 695–704.

[4] Schneemann, A.; Bon, V.; Schwedler, I.; Senkovska, I.; Kaskel, S.; Fischer, R. A. *Chemical Society Reviews* **2014**, *43*, 6062–6096.

[5] Kitagawa, S.; Kitaura, R.; Noro, S. *Angewandte Chemie-International Edition* **2004**, *43*, 2334–2375.

[6] Ferey, G.; Serre, C. *Chemical Society Reviews* **2009**, *38*, 1380–1399.

[7] Uemura, K.; Matsuda, R.; Kitagawa, S. *Journal of Solid State Chemistry* **2005**, *178*, 2420–2429.

[8] Serre, C.; Millange, F.; Surble, S.; Ferey, G. *Angewandte Chemie-International Edition* **2004**, *43*, 6286–6289.

[9] Murdock, C. R.; Hughes, B. C.; Lu, Z.; Jenkins, D. M. *Coordination Chemistry Reviews* **2014**, *258*, 119–136.

[10] Serre, C.; Mellot-Draznieks, C.; Surble, S.; Audebrand, N.; Filinchuk, Y.; Ferey, G. *Science* **2007**, *315*, 1828–1831.

[11] Fletcher, A. J.; Thomas, K. M.; Rosseinsky, M. J. *Journal of Solid State Chemistry* **2005**, *178*, 2491–2510.

[12] Bureekaew, S.; Shimomura, S.; Kitagawa, S. *Science and Technology of Advanced Materials* **2008**, *9*, 14108.

[13] Dybtsev, D. N.; Chun, H.; Kim, K. *Angewandte Chemie-International Edition* **2004**, *43*, 5033–5036.

[14] Kuppler, R. J.; Timmons, D. J.; Fang, Q. R.; Li, J. R.; Makal, T. A.; Young, M. D.; Yuan, D. Q.; Zhao, D.; Zhuang, W. J.; Zhou, H. C. *Coordination Chemistry Reviews* **2009**, *253*, 3042–3066.

[15] Zhang, L.; Jiang, K.; Jiang, M. D.; Yue, D.; Wan, Y. T.; Xing, H. B.; Yang, Y.; Cui, Y. J.; Chen, B. L.; Qian, G. D. *Chemical Communications* **2016**, *52*, 13568–13571.

[16] Zhang, L.; Cui, X. L.; Xing, H. B.; Yang, Y.; Cui, Y. J.; Chen, B. L.; Qian, G. D. *Rsc Advances* **2017**, *7*, 20795–20800.

[17] Dubbeldam, D.; Torres-Knoop, A.; Walton, K. S. *Molecular Simulation* **2013**, *39*, 1253–1292.

[18] Dubbeldam, D.; Calero, S.; Ellis, D. E.; Snurr, R. Q. *Molecular Simulation* **2015**, *42*, 81–101.

[19] Mayo, S. L.; Olafson, B. D.; Goddard, W. A. *Journal of Physical Chemistry* **1990**, *94*, 8897–8909.

[20] Rappe, A. K.; Casewit, C. J.; Colwell, K. S.; Goddard, W. A.; Skiff, W. M. *Journal of the American Chemical Society* **1992**, *114*, 10024–10035.

[21] Potoff, J. J.; Siepmann, J. I. *AIChE Journal* **2001**, *47*, 1676–1682.

[22] Liu, B.; Smit, B.; Rey, F.; Valencia, S.; Calero, S. *Journal of Physical Chemistry C* **2008**, *112*, 2492–2498.

[23] Harris, J. G.; Yung, K. H. *Journal of Physical Chemistry* **1995**, *99*, 12021–12024.

[24] Fischer, M.; Hoffmann, F.; Froba, M. *Chemphyschem* **2010**, *11*, 2220–2229.

[25] Wilmer, C.; Kim, K. C.; Snurr, R. Q. *The Journal of Physical Chemistry Letters* **2012**, *3*, 2506–2511.

[26] Widom, B. *The Journal of Chemical Physics* **1963**, *39*, 2808–2812.

[27] Zhou, R.; Berne, B. J. *The Journal of Chemical Physics* **1997**, *107*, 9185–9196.

[28] Nose, S. *Molecular Physics* **2002**, *100*, 191–198.

[29] Dubbeldam, D.; Krishna, R.; Snurr, R. Q. *The Journal of Physical Chemistry C* **2009**, *113*, 19317–19327.

[30] Fairen-Jimenez, D.; Moggach, S. A.; Wharmby, M. T.; Wright, P. A.; Parsons, S.; Duren, T. *Journal of the American Chemical Society* **2011**, *133*, 8900–8902.
[31] Garberoglio, G.; Taioli, S. *Microporous and Mesoporous Materials* **2012**, *163*, 215–220.
[32] Balestra, S. R. G.; Bueno-Perez, R.; Hamad, S.; Dubbeldam, D.; Ruiz-Salvador, A. R.; Calero, S. *Chemistry of Materials* **2016**, *28*, 8296–8304.
[33] Mellot-Draznieks, C.; Serre, C.; Surble, S.; Audebrand, N.; Ferey, G. *Journal of the American Chemical Society* **2005**, *127*, 16273–16278.
[34] Serre, C.; Millange, F.; Thouvenot, C.; Nogues, M.; Marsolier, G.; Louer, D.; Ferey, G. *Journal of the American Chemical Society* **2002**, *124*, 13519–13526.
[35] Yang, S. H.; Lin, X.; Lewis, W.; Suyetin, M.; Bichoutskaia, E.; Parker, J. E.; Tang, C. C.; Allan, D. R.; Rizkallah, P. J.; Hubberstey, P.; Champness, N. R.; Thomas, K. M.; Blake, A. J.; Schroder, M. *Nature Materials* **2012**, *11*, 710–716.
[36] Myers, A. L.; Prausnitz, J. M. *Aiche Journal* **1965**, *11*, 121–127.

CHAPTER 9

Acetylene Storage and Separation using Metal-Organic Frameworks with Open Metal Sites

Azahara Luna-Triguero, José Manuel Vicent-Luna, Rafael M. Madero-Castro, Paula Gómez-Álvarez, and Sofía Calero

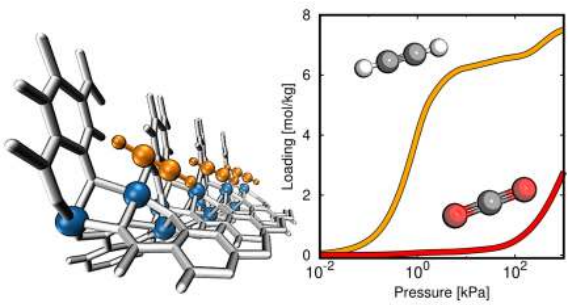

Efficient separation and storage of gas streams involving light hydrocarbons is essential for industrial applications. They are widely used as energy resources and/or chemical raw materials in various chemical reactions. Here we focus on the separation of acetylene from methane and carbon dioxide. The separation of acetylene from carbon dioxide is especially challenging due to the similar kinetic diameter and boiling points of the molecules. In recent years, considerable progress has been made on the adsorption-based separation using porous Metal-Organic Frameworks (MOFs). Most reported studies are experimental. We present a computational study on these gas separations using a variety of MOFs. This allows to investigate the competitive gas adsorption, which is experimentally challenging, as well as to understand the adsorption mechanisms at the molecular level, which in turn allows further experimental MOF design for this application. MOFs with open metal sites and particularly Fe-MOF-74 seem good for this separation, with a trade-off between physical adsorption capacity and selectivity. The characteristics of the interaction between the MOFs and the guest molecules are comprehensively investigated, including the development, based on experimental single-adsorption isotherms, of a specific parametrization to account for the interactions of acetylene with the open metal sites. The agreement with available experimental data and the calculated values on volumetric and calorimet-

ric adsorption as well as binding sites for the pure components points to the reliability of the models and methods to successfully predict the separation of the mixtures.

INTRODUCTION

Acetylene is a very important chemical feedstock for modern industry from which many widely used polymer products such as polyester plastics are synthesized.[1,2] However, current acetylene industrial production involves one of the most challenging gas separations in the chemical industry. Acetylene is mainly produced by the cracking of petroleum, coexisting with some other spin-offs, such as carbon dioxide and methane. Overall, the separation of small gas molecules has been a technological challenge to obtain high-purity gases for chemical and petrochemical industry. The purification of acetylene is particularly difficult. The molecule of acetylene is quite different than the molecule of methane but very similar to the carbon dioxide in terms of shape (linear), dimensions (3.32 × 3.34 × 5.7 $Å^3$ for acetylene and 3.18 × 3.33 × 5.36 $Å^3$ for carbon dioxide), and physical properties. For example the boiling points of acetylene and carbon dioxide are 189.3 K and 194.7 K, respectively.[3] Hence, conventional approaches for gas separation such as molecular sieving (discrimination on the basis of size) and cryogenic distillation are poorly efficient and very energy-consuming.[4,5] High-capacity storage of gas fuel iscrucial too, but acetylene is difficult to safely store and transport because of its explosiveness when compressed.[6]

Porous Metal-Organic Frameworks (MOFs) bring promising solutions to the above problems based on physisorption. This is due to their excellent performance for gas separation and storage.[7–10] A certain number of MOFs have been designed and proposed for the purification of acetylene from methane and carbon dioxide.[6,11–13] In principle, fine-tuning of pore size in MOFs could improve gas separation. Also, pore surface functionalization can maximize the tiny differences between acetylene and carbon dioxide toward specific recognition and thus their selective separation.[14,15]

To date, a few MOFs have been designed and characterized as successful for acetylene separation and storage. In the study of Pang et al.[16], a porous MOF named FJI-H8 with both suitable pore space and rich open metal sites was proposed for efficient storage of acetylene at room conditions. Li et al.[17] reported a rod-packing 3D microporous hydrogen-bonded organic framework HOF-3 showing preferential adsorption of acetylene over carbon dioxide. This was attributed to its unique pockets and pore surfaces. Lin et al.[18] proved that a micro-

porous material [$Zn(dps)_2(SiF_6)$] (UTSA-300, dps = 4,4'-dipyridylsulfide) with two-dimensional channels of about 3.3 Å can adsorb large amounts of acetylene and exclude the molecules of carbon dioxide at room conditions due to the strong C-H $\cdots$ F and $\pi - \pi$ stacking interactions within its closed-pores. Zhang et al.[14] reported a Zn-based MOF with exposed amino functional group ZJU-195 with potential for high acetylene storage and C_2H_2/CO_2 and C_2H_2/CH_4 separations ascribed to the presence of the functional groups. Open metal sites in MOFs play a key role in adsorption of molecules with quadrupole moment and olefins too. Xiang et al.[19] found that HKUST-1 was optimal for acetylene storage among a number of MOFs due to the strong interactions with the unsaturated Cu^{2+} sites. Recently, M-MOF-74 (M = Co, Mg, Fe, Ni and Mn) series have been found optimal for separation of light hydrocarbon mixtures including olefins.[20–24]

Most of the above-exposed literature are experimental studies. These studies on mixtures are nontrivial, given the difficulty of measuring the composition in the gas phase of the experimental setup. In this sense, molecular simulation (MS) techniques are a useful and complementary tool. Experiments provide data sets to test theoretical models used in MS. In turn, MS allows the assessment of the competitive adsorption as well as the elucidation of the underlying microscopic behavior, providing key information for designing novel materials for this separation. This way, we performed a computational study to explore adsorption of acetylene, carbon dioxide, and methane in MOFs with high surface areas and different pore geometries, as well as in MOFs containing open metal sites, which act as enhanced binding sites. In particular we selected two members of the MOF-74 family, Fe-MOF-74 and Co-MOF-74; two MOFs with copper paddle-wheel nodes possessing an open Cu(II) site, namely Cu-BTC and PCN-16; and two MOFs with high pore volume and without OMs, IRMOF-1 and ZJNU-30. To assess their potential for acetylene purification, we calculated the adsorption isotherms of single component and binary C_2H_2/CO_2 and C_2H_2/CH_4 mixtures, from which we obtained the adsorption selectivity. Experimentally, gas selectivity is usually obtained from measured isotherms in conjunction with the Ideal Adsorbed Solution Theory (IAST), because of the difficulty of measuring adsorption equilibrium data of gas mixtures. Heats of adsorption as a function of the loading were also extracted from our simulations. The obtained macroscopic behavior was compared with experimental data and comprehensively discussed in terms of binding sites and gas-framework interactions.

Standard force fields often fail in describing olefin adsorption in the OMs. The OMs interact strongly with alkenes and alkynes by the π bond, where the unsaturated hydrocarbons donate an electron to the unfilled orbital of the OMs. In turn,

there is a back-donation from the orbital of the metal center to the π antibonding orbital of the olefin. This effect is commonly known as π-complexation. Unfortunately, generic force fields do not account for these donor-acceptor interactions between the double or triple bond of unsaturated hydrocarbons and MOFs with OMs. Previous studies[24–26] reported a modification to the potential energy that takes into account the specific interactions between hydrocarbons with multiple bonds and the OMs. Becker et al.[24] show the potential of polarizable force fields to predict the adsorption of olefins in a series of MOF-74 family. Heinen et al.[25] included a DFT-based potential as part of the classical force field to investigate the ethylene/ethane separation in Cu-BTC. These techniques improve significantly the performance of generic force fields for adsorption MOFs where the π-complexation is the key factor. However, the drawback is that this modifications of the force field functional form and the use of additional molecular simulation techniques. It also entails high computational cost. In recent studies,[22,27] we reported that standard classical force fields can also reproduce the experimental adsorption of olefins and paraffins in MOFs with OMs sush as M-MOF-74 family and Cu-BTC if the force field parameters are properly fitted. In this work we also parametrize the cross Lennard-Jones interactions for acetylene and the MOFs with OMs by fitting to available experimental pure-component isotherms.

METHODOLOGY

For the coordinatively unsaturated metal site MOFs, we have focused on the cobalt and iron variants of M-MOF-74 and on two MOFs with copper paddle-wheel nodes possessing an open Cu(II) site. M-MOF-74 is also known as CPO-27-M [M_2 (2,5-dioxidoterephthalate), M = Co, Fe][28,29] and has an open M(II) site. The two MOFs with copper paddle-wheel nodes are PCN-16 [Cu_2 (ethynediyl-bis (benzenedicarboxylate))],[30] and Cu-BTC[31] (also known as HKUST-1) [Cu_3 (1,3,5-benzene- tricarboxylate)$_2$]. The two MOFs without OMs theat we selected are IRMOF-1,[32] also known as MOF-5. [Zn_4O (benzenedicarboxylate)$_3$] is representative among these MOFs with properties largely driven by their surface area and pore geometry. MOF ZJNU-30 was selected for been recently synthetized and reported for olefin separation.[33]

The framework connectivity and pore size distributions of the MOFs are displayed in Figures 1 and 2, respectively. PCN-16 and Cu-BTC possess a common copper paddle-wheel node, coupled through extended multi-carboxylate ligands. PCN-16 is formed by one relatively small spherical cage of approximately 7 Å other elliptical cage extended along the *c*-axis. Cu-BTC consists of two large central cavities of 10 and 11 Å in diameter surrounded by small cavities of 5 Å in diameter. These cavities are connected through triangular-shaped 3.5 Å diameter apertures.

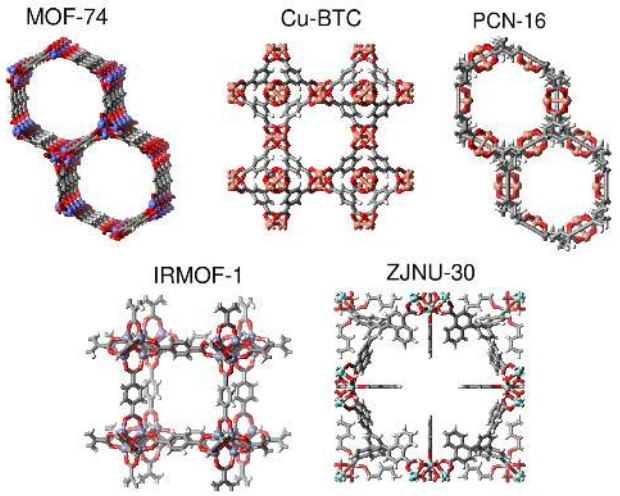

Figure 1. Schematic representation of framework connectivity for MOFs used in this work.

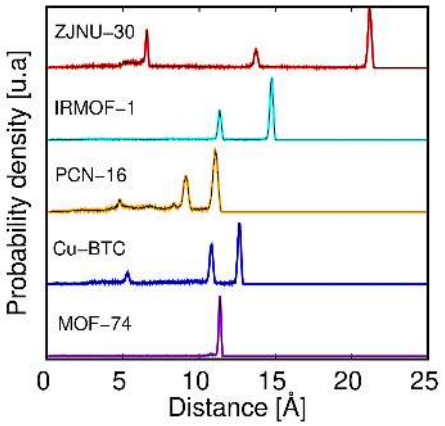

Figure 2. Pore size distribution of the MOFs used in this work.

Contrary to other MOFs considered here, M-MOF-74 lacks of enclosed pores. It consists of hexagonal pore channels with metal clusters that propagate along the *c*-axis . IRMOF-1contains a largely open pore within a simple cubic framework of Zn_4O nodes and benzene-dicarboxylate linkers. This open structure has relatively high surface area and thus allows for gas storage and transport. ZJNU-30 is a Zr-based MOF with a C3-symmetrical trigonal tricarboxylate linker. The structure has a cubic symmetry with cell parameters of 28.35 Å. This MOF was reported with octahedral and cuboctahedral cages of about 14 and 22 Å in diameter, respectively. A previous computational study revealed a third cavity of about 7 Å in diameter.[23]

We performed adsorption isotherms for pure component and equimolar binary mixtures at 318 K and 298 K, respectively, using Monte Carlo simulations in the grand canonical ensemble (μVT). The chemical potential is related to the imposed values of fugacity, from which pressure can be determined using the Peng-Robinson equation of state.[34] Simu-

lations were performed using RASPA software.[35,36] The Monte Carlo moves involve molecular translation, rotation, and insertion/deletion as well as identity changes in the case of the mixtures. Each point of the isotherm is obtained after equilibration of 10^4 cycles followed by production of 10^5 cycles for pure isotherms and 5×10^5 for mixtures. We performed energy minimizations of Fe-MOF-74 with a single molecule of acetylene and carbon dioxide to measure the binding geometry of these components. The most favorable configuration of the adsorbates inside the pores was also calculated at loading corresponding to 100 kPa. The energy minimizations were conducted using Baker's method[37] in the canonical ensemble (NVT). The positions of the framework atoms were fixed at crystallographic positions during the simulations.

The non-bonded energy potential consists of guest-guest and host-guest Lennard-Jones (L-J) and electrostatic interactions. The potential is truncated and shifted with *cutoff* distance set to 12 Å and the periodic boundary conditions exerted in the three dimensions. For each MOF, the number of unit cells used to construct the simulations box fulfills that the minimum length in each of the coordinate directions is larger than twice the *cutoff* distance. The Lennard-Jones parameters for the framework atoms are taken from DREIDING[38] and from UFF[39] for the metal atoms. The models used to describe the adsorbates are taken from the literature and consist on one atom (or set of atoms) with L-J interacting centers and point charges. Methane was described with a united-atom model with effective interaction centers.[40] Full-atom models were used for carbon dioxide and acetylene.[26,41] Lorentz-Berthelot mixing rules were applied to account for cross L-J interactions except for those corresponding to acetylene with the MOFs with OMs, which were fitted to available experimental data on pure-component adsorption equilibrium because of the π-interaction, as noted in previous section. The obtained parameters are collected in Table A7.1 in the Appendix 7. We used a set of effective point charges which reproduce the adsorption of carbon dioxide in the six MOFs. An initial set of point charges of the MOFs were obtained using the EQeq[42] method based on Ewald sums, except for Cu-BTC and IRMOF-1 , which were taken from references 43 and 44. These sets of charges were slightly rescaled by multiplying by a factor to match the available experimental isotherms. The set of charges can be found in Table A7.2 and the framework atoms are labeled as shown in Figure A7.1-A7.3.

We calculated the electrostatic field to study the influence of it in the configuration of the molecules inside the structure of Fe-MOF-74. The electrostatic field in a given point is calculated using the superposition principle. We selected an initial location point at the center of the channel and the electric field is calculated at this point. To do so, we take into account all

the atoms in a coordination sphere with radio R_0 (R_0=cell length of the structure at initial point) accounting of the periodic boundary conditions. R_0 radio is that that ensure an error in the electric field below 0.1% . Once the electric field E_0 is calculated, we move along the direction of the electric field with a displacement of dl=0.2 Å where $\vec{r}_1 = \vec{r}_0 + \frac{\vec{E}_0}{|E_0|} dl$ we repeat this procedure 2000 times, building the field lines.

Results and Discussion

Single-component adsorption

The unary adsorption isotherms of acetylene, carbon dioxide and methanein the targeted MOFs were calculated using GCMC simulations. Results are depicted in Figure 3, and correspond to 318 K. We calculated the adsorption isotherms at several temperatures in order to compare with available experimental data (Figure A7.4 in the Appendix 7). In general terms, the isotherms that we have obtained with molecular simulation match those obtained experimentally. This validates the models and computational strategies described in the methodology. Although in general the developed parametrization for acetylene adsorption in MOFs with OMs reproduce adsorption successfully, the calculated isotherms slightly overestimate the experimental uptakes in the members of MOF-74 family. Note that adsorption isotherms in Figure A7.4 in the Appendix 7 are plotted up to 10^3 kPa, since experimental operational conditions typically correspond to low/room pressure due to the explosive character of acetylene. Although we are also interested in this pressure range for the separation, to examine the saturation uptakes related with the storage capacity from theoretical point of view. The estimation of uptakes at high pressures is other advantage of molecular simulation. As it can be observed from Figure 3, carbon dioxide shows the highest saturation uptakes regardless of the MOF. Although IRMOF-1 and ZJNU-30 has an impressive uptake at high pressure and can store more than the MOFs with OMs, the onset adsorption pressures for these MOFs are about 100 kPa and virtually the same for all the adsorbates. This makes them useless for this gas separation at low-cost operational conditions. For MOFs with open metal sites the adsorption of carbon dioxide and acetylene, occurs at quite lower values of pressure, and especially for the latter. This is most remarkable for Fe-MOF-74, and makes of it a possible adsorbent for the challenging C_2H_2 /CO_2 separation. It is worth noting that the adsorption isotherms of the MOF pairs Co/Fe-MOF-74, Cu-BTC/PCN-16 and IRMOF-1/ZJNU-30 MOF are similar.

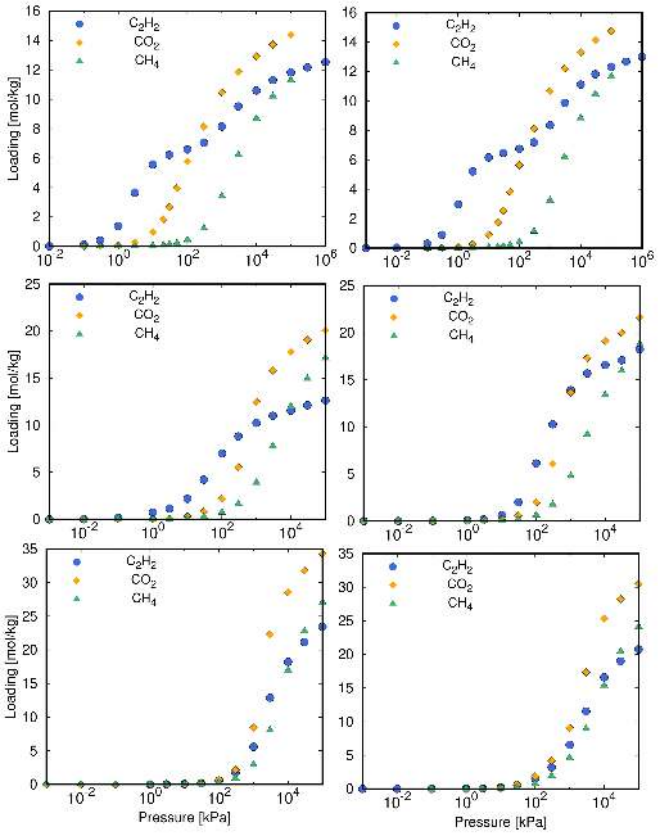

Figure 3. Adsorption isotherms of acetylene (blue circles), carbon dioxide (yellow diamonds), and methane (green triangles) in a) Co-MOF-74, b) Fe-MOF-74, c) Cu-BTC, d) PCN-16, e) IRMOF-1, and f) ZJNU-30 at 318 K.

In addition to adsorption isotherms, we calculatedthe isosteric heat of adsorption at the different loadings. The isosteric heat of adsorption, Q_{st}, is defined as the difference in the partial molar enthalpy of the adsorbate between the gas phase and the adsorbed phase according to:

$$Q_{st} = H_b - \left[\frac{\partial(U_{ad} - U_{intra})}{\partial N_{ad}}\right]_{V,T}$$

where H_b is the enthalpy of adsorbate in the bulk phase, U_{ad} is the total adsorption energy including contributions from both adsorbate-adsorbent and adsorbate-adsorbate interactions, U_{intra} is the total intramolecular energy of the adsorbate, and N_{ad} is the number of adsorbed molecules. H_b is simply assumed to be RT in which R is the ideal gas constant and T the temperature. This is acceptable when the bulk phase behaves as an ideal gas. This property was computed from data on

volumetric adsorption using the fluctuation method as follows:

$$Q_{st}\langle N\rangle = RT + \langle U_g\rangle - \frac{\langle UN\rangle - \langle U\rangle\langle N\rangle}{\langle N^2\rangle - \langle N\rangle^2}$$

where U and U_g denote the total energy of the system and the guest energy contribution (null for rigid models), respectively, and N is the number of adsorbed particles. The brackets indicate an ensemble average over a GCMC simulation. Results concerning the heat of adsorption of acetylene, carbon dioxide, and methane are shown in Figure 4 for Fe-MOF-74 and IRMOF-1 as representative MOFs for selective adsorption and adsorption storage, respectively, based on Figure 3. Whereas the isosteric heat of adsorption for the molecules of methane is low and similar in the two MOFs, it is notably larger in Fe-MOF-74 than in IRMOF-1 for carbon dioxide and acetylene, especially the latter. This evidences the strong effect of the open metal sites for adsorbates with quadrupole moment. Q_{st} at low-coverage indicates the adsorbent-adsorbate affinity, the highest is the heat of adsorption, the strongest is the interaction of the molecule with the structure. It is worth noting that the isosteric heat of adsorption for acetylene in Fe-MOF-74 (about 45 kJ/mol) is higher than that for carbon dioxide (about 30 kJ/mol), due to the *pi*-complexation phenomena for the alkyne.

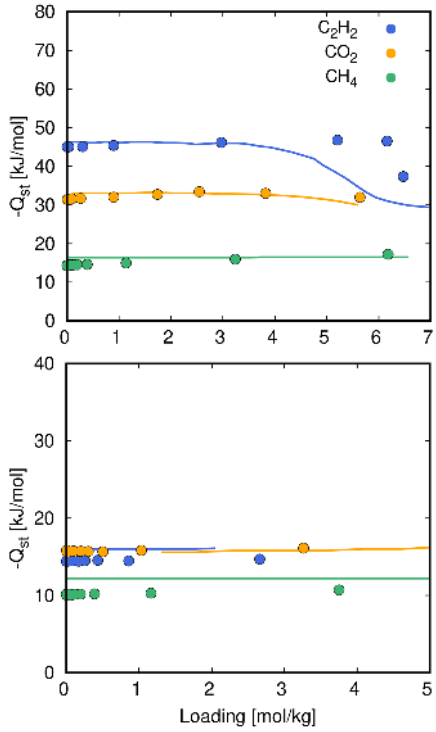

Figure 4. Calculated isosteric heats of adsorption (points) for acetylene, carbon dioxide, and methane as a function of the loading in Fe-MOF-74 (top) and IRMOF-1 (bottom). Lines correspond to experimental data taken from literature.[19,45–48]

The isosteric heats for the remaining MOFs and the comparison with reported experimental data is provided in Figure A7.5. As for the adsorption isotherms, our predictions show satisfactory consistency with experimental data, although slight quantitative differences are evident for acetylene, especially in Cu-BTC. Again, we found that at low loadings the MOFs that possess open metal centers (Co-MOF-74, Cu-BTC, PCN-16) exhibit higher isosteric heats of adsorption as compared to the

fully coordinated metal MOF ZJNU-30.

The curve shape that indicates the variation of the heats of adsorption with loadings, are distinctly different depending on the guest and also on the MOF. While a plateau of 10-15 kJ/mol is observed for methane across the uptake range regardless of the MOF, increasing and decreasing trends are overall observed for carbon dioxide and acetylene, respectively, at high uptakes. It is important to note that the isosteric heat is a combination of host-guest and guest-guest interactions. The host-guest and guest-guest potential interactions along the whole adsorption processes are reported in Figure 5 and A7.6.

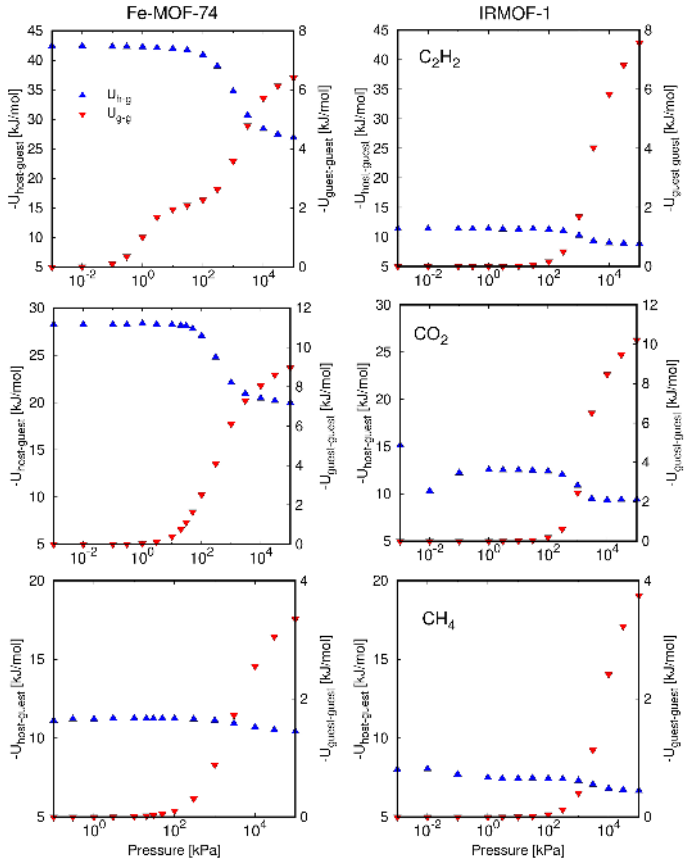

Figure 5. Potential energy of host-guest (blue) and guest-guest (red) interactions as a function of the pressure for acetylene, carbon dioxide, and methane in Fe-MOF-74 and IRMOF-1 at 318 K.

On the one hand, the host-guest interactions generally decay with loading as the strong binding sites are filled, and then less favorable adsorption sites are available for subsequent gas molecules. MOFs with OMs show higher host-guest interactions with acetylene due to the π-complexation of the triple bond with the exposed metals. On the other hand, guest-guest interactions tend to increase with pressure as the density of the gas increases. This interaction in the studied MOFs has the following hierarchy: carbon dioxide > acetylene > methane. Should be noted that the guest-guest interaction exhibits a stepped shape for acetylene in the MOF-74 family, this phenomenon is also found in pure adsorption isotherms with a plateau about 6 mol/kg (Figure 3). In contrast, CO_2 -CO_2 interactions at high pressure (uptakes) show either the absence of this stepped trend (in the MOF-74 members) or an increasing trend (in Cu-BTC and PCN-16).

From here on out, we will focus on Fe-MOF-74 and IRMOF-1. Figure 6 depicts the average occupational profiles of the adsorbates in these MOFs at 318 K at saturation pressures. Those for low and saturation pressures for the rest of the MOFs are plotted in Figures A7.7-A7.11. The occupancy profiles for Fe-MOF-74 clearly show that the OMs are the primary adsorption sites, even for methane. The gas molecules are mainly adsorbed in Fe-MOF-74 in the six corners of the hexagonal channels at low loadings,

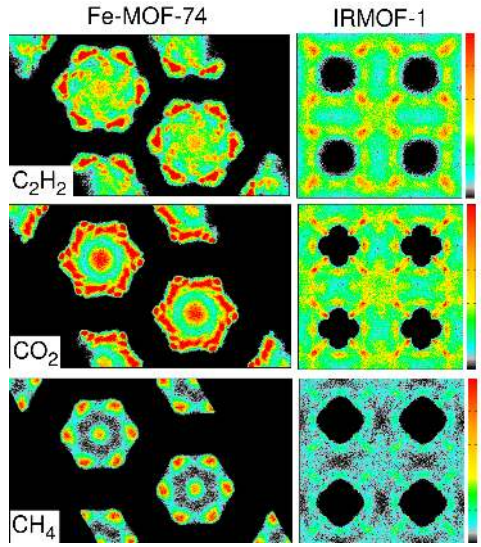

Figure 6. Average occupational profiles of pure adsorption of acetylene, carbon dioxide, and methane at saturation loadings in Fe-MOF-74 and IRMOF-1.

where the five-coordinated metal ions are located. With the increase in uptake, molecules also adsorb in the center of the hexagonal channels. This filling occurs in different manners depending on the adsorbate. The subsequent filling of acetylene is governed by the electrostatic interactions with the surface as it is evident from the more dense zones (in red) and the electrostatic field of the MOF plotted in Figure 7. Carbon dioxide molecules however form a second layer around the metal centers and then mainly occupy the center of the channel. The average occupation profiles corresponding to IRMOF-1 are relatively more homogeneous due to

the absence of enhanced adsorption sites. The results indicate that at relatively low pressures (<100 kPa) regions close to the linkers, located above and below the center of the aromatic rings, are preferred. Gas adsorption occurs near the inorganic part and gradually increases around the organic linker. Although confinement effects partly play a role on the adsorption mechanisms in this MOF, the considerably denser filling of acetylene and carbon dioxide than methane at the same pressure evidences the relevance of the gas-surface electrostatic interactions.

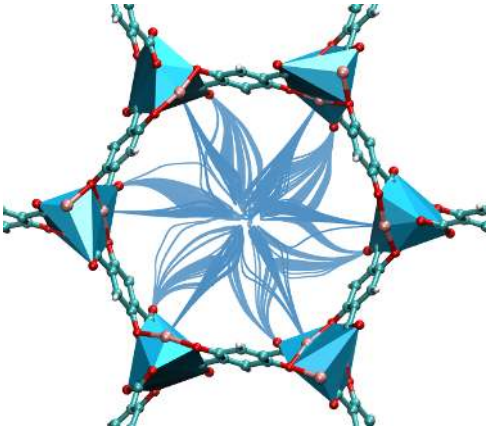

Figure 7. Electrostatic field from the center of the channel of M-MOF-74.

Figure 8 (top) depicts the most stable configurations of carbon dioxide and acetylene in Fe-MOF-74 for medium values of loadings (100 kPa) obtained from energy minimizations. Results confirm the exposed metals as preferential sites but show clearly distinct molecular configurations of these guest gases around the metal despite being linear-shaped and of similar sizes. To gain insights, we conducted energy minimizations for a single molecule. Results are plotted in Figure 8 (bottom), together with reported experimental data. It can be gleaned from this figure that acetylene molecules locate almost parallel with respect to the plane formed by the metal ion and the four framework oxygen atoms, and that carbon dioxide molecules form a markedly angular Fe···O-C-O complex with one of the oxygen atoms pointing to the metal site. These binding geometries for acetylene and carbon dioxide can be rationalized in the basis of the π-complexation and its polarizability, respectively. The consistency with experimental data[46,47] are additional validation of the used methods. Quantitatively, the simulated binding distances and angles almost match experimental data for acetylene whereas they are non-negligibly overestimated for carbon dioxide. We found the oxygen of the carbon dioxide to be at 2.43 Å from the metal center, with a Fe···O-C-O angle of 139°. The obtained average distances of the two carbon atoms in acetylene from the metal center are 2.57 Å and 2.63 Å, with a C-C···Fe angle of 79.6°. Overall, the above results indicate that the carbon dioxide and acetylene binding at the open metal sites governs their adsorption, but that the microscopic underlying mechanisms are rather distinct.

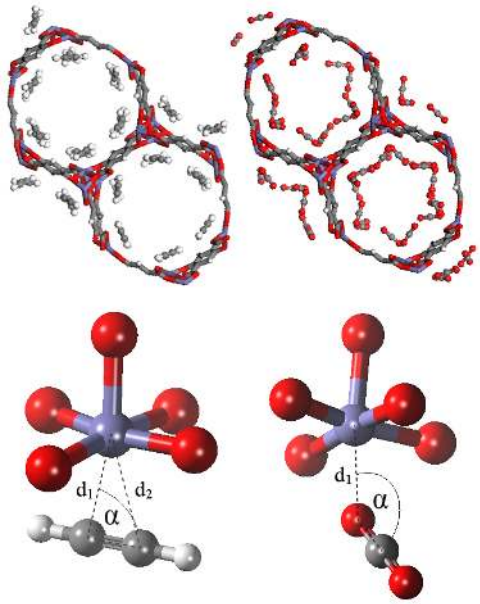

	C_2H_2		CO_2	
	Sim	Exp*	Sim	Exp*
d_1 [Å]	2.63	2.52	2.43	2.29
d_2 [Å]	2.57	2.48		
α [°]	79.6	77	139	106

Figure 8. Most stable configuration and binding geometry of acetylene and carbon dioxide within the pores of Fe-MOF-74 at 100 kPa. Experimental data [ref] is added for comparison

Competitive adsorption

Once the models and force fields have been demonstrated to satisfactorily predict volumetric and calorimetric adsorption of the pure compounds, as well as the binding geometries, we have used them to assess the competitive adsorption. Figure 9 shows the adsorption isotherms of equimolar binary C_2H_2/CO_2 and C_2H_2/CH_4 mixtures in Fe-MOF-74 and IRMOF-1 at room temperature. For the two mixtures, onset adsorption in IRMOF-1 occurs from virtually the same pressure of 100 kPa for both components, so adsorption-based separation at low/room pressure is not viable. The separation of carbon dioxide from acetylene in IRMOF-1at high pressure is due to the condensation of the components and their liquid densities, at room temperature the density of carbon dioxide is practically twice than that for acetylene (1178 and 622 kg/m^3). Indeed the loading of acetylene decreases when the values of pressure are above 103 kPa. The same occurs for C_2H_2/CH_4 mixture, at high pressure the condensation of the components leads to the separation of acetylene over methane. In this case the densities are much alike (622 and 423 kg/m3) and therefore the separation is less significant. Opposite than for IRMOF-1, the onset adsorption of acetylene in Fe-MOF-74 is two orders of magnitude lower than for carbon dioxide and methane. Adsorption of the latter components is negligible until acetylene uptake is about 6-7 mol/kg, *i.e.* when all positions near the unsaturated metal centers have been occupied by the molecules of acetylene. This occurs slightly above atmospheric pressure. Therefore, Fe-MOF-74 seems good candidate for the separation at room conditions. Though other MOFs with open metal sites also separate acetylene from carbon dioxide, Fe-MOF-74 provides the best adsorption selectivity (see Figure A7.13).

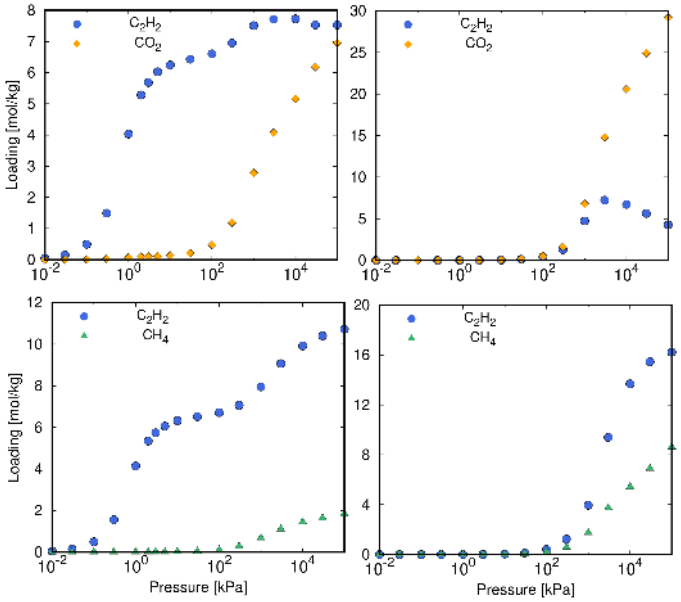

Figure 9. Equimolar adsorption isotherms of acetylene/carbon dioxide (top) and acetylene/methane (bottom) mixtures in Fe-MOF-74 (left) and IRMOF-1 (right) at 298 K.

The adsorption selectivity is an important value on the evaluation of a certain material for the separation of binary mixtures by equilibrium adsorption. This is a pairwise property controlled by the ratio of adsorptions of two adsorbates. The selectivity of one component (A) over another component (B) is defined as:

$$S_{AB} = \frac{x_A/y_A}{x_B/y_B}$$

where x_i and y_i are the molar fractions in the adsorbed phase and in the bulk phase, respectively, for i component. For equimolar binary mixtures $y_A = y_B$ and therefore, $S_AB = x_A/x_B$. From the binary adsorption isotherms (Figure 9), we determined C_2H_2/CO_2 and C_2H_2/CH_4 selectivities in IRMOF-1 and Fe-MOF-74 throughout the pressure range. Results are depicted in Figure 10. As shown in the figure, the highest values of selectivity exhibit a plateau at low pressures. Selectivity decreases from a certain pressure that depends on the adsorbent and adsorbate. MOFs that possess open metal sites and especially Fe-MOF-74 have large adsorption selectivity in favor of acetylene. The adsorption in IRMOF-1 and ZJNU-30, is highly dependent on the surface area and independenl on the adsorbate. For this reason the selectivity is about 1 up to atmospheric pressure. At high pressure these MOFs show an inverse separation of carbon dioxide adsorption over acetylene with maxima selectivity values that of about 10.

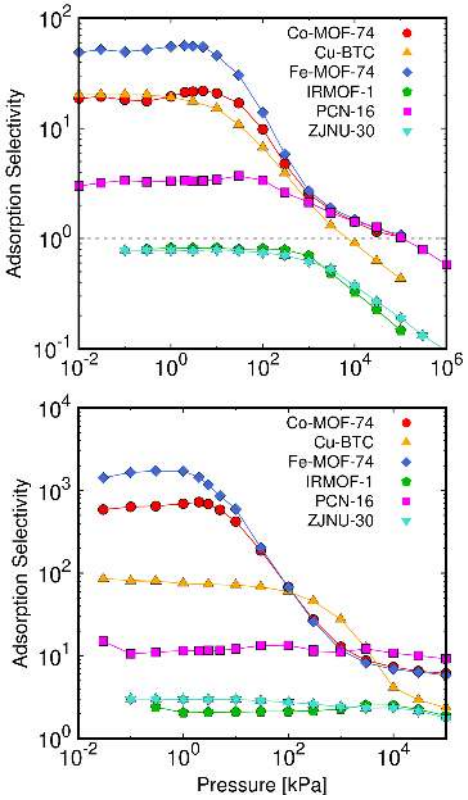

Figure 10. C_2H_2/CO_2 (top) and C_2H_2/CH_4 (bottom) adsorption selectivity obtained from the adsorption isotherms of equimolar binary mixtures at 298 K.

Although in MOF-74 the selectivity values for C_2H_2/CO_2 are lower than for C_2H_2/CH_4, they are still extremely high for this challenging gas separation.

Figure 11 sheds light on the pore-filling mechanisms of equimolar C_2H_2/CO_2 mixture in Fe-MOF-74. The figure shows the adsorption sites of acetylene (in red) and carbon dioxide (in blue) for medium and high loadings (at 103 kPa and 105 kPa, respectively). The higher affinity of the alkyne to the exposed Fe's compared to carbon dioxide due to the *pi* interaction leads to its relatively more favorable adsorption around the metal, which explains the fast adsorption of acetylene. Once the available high-energy sites are bound by acetylene molecule, carbon dioxide adsorption occurs in the pore channels. This pore filling seems to be mainly governed by electrostatic interactions (Figure 7). When adsorbates form a dense phase within the pores (high pressure of 10^5 kPa), the uptakes of carbon dioxide are comparable to those of acetylene (Figure 9). Acetylene is partially excluded by carbon dioxide and it is almost located around the metal centers, while carbon dioxide is located in the bilayer surrounding the metals and in the channel center. As above mentioned, the density of carbon dioxide is twice than that for acetylene in liquid phase, the high difference in density leads to the inversion of the uptakes at high pressures by condensation.

CONCLUSIONS

We investigate the performance of a number of Metal-Organic Frameworks for acetylene separation from methane and from carbon dioxide. Our results on volumetric and calorimetric adsorption of pure components, and on binding geometries, agree with available experimental data. Classical simulations and the models

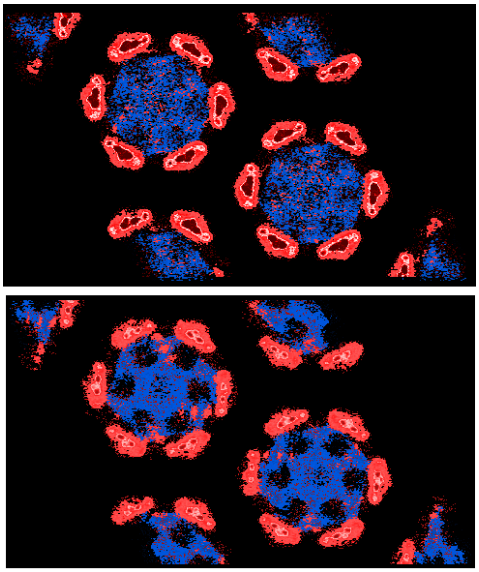

Figure 11. Adsorption sites of carbon dioxide (blue) and acetylene (red) corresponding to adsorption of the equimolar binary mixture in Fe-MOF-74 at 10^3 kPa (top) and 10^5 kPa (bottom) in Fe-MOF-74 at 298 K.

developed in this work proved suitable to characterize the gas-surface interactions, even those that form *pi*-complexation or polarizability with the open metal centers. Overall, MOFs with high-energy sites perform better than MOFs with high surface area. Among the MOFs with OMs, we found that Fe-MOF-74 is the best candidate for the separations, with high adsorption selectivity values for both acetylene/methane and acetylene/carbon dioxide gas mixtures. The highest values of selectivity at 298 K correspond to low/room pressure, since acetylene binds to the OMs until all these sites are saturated. The use of Fe-MOF-74 at room conditions (low-cost operational conditions) with the additional advantage of possessesing sufficient surface area to yield significant storage capacities.

Bibliography

[1] Pässler, P.; Hefner, W.; Buckl, K.; Meinass, H.; Meiswinkel, A.; Wernicke, H.-J.; Ebersberg, G.; Müller, R.; Bässler, J.; Behringer, H.; Mayer, D. *Ullmann's Encyclopedia of Industrial Chemistry*; 2011.

[2] Stang, P. J.; Diederich, F. *Modern acetylene chemistry*; John Wiley & Sons, 2008.

[3] Reid, C. R.; Thomas, K. M. *The Journal of Physical Chemistry B* **2001**, *105*, 10619–10629.

[4] Li, Z.; Schweitzer, N. M.; League, A. B.; Bernales, V.; Peters, A. W.; Getsoian, A. â.; Wang, T. C.; Miller, J. T.; Vjunov, A.; Fulton, J. L.; Lercher, J. A.; Cramer, C. J.; Gagliardi, L.; Hupp, J. T.; Farha, O. K. *Journal of the American Chemical Society* **2016**, *138*, 1977–1982.

[5] Zhai, Q.-G.; Bu, X.; Mao, C.; Zhao, X.; Feng, P. *Journal of the American Chemical Society* **2016**, *138*, 2524–2527.

[6] Matsuda, R.; Kitaura, R.; Kitagawa, S.; Kubota, Y.; Belosludov, R. V.; Kobayashi, T. C.; Sakamoto, H.; Chiba, T.; Takata, M.; Kawazoe, Y.; Mita, Y. *Nature* **2005**, *436*, 238–241.

[7] Ma, S.; Zhou, H.-C. *Chemical Communications* **2010**, *46*, 44–53.

[8] Li, J.-R.; Sculley, J.; Zhou, H.-C. *Chemical Reviews* **2012**, *112*, 869–932.

[9] Adil, K.; Belmabkhout, Y.; Pillai, R. S.; Cadiau, A.; Bhatt, P. M.; Assen, A. H.; Maurin, G.; Eddaoudi, M. *Chemical Society Reviews* **2017**, *46*, 3402–3430.

[10] Li, J.-R.; Ma, Y.; McCarthy, M. C.; Sculley, J.; Yu, J.; Jeong, H.-K.; Balbuena, P. B.; Zhou, H.-C. *Coordination Chemistry Reviews* **2011**, *255*, 1791–1823.

[11] Chang, G.; Li, B.; Wang, H.; Hu, T.; Bao, Z.; Chen, B. *Chem. Commun.* **2016**, *52*, 3494–3496.

[12] Lin, R.-B.; Xiang, S.; Xing, H.; Zhou, W.; Chen, B. *Coordination Chemistry Reviews* **2017**,

[13] Fan, W.; Wang, X.; Liu, X.; Xu, B.; Zhang, X.; Wang, W.; Wang, X.; Wang, Y.; Dai, F.; Yuan, D.; Sun, D. *ACS Sustainable Chemistry & Engineering* **2019**, *7*, 2134–2140.

[14] Zhang, L.; Jiang, K.; Li, Y.; Zhao, D.; Yang, Y.; Cui, Y.; Chen, B.; Qian, G. *Crystal Growth & Design* **2017**, *17*, 2319–2322.

[15] Zhang, L.; Jiang, K.; Yang, Y.; Cui, Y.; Chen, B.; Qian, G. *Journal of Solid State Chemistry* **2017**, *255*, 102–107.

[16] Pang, J.; Jiang, F.; Wu, M.; Liu, C.; Su, K.; Lu, W.; Yuan, D.; Hong, M. *Nature communications* **2015**, *6*, 7575.

[17] Li, P.; He, Y.; Zhao, Y.; Weng, L.; Wang, H.; Krishna, R.; Wu, H.; Zhou, W.; O'Keeffe, M.; Han, Y.; Chen, B. *Angewandte Chemie International Edition* **2015**, *54*, 574–577.

[18] Lin, R.-B.; Li, L.; Wu, H.; Arman, H.; Li, B.; Lin, R.-G.; Zhou, W.; Chen, B. *Journal of the American Chemical Society* **2017**, *139*, 8022–8028.

[19] Xiang, S.; Zhou, W.; Gallegos, J. M.; Liu, Y.; Chen, B. *Journal of the American Chemical Society* **2009**, *131*, 12415–12419.

[20] Xiang, S.; Zhou, W.; Zhang, Z.; Green, M.; Liu, Y.; Chen, B. *Angewandte Chemie International Edition* **2010**, *49*, 4615–4618.

[21] Hou, X.-J.; He, P.; Li, H.; Wang, X. *The Journal of Physical Chemistry C* **2013**, *117*, 2824–2834.

[22] Luna-Triguero, A.; Vicent-Luna, J.; Becker, T.; Vlugt, T.; Dubbeldam, D.; Gómez-Álvarez, P.; Calero, S. *ChemistrySelect* **2017**, *2*.

[23] Luna-Triguero, A.; Vicent-Luna, J.; Poursaeidesfahani, A.; Vlugt, T.; Sánchez-De-Armas, R.; Gómez-Álvarez, P.; Calero, S. *ACS Applied Materials and Interfaces* **2018**, *10*.

[24] Becker, T.; Luna-Triguero, A.; Vicent-Luna, J.; Lin, L.-C.; Dubbeldam, D.; Calero, S.; Vlugt, T. *Physical Chemistry Chemical Physics* **2018**, *20*.

[25] Heinen, J.; Burtch, N. C.; Walton, K. S.; FonsecaâĂĚGuerra, C.; Dubbeldam, D. *Chemistry âĂŞ A European Journal* **2016**, n/a–n/a.

[26] Fischer, M.; Hoffmann, F.; Froba, M. *Chemphyschem* **2010**, *11*, 2220–2229.

[27] Luna-Triguero, A.; Vicent-Luna, J.; Gómez-Álvarez, P.; Calero, S. *Journal of Physical Chemistry C* **2017**, *121*.

[28] Dietzel, P. D. C.; Morita, Y.; Blom, R.; Fjellvåg, H. *Angewandte Chemie* **2005**, *117*, 6512–6516.

[29] Bhattacharjee, S.; Choi, J.-S.; Yang, S.-T.; Choi, S. B.; Kim, J.; Ahn, W.-S. *Journal of Nanoscience and Nanotechnology* **2010**, *10*, 135–141.

[30] Sun, D.; Ma, S.; Simmons, J. M.; Li, J.-R.; Yuan, D.; Zhou, H.-C. *Chem. Commun.* **2010**, *46*, 1329–1331.

[31] Li, H.; Eddaoudi, M.; O'Keeffe, M.; Yaghi, O. M. *Nature* **1999**, *402*, 276.

[32] Eddaoudi, M.; Kim, J.; Rosi, N.; Vodak, D.; Wachter, J.; O'Keeffe, M.; Yaghi, O. M. *Science* **2002**, *295*, 469–472.

[33] Liu, H. M.; He, Y. B.; Jiao, J. J.; Bai, D. J.; Chen, L.; Krishna, R.; Chen, B. L. *Chemistry-a European Journal* **2016**, *22*, 14988–14997.

[34] Robinson, D. B.; Peng, D.-Y.; Chung, S. Y. K. *Fluid Phase Equilibria* **1985**, *24*, 25–41.

[35] Dubbeldam, D.; Torres-Knoop, A.; Walton, K. S. *Molecular Simulation* **2013**, *39*, 1253–1292.

[36] Dubbeldam, D.; Calero, S.; Ellis, D. E.; Snurr, R. Q. *Molecular Simulation* **2015**, *42*, 81–101.

[37] Baker, J. *Journal of Computational Chemistry* **1986**, *7*, 385–395.

[38] Mayo, S. L.; Olafson, B. D.; Goddard, W. A. *Journal of Physical Chemistry* **1990**, *94*, 8897–8909.

[39] Rappe, A. K.; Casewit, C. J.; Colwell, K. S.; Goddard, W. A.; Skiff, W. M. *Journal of the American Chemical Society* **1992**, *114*, 10024–10035.

[40] Potoff, J. J.; Siepmann, J. I. *AIChE Journal* **2001**, *47*, 1676–1682.

[41] Harris, J. G.; Yung, K. H. *Journal of Physical Chemistry* **1995**, *99*, 12021–12024.

[42] Wilmer, C.; Kim, K. C.; Snurr, R. Q. *The Journal of Physical Chemistry Letters* **2012**, *3*, 2506–2511.

[43] Castillo, J. M.; Vlugt, T. J. H.; Calero, S. *Journal of Physical Chemistry C* **2008**, *112*, 15934–15939.

[44] Dubbeldam, D.; Frost, H.; Walton, K. S.; Snurr, R. Q. *Fluid Phase Equilibria* **2007**, *261*, 152–161.

[45] Simmons, J. M.; Wu, H.; Zhou, W.; Yildirim, T. *Energy & Environmental Science* **2011**, *4*, 2177–2185.

[46] Queen, W. L.; Hudson, M. R.; Bloch, E. D.; Mason, J. A.; Gonzalez, M. I.; Lee, J. S.; Gygi, D.; Howe, J. D.; Lee, K.; Darwish, T. A. *Chemical Science* **2014**, *5*, 4569–4581.

[47] Bloch, E. D.; Queen, W. L.; Krishna, R.; Zadrozny, J. M.; Brown, C. M.; Long, J. R. *Science* **2012**, *335*, 1606–1610.

[48] Mason, J. A.; Veenstra, M.; Long, J. R. *Chemical Science* **2014**, *5*, 32–51.

CHAPTER 10

CONCLUSIONS

- The first part of this thesis, comprising chapters 2 and 3, deals with the performance of pure silica zeolites in the adsorption and separation of saturated/unsaturated hydrocarbons and hydrocarbon isomers. Since the chemical composition of the considered zeolites is the same (oxygen and silicon), it is the effect of zeolite topology and pore sizes which is examined to this end. The main conclusions in this regard follow:

  1. The zeolite topology exerts an important influence in the Henry coefficients and heats of adsorption of saturated and unsaturated linear hydrocarbons. While isosteric heats of adsorption of hydrocarbons linearly increases with the chain length in channel-like zeolites, the trend for α-olefins in cage-like zeolites evidences, similarly to paraffins, window effects. This shape selectivity is however found to become weaker for either olefins with the double bound located at intermediate positions or diolefins, due to the less conformational freedom of these molecules.

  2. The non-monotonic linear trend of the Henry coefficients as a function of the chain lenght can be exploited for separation purposes. The ideal adsorption selectivity shows that the window effect allows olefin/paraffin and olefin/olefin separations for linear hydrocarbons with chain lenghts conmmesurate with the cage size of the zeolites.

  3. The zeolite topology and pore sizes are also key for the separation of linear and branched hydrocarbon isomers. There are two main processes that are exploited to perform gas separations using porous materials: The first mechanism is controlled by the preferential equilibrated uptake of the adsorbent

for one species relative to another; the second is accomplished due to great differences in diffusion coefficients of the mixture of components through the pore. By assessing for a set of selected zeolites the adsorption of the gas mixture and the dynamics for hexane isomers, a stepped separation process was proposed. Self-diffusion coefficients of n-hexane were found relatively higher, and therefore it can be kinetically isolated from the mixture. In particular, OBW zeolite could potentially operate as a molecular sieve for separating n-hexane. The bulky 2,2-dimethylbutane can be excluded using zeolites with narrow pores (SFS). The remaining components showed similar kinetic behavior, but some zeolite topologies (BEA, SFE, SSY) were found significantly selective to separate 2,3-dimethylbutane based on equilibrium adsorption.

- The study of alkane/alkene adsorption-based separation is extended to MOFs with open metal sites in the second block of this thesis, which comprises chapters 4-6. The main conclusions follow:

4. Generic force fields combined with usual mixing rules to define host-guest interactions fail in reproducing the pure adsorption isotherms of olefins in MOFs with exposed metals. The parametrization of these cross interactions appears then needed, and was successfully developed and validated based on available experimental data at various thermodynamic conditions.

5. Because of the nature of the models and the procedure followed to develop the cross host-guest parameters, they were proved transferable to longer hydrocarbons.

6. The equimolar olefin/paraffin mixtures reveal that the π-complexation between the double bond and the metal of the studied MOFs plays a fundamental role in the separation of the constituents. In all the studied cases the olefin is adsorbed over the paraffin.

7. As relevant example of MOFs with open metal sites, various members of the M-MOF-74 series were examined. Although their adsorption capacities were obtained similar, since this property is mainly determined by the pore volume,

the alkane/alkene adsorption selectivity was found strongly dependent on the nature of the metallic cluster. Fe and Mn-MOF-74 showed the best separation performance.

8. The consistency of our computational adsorption study of isobutane and isobutene in Cu-BTC MOF with experimental data evidences the suitability of specific parametrization for host-guest interactions also for branched hydrocarbons.

9. Cu-BTC is found able to selectively retained olefins over paraffins for linear hydrocarbons from C2 to C5 chains and for isobutane/isobutene mixture. This separation performance is especially remarkable for the branched C4 mixture, with the highest adsorption selectivity throughout the pressure range. Among the alkane/alkene mixtures of linear hydrocarbons, the adsorption selectivity decreases with preassure and the studied mixtures show similar separation at ambient conditions.

10. The separation capability of MOFs with open metal sites can also be exploited for diolefin/olefin separations. The diolefin, 1,3-butadiene, shows the highest affinity with the metal center.

11. The specific interaction of the open metal centers of the MOF with the double bond of the olefins is also affected by the molecular geometry, which allowed the separation of butene isomers in Fe-MOF-74. This is due to the kinetic diameter of the molecules and to the second preferential adsorption sites within the MOF.

- The third block of this thesis, comprising chapters 7-9, deals with the adsorption-based separation of light gases. The main conclusions follow:

12. The study of more than 200 pure silica zeolites for competitive adsorption of light saturated and unsaturated hydrocarbons evidences that, in general, these porous materials are unsuitable for the separation.

13. To achieve olefin/paraffin separation using zeolites, it is needed the use aluminosilicates with extra-framework cations that interact strongly with the olefins. Divalent cations, Ca^{2+} in this case, show stronger affinity due to the formation of π-bond with the olefins and allowing better separation performance that aluminosilicates with Na^{+} extra-framework cations.

14. To reproduce the adsorption of olefins in aluminosilicates, point charged models for adsorbates are required. These models in combination with an appropiate force field allow to reproduce also the binding geometries obtained with DFT calculations.

15. Unlike for paraffins, geometrical optimization of the aluminosilicates was demonstrated crucial for olefin adsorption, due to their more reactive nature.

16. Framework flexibility plays an important role in adsorption-based separations. Therefore, the prediction of the separations in flexible materials should not be estimated using ideal adsorption solution theory.

17. The knowledge of adsorption mechanisms and structural behavior is necessary to make accurate predictions of mixtures separation. Molecular simulation can complement the experimental work and lead to improve the prediction of separation in flexible MOFs for practical applications.

18. The specific interaction of MOFs with open metal sites with alkenes and alkynes allow to performe challenging separations such as C_2H_2/CO_2, which are molecules with similar sizes and shapes, as well as with similar physical properties.

19. As for alkenes, generic force fields combined usual mixing rules were found unsuitable to account for the interactions of alkynes, in particular acetylene, with MOFs with open metal sites. Host-guest interactions were parametrized according to available experimental data.

20. The use of full atom and charged models for carbon dioxide and acetylene in conjunction with the developed specific host-guest interactions for the latter, allowed an accurate description of the CO_2/C_2H_2 in MOFs with OMs.

The following properties were satisfactorily predicted: 1) pure adsorption isotherms; 2) heats of adsorption; 3) energies of adsorption; and 4) binding geometries.

Overall, molecular simulations has been proven a useful tool to complement experimental adsorption data in the field. Apart from allowing the prediction of multi-component mixtures, which is often experimentally challenging, it allows to understand the microscopic mechanisms governing the adsorption behavior of olefins and paraffins.

Resumen y Conclusiones
(Summary and conclusions in Spanish)

En esta tesis se estudia la adsorción y separación de alcanos, alquenos y alquinos en materiales porosos para aplicaciones industriales. La separación de mezclas de gases para el uso de los diferentes componentes como materiales en la industria química continua siendo un reto a día de hoy. El proceso más extendido es la destilación criogénica. Este método de separación es muy costoso en términos energéticos debido a las condiciones operacionales. Puesto que esta basado en la diferencia en los puntos de ebullición de los gases de la mezcla, es ineficiente para la separación de gases con propiedades físico-químicas similares, cómo en el caso que nos ocupa. Una de las alternativas más prometedoras a la destilación es la separación por adsorción en materiales porosos, ya que es más eficiente energéticamente, y aprovecha las pequeñas diferencias de los componentes ya sean cinéticas y/o temodinámicas para conseguir la separación. A lo largo de la tesis se estudian la adsorción y separación de distintas mezclas en estado gaseoso, alcano/alcano, alcano/alqueno, alqueno/alqueno, alqueno/alquino utilizando técnicas avanzadas de simulación molecular. Para conseguir separar compuestos muy similares entre sí, la elección del material es un punto clave que garantiza que la eficiencia y el diseño de los procesos sea realista. Durante la tesis se estudian y analizan una gran cantidad de materiales y sus propiedades con el fin de determinar las características que debe reunir un material para poder separar de forma eficiente una mezcla dada. En estos términos se estudian: la topología, la composición, la capacidad para adsorber cierto gas, la flexibilidad estructural inducida por el adsorbato, la difusión de las moleculas en el interior del material y las configuraciones más estables (y por lo tanto más probables) en condiciones conocidas, entre otras. Los distintos capítulos de esta tesis se pueden agrupar en tres bloques diferenciados de acuerdo al los sistemas que en ellos se estudia: 1) Adsorción y separación de isomeros de hidrocarburos utilizando zeolitas pura sílice; 2) Uso de estructuras organometálicas, MOFs por sus siglas en inglés, con metales expuestos para la separación de olefinas/parafinas; 3) Mecanismos de adsorción de gases

pequeños para aplicaciones en separación. A continuación se resume brevemente cada uno de los bloques y los capítulos que los conforman.

Adsorción y separación de isómeros de hidrocarburos utilizando zeolitas pura sílice. Capítulos 2 y 3.

En el capítulo 2 se estudia el efecto de la topología de las zeolitas en las energías y entropía de adsorción y en los coeficientes de Henry en hidrocarburos lineales. Se estudian cuatro zeolitas, tres de ellas con topología tipo caja, CHA, ERI e ITQ-29, y una zeolita con canales unidimensionales a modo de control, OFF. En este capítulo se evalúan las distintas magnitudes en función de la longitud de la cadena. Se analizan no sólo los efectos producidos por los alcanos, sino también el de los isómeros de alquenos con el doble enlace en distintas posiciones, y el de los 1,4-dienos. En base a lo obtenido, se estima la capacidad de separación de las distintas estructuras en base a la selectividad ideal de los distintos pares con la misma longitud de cadena.

En el capítulo 3 se realiza un extenso estudio en un gran número de zeolitas con el fin de evaluar su capacidad para la separación de isómeros del hexano que se encuentran en una mezcla equimolar. Se llevan a cabo simulaciones de isotermas de adsorción mono y multicomponente a una temperatura de 433 K. Se realizan simulaciones por dinámica molecular (MD) para obtener las propiedades de transporte de los componentes (difusión) utilizando como punto de partida la configuración en el equilibro en presión de saturación. Todo esto con el propósito de diseñar un proceso de separación por pasos para los isómeros del hexano.

Las principales conclusiones que se pueden extraer de los resultados obtenidos en este bloque son:
La topoloía de la zeolita ejerce una gran influencia en los coeficientes de Henry y el calor de adsorción tanto en hidrocarburos saturados como en insaturados. Concretamente, el calor de adsorción en función de la longitud de cadena de alcanos lineales, muestra un efecto conocido como efecto ventana. Este mismo comportamiento se observa en alquenos con el doble enlace en la primera posición, mientras que se atenúa o incluso desaparece cuando el doble enlace se sitúa en posiciones intermedias en la molécula así como para los dienos. Esto se debe a la perdida de grados de libertad de las moléculas en comparación con sus análogas.
El crecimiento no lineal de los coeficientes de Henry en función de la longitud de la cadena se puede explotar con fines de separación. Los resultados obtenidos para la

selectividad ideal predicen que el efecto ventana permite la separación de olefinas de parafinas y de isómeros de olefinas cuyos tamaños sean similares a los de las cajas de la zeolita.

La topología de la zeolita es también clave para la separación de isómeros del hexano. Es posible diseñar un proceso de separación en base a la adsorción y al coeficiente de difusión de los componentes en las distintas zeolitas. En general el hexano muestra mayores coeficientes de difusión que los demás isómeros, por lo que puede ser separado cinéticamente de ellos. Por otra parte, el 2,2-dimetilbutano puede ser fácilmente separado con zeolitas de poros estrechos debido a su tamaño. Los tres isómeros restantes presentan, en general, difusiones similares, pero algunas zeolitas mustran la habilidad de separar el 2,3-dimetilbutano de la mezcla, siendo éste el isómero con mayor octanaje, y por ende el más deseado.

Uso de MOFs con metales expuestos para la separación de olefinas/parafinas. Capítulos 4, 5 y 6.

En los capítulos 4 y 5 se estudian la adsorción y separación de olefina/parafina con dos y tres átomos de carbono (C2, C3) en diversos MOFs con metales expuestos, M-MOF-74 (con M=Co, Fe, Mn y Ni) y Cu-BTC. Los campos de fuerza genéricos no són capaces de reproducir la adsorción de olefinas en este tipo de MOFs debido a la interacción específica de los dobles enlaces con los centros metálicos. Por ello se desarrollan un conjunto de parámetros para las interacciones adsorbato-adsorbente utilizando un ajuste a los valores experimentales. Utilizando estas interacciones específicas se llevan a cabo simulaciones de isotermas de adsorción equimolares de etano/eteno y propano/propeno con el fin de predecir la separación de las mismas. Para el análisis de la separación, se calcula la selectividad de adsorción en función de la presión. En el capítulo 4 también se estudia la selectividad para diferentes composiciones de la mezcla inicial a unas condiciones de presión y temperatura fijas. Siguiendo el mismo procedimiento, en el capítulo 5 se extiende el estudio en el Cu-BTC a hidrocarburos de cadena más larga (C2-C5). Además se desarroyan parámetros para el potencial Lennard-Jones con objeto de obtener la adsorción de los hidrocarbuos ramificados, isobutano e isobuteno.

Utilizando los parámetros desarrollados en los capítulos 4 y 5, en el capítulo 6 se estudia la capcidad de los MOFs con centros metálicos expuestos para separar los isómeros lineales del buteno y el 1,3-butadieno de una mezcla. Con el fin de estudiar los mecanismos de adsorción se computan las isotermas de adsorción monocomponente así como los calores de adsorción. Se calculan las isotermas de adsorción multicomponete en los

MOF, ZJNU-30, Co-, Fe-MOF-74, Cu-BTC y en la zeolita pura silice RRO. Se diseña un proceso realista de purificación basado en separación por adsorción partiendo de la mezcla equimolar de cuatro componentes.

A partir de los resultados de este bloque, se llega a las siguientes conclusiones:
Puesto que los campos de fuerza genéricos no reproducen la adsorción de olefinas en MOFs con metales expuestos, la parametrización de las interacciones adsorbato-adsorbente son una buena solución ya que son capaces de reproducir de forma sencilla y con exactitud las isotermas de adsorción en dichos sistemas sin la necesidad de añadir métodos más complejos, lo que conllevaría un aumento del tiempo de simulación. Además de ser una aproximación sencilla, la forma en la que se desarrollan estos campos de fuerza hace que sean transferibles a hidrocarburos de cadena más larga.
Las separaciones equimolares de olefinas/parafinas, revelan que el enlace covalente formado por el doble enlace y el centro metálico de los MOFs estudiados juegan un papel fundamental en la separación de los componentes. En todos los casos se adsorben de forma preferente las olefinas frente a las parafinas.
Aunque los M-MOF-74 presentan una capacidad similar tanto para los alcanos como para los alquenos, la selectividad de adsorción está fuertemente influenciada por la naturaleza del metal. El Fe- y el Mn-MOF-74 resultan ser los mejores candidatos para la separación etano/eteno y propano/propeno.
La parametrización de las interacciones cruzadas demuestra dar buen resultado también para los hidrocarburos ramificados, reproduciendo la adsorción experimental en el Cu-BTC. En vista de los resultados de las mezclas binarias, este MOF es capaz de separar olefinas de parafinas. Muestra una selectividad de en torno a 3 para todos los pares en condiciones ambiente, aunque se predice una mejor separación de la mezcla isobutano/isobuteno en todo el rango de presiones.
La capacidad de separación de los MOFs con centros metálicos expuestos se puede explotar para la separación de olefinas/diolefinas, debido a que el 1,3-butadieno muestra una afinidad mayor con el metal. La interacción específica del metal con el doble enlace se ve afectada por la geometría de la molécula lo que permite la separación de los isómeros del buteno debido a dos principales factores: 1) el diámetro cinético de las moléculas y 2) la aparición de un segundo sitio preferente de adsorción en el Fe-MOF-74.

Mecanismos de adsorción de gases pequeños para aplicaciones en separación. Capítulos 7, 8 y 9.

En el capítulo 7 se crean las estructuras de los aluminosilicatos con topología LTA y

FAU con varias composiciones siguiendo un procedimiento por pasos. Se optimizan las celdas de las diferentes zeolitas incluyendo los cationes y se analiza la influencia de la minimización de las estructuras en la reproducción de las isotermas de adsorción experimentales. Se desarrollan un conjunto de parámetros para describir la interacción entre el doble enlace de las olefinas y los cationes de las zeolitas. Con estos parámetros se computan las adsorciones de mezcla en aluminosilicatos con distintas composiciones con el fin de analizar el efecto de la naturaleza y la cantidad de cationes de las zeolitas y su influencia en la separación de olefinas de parafinas.

En el capítulo 8 se realiza un estudio estructural del MOF de zirconio, ZJU-198. Se encuentra una transición de fase en este MOF inducida por los adsorbatos. Esta flexibilidad estructural es la causa de la separación de gases ligeros de tamaño similar. El estudio muestra que el acetileno, el dióxido de carbono y el eteno son capaces de inducir un fenómeno de respiración en el ZJU-198, permitiendo que estos gases se adsorban de manera preferente sobre aquellos que no son capaces de producir el cambio de fase estructural; el nitrógeno y el metano.

En el capítulo 9 se investiga la separación de dióxido de carbono, acetileno y metano en diferentes MOFs. La separación C_2H_2/CO_2 es particularmente costosa debido a que, tanto el tamaño como las propiedades físico-químicas de estas moléculas, son muy similares. Exploramos la capacidad de separación de MOFs con y sin metales expuestos así como los mecanismos de adsorción de las isotermas mono y multicomponente, las energías de adsorción y las configuraciones más estables de las moléculas en los poros de las estructuras.

Las conclusiones más relevantes de este bloque son:
Del extenso estudio en más de 200 topologías se concluye que, excepto casos muy particulares, las zeolitas pura silice no son buenas candidatas para la separación de olefinas/parafinas. Para conseguir este proposito es necesario utilizar aluminosilicatos ya que los cationes de estas estructuras interaccionan más fuertemente con los dobles enlaces de las olefinas. Los cationes divalentes, Ca^{2+} en este caso, muestran una mayor afinidad por las olefinas y por lo tanto se predice una mejor separación con las zeolitas con cationes de calcio que la que se obtiene para aluminosilicatos con cationes de sodio. Para reproducir la adsorción de las olefinas en zeolitas con cationes es necesario utilizar modelos con cargas para estos adsorbatos. La combinación de estos modelos con el campo de fuerza apropiado permiten reproducir también las geometrias obtenidas con cálculos DFT. La optimización de la geometría de las estructuras demuestra ser un punto crucial

en la reproducción de la adsorción de las olefinas, mientras que la influencia de ésta en la adsorción de las parafinas es prácticamente nula.

La flexibilidad estructural juega un papel importante el la predicción de la separación, por ello no es recomendable estimarla utilizando métodos que no tienen en cuenta la movilidad de la estructura y/o la interacción entre los adsorbatos como por ejemplo IAST (ideal adsorption solution theory). Para conseguir predicciones exactas es necesario conocer los mecanismos de adsorción y el comportamiento estructural. En ese sentido, la simulación molecular puede complementar los resultados experimentales y mejorar la predicción de la separación de mezclas que contienen olefinas y parafinas.

Las interacciones específicas de los MOFs con metales expuestos con los dobles y triples enlaces de alquenos y alquinos permite la separación de mezclas de otro modo costosas de conseguir como C_2H_2/CO_2. Como en el caso de las olefinas, es necesario desarrollar conjuntos de parámetros cruzados específicos para la interacción acetileno-centro metálico. El uso de modelos con cargas para el acetileno y el dióxido de carbono y de interacciones específicas cuando sea necesario permite una descripción fiel de los sistemas y permite predecir: 1) isotemas de adsorción; 2) energías de adsorción y 3) geometría preferente de las moléculas en las cavidades de los MOFs. Todo esto garantiza una predicción certera de las separaciones de alcanos, alquenos y alquinos con materiales porosos cristalinos.

Appendix 1

Understanding and Exploiting Window Effects for Adsorption and Separations of Hydrocarbons

Table A1.1 Lennard-Jones parameters used in this work. σ_{ij} in Å and $\frac{\varepsilon_{ij}}{k_B}$ in K.

	O		$CH_3\_sp_3$		$CH_2\_sp_3$		$CH_2\_sp_2$		CH_sp_2	
	σ_{ij}	ε_{ij}	σ_{ij}	ε_{ij}	σ_{ij}	ε_{ij}	σ_{ij}	ε_{ij}	σ_{ij}	ε_{ij}
$CH_3\_sp_3$	3.48	93	3.76	108	3.86	77.77	3.72	100.22	3.75	75.66
$CH_2\_sp_3$	3.58	60.5	3.86	77.77	3.96	56	3.82	72.17	3.85	54.48
$CH_2\_sp_2$	3.53	82.05	3.72	100.22	3.82	72.17	3.685	93	3.71	70.21
CH_sp_2	3.502	55.215	3.75	75.66	3.85	54.48	3.71	70.21	3.74	53

The intramolecular interaction is defined as::

$$U^{intra} = U^{bond} + U^{bend} + U^{torsion}$$

In all the cases, the subscripts x and y in CH_x and CH_y are x =2 or 3; y =1 or 2

$$U^{bond} = \frac{1}{2} k_1 (r - r_0)^2$$

$$\begin{aligned}
&CH_x - CH_x;\ \frac{k_1}{k_B} = 96500\ \frac{K}{\text{Å}};\ r_0 = 1.54\ \text{Å} \\
&CH_CH_x;\ \frac{k_1}{k_B} = 321171.55\ \frac{K}{\text{Å}};\ r_0 = 1.495\ \text{Å} \\
&CH_2 = CH_y;\ \frac{k_1}{k_B} = 96500\ \frac{K}{\text{Å}};\ r_0 = 1.33\ \text{Å} \\
&CH = CH;\ \frac{k_1}{k_B} = 674885.96\ \frac{K}{\text{Å}};\ r_0 = 1.346\ \text{Å}
\end{aligned} \tag{1.1}$$

$$U^{bend} = \frac{1}{2}k_2(\cos\theta - \cos\theta_0)^2$$

$$CH_x - CH_2 - CH_x;\ \frac{k_2}{k_B} = 62500\ \frac{K}{\text{rad}^2};\ \theta_0 = 114$$
$$CH_2 = CH - CH_x;\ \frac{k_2}{k_B} = 70420\ \frac{K}{\text{rad}^2};\ \theta_0 = 119.7$$
$$CH = CH - CH_x;\ \frac{k_2}{k_B} = 22008.11\ \frac{K}{\text{rad}^2};\ \theta_0 = 125.5$$

$$U^{torsion} = p_0 + p_1[1 + \cos\phi_{ijkl}] + p_2[1 - \cos 2\phi_{ijkl}] + p_3[1 + \cos 3\phi_{ijkl}]$$

$$CH_x - CH_2 - CH_2 - CH_x;\ \frac{p_0}{k_B} = 0.0\,K;\ \frac{p_1}{k_B} = 335.03\,K;\ \frac{p_2}{k_B} = -68.19\,K;\ \frac{p_3}{k_B} = 791.32\,K$$
$$CH_y = CH - CH_2 - CH_x;\ \frac{p_0}{k_B} = 685.96\,K;\ \frac{p_1}{k_B} = 86.31\,K;\ \frac{p_2}{k_B} = -109.71\,K;\ \frac{p_3}{k_B} = 282.08\,K$$

$$U^{torsion} = c_0[1 + (\cos c_1\phi_{ijkl} - c_2)]$$

$$CH_x - CH = CH - CH_x;\ \frac{c_0}{k_B} = 2364.27\,K;\ c_1 = -2;\ c_2 = 189$$

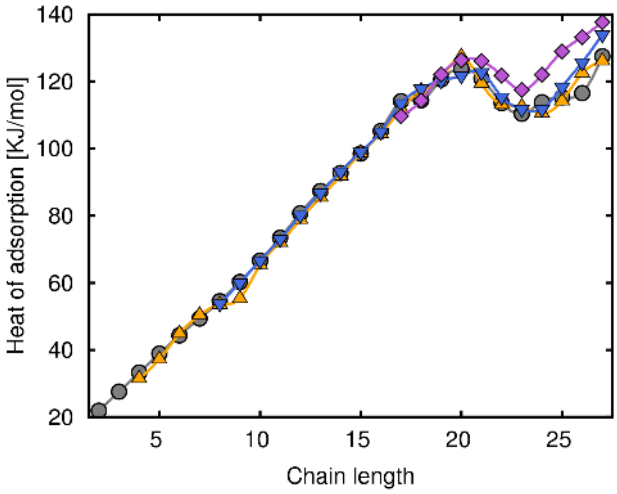

Figure A1.1 Heats of adsorption as a function of the chain length for alkanes (grey symbols) and their respective alkenes with the double bond located in position 2 (yellow symbols), position 4 (blue symbols), and at every four carbon atoms (pink symbols) in ITQ-29 zeolites at 600 K.

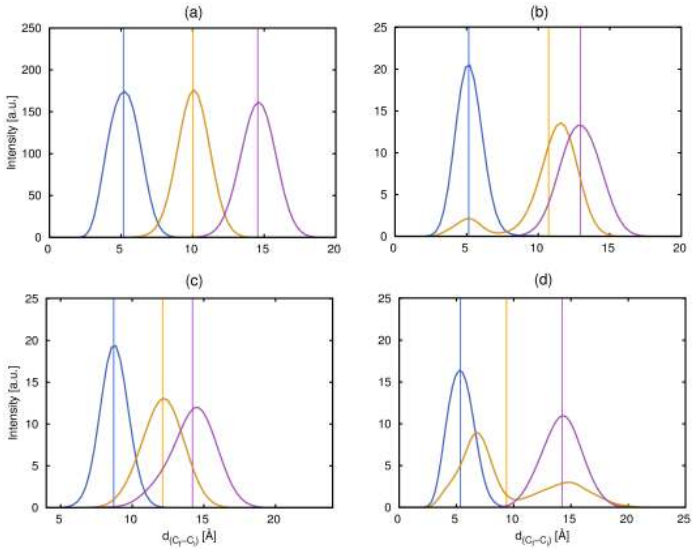

Figure A1.2 Distribution of the distance value along the time between the extreme carbon atoms of alkanes with a short chain (blue), a chain commensurating with the framework cage (yellow), and a larger chain (violet) in a) OFF, b) CHA, c) ERI, and d) ITQ-29 zeolites.

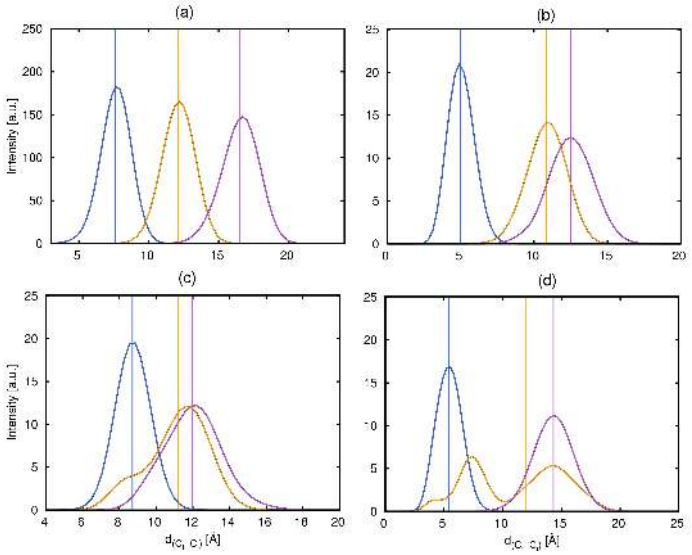

Figure A1.3 Distribution of the distance value along the time between the extreme carbon atoms of 4-alkenes with a short chain (blue), a chain commensurating with the framework cage (yellow), and a larger chain (violet) in a) OFF, b) CHA, c) ERI, and d) ITQ-29 zeolites.

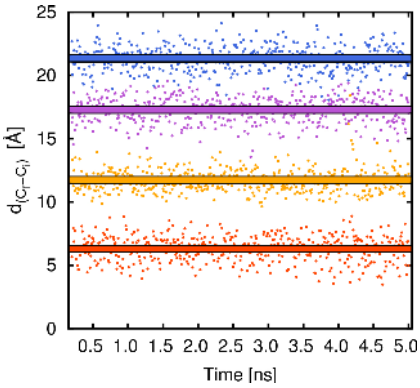

Figure A1.4 Distance between the extreme carbon atoms as a function of the simulation time for a 2-alkene of 20 carbon atoms in OFF (blue), CHA (yellow), ERI (violet) and ITQ-29 (red) zeolites

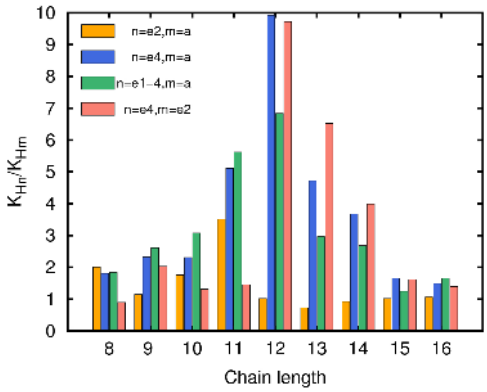

Figure A1.5 Selectivity at low coverage from Henry coefficients plotted against the chain length for 4-alkene/alkane separation in OFF, CHA, ERI and ITQ-29 zeolites at 600 K.

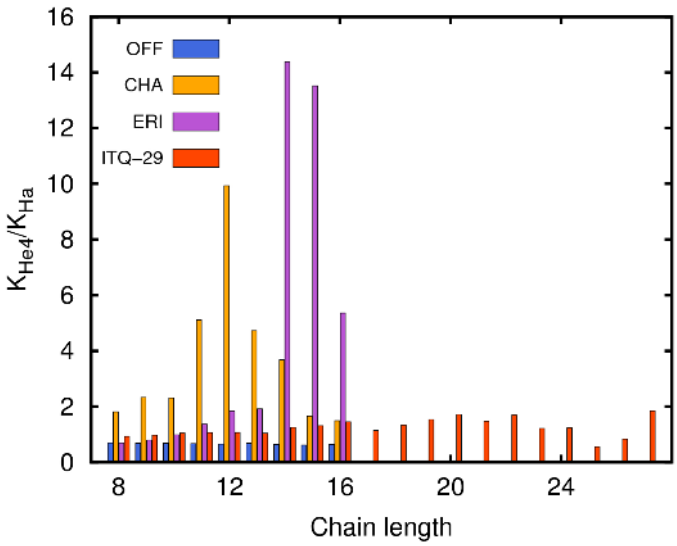

Figure A1.6 Selectivity at low coverage from Henry coefficients plotted against the chain length for various adsorbate pairs in CHA zeolite at 600 K. Nomenclature used for the hydrocarbons: alkane (a), alkenes with double bond at position 2 (e2), position 4 (e4), and positions 2 and 4 (e1-4).

Table A1.2 Energies, enthalpies, and entropies of adsorption at zero coverage at 600 K for alkanes in OFF, CHA, ERI, and ITQ-29 zeolites.

OFF

Chain lenght	$-\Delta U$ $[kJ/mol]$	$-\Delta H$ $[kJ/mol]$	$-\Delta S$ $[J/K/mol]$
2	23.33	28.32	38.88
3	29.52	34.51	49.19
4	33.58	38.57	55.95
5	40.71	45.69	67.83
6	48.36	53.35	80.60
7	55.89	60.88	93.14
8	63.45	68.43	105.73
9	70.78	75.77	117.95
10	78.19	83.18	130.30
11	86.16	91.15	143.57
12	93.06	98.05	155.07
13	100.74	105.72	167.86
14	108.57	113.55	180.91
15	116.00	120.99	193.31
16	123.17	128.15	205.24

CHA

Chain lenght	$-\Delta U$ $[kJ/mol]$	$-\Delta H$ $[kJ/mol]$	$-\Delta S$ $[J/K/mol]$
2	20.39	25.38	33.99
3	27.53	32.52	45.88
4	33.79	38.77	56.30
5	41.31	46.30	68.84
6	48.09	53.08	80.14
7	52.22	57.20	87.02
8	55.71	60.70	92.85
9	58.21	63.20	97.02
10	58.23	63.22	97.06
11	49.52	54.51	82.55
12	43.14	48.13	71.92
13	49.61	54.60	82.72
14	54.59	59.58	91.01
15	60.11	65.10	100.21
16	65.21	70.20	108.72

ERI

Chain lenght	$-\Delta U$ $[kJ/mol]$	$-\Delta H$ $[kJ/mol]$	$-\Delta S$ $[J/K/mol]$
2	22.47	27.45	37.44
3	30.26	35.25	50.43
4	37.09	42.08	61.83
5	45.25	50.24	75.42
6	53.62	58.61	89.38
7	62.51	67.50	104.20
8	71.66	76.65	119.45
9	77.94	82.93	129.93
10	81.54	86.53	135.93
11	81.03	86.01	135.08
12	80.59	85.58	134.36
13	76.97	81.95	128.32
14	66.62	71.61	111.09
15	68.16	73.15	113.66
16	76.60	81.59	127.73

ITQ-29

Chain lenght	$-\Delta U$ $[kJ/mol]$	$-\Delta H$ $[kJ/mol]$	$-\Delta S$ $[J/K/mol]$
2	16.94	21.93	28.23
3	22.61	27.60	37.68
4	28.33	33.32	47.21
5	33.97	38.96	56.60
6	39.38	44.37	65.62
7	44.42	49.41	74.02
8	49.56	54.55	82.59
9	55.30	60.28	92.14
10	61.62	66.61	102.68
11	68.44	73.42	114.04
12	75.75	80.74	126.24
13	82.39	87.38	137.30
14	87.73	92.72	146.20
15	93.54	98.52	155.88
16	100.27	105.25	167.09
17	109.14	114.12	181.88
18	109.40	114.39	182.33
19	115.61	120.60	192.68
20	118.78	123.77	197.96
21	115.88	120.87	193.13
22	100.56	105.55	167.61
23	105.39	110.38	175.66
24	108.82	113.81	181.37
25	110.27	115.26	183.79
26	111.54	116.53	185.91
27	122.50	127.49	204.16

Table A1.3 Energies, enthalpies, and entropies of adsorption at zero coverage at 600 K for 1-alkenes in OFF, CHA, ERI, and ITQ-29 zeolites.

OFF

Chain lenght	$-\Delta U$ $[kJ/mol]$	$-\Delta H$ $[kJ/mol]$	$-\Delta S$ $[J/K/mol]$
2	21.59	26.58	35.98
3	27.37	32.36	45.61
4	31.85	36.84	53.08
5	35.71	40.70	59.51
6	46.30	51.29	77.16
7	53.93	58.92	89.87
8	61.40	66.38	102.31
9	68.94	73.93	114.88
10	76.31	81.30	127.16
11	83.90	88.89	139.81
12	91.34	96.33	152.21
13	98.58	103.56	164.26
14	106.05	111.03	176.71
15	113.34	118.33	188.86
16	120.76	125.75	201.23

CHA

Chain lenght	$-\Delta U$ $[kJ/mol]$	$-\Delta H$ $[kJ/mol]$	$-\Delta S$ $[J/K/mol]$
2	18.96	23.94	31.59
3	25.51	30.49	42.50
4	32.07	37.06	53.45
5	35.74	40.72	59.55
6	46.44	51.43	77.39
7	50.91	55.90	84.84
8	54.56	59.55	90.93
9	57.40	62.39	95.67
10	57.70	62.69	96.19
11	53.84	58.83	89.75
12	44.92	49.91	74.90
13	47.33	52.32	78.91
14	52.65	57.63	87.77
15	60.12	65.11	100.24
16	59.72	64.71	99.57

ERI

Chain lenght	$-\Delta U$ $[kJ/mol]$	$-\Delta H$ $[kJ/mol]$	$-\Delta S$ $[J/K/mol]$
2	20.90	25.89	34.84
3	28.04	33.03	46.73
4	35.06	40.05	58.42
5	39.54	44.53	65.90
6	51.40	56.39	85.66
7	60.21	65.20	100.34
8	69.39	74.38	115.63
9	76.46	81.45	127.41
10	80.02	85.01	133.35
11	79.93	84.92	133.21
12	78.82	83.81	131.37
13	78.27	83.26	130.47
14	78.46	83.45	130.79
15	70.14	75.13	116.92
16	74.39	79.37	124.00

ITQ-29

Chain lenght	$-\Delta U$ $[kJ/mol]$	$-\Delta H$ $[kJ/mol]$	$-\Delta S$ $[J/K/mol]$
2	15.70	20.69	26.16
3	21.07	26.06	35.11
4	26.80	31.79	44.66
5	29.51	34.50	49.18
6	38.08	43.06	63.45
7	43.26	48.25	72.09
8	48.36	53.35	80.59
9	54.14	59.13	90.21
10	60.30	65.28	100.48
11	66.74	71.73	111.22
12	74.06	79.05	123.42
13	80.61	85.60	134.34
14	87.06	92.05	145.08
15	93.13	98.12	155.19
16	99.49	104.4	8 165.81

Table A1.4 Energies, enthalpies, and entropies of adsorption at zero coverage at 600 K for 2-alkenes in OFF, CHA, ERI, and ITQ-29 zeolites.

OFF

Chain lenght	$-\Delta U$ $[kJ/mol]$	$-\Delta H$ $[kJ/mol]$	$-\Delta S$ $[J/K/mol]$
4	31.69	36.68	52.81
5	38.14	43.13	63.56
6	48.57	53.55	80.93
7	55.96	60.95	93.26
8	63.62	68.61	106.02
9	70.41	75.40	117.33
10	78.39	83.38	130.63
11	85.79	90.78	142.96
12	93.52	98.51	155.85
13	100.71	105.70	167.83
14	108.25	113.23	180.38
15	115.41	120.40	192.32
16	122.75	127.74	204.55

CHA

Chain lenght	$-\Delta U$ $[kJ/mol]$	$-\Delta H$ $[kJ/mol]$	$-\Delta S$ $[J/K/mol]$
4	31.69	36.68	52.81
5	39.06	44.05	65.10
6	48.59	53.57	80.97
7	53.46	58.44	89.08
8	58.16	63.15	96.92
9	60.78	65.77	101.31
10	59.17	64.16	98.63
11	55.52	60.51	92.55
12	45.58	50.57	75.99
13	46.80	51.79	78.03
14	52.97	57.96	88.31
15	60.58	65.57	101.00
16	65.00	69.99	108.37

ERI

Chain lenght	$-\Delta U$ $[kJ/mol]$	$-\Delta H$ $[kJ/mol]$	$-\Delta S$ $[J/K/mol]$
4	34.68	39.67	57.80
5	42.54	47.53	70.89
6	53.83	58.82	89.70
7	62.54	67.53	104.22
8	71.53	76.51	119.19
9	78.94	83.93	131.55
10	83.25	88.24	138.74
11	84.80	89.79	141.32
12	84.14	89.12	140.22
13	81.71	86.70	136.19
14	79.95	84.94	133.27
15	66.53	71.52	110.91
16	71.86	76.85	119.79

ITQ-29

Chain lenght	$-\Delta U$ $[kJ/mol]$	$-\Delta H$ $[kJ/mol]$	$-\Delta S$ $[J/K/mol]$
4	26.49	31.47	44.14
5	32.23	37.22	53.71
6	39.92	44.91	66.52
7	45.41	50.40	75.67
8	48.52	53.51	80.86
9	50.30	55.29	83.84
10	60.40	65.39	100.66
11	67.02	72.01	111.68
12	73.88	78.87	123.12
13	80.47	85.46	134.10
14	86.83	91.82	144.70
15	93.71	98.70	156.17
16	99.40	104.39	165.64
17	106.74	111.73	177.89
18	112.22	117.21	187.02
19	116.00	120.99	193.32
20	122.41	127.40	204.02
21	114.41	119.39	190.68
22	108.12	113.10	180.20
23	107.43	112.42	179.05
24	105.51	110.50	175.85
25	109.18	114.17	181.97
26	117.48	122.46	195.80
27	121.04	126.03	201.73

Table A1.5 Energies, enthalpies, and entropies of adsorption at zero coverage at 600 K for 4-alkenes in OFF, CHA, ERI, and ITQ-29 zeolites.

OFF

Chain lenght	$-\Delta U$ $[kJ/mol]$	$-\Delta H$ $[kJ/mol]$	$-\Delta S$ $[J/K/mol]$
8	60.66	65.64	101.08
9	67.95	72.93	113.23
10	75.46	80.45	125.75
11	82.87	87.86	138.10
12	90.31	95.30	150.50
13	97.83	102.82	163.03
14	105.06	110.05	175.07
15	112.57	117.56	187.58
16	120.19	125.18	200.29

CHA

Chain lenght	$-\Delta U$ $[kJ/mol]$	$-\Delta H$ $[kJ/mol]$	$-\Delta S$ $[J/K/mol]$
8	57.26	62.25	95.43
9	59.91	64.90	99.86
10	59.06	64.05	98.45
11	53.75	58.74	89.61
12	57.55	62.53	95.93
13	59.51	64.50	99.20
14	62.75	67.74	104.61
15	62.57	67.56	104.31
16	67.28	72.27	112.16

ERI

Chain lenght	$-\Delta U$ $[kJ/mol]$	$-\Delta H$ $[kJ/mol]$	$-\Delta S$ $[J/K/mol]$
8	68.30	73.29	113.81
9	75.43	80.41	125.69
10	79.81	84.80	133.00
11	81.70	86.69	136.15
12	81.69	86.68	136.15
13	78.51	83.50	130.86
14	77.51	82.50	129.20
15	85.35	90.34	142.26
16	88.55	93.54	147.60

ITQ-29

Chain lenght	$-\Delta U$ $[kJ/mol]$	$-\Delta H$ $[kJ/mol]$	$-\Delta S$ $[J/K/mol]$
8	48.84	53.83	81.39
9	55.05	60.04	91.74
10	61.64	66.63	102.72
11	68.06	73.05	113.42
12	75.19	80.18	125.29
13	81.80	86.79	136.31
14	88.11	93.10	146.84
15	94.04	99.02	156.71
16	100.02	105.00	166.67
17	108.47	113.46	180.77
18	112.90	117.89	188.15
19	115.32	120.31	192.19
20	116.77	121.76	194.61
21	117.74	122.73	196.23
22	110.39	115.38	183.98
23	106.83	111.82	178.05
24	106.78	111.77	177.97
25	113.41	118.40	189.01
26	120.69	125.68	201.16
27	129.04	134.02	215.06

Table A1.6 Energies, enthalpies, and entropies of adsorption at zero coverage at 600 K for alkenes with double bonds at positions 1 and 4 in CHA and ERI zeolites.

CHA

Chain lenght	$-\Delta U$ $[kJ/mol]$	$-\Delta H$ $[kJ/mol]$	$-\Delta S$ $[J/K/mol]$
6	44.42	49.41	74.02
7	50.75	55.74	84.58
8	56.28	61.27	93.80
9	59.38	64.37	98.97
10	59.58	64.57	99.31
11	56.48	61.47	94.16
12	54.99	59.97	91.66
13	56.07	61.06	93.47
14	61.42	66.40	102.39
15	61.28	66.27	102.16
16	64.93	69.91	108.24

ERI

Chain lenght	$-\Delta U$ $[kJ/mol]$	$-\Delta H$ $[kJ/mol]$	$-\Delta S$ $[J/K/mol]$
6	48.38	53.36	80.61
7	56.71	61.70	94.50
8	65.73	70.72	109.53
9	73.84	78.83	123.05
10	78.59	83.57	130.96
11	81.40	86.39	135.66
12	81.84	86.83	136.40
13	80.38	85.37	133.97
14	81.45	86.44	135.77
15	80.35	85.34	133.93
16	82.11	87.10	136.87

Table A1.7 Energies, enthalpies, and entropies of adsorption at zero coverage at 600 K for alkenes with a double bond every 4 carbon atoms in ITQ-29 zeolite.

ITQ-29

Chain lenght	$-\Delta U$ $[kJ/mol]$	$-\Delta H$ $[kJ/mol]$	$-\Delta S$ $[J/K/mol]$
17	104.68	109.66	174.44
18	109.31	114.30	182.16
19	117.12	122.10	195.18
20	121.37	126.35	202.26
21	121.10	126.09	201.83
22	116.74	121.72	194.55
23	112.52	117.50	187.52
24	117.03	122.02	195.04
25	123.94	128.92	206.55
26	128.20	133.19	213.66
27	132.69	137.68	221.14

Appendix 2

Adsorptive process design for separation of hexane isomers using zeolites

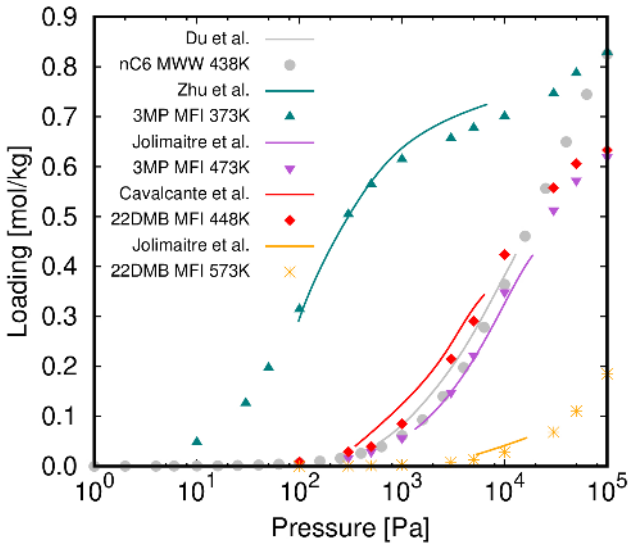

Figure A2.1 Computed adsorption isotherms of hexane isomers in MWW and MFI zeolites compared to available experimental data.[1–5]

Table A2.1 Host-guest and guest-guest Lennard-Jones parameters used in this work. ε/k_B [K] in top row and σ [Å] in bottom row of each field. The parameters are taken from references 6 and 7.

	O	CH_4	CH_3	CH_2	CH	C
CH_4	115	158.5	130.84	94.21	51.91	11.26
	3.47	3.72	3.74	3.84	4.17	4.87
CH_3	93	130.84	108	77.77	42.85	9.3
	3.48	3.74	3.76	3.86	4.19	4.9
CH_2	60.5	94.21	77.77	56	30.85	6.69
	3.58	3.84	3.86	3.96	4.3	5.03
CH	40	51.91	42.85	30.85	17	3.69
	3.92	4.17	4.19	4.3	4.67	5.46
C	10	11.26	9.3	6.69	3.69	0.8
	4.56	4.87	4.9	5.03	5.46	6.38

Blibliography

1 H.W. Du, M. Kalyanaraman, M. A. Camblor and D. H. Olson, Microporous Mesoporous Mater., 2000, 40, 305-312.

2 W. Zhu, F. Kapteijn, B. van der Linden and J. A. Moulijn, Chem. Chem. Phys., 2001, 3, 1755-1761.

3 E. Jolimaitre, M. Tayakout-Fayolle, C: Jallut and K. Ragil, Ind. Eng. Chem. Res., 2001, 40, 914-926.

4 C.L. J. Cavalcante and D. M. Ruthven, Ind. Eng. Chem. Res., 1995, 34, 177-184.

5 E. Jolimaitre, K. Ragil, M. Tayakout-Fayolle and C. Jallut, AIChe J., 2002, 48, 1927-1937.

Appendix 3

Effective Model for Olefin/Paraffin Separation using (Co, Fe, Mn, Ni)-MOF-74

Table A3.1 Set of starting Lennard-Jones cross parameters for the fitting to experimental data. They were calculated from references [1–3] using Lorentz-Berthelot mixing rules. ε_{ij}/k_B in K (top) and σ_{ij} in Å (bottom)

	Guest Pseudoatoms			
	$CH_3\_sp_3$	$CH_2\_sp_3$	$CH_2\_sp_2$	CH_sp_2
O	72.142	51.948	66.945	50.538
	3.397	3.497	3.359	3.387
C	71.895	51.77	66.716	50.364
	3.617	3.717	3.579	3.607
H	28.745	20.698	26.673	20.136
	3.303	3.403	3.266	3.293
Co	27.597	19.872	25.609	19.333
	3.16	3.26	3.122	3.15
Fe	34.555	19.14	24.666	18.621
	3.177	3.277	3.14	3.167
Mn	26.695	19.151	24.679	18.631
	3.199	3.299	3.162	3.189
Ni	28.567	20.57	26.509	20.012
	3.143	3.243	3.105	3.133

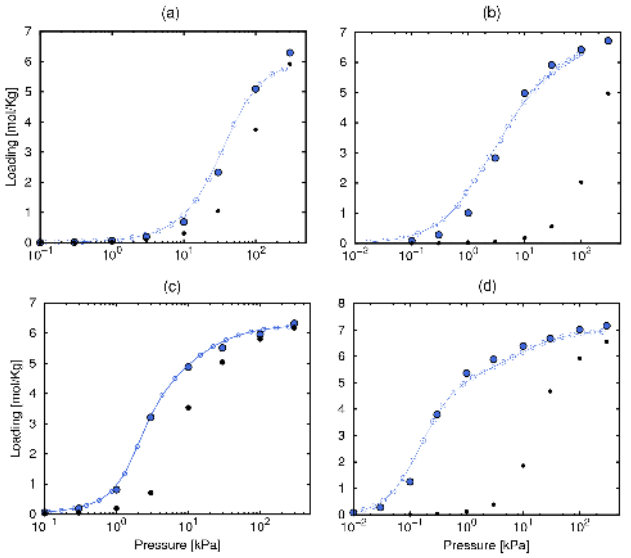

Figure A3.1 Single-component adsorption isotherms of ethane (a), ethene (b), propane (c) and propene (d) in Fe-MOF-74 at 318 K: Experiments (empty symbol),[6] computational data using standard Lorentz-Berthelot mixing rules (small black squares), and using the proposed guest-host force field parametrization (large blue squares).

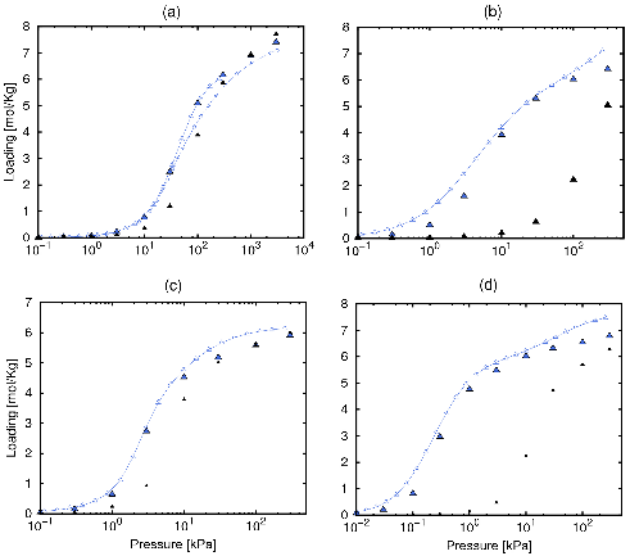

Figure A3.2 Single-component adsorption isotherms of ethane (a), ethene (b), propane (c) and propene (d) in Mn-MOF-74 at 318 K: Experiments (empty symbol),[4] computational data using standard Lorentz-Berthelot mixing rules (small black squares), and using the proposed guest-host force field parametrization (large blue squares).

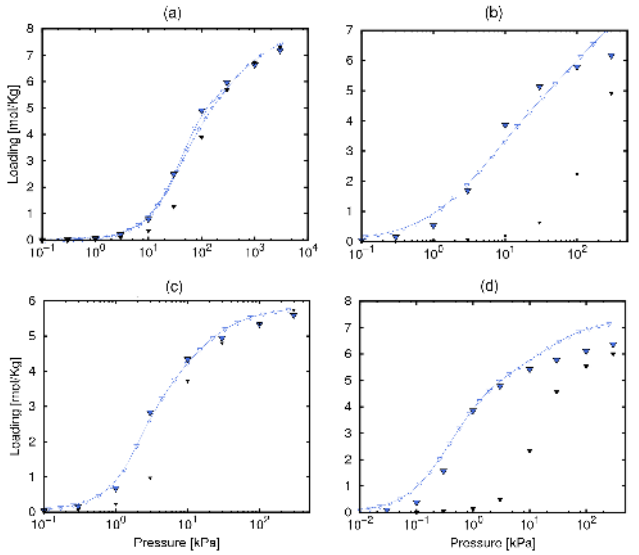

Figure A3.3 Single-component adsorption isotherms of ethane (a), ethene (b), propane (c) and propene (d) in Ni-MOF-74 at 318 K: Experiments (empty symbol),[4] computational data using standard Lorentz-Berthelot mixing rules (small black squares), and using the proposed guest-host force field parametrization (large blue squares).

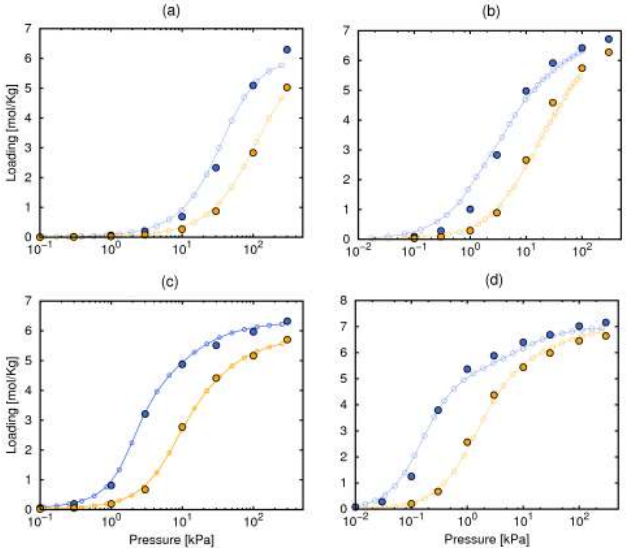

Figure A3.4 Single-component adsorption isotherms of ethane (a), ethene (b), propane (c) and propene (d) in Fe-MOF-74 at 318 K (blue) and 353 K (yellow): Experiments (empty symbol),[1]6 computational using the proposed guest-host force field parametrization (full symbols).

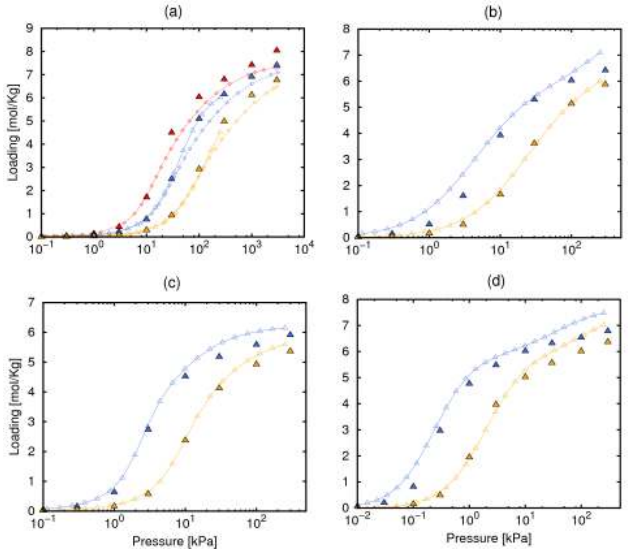

Figure A3.5 Single-component adsorption isotherms of ethane (a), ethene (b), propane (c) and propene (d) in Mn-MOF-74 at 296 K (red), 318 K (blue), 353 K (yellow): Experiments (empty symbol),[4] computational using the proposed guest-host force field parametrization (full symbol). Experimental data for ethane are taken from various sources.[4–7]

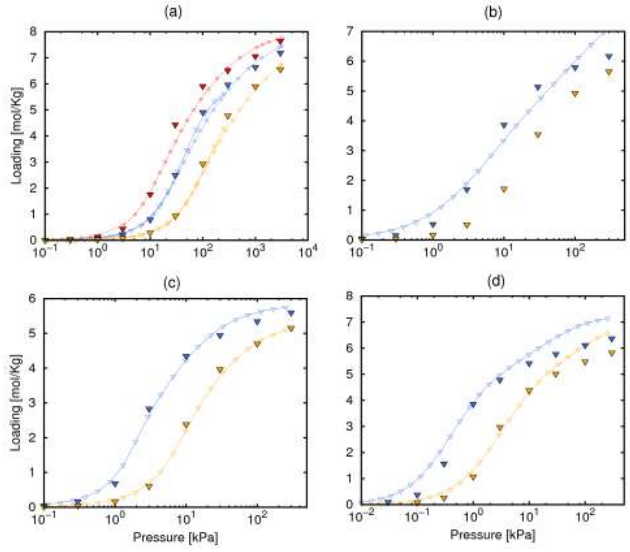

Figure A3.6 Single-component adsorption isotherms of ethane (a), ethene (b), propane (c) and propene (d) in Ni-MOF-74 at 296 K (red), 318 K (blue), 353 K (yellow): Experiments (empty symbol),[4–7] computational using the proposed guest-host force field parametrization (full symbol). Experimental data for ethane are taken from various sources.[4–7]

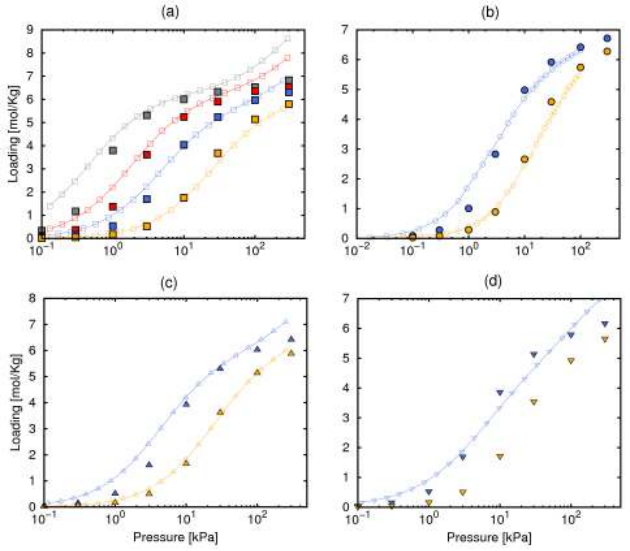

Figure A3.7 Single-component adsorption isotherms of ethene in Co-MOF-74 (a), Fe-MOF-74 (b), Mn- MOF-74 (c), and Ni-MOF-74 (d) at 273 K (grey), 296 K (red), 318 K (blue), 353 K (yellow): Experiments (empty symbol),[4–7] computational using the proposed guest-host force field parametrization (full symbols).

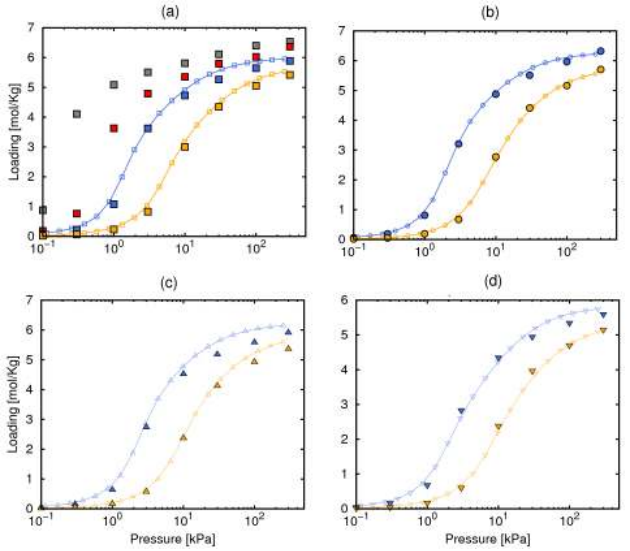

Figure A3.8 Single-component adsorption isotherms of propane in Co-MOF-74 (a), Fe-MOF-74 (b), Mn- MOF-74 (c), and Ni-MOF-74 (d) at 273 K (grey), 296 K (red), 318 K (blue), 353 K (yellow): Experiments (empty symbol),[4–7] computational using the proposed guest-host force field parametrization (full symbols).

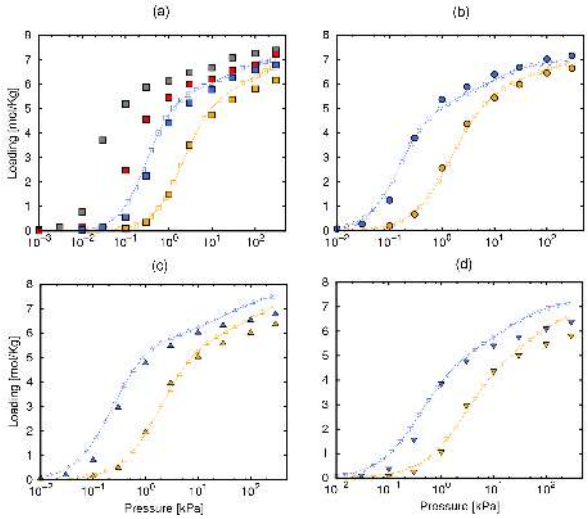

Figure A3.9 Single-component adsorption isotherms of propene in Co-MOF-74 (a), Fe-MOF-74 (b), Mn- MOF-74 (c), and Ni-MOF-74 (d) at 273 K (grey), 296 K (red), 318 K (blue), 353 K (yellow): Experiments (empty symbol),[4–7] computational using the proposed guest-host force field parametrization (full symbols).

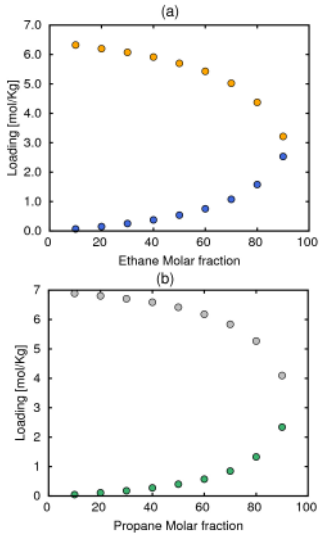

Figure A3.10 Adsorption loading of ethane (blue) / ethene (yellow) (a), and propane (green) / propene (grey) (b) in Fe-MOF-74 at 318 K and 1 bar as a function of the alkane concentrations in the bulk phase for the respective binary mixtures.

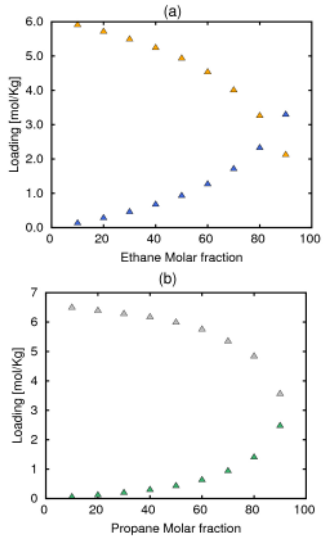

Figure A3.11 Adsorption loading of ethane (blue) / ethene (yellow) (a), and propane (green) / propene (grey) (b) in Mn-MOF-74 at 318 K and 1 bar as a function of the alkane concentrations in the bulk phase for the respective binary mixtures.

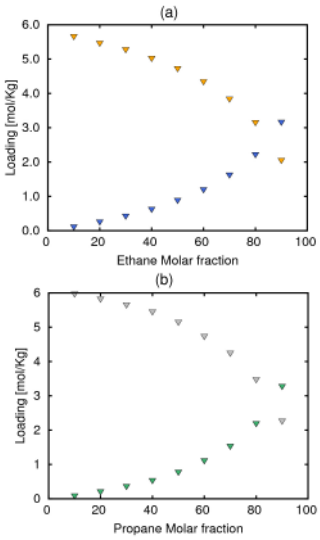

Figure A3.12 Adsorption loading of ethane (blue) / ethene (yellow) (a), and propane (green) / propene (grey) (b) in Ni-MOF-74 at 318 K and 1 bar as a function of the alkane concentrations in the bulk phase for the respective binary mixtures.

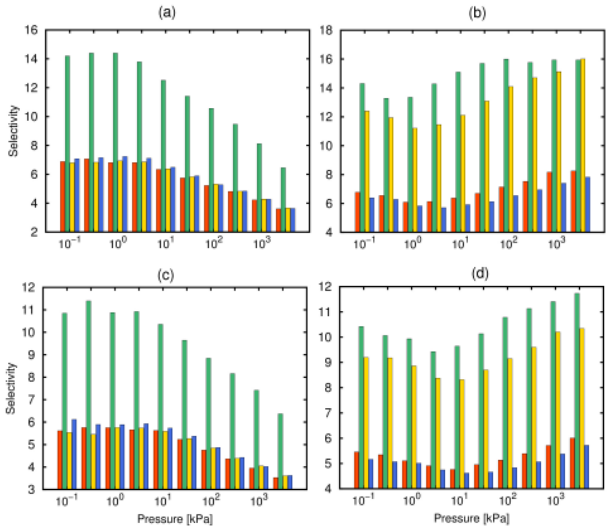

Figure A3.13 Adsorption selectivity of the equimolar ethane/ethane and propane/propene binary mixtures at 318 K (a and b respectively) and at 353 K (c and d) as a function of fugacity in Co-MOF-74 (red), Fe-MOF-74 (green), Mn-MOF-74 (yellow), and Ni-MOF-74 (blue).

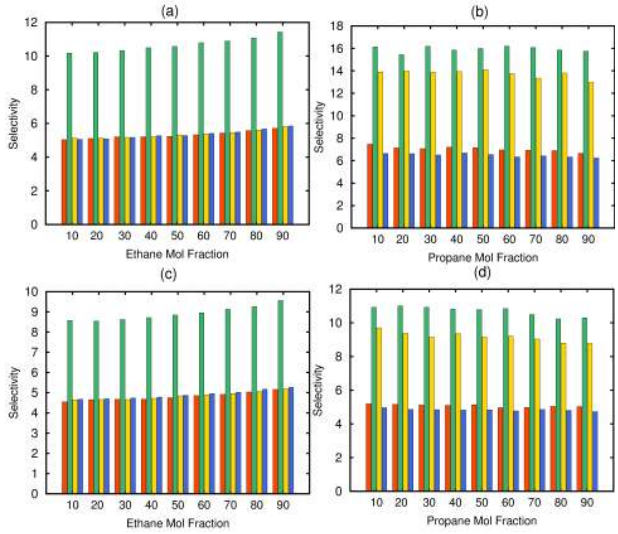

Figure A3.14 Adsorption selectivity of the ethane/ethane and propane/propene binary mixtures at 318 K (a and b respectively) and at 353 K (c and d) as a function of the alkane concentrations in the bulk phase in Co-MOF-74 (red), Fe-MOF-74 (green), Mn-MOF-74 (yellow), and Ni-MOF-74 (blue).

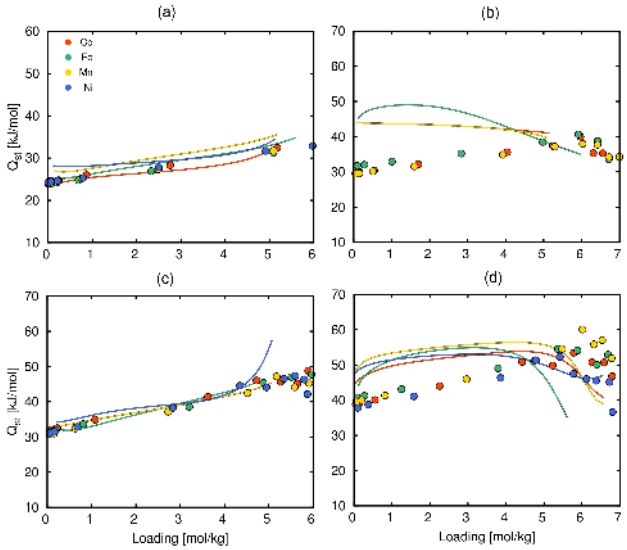

Figure A3.15 Heats of adsorption *vs* hydrocarbon loading computed using the developed force field (points) and taken from the literature 4 (lines) for ethane (a), ethene (b), propane (c), and propene (d).

Blibliography

1 D. Dubbeldam, S. Calero, T. J. H. Vlugt, R. Krishna, T. L. M. Maesen, E. Beerdsen, B. Smit, Phys. Rev. Lett. 2004, 93, 088302-088302.

2 D. Dubbeldam, S. Calero, T. J. H. Vlugt, R. Krishna, T. L. M. Maesen, B. Smit, J. Phys. Chem. B 2004, 108, 12301-12313.

3 B. Liu, B. Smit, F. Rey, S. Valencia, S. Calero, J. Phys. Chem. C 2008, 112, 2492-2498.

4 S. J. Geier, J. A. Mason, E. D. Bloch, W. L. Queen, M. R. Hudson, C. M. Brown, J. R. Long, Chem. Sci. 2013, 4, 2054-2061.

5 Y. He, R. Krishna, B. Chen, Energy & Environmental Science 2012, 5, 9107-9120.

6 E. D. Bloch, W. L. Queen, R. Krishna, J. M. Zadrozny, C. M. Brown, J. R. Long, Science 2012, 335, 1606-1610.

7 P. Mishra, S. Edubilli, B. Mandal, S. Gumma, J. Phys. Chem. C 2014, 118, 6847-6855.

Appendix 4

Improving Olefin Purification using Metal Organic Frameworks with Open Metal Sites

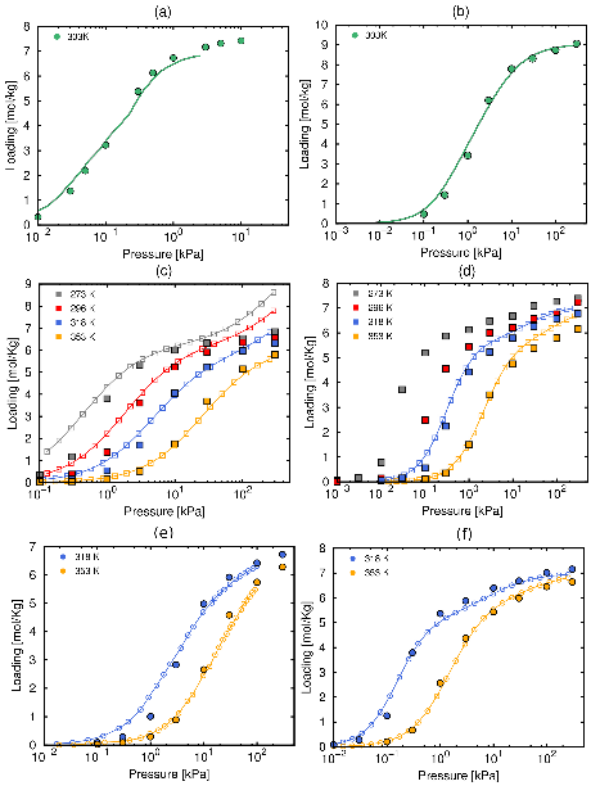

Figure A4.1 Adsorption isotherm of (a) isobutene (b) propene in Cu-BTC (c) ethene (d) propene in Co-MOF-74 (e) ethene and (f) propene in Fe-MOF-74. Comparison of simulations (closed symbols) and experimental data (lines and open symbols) taken from literature. [1–6]

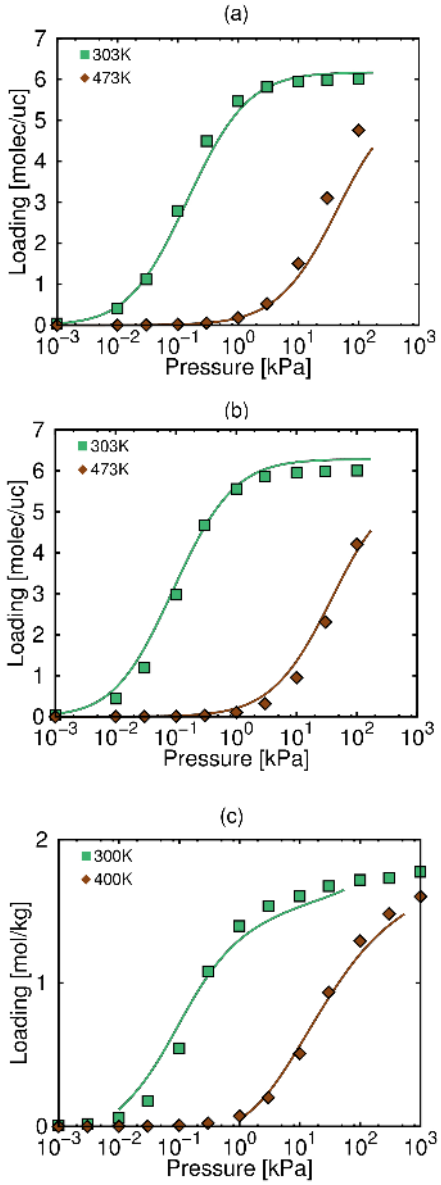

Figure A4.2 Adsorption isotherm of (a) 1,3-butadiene, (b) 2-trans-butene in DDR3 zeolite, and (c) 1- butene in MFI zeolite. Comparison of simulations (symbols) and experimental data (lines) taken from literature. [8,9]

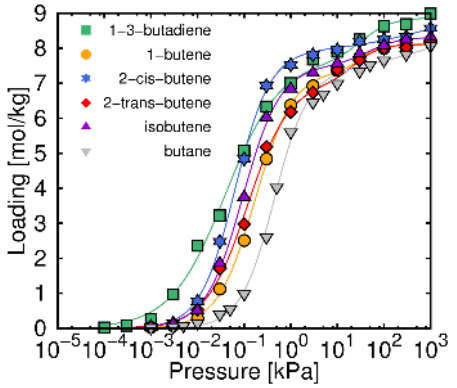

Figure A4.3 Pure adsorption isotherms of 1-3-butadiene, 1-butene, 2-cis-butene, 2-trans-butene, butane, and isobutene in Cu-BTC. Simulation (symbols) and isotherm fit (lines)

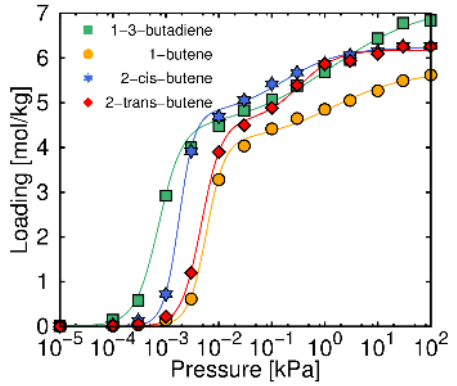

Figure A4.4 Pure adsorption isotherms of 1,3-butadiene, 1-butene, 2-cis-butene, and 2-trans- butene in Co-MOF-74. Simulation (symbols) and isotherm fit (lines).

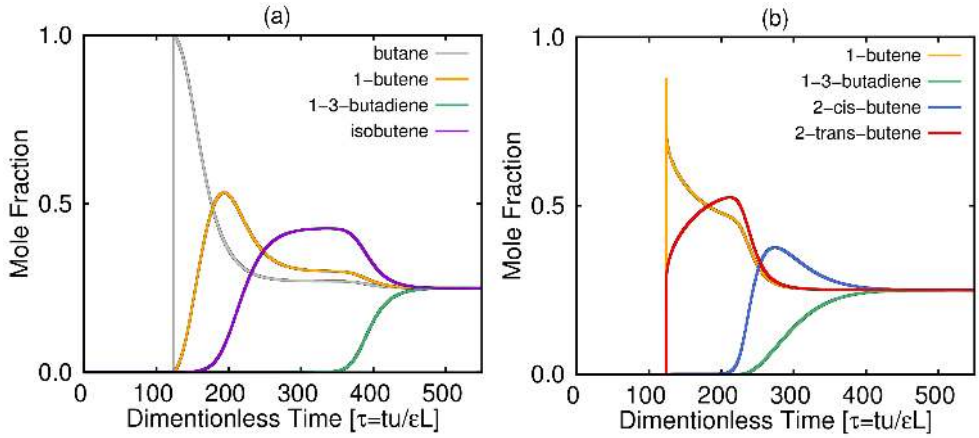

Figure A4.5 Transient breakthrough simulations for the separation of an equimolar multicomponent mixture of (a) 1,3-butadiene, 1-butene, butane, and isobutene and (b) 1,3-butadiene, 1-butene, 2- cis-buetene, and 2-trans-butene in Cu-BTC.

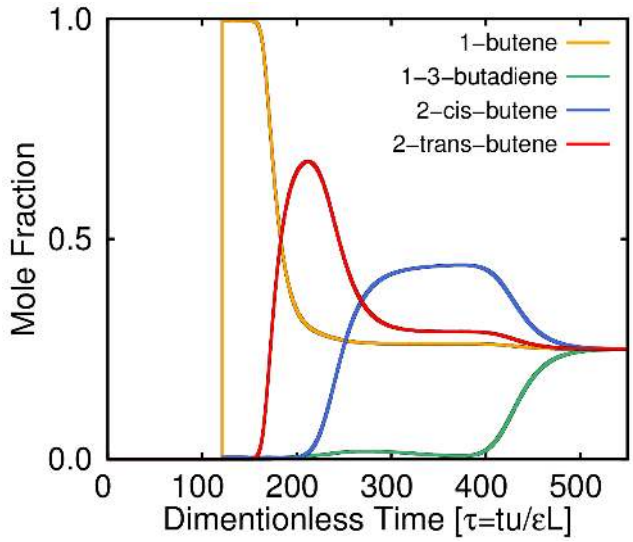

Figure A4.6 Transient breakthrough simulations for the separation of an equimolar multicomponent mixture of 1,3-butadiene, 1-butene, 2-cis-buetene, and 2-trans-butene in Co-MOF-74.

Table A4.1 Lennard-Jones parameters characterizing cross interactions between hydrocarbon (saturated and unsaturated) and framework atoms developed in previous work.[ref] ε_{ij}/k_B in K (top) and σ_{ij} in Å (bottom)

	Guest Pseudoatoms			
MOF-74	$CH_3\_sp_3$	$CH_2\_sp_3$	$CH_2\_sp_2$	CH_sp_2
O	72.142	51.948	66.945	50.538
	3.397	3.497	3.359	3.387
C	71.895	51.77	66.716	50.364
	3.617	3.717	3.579	3.607
H	28.745	20.698	26.673	20.136
	3.303	3.403	3.266	3.293
Co	27.597	19.872	25.609	19.333
	3.16	3.26	3.122	3.15
Fe	34.555	19.14	24.666	18.621
	3.177	3.277	3.14	3.167

Table A4.2 Binding Energies calculated with Perdew-Burke-Ernzerhof exchange correlation functional with an effective correction of 2 eV (PBE+U) and average equilibrium distances in Fe-MOF-74.

Adsorbates	**Binding Energies [kJ/mol]**		**Average Distances [Å]**	
	This work	Ref 10	This work	Ref 10
1,3-butadiene	-79.89	-	2.43	-
1-butene	-72.74	-55.2	2.84	2.32
2-cis-butene	-60.63	-40.9	2.97	3.15
2-trans-butene	-65.41	-31.4	3.2	3.31
isobutene	-	-41.8	-	2.7

Pure adsorption isotherms were fitted using Lagmuir-Freundlich dual-site model:

$$q = \frac{q_{sat1} b_1 P^{\alpha_1}}{1 + b_1 P^{\alpha_1}} + \frac{q_{sat2} b_2 P^{\alpha_2}}{1 + b_2 P^{\alpha_2}}$$

Table A4.3 Fitting parameters of 1-butene, 1-3-butediene, 2-cis-butene, 2-trans-butene, butane, and isobutene in Cu-BTC.

Adsorbates	q_{sat1} [mol/kg]	b_1	α_1	q_{sat2} [mol/kg]	b_2	α_2
1-butene	7.3758	6.4497	1.0629	0.71259	3.33E-04	2.3299
1-3-butadiene	7.659	11.003	0.74318	1.2163	8.29E-03	1.3622
2-cis-butene	7.9261	23.988	1.1539	1.0823	3.29E-02	0.54052
2-trans-butene	7.03	7.8757	0.96746	1.0884	7.00E-03	1.5731
Butane	7.2946	2.6869	1.2033	1.2978	3.43E-02	0.5178
Isobutene	7.5068	13.064	1.0847	0.8111	7.31E-03	1.282

Table A4.4 Fitting parameters of 1-butene, 1-3-butediene, 2-cis-butene, 2-trans-butene, butane, and isobutene in Fe-MOF-74

Adsorbates	q_{sat1} [mol/kg]	b_1	α_1	q_{sat2} [mol/kg]	b_2	α_2
1-butene	4.5154	0.0873	1.9612	1.6827	0.0097	0.6267
1-3-butadiene	5.2121	10.0805	1.5476	2.23066	0.01107	0.7095
2-cis-butene	5.3324	1.5687	1.5687	1.1988	0.0087	1.0577
2-trans-butene	4.529	0.1346	2.5819	1.9506	0.0033	1.1049

Table A4.5 Fitting parameters of 1-butene, 1-3-butediene, 2-cis-butene, 2-trans-butene, butane, and isobutene in Co-MOF-74

Adsorbates	q_{sat1} [mol/kg]	b_1	α_1	q_{sat2} [mol/kg]	b_2	α_2
1-butene	4.1031	5.17E+05	2.5582	1.5916	1.5916	0.6099
1-3-butadiene	4.4017	1.50E+06	1.9692	2.7975	2.7975	0.4842
2-cis-butene	4.7214	1.62E+08	2.983	1.5144	1.5144	0.7964
2-trans-butene	4.5822	1.76E+05	2.2532	1.5964	1.5964	1.2216

Blibliography

1 Yoon, J. W.; Jang, I. T.; Lee, K. Y.; Hwang, Y. K.; Chang, J. S., Bull. Korean Chem. Soc. 2010, 31, 220-223.

2 Hartmann, M.; Kunz, S.; Himsl, D.; Tangermann, O.; Ernst, S.; Wagener, A., Langmuir 2008, 24, 8634-8642.

3 Geier, S. J.; Mason, J. A.; Bloch, E. D.; Queen, W. L.; Hudson, M. R.; Brown, C. M.; Long, J. R., Chem. Sci. 2013, 4, 2054-2061.

4 Bloch, E. D.; Queen, W. L.; Krishna, R.; Zadrozny, J. M.; Brown, C. M.; Long, J. R., Science 2012, 335, 1606-1610.

5 He, Y.; Krishna, R.; Chen, B., Energy Environ. Sci. 2012, 5, 9107-9120.

6 Mishra, P.; Edubilli, S.; Mandal, B.; Gumma, S., J. Phys. Chem. C 2014, 118, 6847-6855.

7 Luna-Triguero, A.; Vicent-Luna, J. M.; Becker, T. M.; Vlugt, T. J. H.; Dubbeldam, D.; GÃşmez- ÃAlvarez, P.; Calero, S., ChemistrySelect 2017, 13,665-672.

8 Gucuyener, C.; van den Bergh, J.; Joaristi, A. M.; Magusin, P. C. M. M.; Hensen, E. J. M.; Gascon, J.; Kapteijn, F., J. Mater. Chem. 2011, 21, 18386-18397.

9 Stach, H.; Lohse, U.; Thamm, H.; Schirmer, W., Zeolites 1986, 6, 74-90.

10 Kim, H.; Jung, Y., J. Phys. Chem. Lett. 2014, 5, 440-446.

Appendix 5

Olefin/paraffin separation using aluminosilicates

Table A5.1 Intramolecular Lennard-Jones sets of parameters and point charges for the framework atoms and cations.ε_{ij}/k_B in K (top) and σ_{ij} in Å (bottom)

	O_{Al}	O_{Si}	Na^+	Ca^{2+}	CH_3	CH_2_sp3	CH_2_sp2	CH_sp2
CH_3	93	93	443.73	400	108.0	77.77	100.22	75.66
	3.48	3.48	2.65	2.6	3.76	3.86	3.723	3.75
CH_sp2	60.5	60.5	310	440.73	77.77	56	72.167	54.48
	3.58	3.58	2.95	2.8	3.86	3.96	3.823	3.85
CH_2_sp2	82.05	82.05	180	120	100.22	72.167	93.0	70.21
	3.53	3.53	2.75	2.95	3.723	3.823	6.685	3.713
CH_2_sp3	55.215	55.215	140	160	75.66	54.48	70.21	53
	3.502	3.502	3.02	3.29	3.75	3.85	3.713	3.74
Na^+	23	23	-	-	443.73	400	180	140
	3.4	3.4	-	-	2.65	2.6	2.75	3.02
Ca^{2+}	18	18	-	-	400	440.73	120	160
	3.45	3.45	-	-	2.6	2.8	2.95	3.29

Atom	O_{Al}	O_{Si}	Si	Al	Na^+	Ca^{2+}
q [e]	-1.20	-1.025	2.05	1.75	1.0	2.0

The description of cation sites in dehydrated structures reported in literature were used as starting point of cation location in NaY, NaX, CaX, LTA5A, and CaA zeolites. Note that during simulations, these cations can move. NaX zeolite exhibits four main preferential sites for cations.[1] At the center of the double six-ring (SI); in the sodalite cages, near to the six-ring shared by the double six-ring and the sodalite (SI'); in the plane of the six-ring shared by the sodalite and the large cavity (SII) and in the large cavity, symmetrically above the plane of four-ring of the sodalite (SIII).The schematic representation of the sites is depicted in Figure A5.1. The cations in zeolite NaY are preferentially located in SI' and SII,[2] and in CaX are preferentially located located in SI', SII, and SIII.[3] Six preferential sites for sodium cations can be found in zeolite LTA4A;[4] at threefold axis near to the six-ring plane (SI); out of the center, but in the planes of the eight-rings (SII) and at the large cavity, on a twofold axis and opposite a four-ring (SIII). In NaCaA (LTA5A) only SI sites are occupied by Na^+ and Ca^{2+} cations symmetrically distributed.[5] CaA has four preferential sites for cations, three of them are SI with slight displacements. Ca^{2+} cations are also found at SII with certain probability.[6]

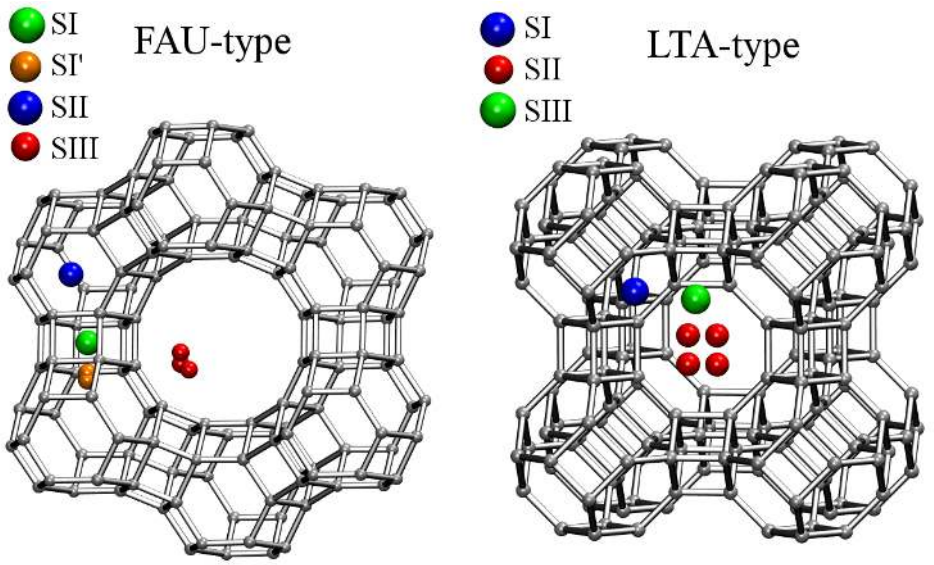

Figure A5.1 Schematic representation of FAU-type and LTA-type zeolites with the location of the cations according to NMR experiments.[1-6]

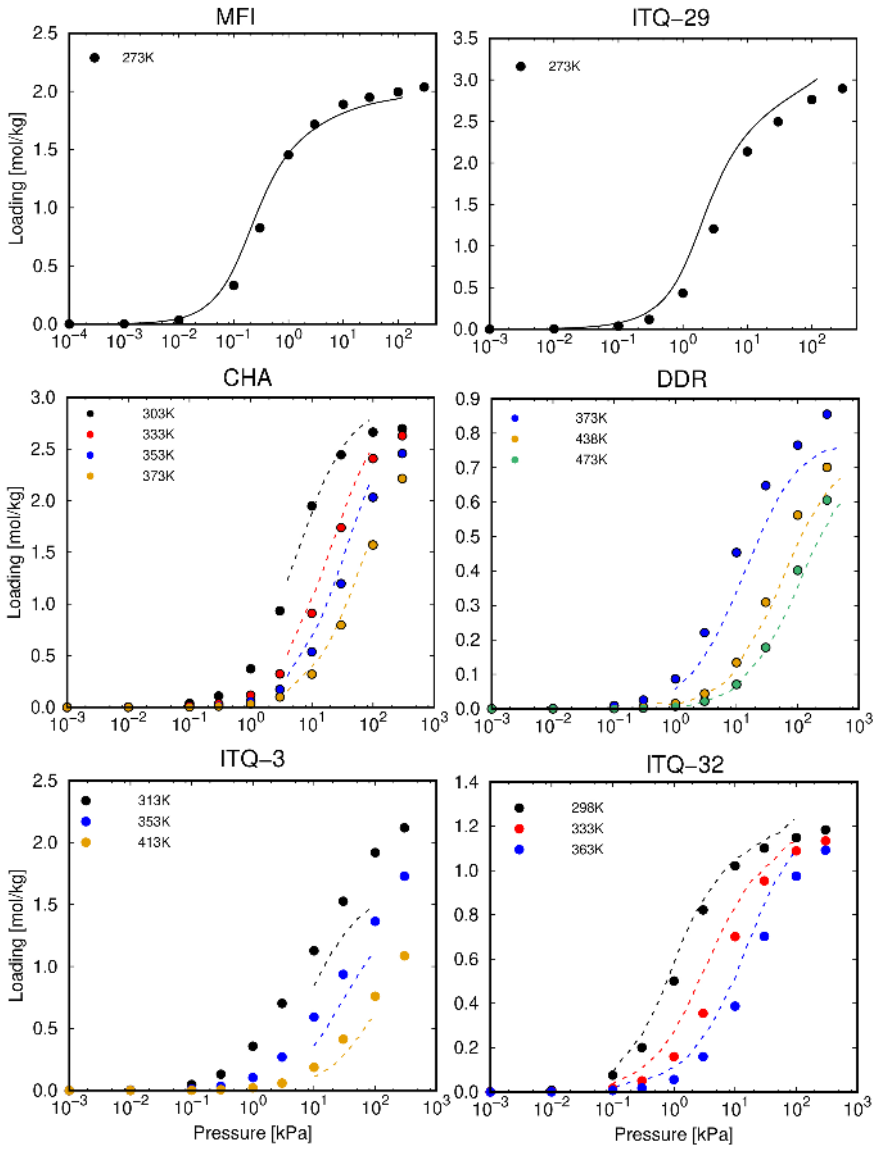

Figure A5.2 Adsorption isotherms of propylene in pure silica zeolites. Comparison of calculated and experimental data measured in this work (solid lines) and taken from the literature (dashed lines).[7–9]

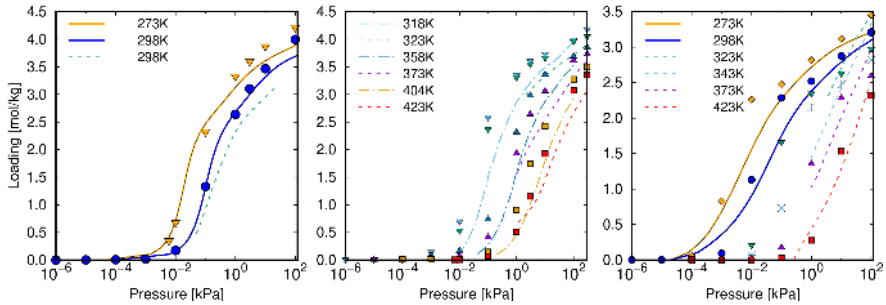

Figure A5.3 Adsorption isotherms of propylene in NaY, NaX and LTA5A at different temperatures. Comparison of calculated and experimental data measured in this work (solid lines) and taken from literature (dashed lines).[10–12]

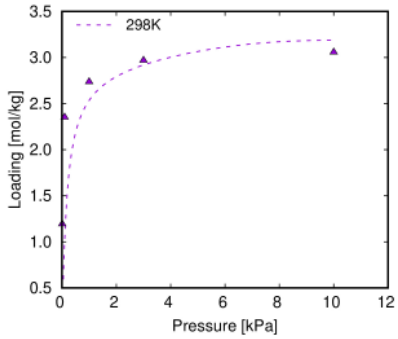

Figure A5.4 Adsorption isotherm of 1-butene in NaY at 298 K. Comparison of calculated and experimental data taken from the literature.[12]

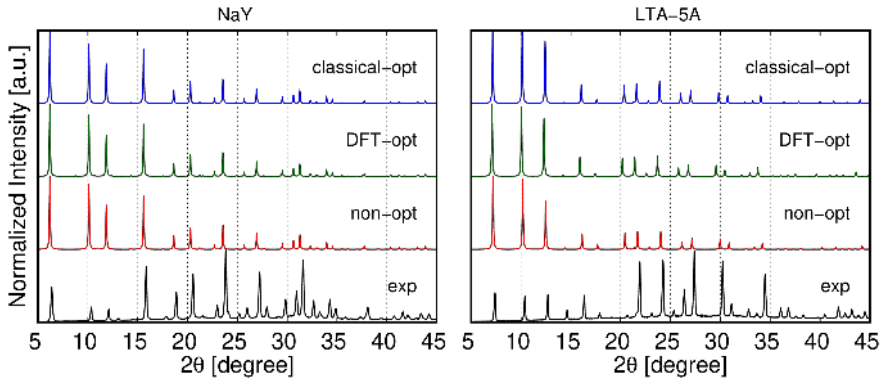

Figure A5.5 PXRD of NaY and LTA5A structures. Comparison between experiment and non-optimized, DFT optimized, and classical optimized structures. For the sake of clarity, the intensities of all peaks of the modelled diffractograms, except the first one at 6-7°, were multiplied by a scaling factor in order to be normalized with the corresponding first peak.

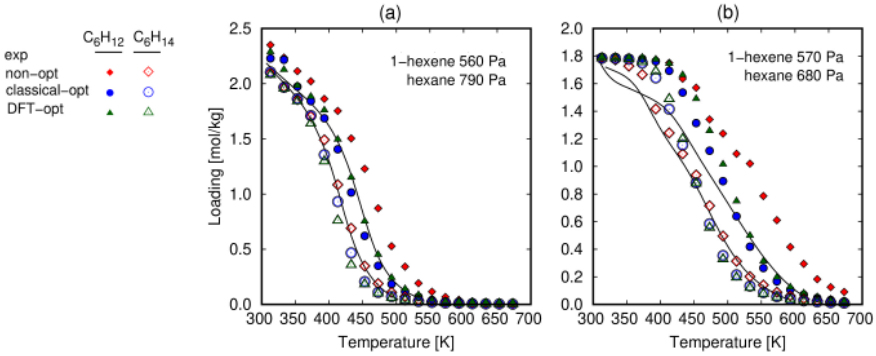

Figure A5.6 Comparison between adsorption isobars of hexane (open symbols) and 1-hexene (closed symbols) in (a) NaY and (b) LTA5A calculated in the non-optimized structures (red diamonds), DFT optimized structures (green triangles) and classically optimized structures (blue circles). Experimental data measured in this work is shown with solid lines.

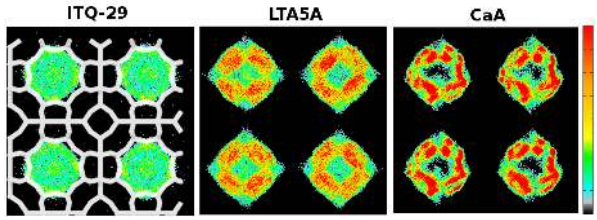

Figure A5.7 Average Occupation profiles for propene in LTA topology zeolites at 100 kPa and 298 K.

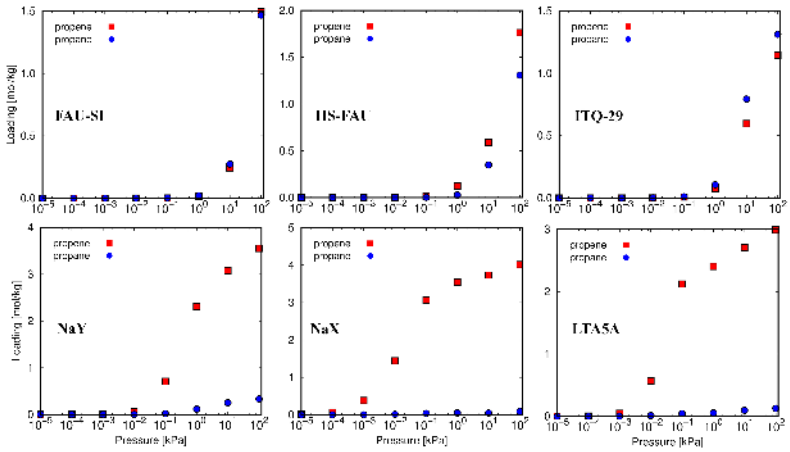

Figure A5.8 Equimolar adsorption isotherms of propane/propylene in pure silica FAU and ITQ-29 zeolites, and HS-FAU, NaY, NaX, and LTA5A aluminosilicates at 298 K.

Blibliography

1 Olson, D. H., Zeolites 1995, 15, 439-443.

2 Kaduk, J. A.; Faber, J., Rigaku J 1995, 12, 14-34.

3 Jang, S. B.; Song, S. H.; Kim, Y., Journal of the Korean Chemical Society 1995, 39, 7-13.

4 Subramanian, V.; Seff, K., A near Zero Coordinate Sodium Ion in Dehydrated Zeolite 4a, Na12-A. The Journal of Physical Chemistry 1977, 81, 2249-2251.

5 Barrachin, B.; de Lara, E. C., Journal of the Chemical Society, Faraday Transactions 2: Molecular and Chemical Physics 1986, 82, 1953-1966.

6 Firor, R. L.; Seff, K., J. Am. Chem. Soc. 1978, 100, 3091-3096.

7 Zhu, W.; Kapteijn, F.; Moulijn, J.; Den Exter, M.; Jansen, J., Langmuir 2000, 16, 3322-3329.

8 Olson, D. H.; Camblor, M. A.; Villaescusa, L. A.; Kuehl, G. H., Microporous Mesoporous Mater. 2004, 67, 27-33.

9 Palomino, M.; Cantín, A.; Corma, A.; Leiva, S.; Rey, F.; Valencia, S., Chem. Commun. 2007, 1233-1235.

10 Narin, G.; Martins, V. F.; Campo, M.; Ribeiro, A. M.; Ferreira, A.; Santos, J. C.; Schumann, K.; Rodrigues, A. E., Sep. Purif. Technol. 2014, 133, 452-475.

11 Grande, C. A.; Gigola, C.; Rodrigues, A. E., Ind. Eng. Chem. Res. 2002, 41, 85-92.

12 Palmas, S.; Polcaro, A. M.; Carta, R.; Tola, G., J. Chem. Eng. Data 1991, 36, 1-4.

Appendix 6

Phase Transition Induced by Gas Adsorption in Metal-Organic Frameworks

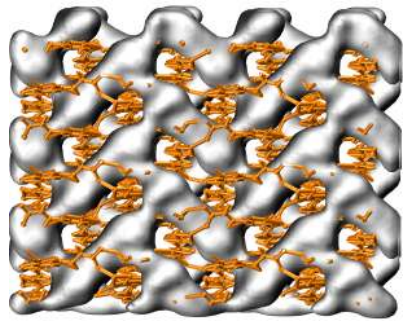

Figure A5.1 Pore connectivity of ZJU-198

Table A6.1 Energies and entropies of adsorption in the low coverage regime.

Structure	**Adsorbates**	ΔU [kJ/mol]	ΔH [kJ/mol]	ΔA [kJ/mol]	ΔG [kJ/mol]	ΔS [J/K/mol]
ZJU-198-NP	CO2	-38.75	-41.23	-6.84	-2.485	-130.01
	C2H2	-37.59	-40.07	-3.63	-2.481	-126.13
	C2H4	-33.37	-35.85	-2.48	-2.480	-111.97
	CH4	-20.81	-23.29	-1.76	-2.479	-69.83
	N2	-21.46	-23.94	-0.81	-2.479	-72.01
ZJU-198-LP	CO2	-40.91	-43.39	-7.96	-2.486	-137.26
	C2H2	-43.72	-46.20	-9.16	-2.487	-146.68
	C2H4	-35.95	-38.43	-7.42	-2.485	-120.62
	CH4	-23.26	-25.74	-4.75	-2.482	-78.04
	N2	-21.64	-24.12	-2.91	-2.481	-72.61

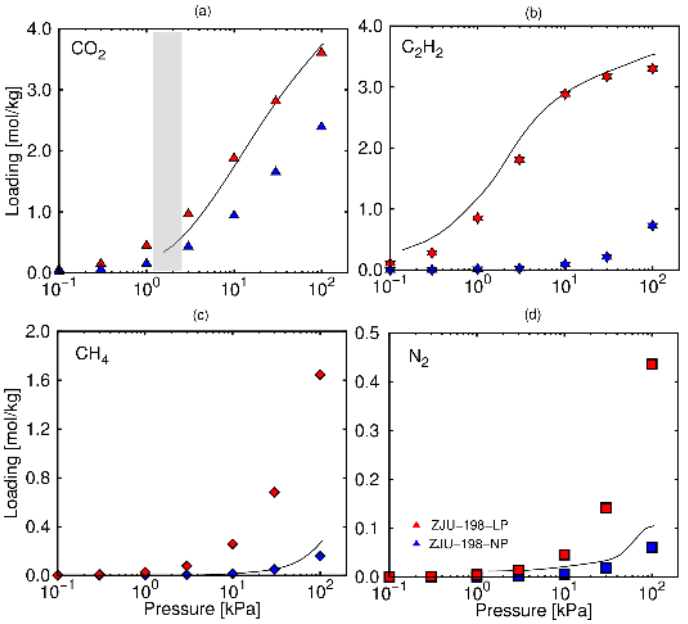

Figure A6.2 Adsorption isotherms of (a) carbon dioxide, (b) acetylene, (c) methane, and (d) nitrogen in ZJU-198-LP (red) and ZJU-198-NP (blue) at 298 K. Experimental data are included for comparison (lines).[1,2] The highlight zone indicates the estimated pressure of the phase transition.

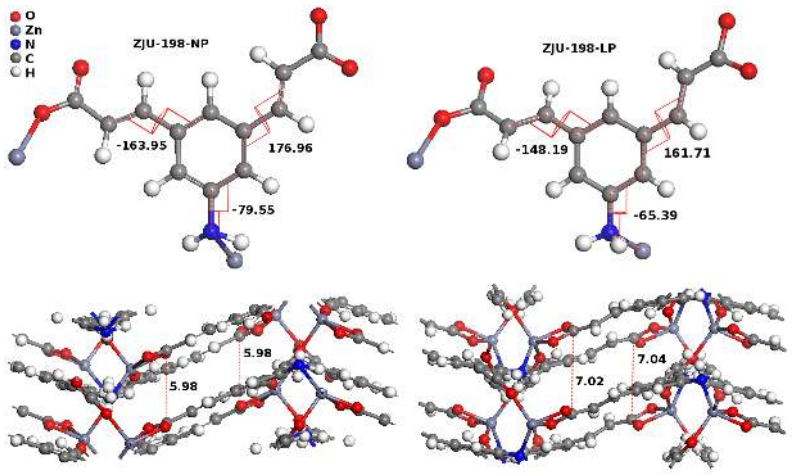

Figure A6.3 Schematic representation of structural changes. Rotation -torsion angles- of the organic linker (top) and representative distances during phase transition for ZJU-198-NP and ZJU-198-LP (bottom).

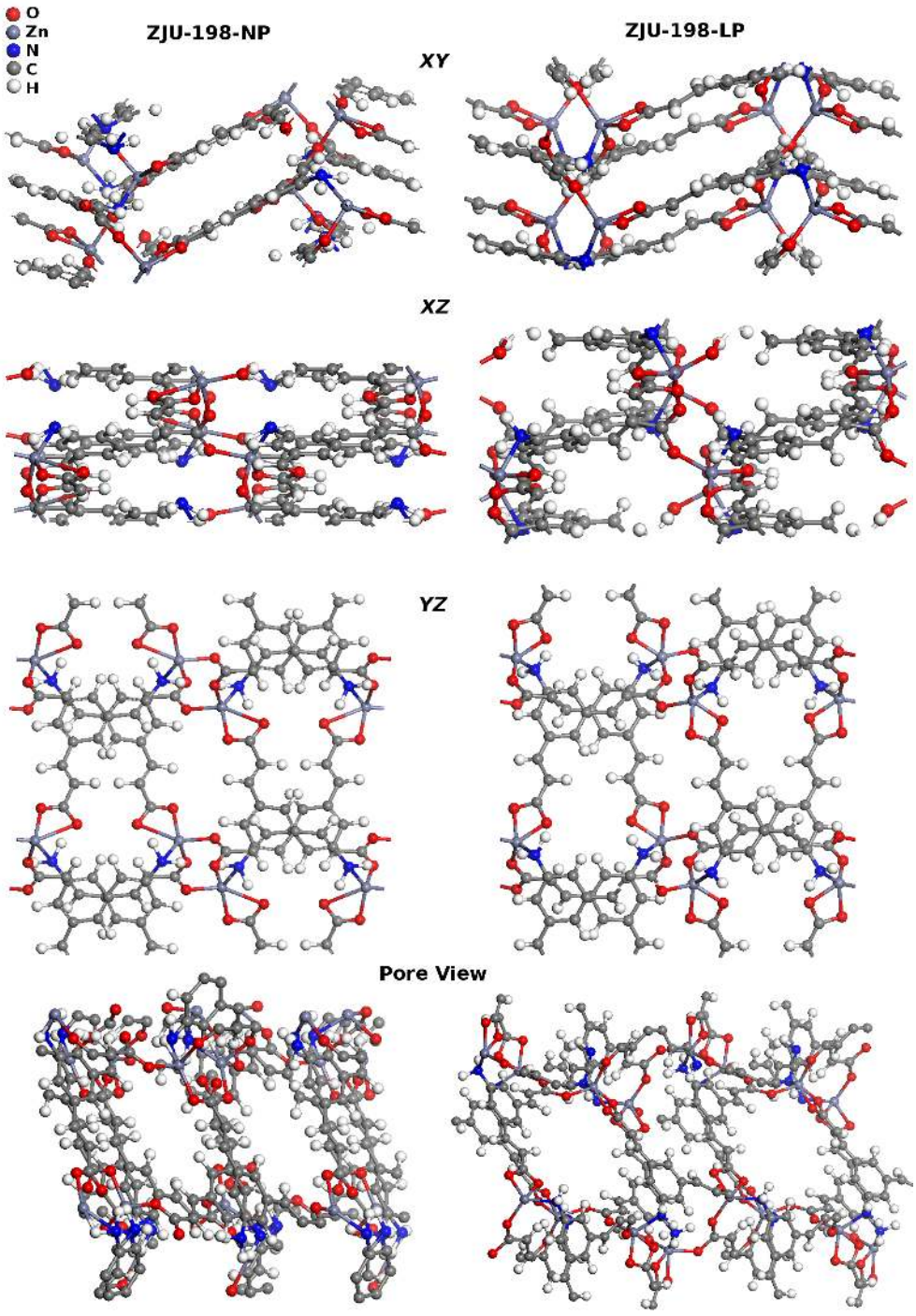

Figure A6.4 Schematic representation of the atomic connectivity of ZJU-198-NP and ZJU-198-LP from several views.

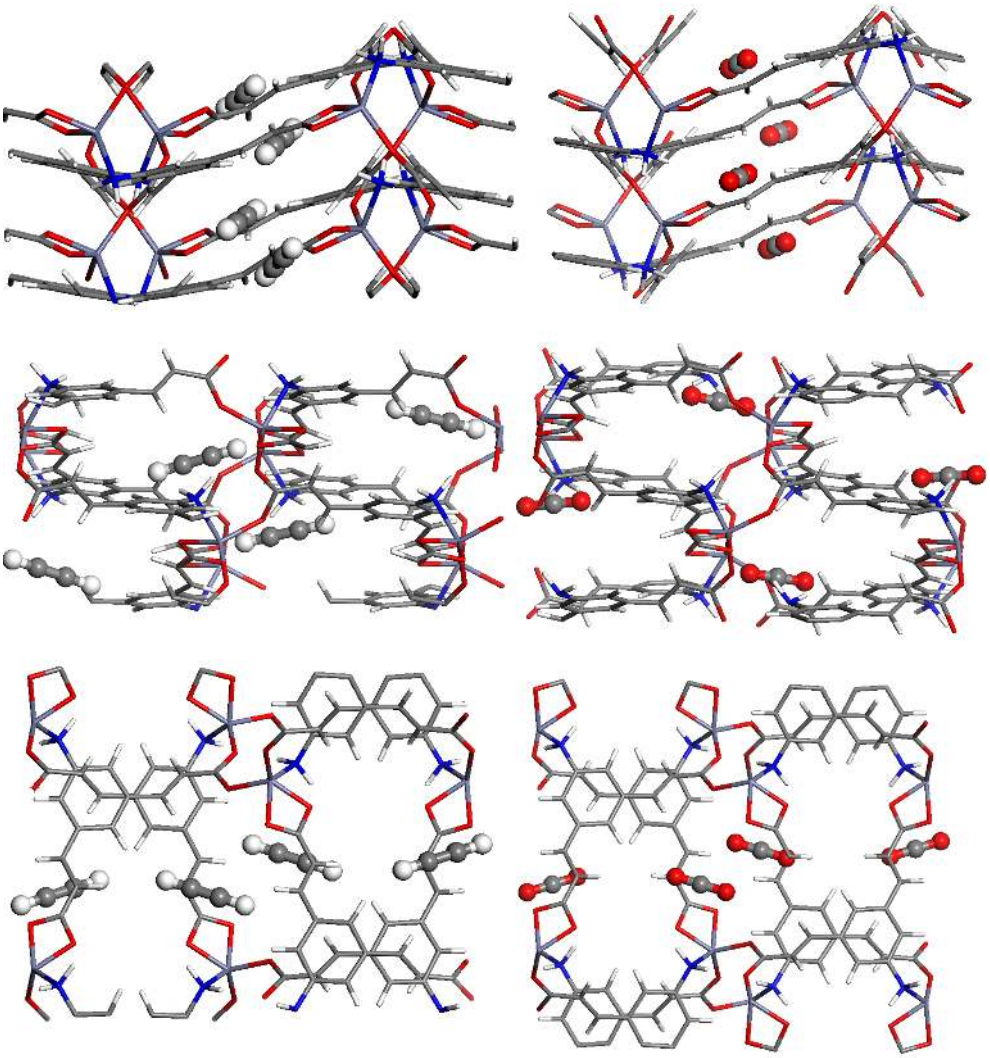

Figure A6.5 Schematic representation of ZJU-198-LP with molecules of carbon dioxide and acetylene adsorbed in the less energetic configurations.

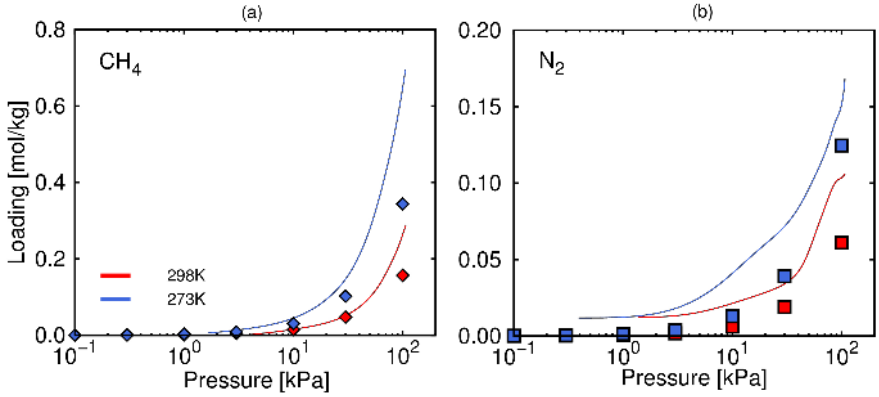

Figure A6.6 Adsorption isotherms of (a) methane and (b) nitrogen in ZJU-198- NP. Calculated data (symbols) and experiments taken from literature (lines).[1,2]

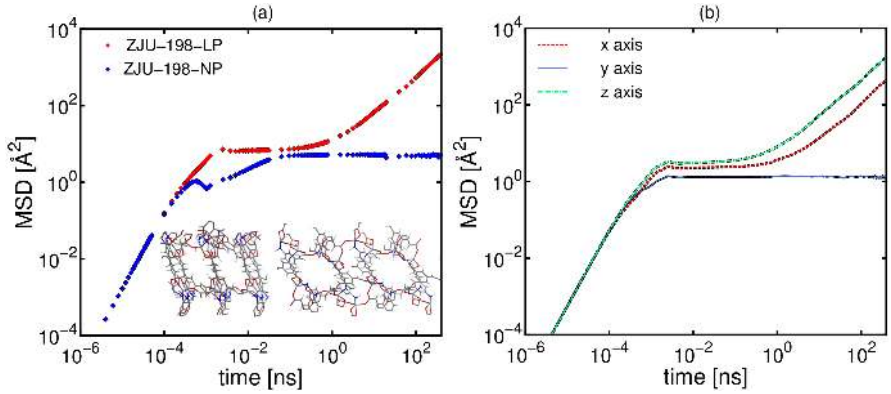

Figure A6.7 Mean Square Displacement (MSD) of carbon dioxide at 298 K in (a) ZJU-198-LP and -NP (b) MSD by axis in ZJU-198-LP.

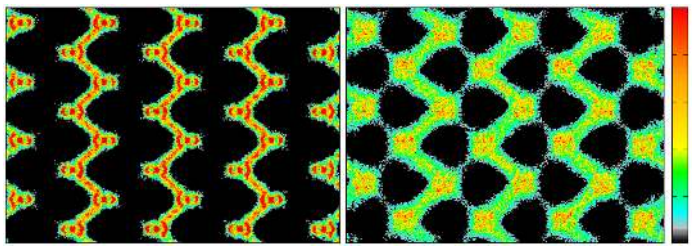

Figure A6.8 Average Occupation profiles of carbon dioxide in the ZX view of ZJU-198-NP (left) and ZJU-198-NP (right).

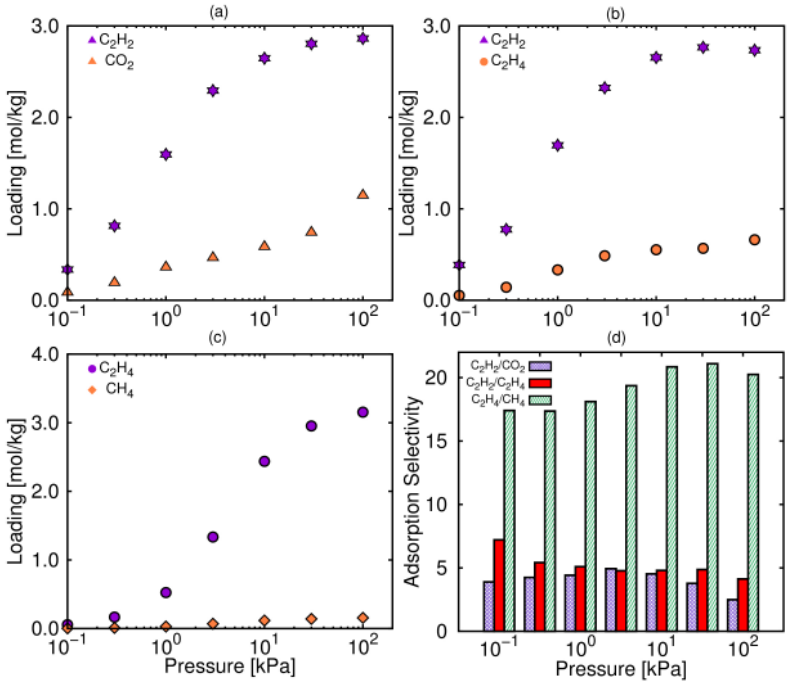

Figure A6.9 Adsorption isotherms of equimolar mixtures (a) C_2H_2 /CO_2 , (b) C_2H_2 /C_2H_4 , and (c) C_2H_4 /CH_4 at 273 K in ZJU-198-LP. (d) Adsorption Selectivity calculated from the adsorption isotherms of the mixtures.

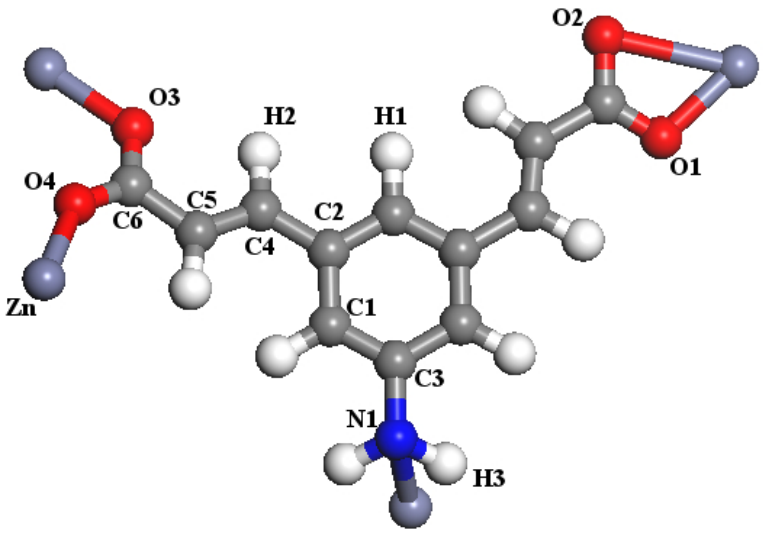

Figure A6.10 Schematic representation of the ZJU-198 organic ligand.

Table A6.2 Kinetic size of the adsorbates.[3]

Molecule	CO_2[3]	C_2H_2[2]	C_2H_4[2]	CH_4[2]	N_2[1]
Kinetic size [Å]	3.18x3.33	3.32x3.34	3.28x4.18	3.82x3.94	3.64x3.64

Table A6.3 Atomic charges calculated for ZJU-198.

Framework Atom	**Charge**
Zn	0.5
O1	-0.465
O2	-0.577
O3	-0.465
O4	-0.5
N1	-0.54
C1	-0.06
C2	-0.01
C3	0.107
C4	-0.145
C5	-0.08
C6	0.62
H1	0.15
H2	0.15
H3	0.15

Blibliography

1 Zhang, L.; Jiang, K.; Jiang, M. D.; Yue, D.; Wan, Y. T.; Xing, H. B.; Yang, Y.; Cui, Y. J.; Chen, B. L.; Qian, G. D., Chem. Commun. 2016, 52, 13568-13571.

2 Zhang, L.; Cui, X. L.; Xing, H. B.; Yang, Y.; Cui, Y. J.; Chen, B. L.; Qian, G. D., RSC Adv. 2017, 7, 20795- 20800.

3 Lin, R.-B.; Xiang, S.; Xing, H.; Zhou, W.; Chen, B., Coord. Chem. Rev. 2017.

Appendix 7

Acetylene Storage and Separation using Metal-Organic Frameworks with Open Metal Sites

Table A7.1 Crossed host-guest interaction parameters between acetylene and M-MOF-74, Cu-BTC, and PCN-16. ε_{ij}/k_B in K (top) and σ_{ij} in [Å] (bottom).

	MOF-74-C$_{(C_2H_2)}$	**Cu-BTC-C**$_{(C_2H_2)}$	**PCN-16-C**$_{(C_2H_2)}$
C	78.9618 3.0548	68.4335 4.0004	73.6977 3.273
H	31.569 2.7917	27.3598 3.6557	29.4644 2.9911
O	79.2335 2.8701	68.6691 3.7584	73.9513 3.0751
Co	40.4134 2.9889	-	-
Fe	38.9246 2.8775	-	-
Cu	-	12.0744 2.7658	30.1861 3.1115

Table A7.2 Point charges of M-MOF-74, PCN-16, and ZJNU-30.

	Co-MOF-74	Fe-MOF-74	PCN-16	ZJNU-30
C1	0.486	0.356	0.527	0.006
C2	-0.207	-0.148	-0.13	0.033
C3	0.2401	0.172	0.055	-0.045
C4	-0.124	-0.088	-0.018	0.013
C5	-	-	0.015	-0.035
C6	-	-	-0.013	0.155
C7	-	-	-	-0.05
C8	-	-	-	0.025
C9	-	-	-	-0.032
C10	-	-	-	-0.006
C11	-	-	-	-0.017
C12	-	-	-	-0.017
C13	-	-	-	-0.005
C14	-	-	-	-0.002
C15	-	-	-	-0.027
C16	-	-	-	0.014
C17	-	-	-	0.027
C18	-	-	-	-0.051
O1	-0.543	-0.601	-0.58	-0.623
O2	-0.611	-0.439	-0.579	-0.237
O3	-0.673	-0.56	-	-0.255
O4	-	-	-	-0.27
H1	0.096	0.0812	-	0.095
H3	-	-	0.07	0.034
H4	-	-	0.08	0.004
H5	-	-	-	0.02
H9	-	-	-	0.012
H10	-	-	-	0.007
H11	-	-	-	0.014
H12	-	-	-	0.016
H15	-	-	-	0.019
H16	-	-	-	0.009
H18	-	-	-	0.028
Co	1.3359	-	-	-
Fe	-	1.2268	-	-
Cu	-	-	1.273	-
Zr1	-	-	-	1.044
Zr2	-	-	-	1.037

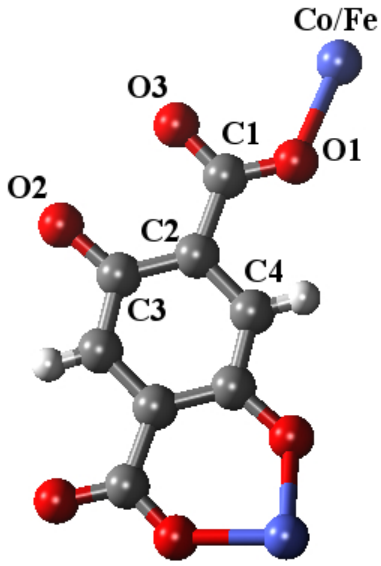

Figure A7.1 Schematic representation of the M-MOF -74 linker and atom labels.

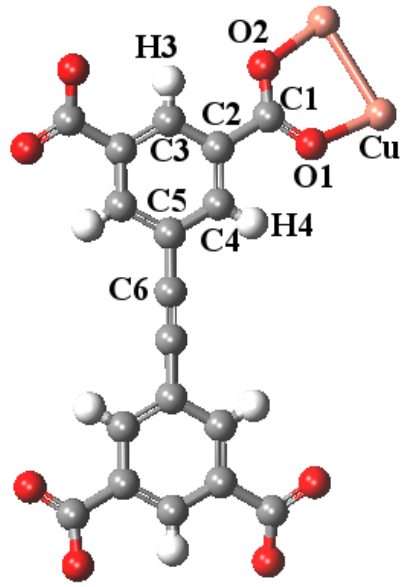

Figure A7.2 Schematic representation of the PCN-16 linker and atom labels.

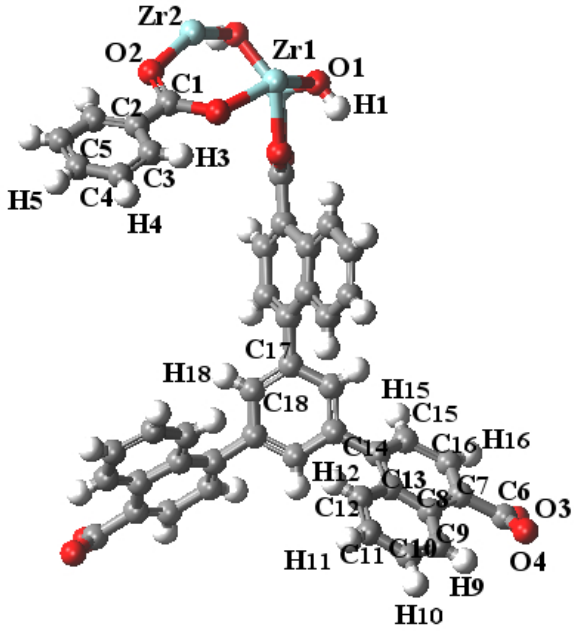

Figure A7.3 Schematic representation of the ZJNU-30 linker and atom labels.

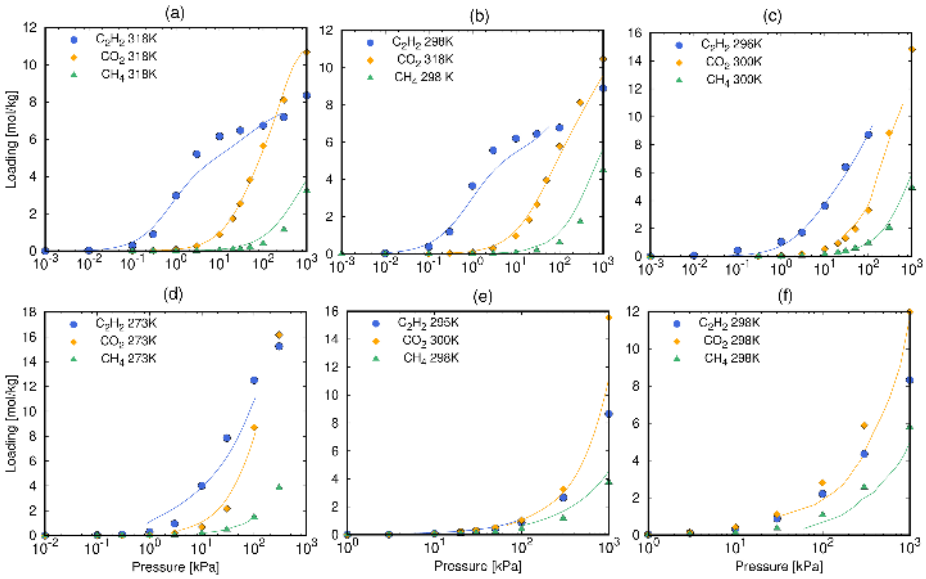

Figure A7.4 Pure adsorption isotherms of acetylene, carbon dioxide and methane. Comparison of computed and experimental results from the literature.[1–8]

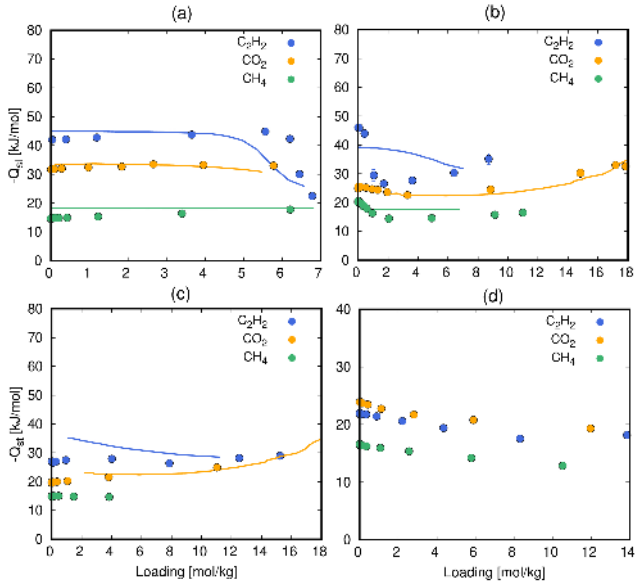

Figure A7.5 Heat of adsorption as a function of the loading of a) Co-MOF-74, b) Cu-BTC c) PCN-16, d) ZIF-8, and e) ZJNU-30. Comparison of simulation and experimental data from literature.[1–6,8]

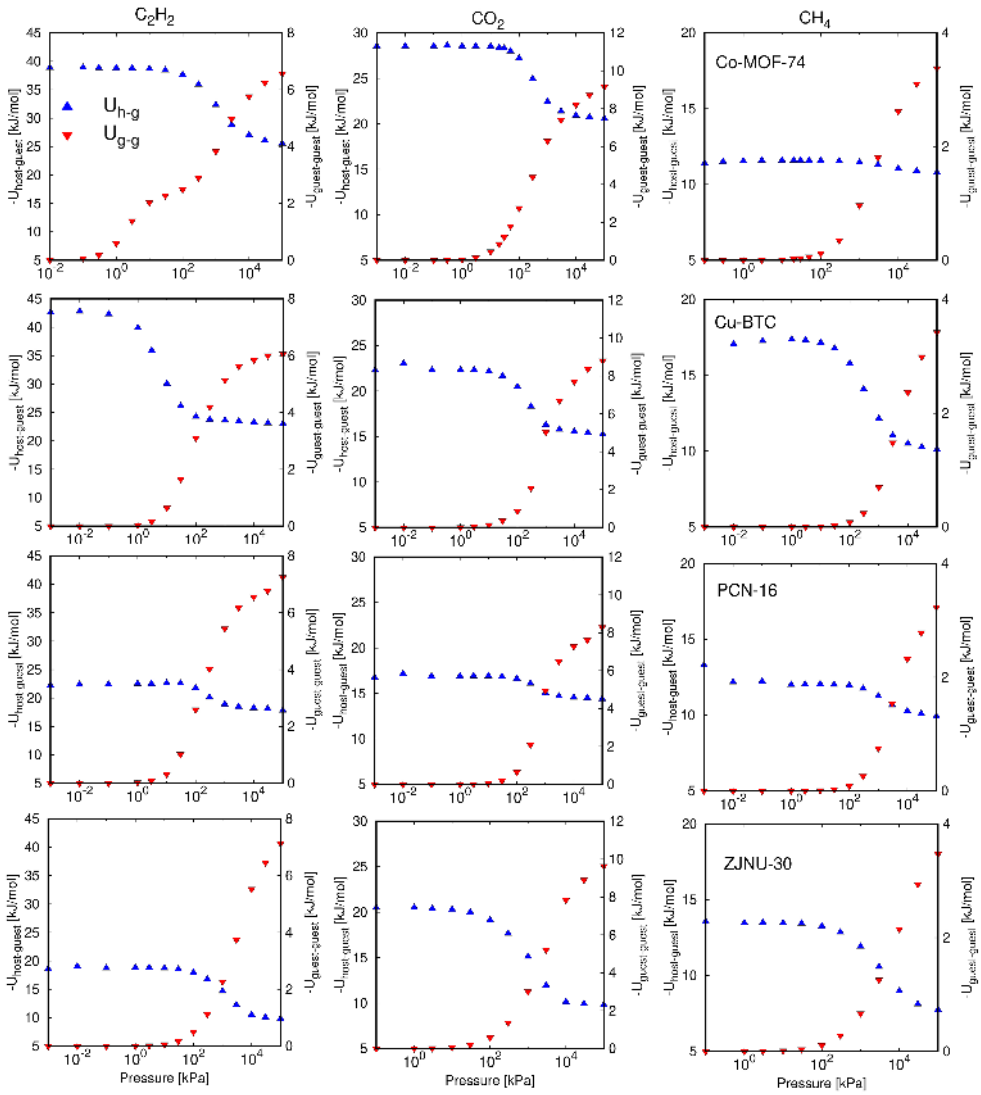

Figure A7.6 Potential energy of host-guest (blue) and guest-guest (red) interactions as a function of the pressure for acetylene, carbon dioxide, and methane in Co-MOF-74, Cu-BTC, PCN-16, ZIF-8, and ZJNU-30 at 318K.

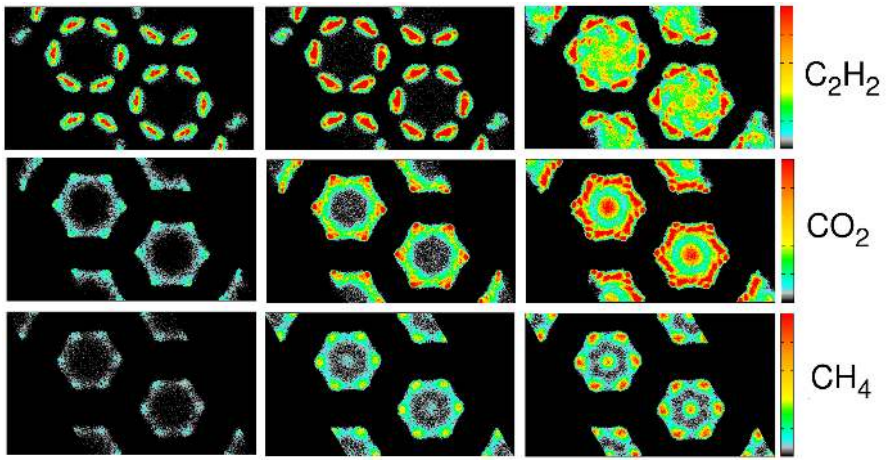

Figure A7.7 Average occupational profiles of pure adsorption of acetylene, carbon dioxide, and methane at low, intermediate, and high loading in Fe-MOF-74.

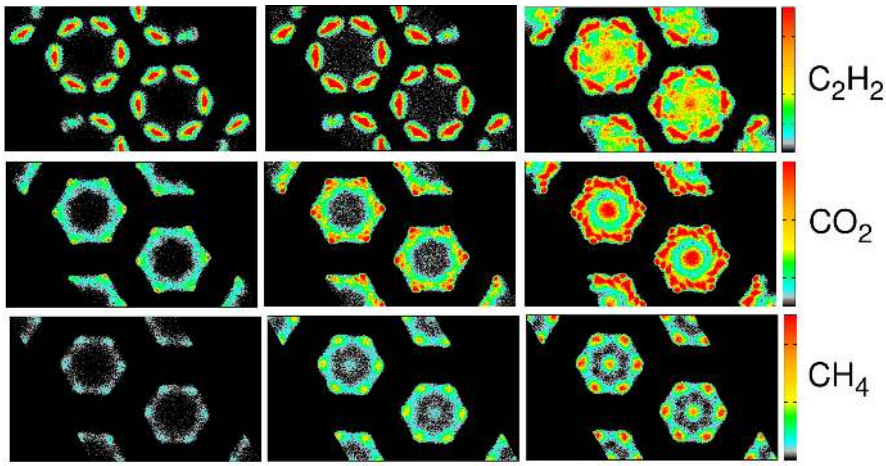

Figure A7.8 Average occupational profiles of pure adsorption of acetylene, carbon dioxide, and methane at low, intermediate, and high loading in Co-MOF-74.

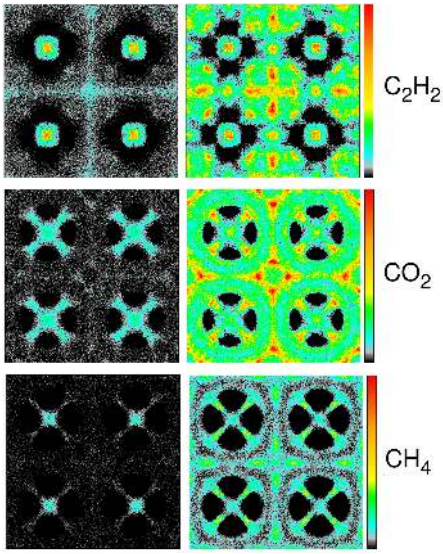

Figure A7.9 . Average occupational profiles of pure adsorption of acetylene, carbon dioxide, and methane at low and high loading in Cu-BTC.

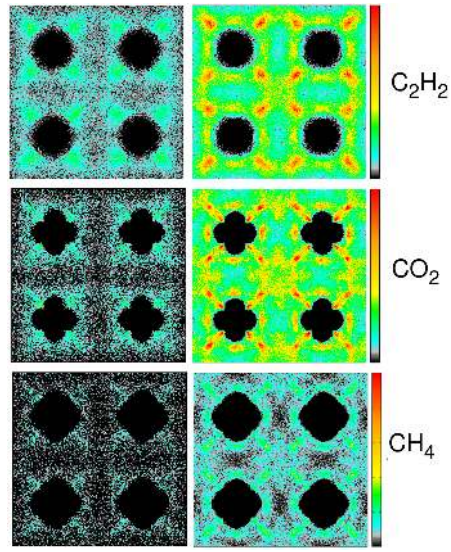

Figure A7.11 Average occupational profiles of pure adsorption of acetylene, carbon dioxide, and methane at low and high loading in IRMOF-1.

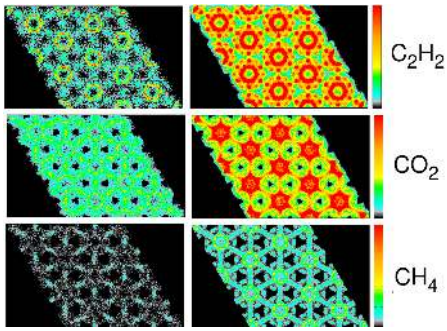

Figure A7.10 Average occupational profiles of pure adsorption of acetylene, carbon dioxide, and methane at low and high loading in PCN-16.

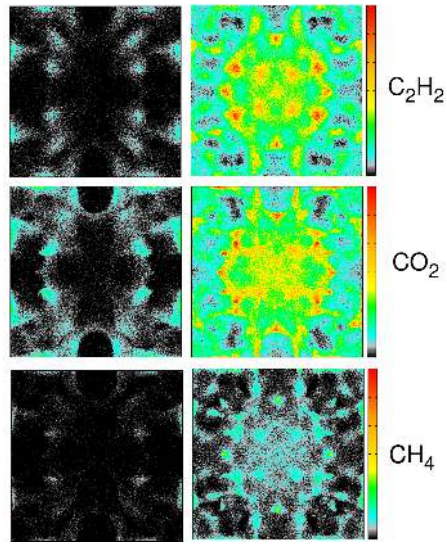

Figure A7.12 Average occupational profiles of pure adsorption of acetylene, carbon dioxide, and methane at low and high loading in ZJNU-30.

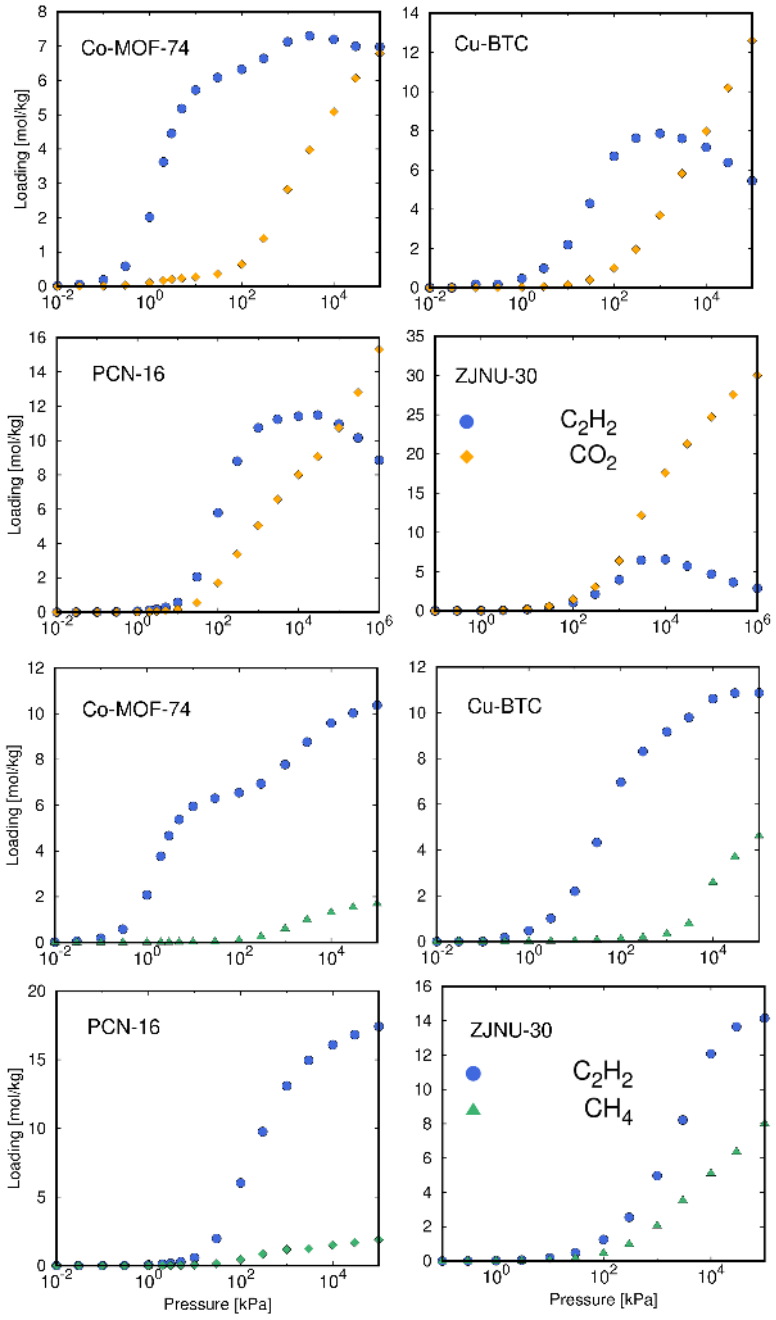

Figure A7.13 Equimolar adsorption isotherms of acetylene/carbon dioxide and acetylene/methane at 298 K.

Blibliography

1 Simmons, J. M.; Wu, H.; Zhou, W.; Yildirim, T., Energy Environ. Sci. 2011, 4, 2177-2185.

2 Queen, W. L.; Hudson, M. R.; Bloch, E. D.; Mason, J. A.; Gonzalez, M. I.; Lee, J. S.; Gygi, D.; Howe, J. D.; Lee, K.; Darwish, T. A., Chem. Sci. 2014, 5, 4569-4581.

3 Geier, S. J.; Mason, J. A.; Bloch, E. D.; Queen, W. L.; Hudson, M. R.; Brown, C. M.; Long, J. R.,Chem. Sci. 2013, 4, 2054-2061.

4 Bloch, E. D.; Queen, W. L.; Krishna, R.; Zadrozny, J. M.; Brown, C. M.; Long, J. R., Science 2012, 335, 1606-1610.

5 Xiang, S.; Zhou, W.; Gallegos, J. M.; Liu, Y.; Chen, B., J. Am. Chem. Soc. 2009, 131, 12415-12419.

6 Hu, Y.; Xiang, S.; Zhang, W.; Zhang, Z.; Wang, L.; Bai, J.; Chen, B., Chem. Commun. 2009, 7551-7553.

7 Zhou, W.; Wu, H.; Hartman, M. R.; Yildirim, T., J. Phys. Chem. C 2007, 111, 16131-16137.

8 Mason, J. A.; Veenstra, M.; Long, J. R., Chem. Sci. 2014, 5, 32-51.

Publications included in this thesis

- **Chapter 2**

  A. Luna-Triguero; J. M. Vicent-Luna; D. Dubbeldam; P. Gómez-Álvarez; and S. Calero. "Understanding and Exploiting Window-Effects for Adsorption and Separations of Hydrocarbons " *J. Phys. Chem. C*, 119 (19236-19243), **2015**.

- **Chapter 3**

  A. Luna-Triguero; P. Gómez-Álvarez; and S. Calero. "Adsorptive process design for the separation of hexane isomers using zeolites " *Phys. Chem. Chem. Phys.*, 19 (5037-5042), **2017**.

- **Chapter 4**

  A. Luna-Triguero; J. M. Vicent-Luna; T. M. Becker; T.J.H. Vlugt; D. Dubbeldam; P. Gómez-Álvarez; and S. Calero. "Effective Model for Olefin/Paraffin Separation using (Co, Fe, Mn, Ni)-MOF-74 " *ChemistrySelect*, 2 (665-672), **2017**.

- **Chapter 5**

  A. Luna-Triguero; J. M. Vicent-Luna; P. Gómez-Álvarez; and S. Calero. "Olefin/Paraffin Separation in Open Metal Site Cu-BTC Metal-Organic Framework " *J. Phys. Chem. C*, 121 (3126-3132), **2017**.

- **Chapter 6**

  A. Luna-Triguero; J. M. Vicent-Luna; A.Poursaeidesfahani; T.J.H. Vlugt; R. Sánchez-de-Armas; P. Gómez-Álvarez; and S. Calero. "Improving Olefin Purification using Metal Organic Frameworks with Open Metal Sites " *ACS Appl. Mater. Interfaces*, 10 (16911-16917), **2018**.

- **Chapter 7**

  A. Luna-Triguero; A. Sławek; R. Sánchez-de-Armas; J.J. Gutiérrez-Sevillano; C. O. Ania; J. B. Parra; J. M. Vicent-Luna; and S. Calero. “Olefin/paraffin Separation Using Aluminosilicates ” *Submitted*, **2019**.

- **Chapter 8**

  A. Luna-Triguero; J. M. Vicent-Luna; and S. Calero. “Phase Transition Induced by Gas Adsorption in Metal-Organic Frameworks ” *Chem. Eur. J.*, 24 (8530-8534), **2018**.

- **Chapter 9**

  A. Luna-Triguero; J. M. Vicent-Luna; R. M. Madero-Castro; P. Gómez-Álvarez; and S. Calero. “Acetylene Storage and Separation using Metal-Organic Frameworks with Open Metal Sites ” *Submitted*, **2019**.

Other Publications directly related to this thesis

- A. Luna-Triguero; A. Sławek; H. P. Huinink; T. J. H. Vlugt; A. Poursaeidesfahani; J. M. Vicent-Luna; and S. Calero “Enhancing the Water Capacity in Zr-based Metal-Organic Framework for Heat Pump and Atmospheric Water Generator Applications ” *ACS Appl. Nano Mater.*, DOI: 10.1021/acsanm.9b00416, **2019**

- J. Rogacka; F. Formalik; A. Luna-Triguero; L. Firlej; B. Kuchta; and S. Calero “Intermediate States Approach for Adsorption Studies in Flexible Metal-Organic Frameworks ” *Phys. Chem. Chem. Phys.*, 21, (3294-3303), **2019**

- T. M. Becker; A. Luna-Triguero; J. M. Vicent-Luna; L. Li-Chiang; D. Dubbeldam; S. Calero; and T.J.H. Vlugt “Potential of Polarizable Force Fields for Predicting the Separation Performance of Small Hydrocarbons in M-MOF-74 ” *Phys. Chem. Chem. Phys.*, 20 (28848-28859), **2018**

- J. G. Min; A. Luna-Triguero; Y. Byun; S. R. G. Balestra; J. M. Vicent-Luna; S. Calero; M. Camblor; and S. B. Hong, “Stepped Propane Adsorption in Pure-Silica ITW Zeolite ” *Langmuir*, 34 (4774-4779), **2018**.

- J. M. Vicent-Luna; A. Luna-Triguero; and S. Calero “Storage and Separation of Carbon Dioxide and Methane in Hydrated Covalent Organic Frameworks” *J. Phys. Chem. C*, 120 (23756-23762), **2016**

Acknowledgements/Agradecimientos

Al llegar al final de esta tesis, ese ente, ni persona ni cosa que me ha acompañado en sueños -y alguna que otra pesadilla- los últimos años toca sentarse a reflexionar.

Con todo el orgullo que se puede sentir al llegar al objetivo por el que se lucha, me deja también una sensación de vacío, de nostalgia, pero también de gratitud por todas esas personas que, de una forma u otra, lo han hecho posible.

Quiero agradecer a mis directoras Sofía y Paula por su continuo apoyo, por abrirme las puertas de un mundo que me apasiona, por enseñarme mucho, y no solo de ciencia, y en definitiva por estar a mi lado construyendo el principio de mi carrera investigadora.

Gracias a toda la gente del laboratorio, Ro, Juanjo, Ana, Salva, Ismael, Julio, Paco, José O. Carmen, Pilar, Madero, que habeis estado ahí desde el principio, simpre dispuestos a ayudar, a compartir experiencias, a organizar viajes y fiestas. Porque los segundos desayunos en el Santa Clara han salvado muchas mañanas y por las comidas en el laboratorio en las que hemos cambiado el mundo un poquito. Por que a veces hemos deseado tener esa cámara que captase los momentos mas locos, que dicho sea de paso, siempre son los mejores. Sin olvidarnos de Patrick, Said y Rabdel, simpre con la nota acertada, las mejores referencias memorizadas de forma casi mágica y con mucho humor (a veces difícil de entender).

Thank you to the nicest Polish people you can ever met. Thank you to Justyna, the kindest person ever, to try to understand my explanations, even when I don't. To Andrew, thank you to have allways an answer (no matter the hour), you are an example of hard working. Also thanks to Filip and Asia, the funiest and best dancers, Ali still asking for you all.

Quiero dar en especial las gracias a Madero, José O., Carmelo y Bea que han estado ahí desde mucho antes, y estarán depués, gracias por todos los momentos, que han sido muchos (pero muchos, muchos), que sin importar la distancia hemos conseguido estar, reunirnos y seguir sumando momentos con cualquier excusa, o sin ninguna. Porque con vosotros es un placer engordar, y se nos da genial.

A mi gente del *Reencuentro*, San, Yana, Nuri, Xavi(s), Marc, Agata, por las barbacoas de verano, los cafés que se alargan hasta altas horas de la madrugada, las hamburguesas del Cheers y todas las tradiciones que hemos creado. Gracias por estar siempre, por sacar tiempo para encontrarnos entre dos vuelos, un día, media hora y a veces hasta semanas enteras. Me habría encantado estar mas cerca y compartir mas historias, aunque las que tenemos no tienen desperdicio...

Thank you to all the people of the LSRE/LCM to welcome me to their group and make my live here as easy as possible. Thank you to Alexandre to teach me so much and be so patient.

Gracias Jose, mi compañero, mi amigo, mi familia, por el apoyo constante, por ayudarme a caminar, por empujarme a seguir cuando creo que no puedo, y por caernos juntos, porque así levantarse es mas fácil. No podría haber encontrado mejor persona para recorrer el mundo.

A Ali, que has hecho de cada día una aventura y has conseguido que el viaje sea mucho mas intenso y divertido. Mi pequeña gran inspiración.

A mi hermana, la mejor, por demostrar siempre que se puede, por hacer siempre lo que quieres y no rendirte a lo que “deberías”. Por hablar sin hablar, porque no recuerdo mi vida sin tí, pero seguro que faltarían muchas risas. Juntas somos imparables.

A mis padres, que me habeís apoyado siempre, que habeís confiado en mi aun cuando yo no lo hacía. Porque sin vosotros no estaría donde estoy, ni sería lo que soy. Sois un ejemplo a seguir, los mejores abuelos del mundo.

Sin olvidar al resto de mi familia, mis padrinitos, mis abuelos y los abuelos de Ali, a Charo, la mejor canguro del mundo, que habeis estado especialmete cerca estos años.

Gracias.

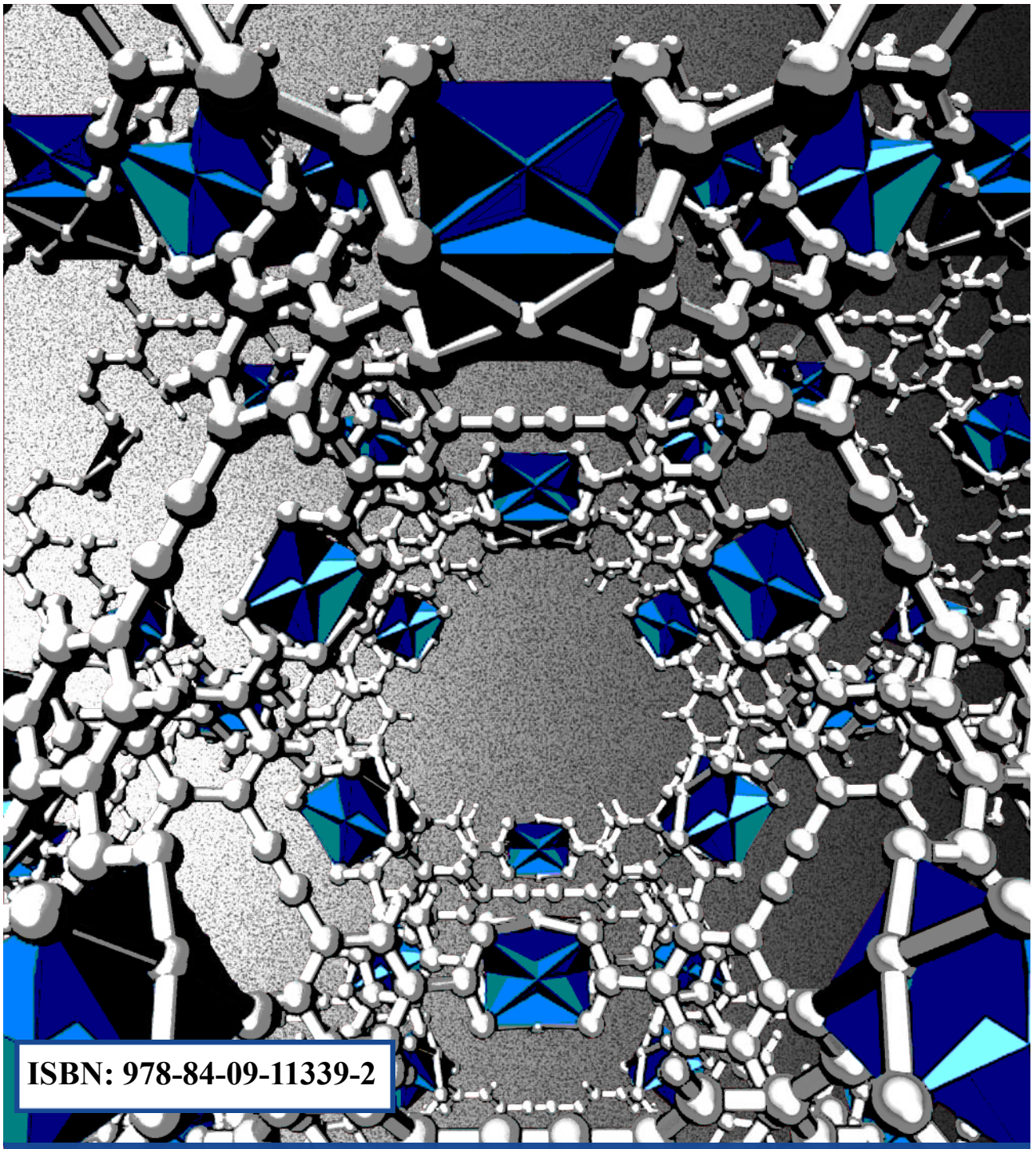

ISBN: 978-84-09-11339-2

UNIVERSIDAD PABLO DE OLAVIDE SEVILLA

GRUPO DE MATERIALES NANOESTRUCTURADOS CON APLICACIONES TECNOLÓGICAS